Degradation study of membrane-electrodes assemblies for durable operation in automotive proton exchange membrane fuel cells

Raphael Riasse

To cite this version:

Raphael Riasse. Degradation study of membrane-electrodes assemblies for durable operation in automotive proton exchange membrane fuel cells. Chemical engineering. Université Grenoble Alpes [2020-..], 2023. English. NNT : 2023GRALI120 . tel-04842205

HAL Id: tel-04842205
https://theses.hal.science/tel-04842205v1

Submitted on 17 Dec 2024

THÈSE

Pour obtenir le grade de

DOCTEUR DE L'UNIVERSITÉ GRENOBLE ALPES

École doctorale : I-MEP2 - Ingénierie - Matériaux, Mécanique, Environnement, Energétique, Procédés, Production
Spécialité : 2MGE - Matériaux, Mécanique, Génie civil, Electrochimie
Unité de recherche : Laboratoire d'Electrochimie et de Physico-Chimie des Matériaux et des Interfaces.

Etude de la dégradation d'assemblages membrane-électrodes de piles à combustible à membrane échangeuse de protons appliquée au domaine des transports pour l'amélioration de leur durée de vie

Degradation study of membrane-electrodes assemblies for durable operation in automotive proton exchange membrane fuel cells

Présentée par :

Raphael RIASSE

Direction de thèse :

Marian CHATENET PROFESSEUR DES UNIVERSITES, Université Grenoble Alpes	Directeur de thèse
Gaël MARANZANA Enseignant chercheur, Université de Lorraine	Co-directeur de thèse
Laetitia DUBAU DIRECTRICE DE RECHERCHE, CNRS	Co-encadrante de thèse
Julien DURST INGENIEUR DOCTEUR, Symbio	Co-encadrant de thèse

Rapporteurs :

Bruno AUVITY
PROFESSEUR DES UNIVERSITES, Université de Nantes
Juan HERRANZ
SENIOR SCIENTIST, Paul Scherrer Institut

Thèse soutenue publiquement le **8 décembre 2023**, devant le jury composé de :

Marian CHATENET PROFESSEUR DES UNIVERSITES, Grenoble INP	Directeur de thèse
Bruno AUVITY PROFESSEUR DES UNIVERSITES, Université de Nantes	Rapporteur
Juan HERRANZ SENIOR SCIENTIST, Paul Scherrer Institut	Rapporteur
Sophie DIDIERJEAN PROFESSEURE DES UNIVERSITES, Université de Lorraine	Examinatrice
Yves WOUTERS PROFESSEUR DES UNIVERSITES, Grenoble INP	Président
Corine BAS PROFESSEURE DES UNIVERSITES, Université de Chambéry	Examinatrice

Invités :

Julien DURST
INGENIEUR DOCTEUR, Symbio
Gaël MARANZANA
PROFESSEUR DES UNIVERSITES, Université de Lorraine

Ever tried. Ever failed. No matter. Try again. Fail again.

Fail better.

Samuel Beckett

Remerciements

Et pour finir la rédaction de cette thèse, il est à présent temps de remercier tous ceux qui m'ont soutenu, accompagné, aidé et qui ont transformé cette thèse en un souvenir et une expérience impérissables.

Dans un premier temps, je souhaite remercier les membres du jury qui ont accepté d'évaluer ces travaux. Je remercie ici Mesdames Sophie Didierjean et Corine Bas ainsi que Messieurs Bruno Auvity, Juan Herranz et Yves Wouters pour la qualité et la pertinence de la discussion qui a suivi la présentation ainsi que pour les conseils apportés (et promis Yves, j'essayerai de de me prémunir autant que possible du fléau des « Du coup », « Au fait » et des « Ben »).

En parlant des personnes qui ont évalué mon travail, comment ne pas penser à Valérie et Olivier, vous qui avez assisté à tous mes CSI pour suivre l'avancée de ma thèse. Merci d'avoir répondu présents à notre appel et d'avoir été si bienveillants.

Il me faut aussi remercier les personnes sans qui cette thèse n'aurait pas eu lieu, notamment la team Faurecia qui a initié toutes les démarches : un grand merci à Christophe Vacquier, Edouard Barrieu, Gauthier Queney et Pierrick Balestriere pour m'avoir lancé dans ce parcours. Ce parcours qui s'est déroulé avec le soutien de Symbio, sous l'impulsion de Renaut, et le service partagé par Luis et Julien de s'occuper du bébé x) Un grand merci à vous deux et à Laurent pour les discussions et l'aide que vous m'avez apporté. Bien sûr je n'oublierai pas l'équipe HVM, Lisa, Nathalia, Joëlle, Mathias… Tant de personnes que j'aurai croisées là-bas !

Mais cette thèse, cela fût aussi et surtout beaucoup de temps passé au LEPMI avec tous mes collègues pendant ces 3 années + 1 Covid…

Parce que la thèse, ce n'est pas des manips qu'on peut toujours faire seul, et que le labo compte des personnes avec une expertise réelle dans ses rangs, je remercie ici Michel et Vincent, pour votre accompagnement sur le Raman et sur l'ICP-MS, ainsi que pour nos discussions musiques/festoches ou encore les petites séances de bricolage debout sur les paillasses pour percer des trous dans tous les murs du labo ! Vincent, un très grand merci à toi pour m'avoir accompagné dans l'achat et l'installation des équipements pour mon banc. On serait quand même bien dans la m…. sans toi ! Merci aussi à l'équipe du CMTC : Joëlle, Frédéric, Rachel, Francine pour vos conseils sur le MEB et la prépa d'échantillons et aussi à Thierry et Stéphane pour votre expertise DRX !

Parce que la thèse, ce n'est pas que de la science, un gros big up à toute l'équipe support avec nos mamans de l'admin ! Claire B., Yasmine, Claire G., Claire T. et Corinne. Tenez bon, votre travail nous est indispensable ! Je reviendrai vous faire un petit coucou à l'occas :p Merci aussi à Alexis, d'avoir rejoint leurs rangs en très bon correspondant info ! Continue de bien faire courir Claire, ça la défoule ! Et Yasmine, pense à râler moins fort :p Bon tu me diras, il parait que ça conserve. Laure, je te glisse ici, tu es fantastique dans toute l'aide et l'énergie que tu apportes, merci pour tout ! Un grand merci à Fannie aussi, notre directrice, pour avoir été à l'écoute de nos discussions et pour son investissement dans la gestion du labo.

Parce que la thèse c'est aussi des rencontres, merci à Christine Lancelon-Pin pour son super accueil au Cermav pour faire des manips trop cools juste avant la soutenance !

Parce que la thèse, c'est aussi des voyages, je remercie l'accueil sensationnel du LEMTA, mon deuxième labo ! Avec les soucis et délais de manip, je n'ai pas pu passer autant de temps chez vous que prévu initialement, mais vous aurez été tellement chouettes… Même quand l'horoscope du matin te dit que la journée sera bof, tu l'oublies dès que tu refermes le journal tellement l'équipe est agréable. Valérie, merci pour l'accueil et les démarches admin, Jérôme, le Seigneur des bancs de test, merci pour ton accompagnement et ton soutien pour que mes manips se passent pour le mieux, merci aussi à mes collègues de bureau, Rémi, Marine et Mégane, mais aussi aux voisins William et Guillaume. Enfin merci à Giuseppe (pour ta recette du tiramisu :p) et à Gaël pour ces très bons moments que j'ai passés en votre compagnie à Nancy, j'ai pas mal de bons souvenirs en tête x) Hâte de vous retrouver à l'occasion !

Parce que la thèse, c'est aussi de l'accompagnement, je tiens à remercier ceux qui m'ont aidé à l'amener à son terme : Julien, Laetitia, Gaël et Marian. Merci d'avoir été aux rendez-vous pour faire le point, de m'avoir apporté vos lumières et d'avoir été si sympathiques et agréables au quotidien ou pendant nos rencontres. Surtout, merci de m'avoir fait confiance et d'avoir donné le meilleur de vous-mêmes pendant ma rédaction, quitte à sacrifier une partie de vos nuits pour me relire quand la deadline semblait beaucoup trop proche. Ce manuscrit voit le jour, et c'est aussi et naturellement grâce à vous.

Et parce que la thèse, c'est aussi le moment de s'amuser et de travailler dans la bonne ambiance, merci à tous mes collègues du LEPMI ! Merci à tous les permanents qui nous encadrent, nous accompagnent et qui montent des projets pour pouvoir nous embaucher, nous, petits non-permanents ! Merci à Clémence et Florent, mes partenaires d'études RDE-GDE-DC : promis Clémence je ferai appel à toi pour mon prochain brainstorming de graphical abstract et au grand Monsieur Vandenburghe (je m'en remets toujours pas x)), le meilleur pour la suite ! Camille, ma grande sœur que je n'ai jamais eue, vas-y moins fort sur le bullying avec tes collègues californiens, ils sont pas prêts XD et Arnaud, pour tous nos échanges, souvent mouvementés x) à vous deux, juste… Merci, seulement vous pourrez comprendre le poids que j'y mets. Mes collègues de bureau de toujours, Matthieu, bon courage mon poulain, garde confiance en toi et je te souhaite de t'épanouir dans la vie ! Sedik, tout le meilleur pour là où le vent t'emmènera ! Aux légendes, Raph et Tristan, dont les prénoms résonnent encore dans le labo. Aux deux Pitchounes d'à côté, Théo et Arthur, à très bientôt au block, bande de grimpeurs de l'extrême. A la précédente génération, Guillaume, Marine, Vivien, Delphine, Marie, Estelle (eh oui, toi aussi !) merci de m'avoir intégré et merci pour votre amitié partagée depuis <3. François, je compte sur toi pour continuer de faire vivre les blind-tests au milieu du labo, tu es mon seul espoir. A la relève, Axelle and Aleksandr, bon courage avec tes gros adsorbats dégueulasses and good luck with the GDE setup and experiments for your PhDs x) Garance, fais en sorte que papi Arnaud râle bien, embête le bien x) Delphine, encore deux ou trois prix de présentation, sinon tu pourras pas soutenir. Continue comme ça Parfait, tu tiens le bon bout ! Mathilde et Youcef, on va continuer de se voir pendant un petit moment encore x) Bon courage à vous dans vos activités ! Et pour finir, Julien… Ils vont tous comté sur toi à présent ;)

Marian… Tu as été mon prof en école et tu m’as fait confiance pour que je démarre une thèse avec toi, tu m’as accompagné et formé pendant cette expérience professionnelle. Je te remercie pour toutes les compétences que j’ai pu acquérir grâce à toi, qu’elles soient scientifiques, bibliographiques, pédagogiques ou relationnelles. Je n’ai pas de doute sur le fait que nous resterons en contact et je garde un très très bon souvenir de tout ce parcours passé à tes côtés.

Et parfois en cours de route, on peut perdre des personnes de vue… Un grand nombre de personnes ont fait partie de ma vie et sont toujours présentes dans mon cœur, malgré le fait que je ne me sente plus légitime de les contacter. Si ces personnes se croient oubliées, sachez qu’il n’en est rien.

Un grand merci à Béatriz, Eileen, Jacky, Nyura et Orrent pour la vaillance et l’epicness de leur aventure qu’il m’est possible de faire vivre aux travers de mes splendides joueurs x) Ça aide bien à décompresser après une semaine de boulot ! A Alix et Guigui, aux Chats, Estelle, Jéjé et Marie, tellement contents de vous compter parmi mes amis proches !

Et pour finir, pour celles et ceux qui m’accompagnent et sont ma famille, Maman, Papa, Clem et Karine, nos Doudou Rémi et Cécile ainsi que Fab et Anne-So et les petits loulous qui l’ont agrandie, mais aussi Marine qui m’a supporté, accompagné et aidé dans la tempête… Je vais essayer de prendre du temps pour pouvoir profiter à nouveau de chacun d’entre vous. Je vous aime et si je suis arrivé là, c’est en partie grâce à vous aussi.

Table of content

List of symbols and abbreviations

Symbols

A_{curve}	Charge under the curve ($\mathrm{A\ V}$)
C_{dl}	Double layer capacitance ($\mathrm{F\ cm_{geo}^{-2}}$)
C_{X}	Solubility of X ($\mathrm{mol\ cm^{-3}}$)
D_{X}	Diffusion coefficient of the reactant X ($\mathrm{cm^2 s^{-1}}$)
$\bar{d}_{\mathrm{N}}$	Number averaged particle size (nm)
$\bar{d}_{\mathrm{S}}$	Surface averaged particle size (nm)
$\bar{d}_{\mathrm{V}}$	Volume averaged particle size (nm)
d_{hkl}	Distance between (hkl) crystallographic plans (nm)
$\bar{d}_{\mathrm{XRD}}$	Mean crystallite size (nm)
ΔE_{ohm}	Voltage loss related to the ohmic drop (V)
$E_{\mathrm{ox/red}}^{0}$	Standard equilibrium potential of the ox/red redox couple (V)
F	Faraday constant charge per mole of electrons ($\mathrm{C\ mol^{-1}}$)
f	Frequency (Hz)
$FWHM$	Full width at half maximum ($°$)
j / j_{geo} or j_{spe}	Geometric ($\mathrm{A\ cm_{geo}^{-2}}$) or specific ($\mathrm{A\ cm_{Pt}^{-2}}$) current density
$j_{\mathrm{X}}^{\mathrm{l}}$ or j_{lim}	Limiting current density related to the reactant X ($\mathrm{A\ cm_{geo}^{-2}}$)
$j_{\mathrm{ct,R}}$	Charge transfer current density of the reaction R ($\mathrm{A\ cm_{geo}^{-2}}$)
j_{dl}	Double layer current density ($\mathrm{A\ cm_{geo}^{-2}}$)
$j_{\mathrm{0,R}}$	Exchange current density of the reaction R ($\mathrm{A\ cm_{geo}^{-2}}$)
$j_{\mathrm{cross-over}}^{\mathrm{H_2}}$	Hydrogen cross-over current density ($\mathrm{A\ cm_{geo}^{-2}}$)
m_{X}	Mass transport kinetics of reactant X ($\mathrm{m\ s^{-1}}$)
$Q_{\mathrm{H^+}}$	Specific charge of proton adsorption ($\mathrm{\mu C\ cm_{Pt}^{-2}}$)
R_{cell}	Overall resistance of the cell ($\Omega\ \mathrm{cm_{geo}^{-2}}$)
R_{ct}	Charge transfer resistance ($\Omega\ \mathrm{cm_{geo}^{-2}}$)
R_{HF}	High frequency resistance ($\Omega\ \mathrm{cm_{geo}^{-2}}$)
R_{p}	Proton transport resistance ($\Omega\ \mathrm{cm_{geo}^{-2}}$)
R_{sc}	Short-circuit resistance ($\Omega\ \mathrm{cm_{geo}^{-2}}$)
T	Temperature (K)
t	Time (s, but often it becomes hours or years)
U_{cell} / $U_{IR\ free}$	Cell voltage or ohmic drop corrected cell voltage (V)
$Z(f)$	Impedance measured at the frequency f ($\Omega\ \mathrm{cm_{geo}^{-2}}$)
$\%_{\mathrm{comp}}$	Compression of the GDL
α	Non-ideal parameter
$\alpha_{\mathrm{a}}/\alpha_{\mathrm{c}}$	Anodic / cathodic symmetry coefficient
δ_{X}	Hydrodynamic diffusion layer thickness of reactant X (m)
$n_{\mathrm{a}}/n_{\mathrm{c}}$	Number of exchanged electron for the reaction at the anode / cathode
η_{mt} / $\eta_{\mathrm{mt,X}}$	Concentration overvoltage / related to the reactant X (V)
η_{R}	Activation overvoltage related to the reaction R (*e.g.* ORR or HOR) (V)
υ	Kinematic viscosity ($\mathrm{m^2 s^{-1}}$)
υ_{b}	Potential / voltage scan rate ($\mathrm{mV\ s^{-1}}$)
Ω	angular rotation velocity ($\mathrm{rad\ s^{-1}}$)

Abbreviations

AFC	Alkaline Fuel Cell
AL	Active Layer
AST	Accelerated Stress Test
BoT	Beginning of Test
BP	Bipolar Plate
BSE	Backscattered Electron
CA	Chronoamperometry
CCM	Catalyst Coated Membrane
CL	Catalyst Layer
CNT	Carbon Nanotubes
COR	Carbon Oxidation Reaction
CPE	Constant Phase Element
CV	Cyclic Voltammetry
DC	Differential Cell
DEMS	Differential Electrochemical Mass-Spectrometer
ECSA	Electrochemically active Surface Area
EoT	End of Test
FCCJ	Fuel Cell Commercialization Conference of Japan
FCH-JU	Fuel Cell and Hydrogen Joint Undertaking
HER	Hydrogen Evolution Reaction
HOPI	High-Oxygen-Permeable Ionomer
HOR	Hydrogen Oxidation Reaction
HSAC	High Surface Area Carbon
H_{upd}	Hydrogen under potential deposition
GC	Graphitized Carbon
GDE	Gas Diffusion Electrode
GDL	Gas Diffusion Layer
GEIS	Galvanostatic Electrochemical Impedance Spectroscopy
GM	General Motors
$^{\mathrm{I}}/_{\mathrm{C}}$	Ionomer to Carbon ratio
IF	Improvement Factor (also EF: Enhancement Factor)
IR	Infrared (thermography)
ICP-MS	Inductively Coupled Plasma Mass-Spectrometer
IEM	Ion Exchange Membrane
Interm1-2	Intermediate characterization 1 or 2
LSC	Long Side Chains (polymer)
MA	Mass Activity $(\mathrm{A}\ \mathrm{g}_{\mathrm{Pt}}^{-1})$
MEA	Membrane Electrodes Assembly
MPL	Microporous Layer
NEDO	New Energy and industrial technology Development Organization
OCV	Open Circuit Voltage (V)
OER	Oxygen Evolution Reaction
ORR	Oxygen Reduction Reaction
PEEK	Polyetheretherketone
PEFC	Polymer Electrolyte Fuel Cell

PEIS	**Potentiostatic Electrochemical Impedance Spectroscopy**
PEM / PEMFC	**Proton Exchange Membrane and PEM Fuel Cell**
PFSA	**Perfluorosulfonic Acid**
PGM	**Platinum Group Metals**
PSD	**Particle Size Distribution**
PTFE	**Polytetrafluoroethylene**
RDE	**Rotating Disk Electrode**
RH	**Relative Humidity**
RHE	**Reversible Hydrogen Electrode**
SA	**Specific Activity ($\mathbf{A\ cm_{Pt}^{-2}}$)**
SEM	**Scanning Electron Microscopy**
SPEIS	**Successive Potentiostatic Electrochemical Impedance Spectroscopy**
SSC	**Short Side Chains (polymer)**
TEM / HRTEM	**Transmission Electron Microscopy / High-Resolution TEM**
TKK	**Tanaka Kikinzoku Kogyo**
US DoE	**United States Department of Energy**
VC	**Vulcan XC72 Carbon**
X-EDS	**X-Ray Energy Dispersive Spectroscopy**
XRD	**X-Ray Diffraction**
XRF	**X-Ray fluorescence**

Small contextualization

Symbio aims to be a major producer of PEMFC systems for heavy mobility, and performance at given cost is crucial for successful industrialization. To that goal, one wants better electrocatalysts to enable given performance at lower Pt-content. The literature is rich with demonstration of “better than Pt/C electrocatalysts” for the ORR, but it is also clear that these materials still fail to be implemented in technical cells – or in other words, when implemented they yield lower performance than expected. The literature is also becoming rich in trying to find explanation to such disappointing facts (pointing at potential inadequate membrane electrode assembly formulation/genesis), but one can also question the methods that enabled researchers to state that their materials are “better than Pt/C electrocatalysts” for the ORR, namely the rotating disk electrode. Indeed, this method is intrinsically limited by severe mass-transport resistance of O_2 dissolved in the liquid electrolyte. So, the first objective of the thesis is to verify, using a three-electrode setup that is compatible with intrinsic ORR activity measurement (like the RDE) but also faster O_2 mass-transport (being essentially in the gas phase and not in liquid phase), whether the promises of the RDE at high potential values/low current densities do also translate to high current densities operation at lower potentials (for half cells) or voltages. Namely, the gas diffusion electrode setup will be tested to validate (or not) the promises of advanced Pt-based ORR electrocatalysts. Subsequently, it will be tested whether these electrocatalyst keep their promises upon accelerated stress tests, performed in segmented cell, in a collaboration with LEMTA.

For industrial deployment, it is clear that sufficient initial performance is not the only endeavor; the systems must also exhibit sufficient reliability and lifetime, which means that the rated power it is sold for should still be met at end-of-life. Being admitted that PEMFC performance do irremediably degrade in operation, guaranteeing a given stack power at end-of-life means that at beginning-of-life, the PEMFC stack shall be able to provide more than its rated power, hence that this rated power will be given at lower stack current and higher cell voltage. Although this should have a positive effect regarding the hydrogen consumption at beginning of life (higher cell voltage being equivalent to better cell efficiency), this could also prove harmful to the cathode electrocatalyst, as higher cathode potential could trigger harsher corrosion of the carbon support and/or of the Pt-based nanoparticles. However, this is essentially a belief, which, though reasonable, has not been demonstrated in practice to date. The ultimate objective of the thesis is therefore to check whether, upon constant cell voltage operation, the degradation rate/mechanisms of Pt/C cathodes vary with the value of the cell voltage.

To respond these important questions, this thesis was organized between an industrial partner, Symbio, and 2 research labs specialized in PEMFC development, LEMTA in Nancy for system aspects, and LEPMI in Grenoble for materials/electrochemical ones.

Chapter I

General context of the thesis: the Proton Exchange Membrane Fuel Cells

Chapter I. General context of the thesis : the Proton Exchange Membrane Fuel Cells

1. Why the research went toward PEMFC for the transportation field ?

Despite the rather ancient fuel cells' history (the term "fuel cell" dating back to the middle of the XIXth century, following experiments performed by Sir W. R. Grove [1]) gaseous voltaic batteries (the other name for fuel cells) had to wait more than a century until more applied and focused researches placed them at the heart of a newly born economy prospect [2,3]. After Sir Grove, another British scientist, F. T. Bacon, managed to implement the spontaneous recombination of hydrogen and oxygen to form water and energy (power) into practical electrical generators. The system developed by F. T. Bacon in 1932 was using an alkaline liquid electrolyte, and was, to the author's knowledge, the first operating fuel cell system in history. American, NASA-driven, space programs brought different technologies of fuel cells to the applied side, and triggered the first developments of ion-exchange membranes (IEM), IEM being the heart and most distinguishable core material that gave its particularity to the proton exchange membrane fuel cell (PEMFC) system. IEM-based fuel cells were used in the early 1960s as power supplies for the Gemini earth-orbiting missions [4]; whatever their success, they nevertheless suffered too high ohmic resistance, due to modest proton conductivity, and disastrous durability (the used sulfonated polystyrene membrane had the mechanical strength of wet journal paper). For these reasons, these IEM fuel cell systems turned out to be replaced by alkaline fuel cells (AFC) for the Apollo space flights that happened in the late 1960s, as well as the space shuttle program in the $1980 - 2000$s [5,6]. NASA had so far kept interest in the PEMFC system and intended to use it for further spatial missions; regenerative systems, also called secondary fuel cell systems, are still under their focus at present [7].

As of today, the global interest focused on the PEMFC keeps on increasing, as corroborated by the evolution of the number of yearly published articles drawn on Figure I – 1 – 1 using only the PEMFC and PEFC (polymer electrolyte fuel cell) keywords on a well-established editing research page (Scopus).

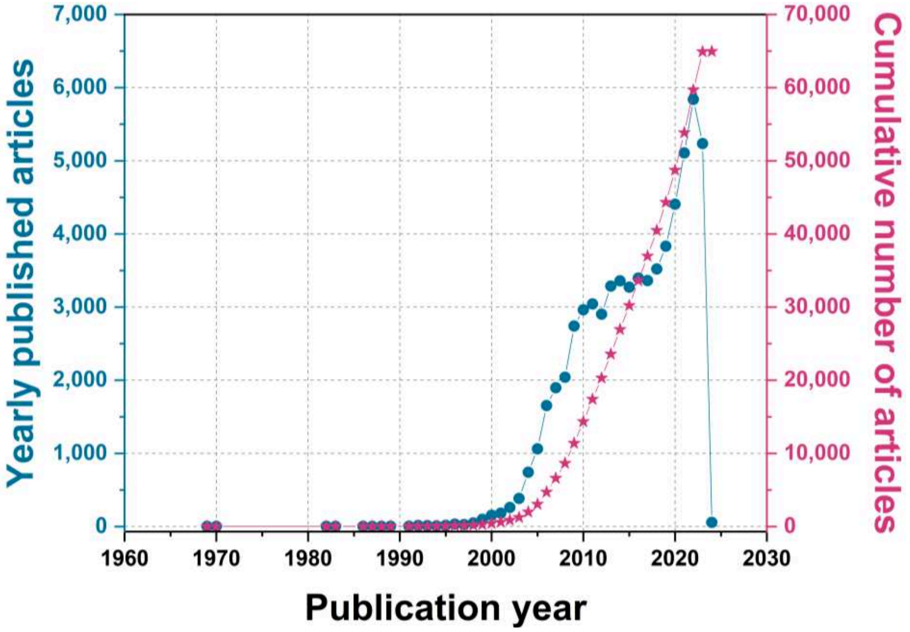

Figure I – 1 – 1: Number of yearly published and cumulative number of published articles found on Scopus using keywords "PEMFC" or "PEFC"

The real beginning of PEMFC research and development initiated in the 1970s, with the mass-production of ion-exchange membranes (e.g. Nafion® [8]) with high proton conduction as well as better mechanical and chemical properties in the conditions of use. Though these were created for alkaline electrolysis processes, it soon appeared they also had an interest for PEMFCs. After this start, there are two slope-breaking timelines at which the number of articles on this topic per year has increased: at the early 2000s and in the mid-2010s. The former steep increase can be explained by several ground-breaking improvements: (i) the catalyst preparation method, enabling much lower platinum (more generally, platinum group metals, PGM) use for much higher developed electrochemical surface area (ECSA; a typical example is high surface area carbon supported platinum particles, for which the ECSA can reach or exceed $100\ \mathrm{m}^2\ \mathrm{g}_{\mathrm{Pt}}^{-1}$ [9]) and (ii) the impregnation of the ionomer in the active layer to increase the platinum utilization in the so-called membrane electrode assembly (MEA), both improvements opening the way to dramatically-improved performance per gram of Pt employed [10]. This increase in performance and reduction of the cost has naturally been followed by the emergence of electric vehicles (from light duty to trucks, buses and trains) development projects in the US, Japan and Europe [11], notably quoting General Motors, Toyota and Alstom for their outstanding and most known work on the field, discussed more in details later on. The latter slope inflexion, on the other hand, can be related to the global (and massive) engagement towards the reduction of greenhouse gas emissions made by governments to slow down global warming. Since a decade, many organizations have raised, focusing on hydrogen-related technologies (water electrolysers and fuel cells) as one solution towards a net zero-emission society at the horizon 2050. Among these organizations, national ones such as ADEME (Ecological Transition Agency, for France) and the US department of Energy, have launched calls for projects to initiate development and partnership in the country on the matter. The national strategy of $8-9$ billion euros for the development of decarbonized hydrogen in France is an example [12,13]. The idea is to create industrial champions that will be the leading actors in the field later on, which requires as a first step to favour research and development. At the national scale, several axes are targeted: (i) to install electrolysers to produce decarbonized hydrogen (from renewable or nuclear electricity), (ii) to develop the heavy mobilities (trucks, buses, trains, etc…) and (iii) to create a hydrogen economy and corresponding decarbonized industrial sector. In addition to these national organizations, the European Union, with its European Clean Hydrogen Alliance, promotes and instigates the creation of an adequate regulatory framework, that aims to capitalize the burgeoning hydrogen economy of the Union as well as help to finance development projects [14]. With its roadmap, Europe wanted to install, from 2020 to 2024, $6\ \mathrm{GW}$ of renewable hydrogen electrolysers in EU to reach a production of 1 million tonnes of hydrogen by that mean, to reach by 2030 $40\ \mathrm{GW}$ of electrolysers power plant and 10 million of tonnes of green hydrogen produced [15]. This is only part of the roadmap, as it also encourages the production of heavy-duty hydrogen vehicles when the fuel cell technology would have become sufficiently mature and cost-effective. This action is led by the Clean Hydrogen Partnership, which is the successor of the Fuel Cell and Hydrogen Joint Undertaking (FCH-JU). International organizations are also federating and gathering data from the development of the hydrogen economy all around the world, with for example the Hydrogen Council: created by CEO from global companies, it is an initiative that gathers 145 companies worldwide to foster a clean energy transition toward a hydrogen economy [16]. It gives interesting data on the number of project proposals on the use of fuel cells or on the development of the refuelling stations, which is a key parameter for the emergence of the hydrogen economy.

The previous lines demonstrate that, economically and politically, one of the world's focus for reaching a net zero-emission economy is hydrogen. It has become, in the last decade, one of the cornerstones of ecological transition. This thesis (modestly) takes part to this effort, being devoted to the development of the proton exchange membrane fuel cell technology for the (heavy) transportation sector.

2. What is a proton exchange membrane fuel cell ?

a) Overview of the system

A fuel cell is an electrochemical generator which produces power and energy by the electrochemical reactions at separated places of at least two reactants. In the case of the proton exchange membrane fuel cell, dihydrogen ($\mathrm{H_2}$, later referred as hydrogen) and dioxygen ($\mathrm{O_2}$, later referred as oxygen) react separately (one speaks about half-reactions) in two regions called active layers (AL). To have separation of the reaction regions, an electrolyte separator is used and can be found in several forms (liquid, polymer, solid). In the case of the PEMFC, this separator – the polymer electrolyte membrane (or proton-exchange membrane), PEM - is a key element; it physically separates the 2 electrodes where the reactions take place (anode for $\mathrm{H_2}$ oxidation and cathode for $\mathrm{O_2}$ reduction) and avoids the direct contact between the reducer (H_2) and oxidant (O_2) molecules. Figure I - 2 - 1 is a schematic that helps to represent the composition of such system, with its multiple core components.

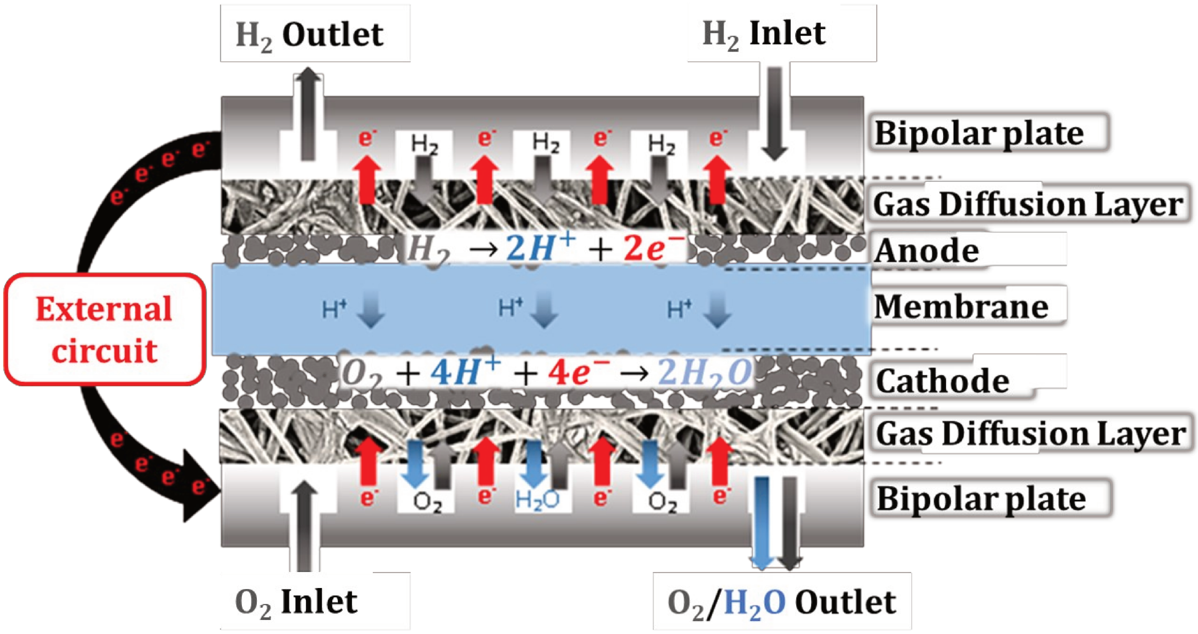

Figure I - 2 - 1: Schematic of the different element constitutive of a PEMFC

The PEMFC is therefore composed of:

- (i) a membrane, which is an electronic insulator that enables transport of protons (H^+) between the two catalytic layers. This ionic conductor also separates (as best as possible) the reducer (H_2) and oxidant (O_2) compartments.
- (ii) two active layers (as previously introduced) or also called catalytic layers (CL) or , which are the places at which the reactions occur. It is where the (usually Pt-based) catalysts are found (not necessarily the same at the anode and cathode).
- (iii) two gas diffusion layers (GDL), often having an overlayer – a microporous layer (MPL) – and which role is to enable a good distribution of the gas reactants at the surface of the active layers, while conducting reactants, heat and water to/from the active layers.
- (iv) bipolar plates (BP), used for macroscopic gas transport in the system, electronic current collection and heat management as well as water removal. These have essentially the same functions as the GDLs, but not at the same characteristic dimensions.

Some vocabulary needs to be defined properly to prevent any misunderstanding in the rest of this manuscript. Electrochemical reactions take place at the interface between an electrode and an electrolyte. The electrode can be defined as an electronic conductor while the electrolyte is an ionic conductor. In PEMFC, this notion of well-defined interface between electronic and ionic conductors is blurred by the production process and the engineering of the electrodes to reach higher performance. In facts, these two conductors are mixed together and deposited to form active layers; their thicknesses cannot be considered negligible. As such, the electrodes are volumic and comprise both ionic and electronic transport (and also gaseous and possibly liquid water transport as well), as highlighted by the change of fabrication process over the years on Figure I – 2 – 2.

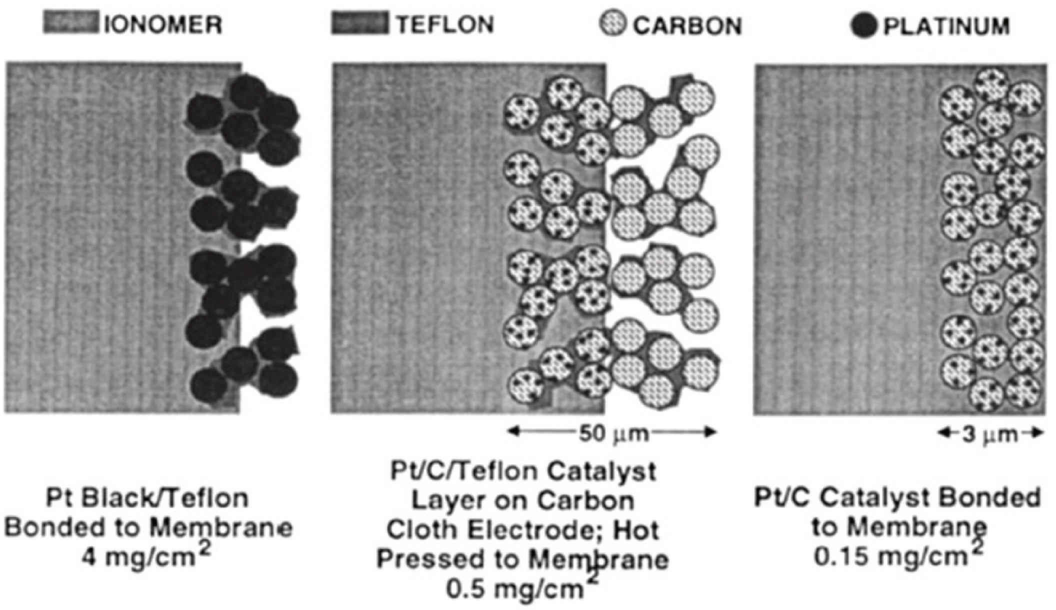

Figure I – 2 – 2: Evolution of the active layers' preparation since the middle of the XXth century. Reprinted from [17]

As the presence of both hydrogen and oxygen at the same place would result in spontaneous combustion of both reactants with the production of water or steam and the release of heat (without electron generation), one of the great aspect of electrochemistry is the possibility to make that overall reaction happen (the recombination of hydrogen and oxygen to form water) but by separating the oxidation of hydrogen (HOR: Hydrogen Oxidation Reaction, Eq. I.1.1) and the reduction of oxygen (ORR: Oxygen Reduction Reaction, Eq. I.1.2) at two different places (the electrodes), enabling to valorise the electrons.

$$\mathrm{H_2} \leftrightarrow 2\mathrm{H^+} + 2\mathrm{e^-} \qquad E°_{\mathrm{H^+/H_2}} = 0\ \mathrm{V}\ vs.\mathrm{RHE} \qquad \text{(Eq. I.1.1)}$$

$$\mathrm{O_2} + 4\mathrm{e^-} + 4\mathrm{H^+} \leftrightarrow 2\mathrm{H_2O} \qquad E°_{\mathrm{O_2/H_2O}} = 1.23\ \mathrm{V}\ vs.\mathrm{RHE} \qquad \text{(Eq. I.1.2)}$$

$$2\mathrm{H_2} + \mathrm{O_2} \leftrightarrow 2\mathrm{H_2O} \qquad \Delta E° = U° = 1.23\ \mathrm{V} \qquad \text{(Eq. I.1.3)}$$

The two electrodes are called the anode (at which the HOR takes place) and the cathode (at which the ORR takes place). The thermodynamical potential ($E°$) at which these reactions can happen is of great importance, as it will impose the thermodynamic (and thus, maximum) cell voltage of a single cell between the anode and cathode. The value of the open circuit voltage is attributed to this thermodynamic value alone: 1.23 V. To this theoretical maximum voltage, additional limitations result from the different physical and chemical processes that happen concomitantly, that overall decrease the usable cell voltage.

$$\Delta E = U_{\mathrm{cell}} = \Delta E^{eq} - \Delta E_{\mathrm{ohm}} - |\eta_{\mathrm{ORR}}| - |\eta_{\mathrm{mt,O_2}}| - |\eta_{\mathrm{HOR}}| - |\eta_{\mathrm{mt,H_2}}| \qquad \text{(Eq. I.1.4)}$$

The overall cell voltage is therefore resulting from the equilibrium potential of each electrode (calculated with the Nernst equation) and of three types of limitation (besides this thermodynamic voltage):

- Ohmic loss (ΔE_{ohm}) that originates from the current density j flowing in electronic/ionic conductors having a certain resistance; the overall cell resistance, R_{cell}, is the sum of the electronic resistance of materials and interfaces and ionic resistance of the membrane and electrodes, resulting in a $\Delta E_{\mathrm{ohm}} = R_{cell} \times j$ voltage loss.
- Kinetics overvoltages (η_{HOR} and η_{ORR}) are related to the activation of the anode and cathode reactions, the latter being dominant in a PEMFC.
- Mass-transport overvoltages ($\eta_{\mathrm{mt,O_2}}$ and $\eta_{\mathrm{mt,H_2}}$) are related to the diffusion and accessibility of the gas reactants to the active sites.

The kinetics and mass-transport overvoltages are algebraic values, being either positive and negative for the HOR (oxidation) or ORR (reduction), respectively. Kinetics equations in electrochemistry are often attributed to behave following the Butler-Volmer equation, which for reactions taken irreversibly in the direction of the oxidation for Eq. I.1.1 and in the direction of the reduction for Eq. I.1.2 (so, from left to right) and for rather large overvoltages, gives Eq. I.1.5 and Eq. I.1.6:

$$j_{\mathrm{ct,HOR}} = j_{0,\mathrm{H_2}} exp\left(\frac{\alpha_{\mathrm{a}} n_{\mathrm{a}} F \eta_{\mathrm{HOR}}}{RT}\right) \tag{Eq. I.1.5}$$

$$j_{\mathrm{ct,ORR}} = -j_{0,\mathrm{O_2}} exp\left(\frac{-\alpha_{\mathrm{c}} n_{\mathrm{c}} F \eta_{\mathrm{ORR}}}{RT}\right) \tag{Eq. I.1.6}$$

With j_{ct} the charge transfer, also called kinetic current density and in our case, the faradaic current density, j_0 the exchange current density (in a simple way, related to the quantity of species consumed and produced at the equilibrium, so to speak, the intrinsic speed of the reaction), α the transfer coefficient (repartition of the energy in favour of one or the other reaction direction, here $\alpha = 0.5$ for both reactions for more simplicity) and n the number of electron exchanged for a given reaction. The large overvoltage assumption is valid for the ORR kinetic equation but not much for the HOR one, as well as the $\alpha = 0.5$ one. They are still used, once again for simplicity in developing the loss terms of Eq. I.1.4. In stationary conditions, where the capacitive current is null, and in conditions where mass-transport is negligible (resulting in $j_{ct} = j$), these two equations can be simplified in:

$$|\eta_{\mathrm{HOR}}| = \frac{RT}{\alpha_{\mathrm{a}} n_{\mathrm{a}} F} ln\left(\frac{j}{j_{0,\mathrm{HOR}}}\right) \tag{Eq. I.1.7}$$

$$|\eta_{\mathrm{ORR}}| = \frac{RT}{\alpha_{\mathrm{c}} n_{\mathrm{c}} F} ln\left(\frac{|j|}{j_{0,\mathrm{ORR}}}\right) \tag{Eq. I.1.8}$$

On the contrary, assuming diffusion is the main mass-transport process occurring in the gas diffusion layers and at the vicinity of the active materials, it is possible to obtain an expression of the mass-transport overvoltage [18] for both reactants:

$$|\eta_{\mathrm{mt}}| = \left|\frac{RT}{2F}\ln\left(1-\frac{j}{\left|j_{\mathrm{O_2}}^{\mathrm{l}}\right|}\right)^{\frac{1}{2}}\left(1-\frac{1}{\left|j_{\mathrm{H_2}}^{\mathrm{l}}\right|}\right)\right| \qquad \text{(Eq. I.1.9)}$$

With j^{l} the limiting current density of the reaction (HOR or ORR). All these limitations have to be taken simultaneously as they apply for even the slightest value of the current density and thus on the whole range of voltage accessible for the system, from 1.23 to 0 V. By combining equations Eq. I.1.4 to Eq. I.1.9, it results:

$$U_{cell} = \Delta E^{eq} - R_{cell}j - \frac{RT}{2F}ln\left(\frac{|j|}{j_{0,\mathrm{ORR}}}\times\left(\frac{j}{j_{0,\mathrm{HOR}}}\right)^{2}\right) + \frac{RT}{2F}\ln\left(\left(1-\frac{j}{\left|j_{\mathrm{O_2}}^{\mathrm{l}}\right|}\right)^{\frac{1}{2}}\left(1-\frac{j}{\left|j_{\mathrm{H_2}}^{\mathrm{l}}\right|}\right)\right) \text{(Eq. I.1.10)}$$

In this thesis, the HOR is not studied and its kinetics and mass-transport losses are considered negligible, considering that the oxidation of hydrogen is a very fast reaction with the Pt/C electrocatalyst materials used at the anode. A deeper focus is made on the oxygen reduction reaction as it is known to be a much more limiting reactions [19,20] and on the different materials developed and studied in the literature to pave the way for better performance. Indeed, $j_{0,\mathrm{ORR}}$, the exchange current density for the ORR is an intrinsic property of the material constitutive of the reaction interface used. On the other hand, $j_{\mathrm{O_2}}^{\mathrm{l}}$ the limiting current density can be modified depending on the operating condition, on the mass-transport properties of the material used and on the production process to make the interface.

In addition, one must add that real cell can suffer non-negligible crossover of gases (because the PEM is not a perfect separation between the anode and cathode), and non-infinite short-circuit resistance (because the PEM is not a perfect electron insulator and/or can be pierced by carbon grains or fibres from the electrodes/GDLs) that can further bias Eq. I.1.4; Chapter II. Experimental section will state more about this issue.

b) Platinum as the catalyst with the highest activity for the ORR

The ORR is known to have a sluggish kinetics, which leads to detrimental kinetics loss and related cell voltage decrease upon increase of the current delivered by the cell. This is explained by its complex reaction mechanism: Eq. I.1.2 shows that 4 electrons are exchanged per molecule of oxygen, leading to at least 4 elementary steps, that often involve adsorbed intermediates [19,21,22]. Such a complicated mechanism makes the use of a catalyst mandatory, a catalyst being a material which does not strictly participate in the global reaction (it is neither consumed nor produced), but facilitates (at least some of) its steps. From several decades of results, it has become common knowledge that for the PEMFC electrode reactions, platinum is the best element to focus research on: Pt catalysts were already used for the spatial application by the NASA and General Motors (GM) in the 1960s [11], but this was done using platinum black, which led to use a high quantity of material for rather poor cell performance, leading to expensive electrodes; in other words, the Pt utilization factor was small. The switch to high Pt utilization factors was made when carbon black-supported platinum nanoparticles were reported by the Los Alamos National Laboratory (LANL) [9,23]; their new electrode preparation process led to high Pt utilization and high effectiveness factors[24]. This of course implied the synthesis of carbon-supported platinum nanoparticles (an example of such material is given on Figure I - 2 - 3 with transmission electron microscope, TEM, pictures), the present state-of-the-art in PEMFC electrodes. The carbon black (particles of $ca.\ 100\ \mathrm{nm}$) is used as support because it is inexpensive, highly available, chemically inert and offers a really good electronic conductivity; its high surface area (on the order of $100 - 1000\ \mathrm{m}^2\ \mathrm{g}_\mathrm{C}^{-1}$) enables the repartition of the platinum nanoparticles with high dispersion (hence high electrochemically active surface area, ECSA in $\mathrm{m}_\mathrm{Pt}^2\mathrm{g}_\mathrm{Pt}^{-1}$, if the electrode is well prepared). The term "catalyst" previously introduced as the material which helps to accelerate the reaction rate is now used for the association of the active nanoparticles (Pt, Pt alloys or else) and of the carbon support used, both being intimately linked.

The impact of the Pt particle size on the activity of the material is however not trivial [25–27]: the decrease in size of the platinum nanoparticles induces an increase of the ECSA (positive effect, owing to that fact that smaller nanoparticles have larger fractions of the surface atoms (that can lead to electrochemistry), versus the bulk particle atoms (that cost materials)), but a decrease in the specific activity, the performance reported to the available catalyst surface (negative effect). This is attributed to stronger adsorption of the oxygenated intermediate species that slows down the rate determining step of the ORR. The mass activity (the performance reported to the mass of catalyst) reflects a balance between these positive and negative contributions: this leads to an optimal size for the mass activity of $ca.\ 3\ \mathrm{nm}$. Thus, platinum-based nanoparticles of $2-10\ \mathrm{nm}$ have become the standard in catalyst development. With such small size, some aging mechanisms come as well and will be discussed later on. It must also be noted that the extent of nanoparticles agglomeration can vary from one catalyst to another, which can have an influence on the initial performance and on the durability. In the example of Figure I - 2 - 3, the extent of agglomeration is high, with very few isolated Pt nanoparticles present.

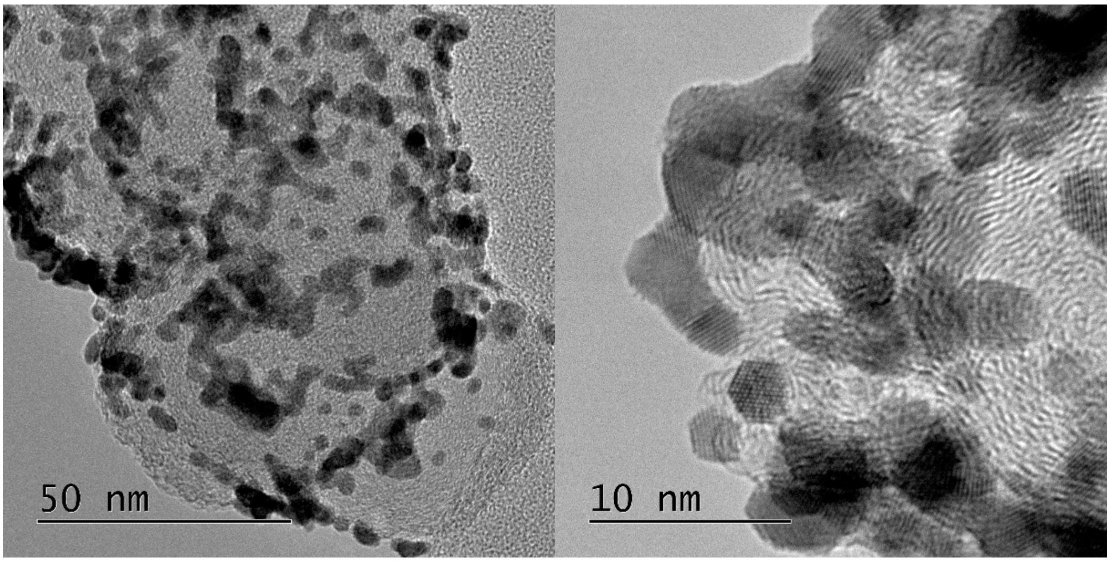

Figure I - 2 - 3: TEM pictures of platinum single metallic nanoparticles on carbon support

Density functional theory calculations are used to determine ways of improvement for the catalysis of the ORR. Platinum is considered to have the lower kinetics losses (among pure metals), as revealed by the Volcano plots on Figure I - 2 - 4 that draw the activity of a material for the ORR as a function of a metal-intermediate (here metal-oxygen) binding energy.

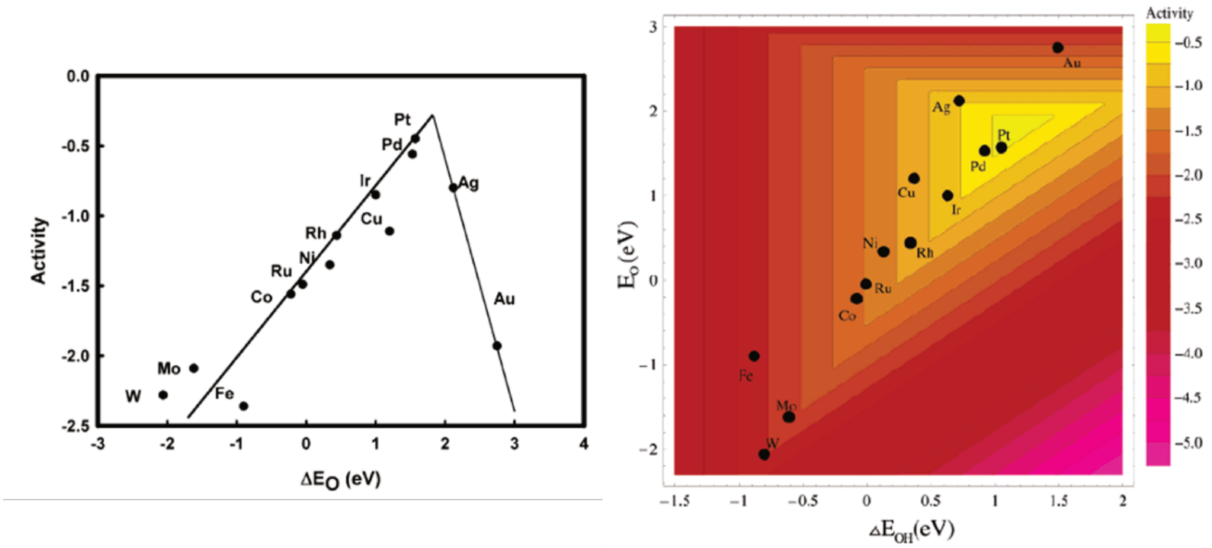

Figure I - 2 - 4: Volcano plots corresponding to the ORR reaction plotting: the activity as a function of the oxygen bond energy (left) and the activity as a function of both the oxygen and hydroxide binding energies (right). Reprinted from Nørskov et al. [19]

On these volcano plots (similar ones can be found for the Hydrogen oxidation or evolution reactions, showing that platinum is here again, the best monometallic catalyst found so far [28]), the higher (left) or yellower (right) the element, the larger its ORR activity. Platinum is the element presenting the best activity for this reaction, but what the trend shows is that there is still room for improvement to reach higher performance (the graphs having a log scale for the y axis). It also gives information on the way to reach this more interesting material: if one combines platinum with a lower oxygen bonding element, it should lead to an increase in activity. This has been studied later by Greeley *et al.* [29], who applied density functional theory to analyse the best material coming from the alloying of platinum with other elements, such as 3d transition metals (Ni, Co, Fe etc…). The volcano plot of Figure I - 2 - 5, relates the relative bonding energy and activity of a single element platinum catalyst with Pt alloys/composites. A positive increase, by at least an order of magnitude, is observed after alloying platinum with these 3d transition metals. The explanation is rather complex; combining Pt and 3d transition metals results in a positive ligand effect with these elements, *i.e.* leads to a contraction (and thus strain) of the lattice versus a single platinum matrix; of course, an electronic effect is also at stake, because the electronic orbitals of Pt differ when it is pure and combined with a hetero element. Another particularity is observed on this last volcano plot: ordering Pt_3Ni to exhibit only a singular (111) crystallite orientation exhibits again an order of magnitude higher performance. These two effects: chemical, on the nature of the alloy, and physical, on the particular crystallographic orientation of the catalyst surface, are of tremendous importance to reach higher intrinsic activity (by the increase of the exchange current density) and so, lower kinetics loss.

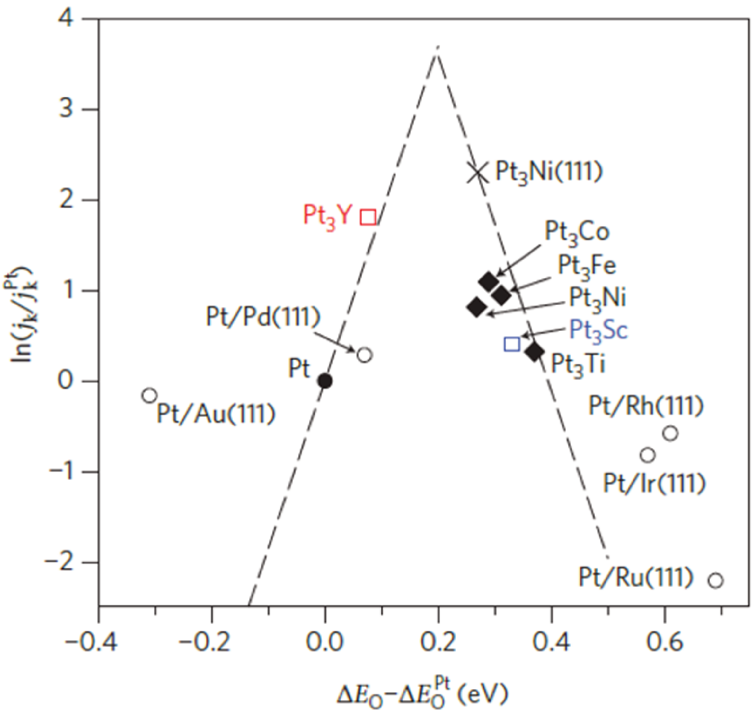

Figure I - 2 - 5: Relative volcano plot for platinum alloy with respect to the activity and bonding of platinum single metallic. Reprinted from [29].

There are multiple ways to play on the improvement of the catalytic activity of a catalyst. The ensemble effect, playing on the crystallographic orientation which will be constitutive of the interface, has been well studied on platinum [20,30]; the most known of these catalyst is $\mathrm{Pt_3Ni}$ octahedra, that lead to major improvement factors (IF) over conventional $\mathrm{Pt/C}$ nanoparticles[1] [31,32], despite suffering from restructuration while aging [33]. The influence of the crystallographic orientation has also been studied on $\mathrm{Pt_{1-x}Co_x}$ catalyst [34,35]. Platinum has been alloyed to almost every element in the periodic table so far, the main aim targeted being to reduce the use of rare and/or noble elements [36–39]. Later on, other groups invented methods to tune the aspect of these alloyed particles, by desired and selective leaching of the non-noble metal [40,41] or deposition on particular surfaces [42–44]. The bi-alloyed catalyst used in Toyota Mirai cars benefits from these advancements [45,46]. The last class of modified nanoparticles for improved activity (and durability) is catalysts with deliberately-introduced defects; counter-intuitively, it was demonstrated by Dubau *et al*. [47,48] and Asset *et al.* [49] that structural defects are good for the intrinsic activity and Chattot *et al.* [50] proved that they can even be used as descriptor to assess the improvement factor measured in liquid electrolyte. These particles with defects (also called hollow nanoparticles or sponges) exhibit also much higher activity than reference platinum catalysts. There are then different ways for improving the intrinsic activity of the catalyst material, but all these measurements were almost performed in fully liquid electrolyte environment, using the rotating disk electrode experimental setup to assess the performance. Ly *et al.* [51] unfortunately showed that despite very good activity in these model conditions, almost all these catalysts failed to

---

[1] The improvement factor, IF, can be defined as the enhancement of ORR kinetic activity of a material versus the one measured in similar conditions for a benchmark, typically commercial Pt/Vulcan XC72 nanoparticles.

maintain this level of improvement when implemented in a real PEMFC cathode environment (Figure I – 2 – 6). Chapter III. New way to assess catalyst performance ? A GDE study will particularly address this issue.

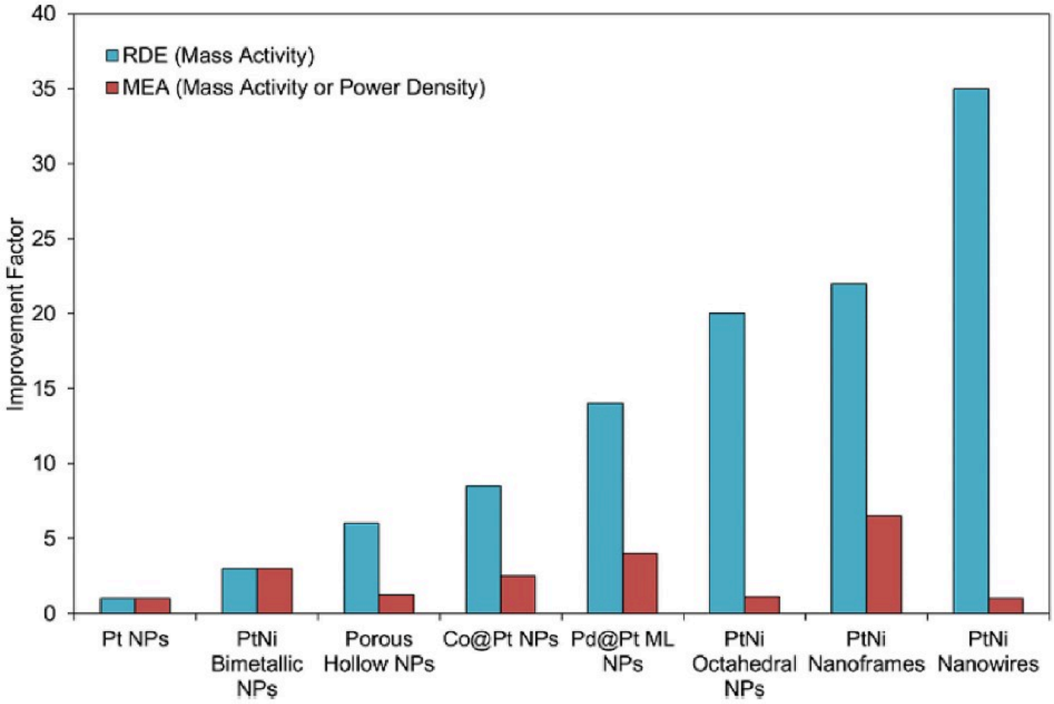

Figure I - 2 - 6: Improvement factors measured in liquid electrolyte (RDE, blue bars) and in PEMFC single cell's MEA (red bars) in the 0.90 - 0.95 V (for MEA and $V\ vs.RHE$ for RDE) region. Reprinted from [51].

3. Future expected breakthrough: the optimal electrode production process

To achieve performance targets fixed by organizations such as the US DoE [52] or NEDO [53,54] (new versions updated regularly, next ones incoming), great improvements of the electrode processing must be achieved. In fact, the disappointing performance obtained while using advanced catalyst materials such as those of Figure I – 2 – 6 point towards a bad utilization or even more specifically of effectiveness of the catalyst after integration in PEMFC cathode [24,55,56]. Improving the way the catalyst is implemented in the cathode architecture (the issue is less dramatic for the anode, owing to the faster HOR kinetics and H_2 mass-transport), depends on the successful interplay between numerous mandatory components: (i) the carbon support on which the active material is deposited, (ii) the ionomer used inside the active layer and (iii) the membrane that separates both electrodes need to be organized so to lead to the best interplay between mass-transport in the gas pores and those filled by the ionomer and/or liquid water, ionic conductivity within the ionomer (and membrane) and of course as many catalytic sites as possible in “triple-phase-boundary” conditions, *i.e*. easily accessed by electrons and ions (protons), but also the O_2 reactant. This is obviously not an easy task and requires tailored engineering at multiple scales.

a) Carbon support choice and influence on the performance of the active layer

The carbon support plays a major role in the structure of the active layer. There are multiple kinds of carbon that can be found in the literature, but let's start with the more traditional one, the carbon black. Among this class of carbon, the most common are Ketjenblack EC-300J (developed surface of $ca.\ 800\ \mathrm{m^2 g_c^{-1}}$, also known as high surface area carbon, HSAC), Vulcan XC-72 (*ca.* $240\ \mathrm{m^2 g_c^{-1}}$, noted XC72 or also VC) or graphitized HSAC ($110-120\ \mathrm{m^2 g_c^{-1}}$, noted GC) [57,58] as they have good electronic conductivity and rather high purity. Due to their difference in surface area, the distribution of the Pt catalyst nanoparticles will not be the same on their surface, and neither their stability. Indeed, the higher the developed surface, the lower the degree of graphitization of the carbon and thus, the lower the stability, as graphite exhibits the better stability among the three types of carbon black [59,60]. For the catalyst based on the GC, the Pt nanoparticles are mainly positioned at the surface of the carbon support, and are thus very sensitive to contamination by the direct contact with the ionomer, as suggested by Kodama *et al.* [61]. This triggered the interest towards mesoporous carbons with controlled pore size, in which catalyst particles can stay without being in contact with the ionomer [62–64], HSAC being an earlier version of this methodology. In that latter case, proton transport is still ensured via water filling pores by capillary condensation, and the active sites inside this porosity remain in proton percolation conditions and still accessible to $\mathrm{O_2}$, as the pores are not too deep. As such, electrodes based on HSAC or other mesoporous carbons can show great compromise between oxygen and protons accessibility [65], stability and reliability (at least if the active layers are properly engineered [66]), and they were chosen for the latest Mirai [46]. By considering that one can increase the accessibility to the catalyst particles by modifying the carbon support, the structure of the active layer itself can be modified by the help of the carbon support fabrication or manufacturing, as shown by Tempelaere *et al.* [66]. This strategy includes another class of carbon material: carbon nanotubes (CNTs). With this oriented-by-nature architecture, the tortuosity of the active layer is much less pronounced than for classical carbon black, then enabling better oxygen, protons and water transport properties [66,67]. The high degree of graphitization of such material also makes it a (more) corrosion-resistant (hence very promising) support. Finally, Lee et al. provided an additional structure that has been realized with more conventional carbon, but by adding more active layer processing to form grooved active layers, improving greatly the performance for a given catalyst [68].

To summarize the different possibilities observed in the literature, Figure I - 3 - 1 schematizes the active layer morphologies/structures achievable with the different carbon mentioned above. Of course, these active layers require adjunction of proper amounts and properly-organized ionomer filaments, as emphasized hereafter.

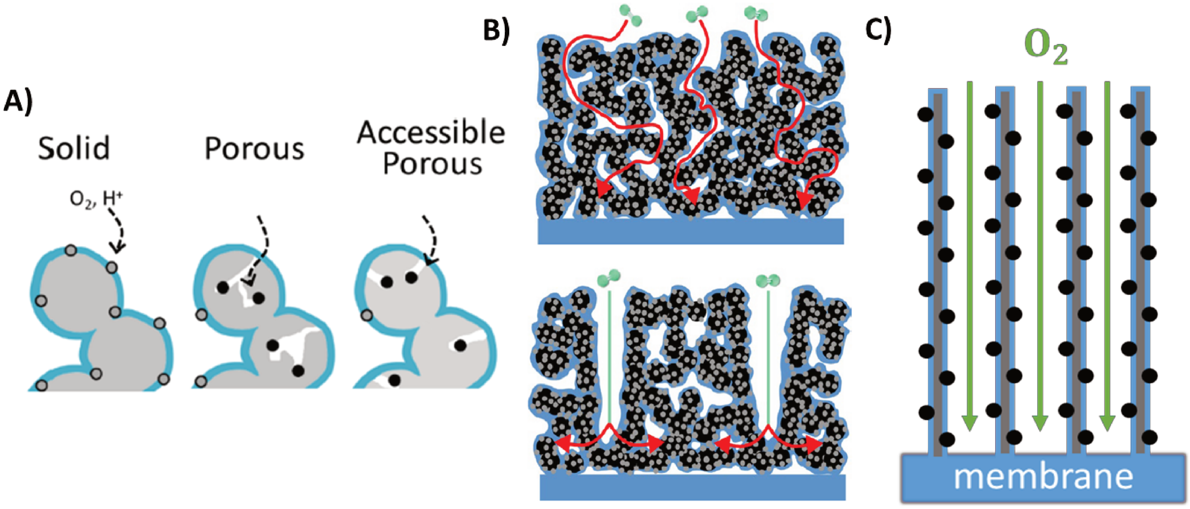

*Figure I - 3 - 1: Improved oxygen accessibility at the active sites using **A)** mesoporous carbon, reprinted from [65], **B)** current active layer structure (top) and grooved electrode proposed by Lee et al. (bottom), reprinted from [68] and **C)** vertically aligned carbon nanotubes active layer schematic representation*

b) Ionomer and membrane

Membranes and ionomers are key components of the PEMFC system; among them, the more used are perfluorosulfonic acid (PFSA) polymers. The one type of polymer most people may know among this class of thermoplastic is the Nafion®. Though it has been developed since a few decades, it is still of prior interest and used up-to-date [69,70], as it presents a good proton conductivity of $0.1\ \mathrm{S\,cm^{-1}}$ [71] and excellent (electro)chemical stability in PEMFC environment. It is thus no secret that Nafion® (a PFSA with long side chains, LSC) or its shorter side chain (SSC) analogues (like Aquivion®), compose the majority of the membranes used to separate both active layers. Many studies have been performed and reviews done on the physical and chemical properties of membranes [72,73]. Of course, since the 1980s, in the will to increase the performance of the electrodes and reach better Pt utilization and effectiveness, ionomer has been mixed in the catalytic ink to have a well recast of ionomer on the catalyst nanoparticles or more generally on the carbon support (as previously detailed for the mesoporous carbon). This favours the transport of the protons to the active site (which is desired), but nevertheless generates an increase of the oxygen transport resistance [66,71]. As suggested by Kongkanand *et al.* and depicted on Figure I - 3 - 2, the ionomer affinity to the platinum nanoparticles makes it adsorb strongly and block its mobility, accumulating water in its presence and thus resulting in higher oxygen transport resistance to the catalytic sites [74]. The precise organization of the ionomer and the Pt/C catalyst is very complex, and the reader is directed to the work of Eikerling *et al.* for more details [75–77]. A strategy to reduce this effect is to graft bulkier side chains to the polymer, so as to create steric hindrance in the chain polymer to prevent deleterious adsorption at the Pt sites and thus keep high local oxygen permeability [78–80]: this is the highly-oxygen-permeable ionomer (HOPI) approach. The author postulates that an ideal situation would be to have different ionomers for the PEM and the active layer; using HOPI in the catalytic ink would enable good oxygen transport to the catalytic sites, while keeping a non-permeable (or at least less permeable) membrane to prevent cross-over of oxygen to the anode (and hydrogen crossover to the cathode) that would result in the formation of hydrogen peroxide.

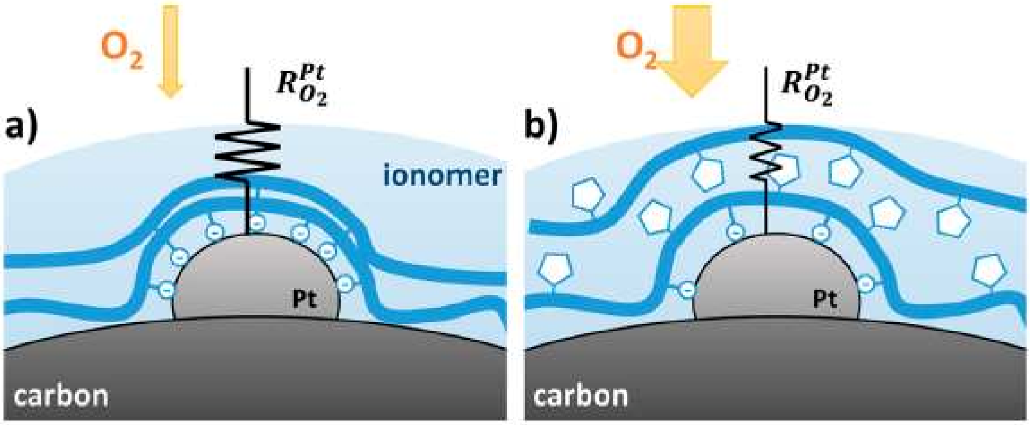

Figure I - 3 - 2: Suggested distribution of a) conventional ionomer and b) high-oxygen-permeable ionomer on platinum particles. Reprinted from [74].

Additionally to these works on the optimization of the active layer ionomer, studies have been performed to increase also the durability of the membrane by adding radical scavengers in its mixture, showing the best performance in increasing the membrane durability with Ce ions [81]: Ce^{3+} ions will oxidize to Ce^{4+} while reducing radicals formed after the production of $\mathrm{H_2O_2}$ and then eventually be reduced back to Ce^{3+} thanks to hydrogen molecules that cross-over the membrane. Finally, some membranes embed $\mathrm{Pt/C}$ nanoparticles, in addition to $\mathrm{Ce(III)}$, and exhibit even higher chemical stability over voltage and relative humidity cycling tests [82]. Moreover, the presence of electroless platinum in the subsurface of the membrane has a positive effect so to limit the hydrogen (and oxygen) crossover, as demonstrated by Watanabe *et al.* [83] and Daniele *et al.* [84].

With all these elements in hand, the newest improvements regarding catalyst synthesis, carbon support development, ink formulation or active layer structuration and membrane strengthening, it is now time to understand the final limiting step that prevent the widespread of PEMFC system, their insufficient durability in operation.

4. Degradation mechanisms of the membrane electrode assemblies

Like any other system, the initial performance measured in PEMFC does not maintain on the duration the system is expected to work (between $4{,}000$ to $8{,}000$ hours for light vehicles applications, or over $40{,}000$ hours for heavy duty applications). At the scale of laboratory research and development, it is totally inacceptable to run cells for such long times ($8{,}800$ hours being a full year). This is the reason why, in order to estimate the durability of the core materials (which were discussed previously: the catalyst material (Pt-based), the carbon support and the membrane-ionomer, assembled in the membrane electrodes assembly) at shorter time scales, accelerated stress tests (AST) have been developed; ASTs aim to increase the degradation rate of the materials, so to evaluate more rapidly the degradation mechanisms of these materials in conditions that mimic (as best as possible) real PEMFC operation.

a) Aging procedures

Different organisms have proposed representative ASTs to enable MEA stability measurements at reasonable time scales; the American US DoE [52] and Fuel Cell Commercialization Conference of Japan (FCCJ)[85] have been the most influencing ones to try to uniform and norm the aging studies. These ASTs are quite similar, as they include steps (and sometimes sweeps) applied between different voltages (the upper and lower voltage limits) with a certain holding time at each voltage[2]. The most widely spread ASTs is the load-cycling AST, that tests the $\mathrm{Pt/C}$ catalyst durability: the load-cycling AST mimics changes of load in the voltage working range of PEMFC, and consists of square waves from 0.6 to $0.95\ \mathrm{V}$ (or $1\ \mathrm{V}$) [86]; triangle waves or (slight) modification of the voltage boundaries can be found also [87,88]. The start-stop AST (square or triangle waves from 1.0 to $1.5\ \mathrm{V}$) is also popular, to test the robustness of the catalyst support. De Bruijn *et al.* summarized long-term PEMFC aging experiments and their impacts on the end of test system [89]. Using all these ASTs and data that can be found in the literature, the different aging mechanisms are usually sort by the material they are affecting, being admitted (of course) that the start-stop AST does not only affect the carbon support and the base-load one does not only affect the Pt nanoparticles.

b) Catalyst degradation

Several mechanisms altering the stability of the catalyst have been reported in the literature. A good summary schematic, presented on Figure I - 4 - 1, has been drawn by Vion-Dury *et al.* [90] that helps to represent to oneself the different processes which have been noticed to date. Concerning the active material degradation, several phenomena have been reported in the literature. The first one is thermodynamics related. In order to gain in utilization of active materials (Pt is scarce and expensive), nanoparticles have been implemented in PEMFC electrodes, which are often found in the $2-3\ \mathrm{nm}$ size for platinum single metallic particles. Holby *et al.* have demonstrated that the surface energy of such small particles induces by itself instability, and that they would be much more stable by simply rising their mean size to $4-5\ \mathrm{nm}$ [91].

---

[2] In three electrode cells (RDE and GDE), the voltages are replaced by potentials, expressed on the Reference Hydrogen Electrode, RHE, scale.

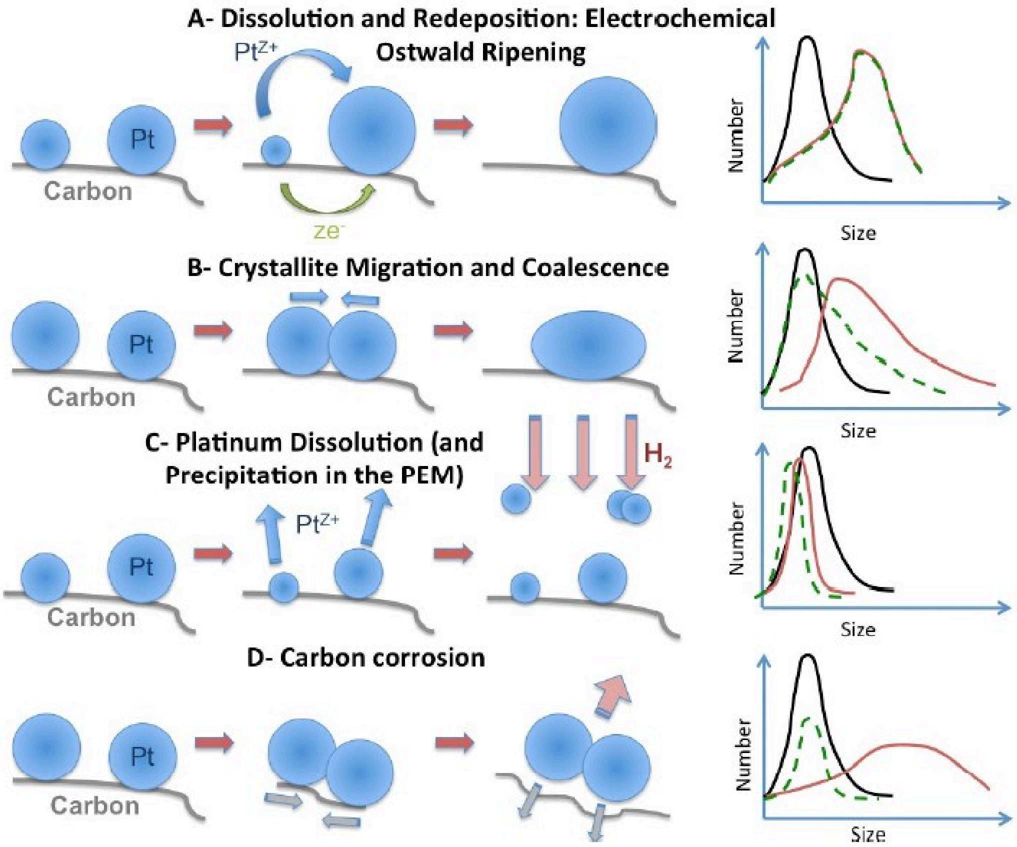

Figure I - 4 - 1: Degradation mechanisms of carbon supported platinum nanoparticles in PEMFC. Left hand-side are schematic of the mechanisms while the right hand-side stands for particle size distribution particular features observed. Reprinted from [90].

Hence, small ($< 4\ \mathrm{nm}$) Pt nanoparticles return to a more stable state by a dissolution and redeposition mechanism that is thermodynamically-driven: Ostwald ripening [91,92]. Ostwald ripening is responsible for the growth of particles either via dissolution of Pt atoms in Pt^{z+} species that diffuse towards bigger particles and are then reduced at their surface (3D Ostwald ripening), or via diffusion of Pt atoms at the surface of the carbon support and deposition on bigger Pt nanoparticles (2D Ostwald ripening). Padgett *et al.* reported an interesting fact on that matter, stating that the nature of the carbon support influences the growth mechanism of the particles [93]; using particular features visible on particle size distribution histograms (the measurements of nanoparticles size by calculating over 200 isolated and non-agglomerated particles), they distinguished that Ketjenblack carbon support and Vulcan XC72 exhibit two distinct growth mechanisms, the former revealing Ostwald ripening features, while the latter reveals more coalescence feature. A systemic study of the group of Strasser highlighted this difference of catalyst behaviours by the presence of mesopores [94]: the presence of intra-carbon pores (the case for Ketjenblack EC300J, much less for Vulcan XC72, not at all for GC) hinders the coalescence (which is proposed to be the dominant mechanism) of supported particles to the profit of Ostwald ripening. Limitation of the growing process is directly linked to the size of the mesopores in which platinum particles are trapped. For all these active nanoparticles growth mechanism, one outcome is for sure the decrease of the electrochemically active surface area of the catalyst: increasing the size of the Pt particles reduces the ratio surface/volume atoms and thus surface/mass of catalyst. This increase in particle size, and so loss of active area, is nonetheless counterbalanced by the higher specific activity of the nanoparticles (size effect) as previously mentioned by Antoine *et al.* [26] or Takasu *et al*. [25]. In any case, the base-load AST is intended to test the robustness of a given catalyst to Ostwald ripening and related ECSA losses.

c) Membrane and ionomer degradation

In addition to Ostwald ripening, the platinum dissolution and formation of $\mathrm{Pt^{z+}}$ ions can lead to ionomer or membrane contamination. In that latter case, due to the cross-over of hydrogen from the anode to the cathode, formation of a platinum band can be observed in the membrane, by the $\mathrm{H_2}$-assisted reduction of $\mathrm{Pt^{z+}}$ ions and nucleation/precipitation of platinum particles in the ionomer (and more likely membrane) [95,96]. This Pt band is not believed to imply limitation nor performance loss other than the dissolution of the platinum (and thus reduction of the ECSA) from the cathode $\mathrm{Pt/C}$ nanoparticles [95,97]. In the case of platinum alloy catalyst, the metal used to alloy with platinum is usually more easily leached [98] in the condition of use in a cathode environment. The leaching of these 3d metal atoms leads to the formation of transition metal cations that thermodynamically cannot be reduced in the membrane by $\mathrm{H_2}$ crossing over, in contrary to platinum cations [99]. This results in gradual poisoning of the membrane/ionomer by these 3d metal cations, that will irremediably replace protons on the polymer sulfonic groups [40,100,101]. This results in a diminution of the water uptake of the membrane and ionomer, a decrease in the proton conductivity and an increase of the oxygen diffusion resistance [102–104]. The presence of such multivalent cations also enhances the production of radicals from $\mathrm{H_2O_2}$ and further degradation of the membrane by cutting off the polymer chains [105], which, combined to the physical crosslinking of the ionomer (several $\mathrm{SO_3^-}$ groups gather around a given multivalent cations) and related increase of the brittleness [97], enhances the risk of pinhole formation [106–109], hence of end-of-life of the MEA.

d) Carbon support degradation

Finally, the last degradation mechanisms to address (as far as the MEA is concerned), is the carbon support corrosion. The carbon oxidation reaction (COR) is thermodynamically favoured when $E > 0.207\ \mathrm{V}\ vs.\mathrm{RHE}$; this means that the COR is favourable on the whole potential range of operation of the cathode catalyst layer [57,99,110]. This is however a thermodynamic value and this does not speak for the (fortunately rather slow) kinetics of the reaction. In practice, the COR is not predominant in the $0.6 - 1\ \mathrm{V}$ voltage range upon cycling [111], and only starts to be detrimental over $1.2\ \mathrm{V}$ [112]. Despite this potential value is not attained in the working time of the cell, this potential can be faced when starts and stops sequences occur [107,113], leading to non-negligible corrosion rate of the carbon support (this is why the start-stop AST is built with potential alternations in the $1 - 1.5\ \mathrm{V}$ range). Using

Differential Electrochemical Mass Spectrometry (DEMS), Roen *et al.* showed that carbon corrosion is however very dependent on the presence of catalyst nanoparticles [114]. Slow for carbon-only electrodes, the COR current is much dramatically increased for carbon-supported platinum particles above $ca.$ 0.6 V: the higher the platinum loading on the carbon support, the higher the COR rate at a given cathode potential, which means that Pt nanoparticles catalyse the corrosion of their carbon support, and this is particularly true when the potential is repeatedly alternated around 0.6 V (hence the definition of the base-load AST, from 0.6 to 0.95 or 1 V). The corrosion of the carbon support, resulting in the evolution of $\mathrm{CO_2}$ has many consequences for the active layer; its initial steps create surface oxygenated groups at the carbon surface, that facilitate the movement of catalyst particles and lead to agglomeration of Pt nanoparticles; when the COR is more intense, the carbon is mainly corroded at the interface with the Pt nanoparticles, leading to their detachment, hence electrical disconnection; electronically disconnected Pt nanoparticles will be inactive for the ORR catalysis. Ultimately, the COR can result in the collapse of the active layer, leaving unsupported and inactive Pt particles inside a rather dense matrix (mixture between amorphized carbon and ionomer), with minimal porosity hence extremely depreciated Pt effectiveness factor [115–117] .

All these mechanisms encountered in the aging study of the active layers of PEMFC are nevertheless not easy to predict and mitigate, as they strongly depend on the nature of the materials employed, the design of the cell and very importantly the operating conditions [109,118]: the relative humidity, the temperature, the reactant partial pressure and the lower and upper voltage boundaries for the ASTs. Graphitized carbons exhibit the higher resistance to the corrosion independently of the experimental conditions, though, even if in presence of Pt nanoparticles, GC carbon will not be enough stable [59].

Conclusion and objectives of the thesis

Proton Exchange Membrane Fuel Cells are good candidates for the replacement of combustion engines in the transportation sector. To match the performance and cost targets fixed to reach a viable hydrogen economy, many improvements are still required on the different elements of the system. Here, only the core elements, constitutive of the membrane electrode assemblies, have been delt with and one can see that the research topics are already quite wide.

Following the structural or chemical effects that can modify a carbon-supported platinum catalyst, new, lab scale synthesised and groundbreaking catalysts are awaited to generate the necessary breakthrough that will make PEMFC become industrially-viable systems. However, proper assessment and integration of these catalyst must be done in practical MEAs, to use them at their full potential; in other words, one wants these materials to be implemented in MEAs that do not imply detrimental mass-transport (of $\mathrm{O_2}$, protons and water) limitations that would dramatically reduce their practical improvement factors with regard to classical carbon supported platinum spherical nanoparticles catalyst (the present state-of-the-art). In addition, a deeper understanding of the degradation mechanisms is still necessary; ways to limit or even avoid them to ensure higher lifetime for these systems is mandatory, assuming that they still rely on non-negligible quantity of noble material, and are thus costly. To that goal, the material approach for sure needs to be coupled with strict stack/system architecture and proper balance of plant management, which of course requires the complete understanding of the processes at stake upon PEMFC (cathode) operation.

The present thesis aims to cope with these issues and is divided into five chapters. The **chapter I**, currently coming to an end, introduced the PEMFC system as well as the different hot research topics on the different constitutive material, as well as their degradation mechanisms, that occur in real life working conditions. The preparation of the different electrodes used, the experimental techniques and the physicochemical characterizations will be developed in **Chapter II**. Introduction to the worldwide used Rotating Disk Electrode setup and to two additional experimental setups, being the Gas Diffusion Electrode and the Differential Cell, will be done in **Chapter III.** This chapter presents the intrinsic activity measurements comparison between these three setups, and shows that the GDE enables closer operating conditions to the real system while assessing the performance of state-of-the-art catalysts, being in that extent a good compromise between the easiness of RDE operation and the reliability of the DC to predict good technical cell performance. Thanks to the GDE device and using low loaded electrodes, it will be verified that advanced catalysts do essentially maintain their enhancement factor over classical $\mathrm{Pt/C}$ catalyst at high current densities, and that proper integration of novel catalysts in well-designed MEAs is the key to good cell performance. In addition to this performance assessment, **Chapter IV** will discuss a degradation study performed on a $\mathrm{Pt_3Co}$ supported on Vulcan XC-72, that has been done using a segmented cell; the local measurement of the current density enables to understand the global and local impact of the different aging protocols found in the literature. Finally, as described in this first chapter, it would be interesting to understand the aging processes happening for a long steady state working period with a simple monometallic Pt on Vulcan XC-72 catalyst. This will be addressed in **Chapter V**, to understand the influence of the working voltage hold on the aging of the cathode active layer.

Chapter II

Experimental section

Chapter II. Experimental section

1. Single cell testing and constant potential aging

The Proton Exchange Membrane Fuel Cell degradation tests are performed using a $25\ \mathrm{cm}^2$ single cell and a Biologic Fuel Cell Test Station FCT-150S (Figure II - 1 - 1), managing the gas flows and the electrochemical measurements. Gas bottles switches and compressed air purifier are installed to enable long-term ($\approx 700\ \mathrm{hours}$) degradation tests without discontinuity of the gas flows. The hydrogen, oxygen and nitrogen gases are 99.999% pure but it is hard to evaluate the purity of the purified compressed air. The cell is operated at constant cell voltage ranging from 0.6 to $0.85\ \mathrm{V}$ (roughly assimilated to the cathode potential: 0.6 to $0.85\ \mathrm{V}\ vs.\ \mathrm{anode}$); these conditions were chosen to assess as much as possible the effect of the cathode potential on the degradation of the cathode catalyst layers, the anode being assumed to be non-limiting (*i.e.* to stay in the potential region close to $0-0.1\ \mathrm{V}$ *vs.* the reversible hydrogen electrode, RHE).

Figure II - 1 - 1: Picture of the Fuel Cell Test Station FCT-150S from Biologic, connected to the home-made gas network.

a) Electrode preparation

Catalyst Coated Membrane (CCM) are prepared at the Symbio facility at Fontaine (Isère, France), by direct deposition of the catalyst layers on the chosen membrane (Gore 775.15), using an ultrasonic spray coater Sono-Tek ExactaCoat® equipped with an Accumist™ nozzle. Three state-of-the-art commercial catalysts have been selected for the single cell study:

Pt/XC72 $47\ \%\mathrm{wt_{Pt}}$ (also named in this manuscript as TEC10V50E, Pt on Vulcan carbon or Pt/VC), Pt_3Co/XC72 $46\ \%\mathrm{wt_{Pt}}$ and $6\ \%\mathrm{wt_{Co}}$ (also referred to as TEC36V52, PtCo on Vulcan carbon or PtCo/VC) and Pt/GC $30\ \%\mathrm{wt_{Pt}}$ (also referred to as TEC10EA30E-HT, Pt on graphitized carbon or Pt/GC). All were provided from Tanaka Kikinzoku Kogyo (TKK). For the latter catalyst, the platinum nanoparticles are deposited on a high surface area carbon that has been graphitized. A fourth catalyst is used for the reference anode catalyst layer: Pt/HSAC $40\ \%\mathrm{wt_{Pt}}$ (later referred to as TEC10E40E, HSAC standing for high surface area carbon).

Regarding the ink formulation, an ionomer to carbon mass ratio of 0.86 is chosen as well as a mass fraction of alcohol in the ink (water, alcohol, ionomer and catalyst) of 0.6. A diluted suspension of Nafion® D2020 is prepared by adding, in similar proportion as the initial suspension, a mixture of isopropanol, Milli-Q grade water and ethanol to obtain $5.26\ \%\mathrm{wt}$ of Nafion® in the used suspension. For the ink preparation, all the different elements are weighed to reach the targeted amount. First, the powder is put into a glass bottle, the Milli-Q grade water is then introduced to wet all the surface and volume of catalyst powder to prevent any combustion with the alcohol. The Nafion® suspension is then added to the mixture and then ethanol. The ink is mechanically stirred using an UltraTurrax agitating tool to disperse it for $15\ \mathrm{minutes}$, then placed in an ultrasonic bath for $30\ \mathrm{minutes}$ in cold water. Later the water is replaced due to the heat release and the bath is restarted for another $30 - \mathrm{minute}$ session. Prior to the ultrasonic spray deposition, the inks are let under magnetic stirring to mature for $3\ \mathrm{days}$.

To prepare the programme for the spray coating, the density of the ink is determined by weighing the pumping syringe before and after filling $20\ \mathrm{mL}$ of ink. The density is then used to estimate the physical parameters (nozzle speed, ink flow rate) for the deposition of the targeted loadings of $0.1\ \mathrm{mg_{Pt}cm_{geo}^{-2}}$ at the anode and $0.4\ \mathrm{mg_{Pt}cm_{geo}^{-2}}$ at the cathode. Following that step, the membrane is placed on the heating plate of the Sono-Tek onto a PTFE (polytetrafluoroethylene) porous sheet and a mask is placed on top to hold it tight. A simple segmented pattern is applied for the nozzle movement. The spraying parameters are adjusted after the first deposition based on the difference between the preliminary estimate and the amount of catalyst deposited (obtained by weighing the membrane before and directly after the spray). If additional deposition is needed, the membrane is put back onto the heating vacuum plate of the ultrasonic spray device. The deposition is made on a surface of $18\ \mathrm{cm}$ by $6\ \mathrm{cm}$. All the anodes are prepared at first and the cathodes are prepared on the day after. Out of these CCM strips, 2 electrodes of $6\ \mathrm{cm}$ by $6\ \mathrm{cm}$ are cut and hot-pressed with two sub-gaskets of $50\ \mathrm{\mu m}$ thick and two gaskets (SP400, $160\ \mathrm{\mu m}$ each) to ensure a good contact between the CCM and the gas diffusion layers (GDL) H24C5 ($270\ \mathrm{\mu m}$ thick each uncompressed) from Freudenberg; the hot-pressing is performed at $140°\mathrm{C}$ with a force of 2 tons on a resulting surface of $8\ \mathrm{cm}$ by $8\ \mathrm{cm}$ (accounting for the PTFE masks and the metallic end plates surface). The resulting compression of the GDL is obtained using the following equation [119]:

$$\%_{comp} = \frac{Total\ MEA\ thickness - Total\ Gasket\ thickness}{Total\ MEA\ thickness} \qquad \text{(Eq. II.1.1)}$$

leading to a compression of $\frac{(540+35)-420}{(540+35)} = 27\ \%$, assuming a CCM thickness of *ca.* $35\ \mu\text{m}$ ($15\ \mu\text{m}$ from the 775.15 Gore membrane and $10\ \mu\text{m}$ for each active layer).

The role of the sub-gaskets is to precisely define the active surface ($5\ \text{cm}$ by $5\ \text{cm}$) and to block the rest of the CCM; this way, the gas tightness of the cell is ensured by the larger surface of the membrane. The resulting electrode is shown on Figure II - 1 - 2 and is ready to be tested. The third and last electrode is kept as prepared for *ex situ* initial physicochemical observations.

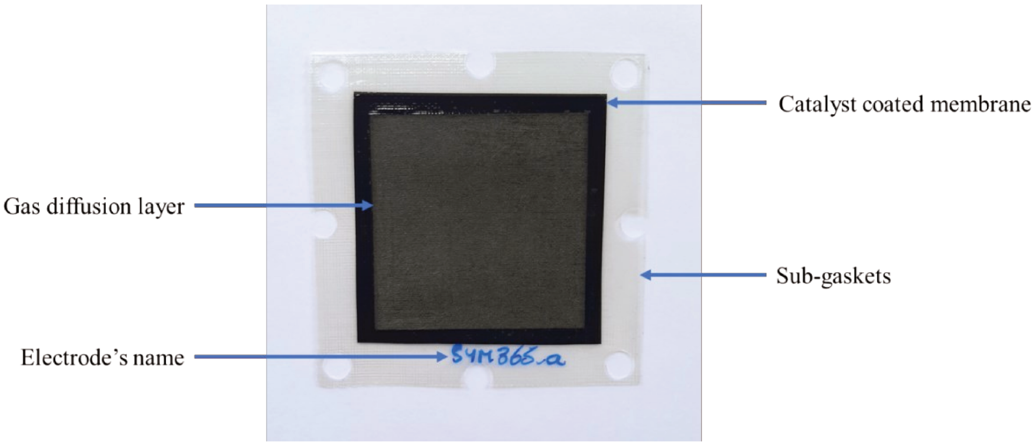

Figure II - 1 - 2: Picture of the as-prepared electrodes after the hot-pressing process

While mounting the cell, eight bolts are used and tightened following a star pattern; the force applied was chosen rather small regarding the bibliography: $6\ \text{N m}$ instead of *ca.* $10\ \text{N m}$ [120–122].

b) Electrochemical protocol and life of the cells

The long-term degradations at constant potentials are supposed to be less damaging over the time than the (deliberately) accelerated stress tests suggested by the Fuel Cell Commercialization Conference of Japan (FCCJ) [85] and the United States Department of Energy (US DOE) [52], which both lead to fast degradations. To better understand the impact of different potentials on the degradation of the cathodic catalyst layer, it is decided to limit as much as possible the potential cycling [123], that may lead to other detrimental degradation mechanisms. To that goal, a minimal quantity of electrochemical characterizations has been chosen to extract information on the state of life of the cell as well as the management of the experimental setup. The experimental cell (Figure II - 1 - 3) is operated at $80°\text{C}$ (heated via heating rods on each terminal plate), the gas lines are put at $120°\text{C}$ to prevent water formation and the humidifiers are stabilized at $64°\text{C}$ (to have a resulting $50\ \%$ relative humidity).

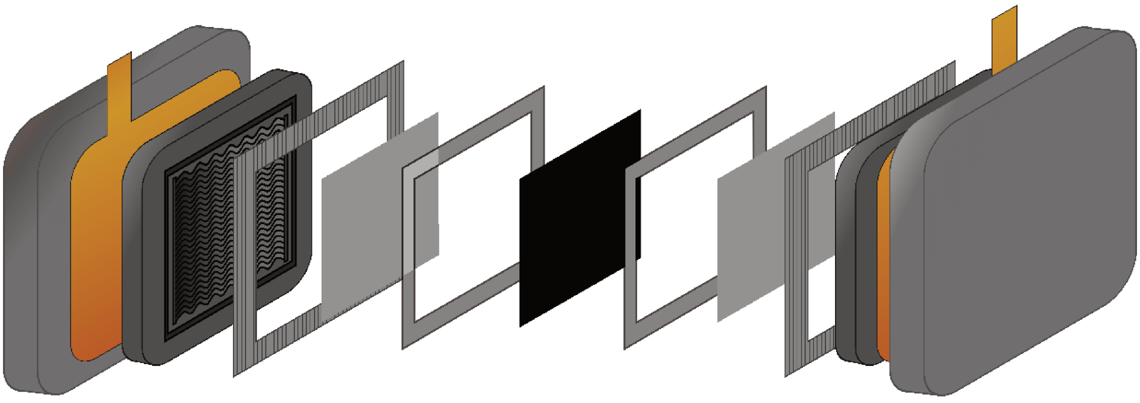

Figure II - 1 - 3:Design of the experimental cell and of the gas channel

The pressure is fixed between atmospheric, 1.5 and $2.0\ \mathrm{bar\ absolute}$, depending on the operating conditions applied. The FCT-150S used is a bit modified to enable self-emptying of the gas condensers and sampling of the water produced inside the cell at given period of time or event.

Beginning of Test, Intermediate characterization 1 and 2 and End of Test (later referred as BoT, Interm1, Interm2 and EoT) are the 4 different stages where potential is cycled during the lifetime of the cell. In each case, a similar sequence of (i) cyclic voltammetries, (ii) potentiostatic electrochemical impedance spectroscopy and (iii) chronoamperometries are performed; whatever the technique, a flow of $210\ \mathrm{mL\ min}^{-1}$ of H_2 at the anode (in fact, the negative pole) and $400\ \mathrm{mL\ min}^{-1}$ of N_2 at the cathode (the positive pole), are applied at an absolute pressure of $1.5\ \mathrm{bar}$. After this sequence, H_2 and N_2 are switched to have H_2 at the working positive pole and N_2 at the working negative pole to access its catalyst state of life and enable the desorption of possible poisoning species at the surface of the catalyst. The role of reference is now held by the “cathode” (which is clearly a name misuse but is done for more clarity) as it is fed with H_2. Each of these sequences of characterizations follows one or several (in the case of the BoT) (iv) polarization curves and is followed by one or several (in the case of the EoT) polarization curves. A mix of procedure is used as a (v) conditioning step to have a reproducible BoT before starting the (vi) aging of the cell. A summary of the different test sequences is given in Figure II - 1 - 4.

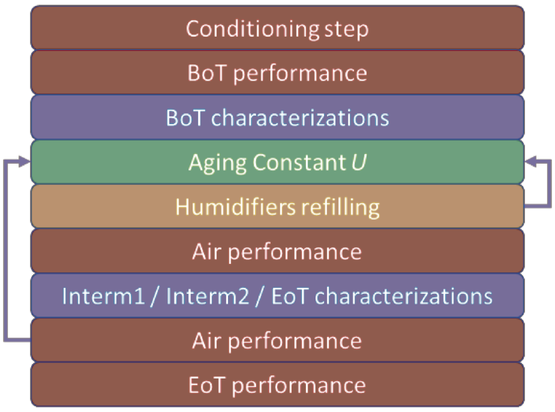

Figure II - 1 - 4: Sequencing of the cell lifetime for potentiostatic degradation

The procedure encompasses as many iterations (right arrow) as needed between aging and refilling of the humidifiers to reach the degradation duration (being *ca.* 7, 14 and 7 days) as well as three iterations (left arrow) for the intermediate characterizations of the active layers.

i. Cyclic Voltammetry (CV)

Cyclic voltammetries performed at three different voltage scan rates of 150, 100 and $50\ \mathrm{mV\ s^{-1}}$ between 0.05 and $0.94\ \mathrm{V}\ vs.\mathrm{anode}$ (which will then be referred as V in the rest of this work, assuming the anode is assimilated to a reference electrode of potential close to $0\ \mathrm{V\ vs.RHE}$) are used for the determination of the Hydrogen Under Potential Deposition ($\mathrm{H_{upd}}$) curve of the positive electrode. This method is used in this work to determine the electrochemically active surface area (ECSA) of platinum in the single cell setup, because carbon monoxide adsorption and stripping (also called CO stripping) is not possible with the present setup. The measurement of the ECSA is made as represented on the blue area of Figure II - 1 - 5, which is a typical CV performed at $150\ \mathrm{mV\ s^{-1}}$: a baseline is taken linear between $0.4\ \mathrm{V}$ and its intersection with the curve at lower voltages. The area of the proton desorption region (A_{curve}, in $\mathrm{A\ V}$ or $\mathrm{mA\ V}$) is measured between the curve and the baseline and leads to the determination of the ECSA following Eq. II.1.2:

$$\mathrm{ECSA} = \frac{A_{\mathrm{curve}}}{v_{\mathrm{b}} * Q_{\mathrm{H^+}}} \qquad \text{(Eq. II.1.2)}$$

with v_{b} the voltage scan rate and $Q_{\mathrm{H^+}}$ the specific charge resulting from the adsorption/desorption of protons on one square centimetre of platinum, this value being equal to $210\ \mathrm{\mu C\ cm_{Pt}^{-2}}$.

As can be seen on Figure II - 1 - 5, there are other areas of interest, such as the adsorption region of the proton (negative voltage scan for the same range of voltages); the charge measured in this region can be averaged with the previous desorption region to refine the ECSA measurement. In the conditions of this degradation study, though, the lower voltage limit of $0.05\ \mathrm{V}\ vs.\mathrm{anode}$ is rather low and in consequence, a non-negligible charge is ascribed to the hydrogen evolution reaction, that leads to an overestimation of the ECSA. This is the reason why A_{curve} is usually calculated using the proton desorption region. At higher potential values, the platinum oxide region is monitored, where Pt-OH and then Pt-O are formed on the positive scan and reduced in the negative one (green and orange regions).

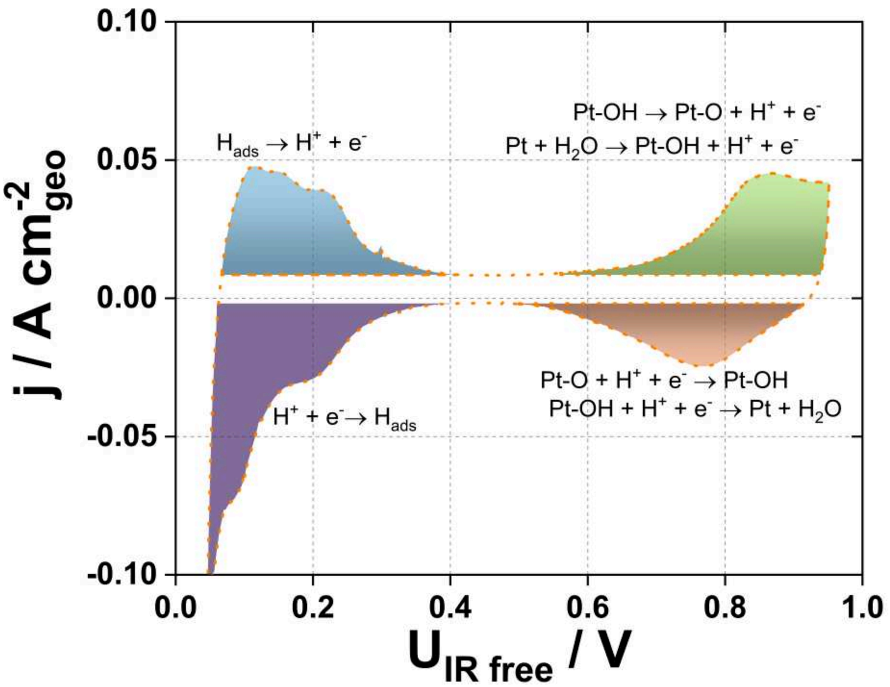

Figure II - 1 - 5: CV enabling the measurement of the H_{UPD} area (leading to the ECSA) and of the Pt-oxide features

ii. Potentiostatic Electrochemical Impedance Spectroscopy (PEIS)

The potentiostatic electrochemical impedance spectroscopy is a very interesting technique that can separate different phenomena that occur at the same time in an electrochemical setup. These phenomena, however, have different intrinsic time constants, that renders possible their separation in the frequency domain. The main hypothesises to use correctly this technique is to set a functioning point invariant in time (steady-state) and to apply variations of the signal in a domain where the system stays linear. A voltage of $0.2\ \mathrm{V}\ vs.$ anode is applied and a waiting time of $60\ \mathrm{s}$ is respected to reach near-stationary conditions. After that, variations of $10\ \mathrm{mV}$ are applied at different frequencies ranging from $50\ \mathrm{kHz}$ to $1\ \mathrm{Hz}$ to keep the characterizations as fast as possible. The resulting impedance spectra can then be used to access the proton conductivity inside the active layer (R_p) and the high-frequency resistance (R_{HF}) using a transmission line model [124–127] (Eq. II.1.3) and a transmission line model modified for the non-ideality of the double layer distribution [128] (Eq. II.1.4) (Figure II - 1 - 6).

$$Z_{\mathrm{mod1}}(f) = R_{\mathrm{HF}} + \sqrt{\frac{R_{\mathrm{p}}}{C_{\mathrm{dl}} 2i\pi f}} * \frac{1}{\tanh\left(\sqrt{2i\pi f R_{\mathrm{p}} C_{\mathrm{dl}}}\right)} \qquad \text{(Eq. II.1.3)}$$

$$Z_{\mathrm{mod2}}(f) = R_{\mathrm{HF}} + \frac{R_{\mathrm{p}}}{\left(R_{\mathrm{p}} C_{\mathrm{dl}} 2i\pi f\right)^{\alpha/2}} * \frac{1}{\tanh\left(\left(2i\pi f R_{\mathrm{p}} C_{\mathrm{dl}}\right)^{\alpha/2}\right)} \qquad \text{(Eq. II.1.4)}$$

These graphs are presented in an orthonormal coordinate system to appreciate visually the 45°-slope characteristic of such models. Left-hand side is a large-scale view of all the points measured and fitted while the right-hand side is a zoom made on the 45°-slope region. Blue symbols stand for the experimental values, which some of them (most at high frequencies) are not used for the fit as they are believed to be measure artifacts. Red stars are the extrapolation of the model to the entirety of the frequency range used for both models while the brown and green stars correspond to the model 1 (ideal case) and model 2 (containing a non-ideal parameter α) respectively.

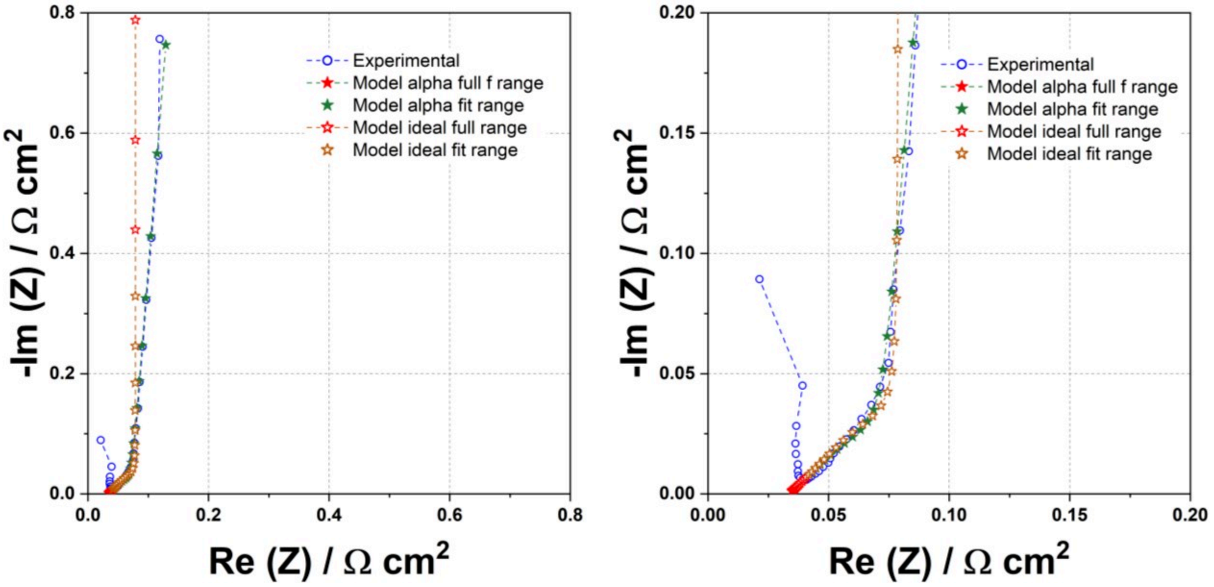

Figure II - 1 - 6: Example of impedance spectra performed at 0.2 V, 50% RH and fit using blocking electrode models with restricted diffusion hypothesis and with (green stars) or without (brown stars) a non-ideal distribution of the double layer capacitance correction

Parameters extracted from the fits:

$$R_{\mathrm{HF-1}} = 34\ \mathrm{m\Omega\ cm^2_{geo}}\ /\ C_{\mathrm{dl-1}} = 0.20\ \mathrm{F\ cm^{-2}_{geo}}\ /\ R_{\mathrm{p-1}} = 135\ \mathrm{m\Omega\ cm^2_{geo}}$$

$$R_{\mathrm{HF-2}} = 34\ \mathrm{m\Omega\ cm^2_{geo}}\ /\ C_{\mathrm{dl-2}} = 0.19\ \mathrm{F\ cm^{-2}_{geo}}\ /\ R_{\mathrm{p-2}} = 111\ \mathrm{m\Omega\ cm^{-2}_{geo}}\ /\ \alpha = 0.95$$

iii. Chronoamperometry (CA)

The chronoamperometry is one of the most basic electrochemical techniques that can be used; it consists of applying a potential or a voltage to an electrochemical system and to record the evolution of the current over time. In the case of a PEMFC single cell fed with H_2 at the negative and N_2 at the positive electrodes, it results in the measurement of two important elements in the life and function of a cell: the H_2 permeation through the membrane and the electrical short-circuit current. The first is related to the high diffusivity of dihydrogen that can easily cross the membrane when a partial pressure (concentration) gradient exists from one side to the other side of the membrane; H_2 diffuses from the H_2-rich region (the negative electrode, fed with H_2) to the H_2-poor region (the positive electrode, fed with N_2). Applying a “sufficient” potential to the positive electrode versus the negative electrode enables to oxidize the crossing H_2 and to detect the quantity of electron by-passing the external circuit due to the too close vicinity of electronic conductor elements (in our case, mostly carbon or platinum) from both electrodes (short-circuit). As both phenomena overlap, it is decided to apply 5 different voltages (0.3, 0.4, 0.5, 0.6 and 0.7 V) for 3 minutes each and to record the stabilised current (over the last minute) as shown on Figure II - 1 - 7 (where it is supposed to be rather stationary). The evolution of these stationary currents is plotted in a second time as a linear regression assumed to follow:

$$I_{\text{stationary}} = \frac{1}{R_{\text{sc}}} * U_{\text{cell}} + I_{\text{cross-over}}^{\text{H}_2} \qquad \text{(Eq. II.1.5)}$$

where R_{sc} is the short-circuit resistance and $I_{\text{cross-over}}^{\text{H}_2}$ is the hydrogen oxidation current at the cathode resulting from its cross-over through the membrane.

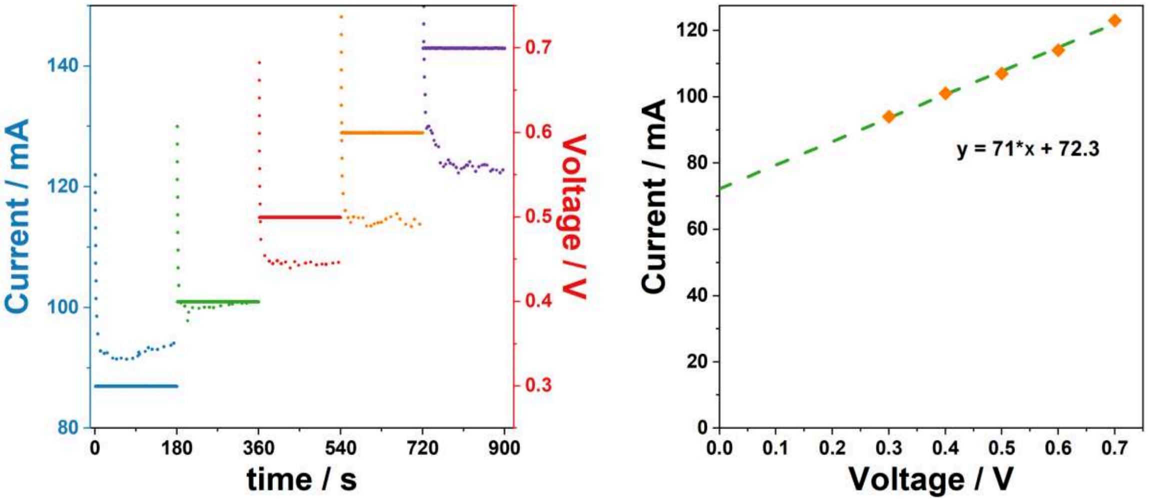

Figure II - 1 - 7: Determination of the short-circuit resistance and of the hydrogen cross-over current using chronoamperometries (left) and fitting the stationary currents with a linear function (right)

These parameters will be used to assess the state of life of the membrane; the higher the hydrogen cross-over current, the more damaged the membrane; the same goes with the inverse of the short-circuit resistance. It can however be noted that for very low resistance, as well as very high cross-over current, the other parameter will not be measurable. For membrane at the beginning of life, $R_{\text{sc}} \approx 250 - 300 \text{ Ohm cm}_{\text{geo}}^2$ and $I_{\text{cross-over}}^{\text{H}_2} \approx 2.5 - 3 \text{ mA cm}_{\text{geo}}^{-2}$.

iv. *Polarization curves*

Among all the characterizations to test and understand how a catalyst layer works, performance curves are needed in addition to inert atmosphere (H_2/N_2) measurements. Polarization curves under Hydrogen/Oxygen (H_2/O_2) and Hydrogen/Air (H_2/Air) are performed and have the same type of protocol as cyclic voltammetries. The voltage of the cell is cycled between the open cell voltage (OCV) and $0.56\ \mathrm{V}$ (without dynamic correction of the ohmic drop) at a voltage scan rate of $10\ \mathrm{mV\ s^{-1}}$ and two cycles are carried out. Minimum flows of $210\ \mathrm{mL\ min^{-1}}$ for H_2 and $400\ \mathrm{mL\ min^{-1}}$ for both O_2 and Air are fixed, and stoichiometric coefficients are fixed at 1.5 for regular polarization curves; the current evolution is monitored over time and the flow rates are scaled progressively to follow the desired stoichiometry. The pressure is either fixed at 1.5 or $2.0\ \mathrm{bar\ absolute}$ (bara). For BoT and EoT performance characterizations, curves are performed for all four following conditions: H_2/Air $1.5\ \mathrm{bara}$, H_2/Air $2.0\ \mathrm{bara}$, H_2/O_2 $1.5\ \mathrm{bara}$ and H_2/O_2 $2.0\ \mathrm{bara}$. For intermediate characterizations (before and after Interm1 and Interm2), only polarization curves at $1.5\ \mathrm{bara}$ under H_2/Air flows are performed. For this case, the idea is to identify the presence or not of reversible performance losses.

v. Conditioning step

To start reproducibly the cell, a conditioning protocol is carried out under H_2/Air at stoichiometric coefficients of 2 on both sides. A cell voltage of $0.6\ \mathrm{V}$ is applied for $2\ \mathrm{hours}$ with PEIS at the same voltage intercalated every $30\ \mathrm{minutes}$. At the end of the conditioning step, a polarization curve with the same conditions as the one detailed in the section iv) but with stoichiometric coefficients of 2 is acquired.

vi. Aging protocol

It is decided that the study of long-term degradation would be done under H_2/Air at constant potential with the same minimal flows of $210\ \mathrm{mL\ min^{-1}}$ for H_2 and $400\ \mathrm{mL\ min^{-1}}$ for Air as for all electrochemical techniques. The cell is operated as previously mentioned: $80°\mathrm{C}$, gas lines at $120°\mathrm{C}$ and humidifiers at $64°\mathrm{C}$ to reach a relative gas humidification of $50\ \%$. The initial pressure at OCV is $1.5\ \mathrm{bar\ absolute}$. Just after an aging voltage (no dynamic correction of the ohmic drop) is applied (CA technique), the pressures are modified and need to be readjusted to $1.5\ \mathrm{bara}$ on each side. This phenomenon is not very well understood and believed to be intrinsically related to the test station and the consumption of gases – production of water. After stabilization of the pressures, the cell is let alone for two days. As the humidifiers of the test bench need to be refiled regularly in certain conditions (for example, 0.6 and $0.7\ \mathrm{V}$ where the current and as a result, the gas flows, is much higher than at 0.8 and $0.85\ \mathrm{V}$). Independently of the aging voltage, the cell is then stopped three times a week (Monday, Wednesday, and Friday) to refill the humidifiers and to have the same action on the bench for every cell as it might be damageable due to voltage changes. To refill, the aging protocol is stopped, the pressures are readjusted before being reduced to atmospheric. The flows of gases are set to zero and Milli-Q grade water ($> 15\ \mathrm{M\Omega\ cm}$) is put into the humidifiers. The cell voltage progressively decreases toward $0.05\ \mathrm{V}$. Upon refill, gas flows are set to their respective values and pressure is increased to $1.5\ \mathrm{bara}$. The degradation test can be started again.

2. Segmented Cell

This PhD is done in collaboration with the LEMTA laboratory in Nancy. This lab has developed a segmented PEMFC in which the cathode current collection plate is divided into 20 segments, as represented on Figure II - 2 - 1, each segment having the same surface (being $\frac{1}{20} * 25 = 1.25\ \mathrm{cm}^2$). The flow field configuration is a counter-flow (Air-Nitrogen inlet is placed at the same position than the Hydrogen outlet and vice-versa) and all the 20 segments are placed following a $5 - \mathrm{serpentine}$ flow field path design.

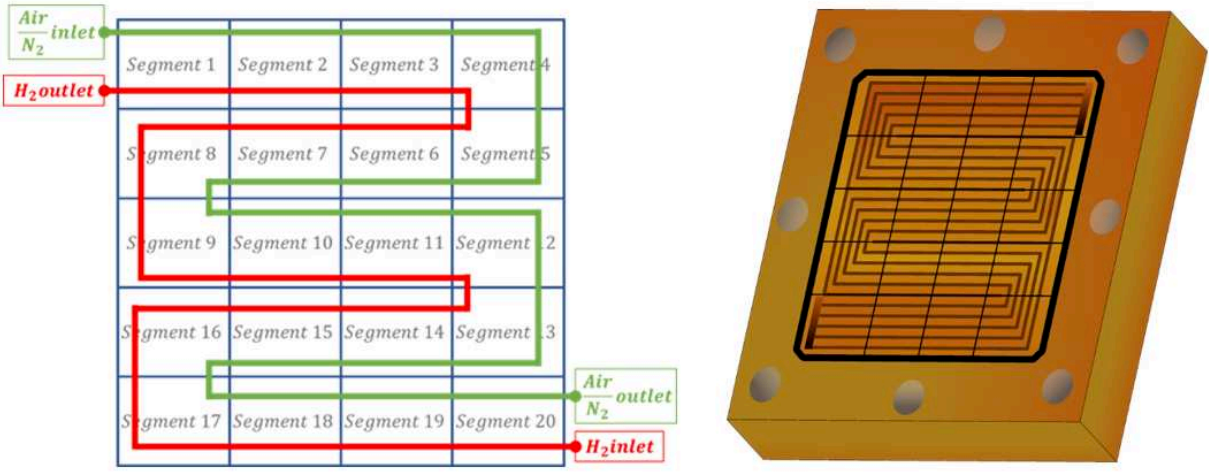

Figure II - 2 - 1: Schematic representation of the flow field of the LEMTA's segmented cell

a) Experimental setup

The experimental setup is home-made and all the communications between the different instruments are operated using the LabView® software. This enables the coordination of all the balance of plant, as can be seen on the picture of Figure II - 2 - 2. Flow controllers (Brooks SLA5850, Mass Flow) are used for Nitrogen, Air and Hydrogen with two calibres for the two latter to regulate the gas flow rate with the desired stoichiometric coefficient when being at low and high current densities. Three humidifiers with frits for a better gas dispersion and a more efficient humidification are used for all three gases. Water condensation is not possible in the gas lines because they are heated over the temperature of the humidifiers. Foam is wrapped around the gas lines to keep the heat and ensure a homogeneous heat distribution and that no cold point will form along the gas channels. Water condensers and pressure controllers (Brooks SLA5800, Pressure Controller) are put at the end of the tubing, downstream of the cell. In the following, if the pressure is regulated, it means that at the end of the gas network the pressure will be regulated but then, inside the cell, the pressure will be slightly over this value, accounting for the pressure losses of the channels and of the network. Finally, all the twenty segments of the cathode current collector are connected to an acquisition card (USB X Series, National Instruments) to record locally the current for the electrochemical diagnosis of the cell. All the currents are then summed up and dissipated into the load. A function generator (33210A, Agilent) is coupled with the load (PLI Series Electronic Load, H&H) to add controlled sinusoidal components to the direct current (DC) for galvanostatic electrochemical impedance spectroscopy (GEIS) measurements. The final instrument available on the test bench is a power supply (E3614A DC Power Supply, Hewlett Packard), useful for degradation protocol such as load cycling ($0.6-1\ \mathrm{V}$) for instance.

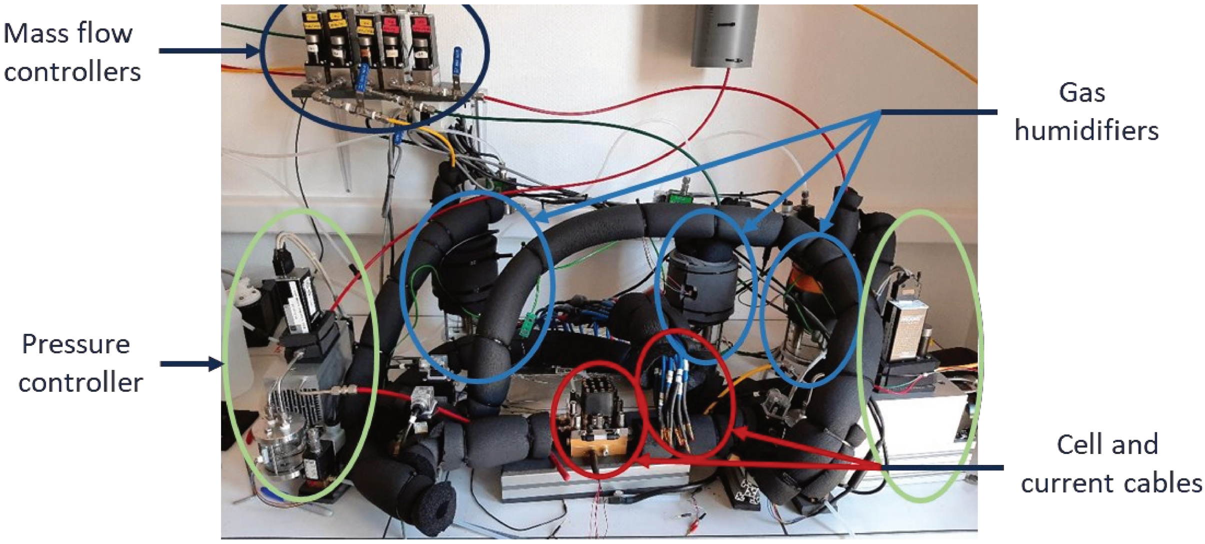

Figure II - 2 - 2: Picture of the segmented cell and its balance of plant

b) Segmented cell studies

PTFE wedges of $150\ \mu\mathrm{m}$ are placed on each side of the membrane to limit the MEA compression to 30%. If not mentioned specifically in the different sections, all the experiments and electrochemical characterizations are done at a cell temperature of $80°\mathrm{C}$ using water as heat-carrying fluid and a thermostatic bath (F 25, Julabo). The anode and cathode gases' relative humidities are fixed equal at 50%.

i. End of life analysis of CCM aged with constant potential protocol

The electrodes aged at LEPMI using the FCT-150S and the constant potential protocol are vacuum packaged and brought to LEMTA for a segmented cell analysis to identify if the degradation is homogeneous on the whole surface of the CCM. A break-in procedure similar to the beginning-of-life done at LEPMI is applied: 2 hours holding period at $0.6\ \mathrm{V}$, this time with fixed flow rates ($35\ \mathrm{NL\ h^{-1}}$ for the hydrogen flow rate at the anode and $80\ \mathrm{NL\ h^{-1}}$ for the air flow rate at the cathode). This would lead to a stoichiometric coefficient of 2 on each side for a given current of $40\ \mathrm{A}$. This break-in procedure enables to restart the cell without applying a heavy cycling procedure that could be done under H_2/N_2 or H_2/Air atmospheres and would be significantly damaging the voltage control expected in this study. Several electrochemical techniques have been used to replicate the end-of-life protocol used in LEPMI.

ii. *Degradation of Pt_3Co CCM using potential cycling tests under H_2/N_2 atmosphere*

Pt_3Co electrodes have been prepared at the same time than the Pt only electrodes used for the previous study. In the case of Pt_3Co CCMs, it is decided to experiment different aging protocols such as Load Cycling ($0.6 - 1\ \mathrm{V}$), Start-up/Shut-down (1 – 1.5 V) and variations of these two: by decreasing the lower voltage boundary ($0.1 - 1\ \mathrm{V}$) and a mix of the two latter to affect tremendously the active layers ($0.1 - 1 - 1.5 - 1\ \mathrm{V}$). $30\mathrm{k}$ cycles are targeted, leading to $60\mathrm{k}$ voltage steps for the three first protocols, $15\mathrm{k}$ cycles are done for the four-step procedure to have the same number of steps and the same aging duration (3 s for each step resulting in *ca.* $50\ \mathrm{h}$ of test, without considering the time needed to switch from one voltage step to another). For the degradation only, the temperature of the N_2 and H_2 humidifiers are increased to $78°\mathrm{C}$ (resulting in 92% RH) and the gas lines are heated up to $85°\mathrm{C}$. As no particular care to prevent the cell from too much voltage cycling is done regarding the aging procedures, an in-house conditioning protocol is applied in this study.

c) Electrochemical protocols

i. *In-house break-in*

A succession of three voltage steps is repeated to condition the CCMs at atmospheric pressure before any performance measurements. A 45 s-long $0.6\ \mathrm{V}$ hold is followed by a 30 s OCV rest to finish with $60\ \mathrm{s}$ at $0.3\ \mathrm{V}$ to alternate between hydrating, drying and highly hydrating conditions. This sequence is repeated 50 times with stoichiometric coefficients of 3 at the cathode and 1.5 at the anode. The initial flow rates, used for the very first cycle, are fixed considering currents of 20, 2 and $40\ \mathrm{A}$ are reached for the steps at $0.6\ \mathrm{V}$, OCV and $0.3\ \mathrm{V}$ respectively. For the following sequences, the flow rates are modified using the current delivered in the previous sequence to match the desired stoichiometric coefficients, the flow rates of steps at cycle i being calculated with the current measured at the same step in cycle $i-1$.

ii. Chronopotentiometry – Live I charge

Galvanostatic steps are applied at $25\ \mathrm{A}$ at beginning-of-life to stabilize the current before doing Galvano impedance spectroscopy (see section thereafter). Stoichiometric coefficients are similar to the break-in and fixed to respectively 3 and 1.5 for the air and hydrogen flows. After the aging procedure, the galvanostatic steps are also performed at $12.5\ \mathrm{A}$, as 25 A might not be achieved anymore due to major damage done to the CCMs. These steps are applied for a duration of 30 minutes to 1 hour until a stable voltage is reached. It is also used as a long-term waiting step for overnight experiments, to keep a well humidified interface.

iii. Galvanostatic Electrochemical Impedance Spectroscopy (GEIS)

The GEIS in segmented cell are always placed after a Live I charge step (cf. previous section) at the same current. The gas flows parameters are kept identical to the previous current hold to stay on the stationary point obtained. The applied amplitude used is equal to 10% of the stationary current ($2.5\ \mathrm{A}$ for $25\ \mathrm{A}$ holding point and $1.25\ \mathrm{A}$ for $12.5\ \mathrm{A}$ holding point). Frequency ranges from $10\ \mathrm{kHz}$ to $0.02\ \mathrm{Hz}$ with a varying number of periods and of points per period for each frequency. The number of points per frequency is almost kept constant equal to $8{,}000$ with 100 periods analysed at $10\ \mathrm{kHz}$ and 2 periods at $0.02\ \mathrm{Hz}$ to have an experimental time of the overall spectroscopy of *ca.* 10 minutes. For high frequencies (above $300\ \mathrm{Hz}$) each impedance is analysed separately for each segment, whereas for low frequencies, all the impedance are made concomitantly for all the segments. In the end, the impedance, depending on the frequency f, can be calculated using the amplitude and phase ratio of both the current and voltage via the following equations:

$$Z(f) = A(f) * \left[\, \cos\big(\varphi(f)\big) + i * \sin\big(\varphi(f)\big) \,\right] \qquad \text{(Eq. II.2.1)}$$

With $A(f) = \frac{\bar{U}(f)}{\bar{I}(f)}$ the amplitude of the signal and $\varphi(f) = \varphi^{\mathrm{U}}(f) - \varphi^{\mathrm{I}}(f)$ its phase.

All the amplitude and phase of both current and voltage are obtained using an in-house Matlab® computing program to fit the shifts regarding the applied signal. The $Z(f)$ are then displayed in a Nyquist plot.

iv. Polarization curves

The polarization curves are a succession of $30\ \mathrm{s}$ current steps ranging from 0 to $100\ \mathrm{A}$ with minimal reactant flows rules: if the flow rate at a given current, with respect to the stoichiometric coefficient applied, is inferior to $1\ \mathrm{NL\ h^{-1}}$, then $0.5\ \mathrm{NL\ h^{-1}}$ are added for the H_2 flow. In the case of the air flow, if the calculated flow is below $6\ \mathrm{NL\ h^{-1}}$, $1\ \mathrm{NL\ h^{-1}}$ is added. It leads to flow rates of H_2 and air respectively equal to 0.5 and $1\ \mathrm{NL\ h^{-1}}$ for the initial step. A voltage threshold of $0.3\ \mathrm{V}$ is also set to avoid cell reversal. Once the voltage falls down this value for half the duration of the step, the decrease in current step starts to return to the OCV. These tests are performed with two different sets of stoichiometric coefficients: the classic 3 cathode / 1.5 anode and an iso 1.5 / 1.5 to close the performance to more realistic conditions.

v. Chronoamperometry - Permeation

Akin to the Chronoamperometry (CA) section hereabove, a multi-step potential hold is applied to determine the amount of hydrogen crossing over through the membrane to the cathode and to have an estimation of the short-circuit that may be present in the surface of the tested CCMs.

vi. Cyclic voltammetry

Depending on the study, one (Pt_3Co cycling degradation) or three (Potentiostatic degradation) cyclic voltammogram sequences are performed over a wide range of voltage. In the case of the degradation study of Pt_3Co electrocatalyst, a two-cycles voltamperometry at $50\ \mathrm{mV\ s^{-1}}$ is done from 0.1 to $0.7\ \mathrm{V}$ with 600 points per cycle. For the *post mortem* analysis of the potentiostatic degradation study, a succession of two CVs at 150, 100 and $50\ \mathrm{mV\ s^{-1}}$ are plotted from 0.05 to $0.94\ \mathrm{V}$, with same number of points to see the likeliness or the difference with the CVs performed during the end-of-life at LEPMI.

3. Liquid and Half Cell electrochemical experiments

In this section, procedures and protocols for catalysts' intrinsic activity determination will be dealt with in two environments: a liquid cell with the widely known rotating disk electrode (RDE) and in a half cell configuration known as the gas diffusion electrode (GDE). The preparation of the electrode and the specificity of the experimental approaches in both cases will be presented.

a) Catalysts used and electrodes preparation

During this work, a total of 3 platinum-based catalysts have been studied. The term catalyst will be used in this manuscript for the combination of the metal nanoparticles, having the main catalytic effect, and of its carbon particles, on which the metallic nanoparticles are supported. The different catalysts tested, and their denomination are listed hereafter:

- TEC10V50E – Platinum $47\ \%\mathrm{wt}_{\mathrm{Pt}}$ on Vulcan XC-72 noted **Pt/VC**
- TEC36V52 – Platinum $46\ \%\mathrm{wt}_{\mathrm{Pt}}$ - Cobalt $6\ \%\mathrm{wt}_{\mathrm{Co}}$ alloy Pt_3Co on Vulcan XC-72 noted **PtCo/VC**
- TEC10EA30E-HT – Platinum $30\ \%\mathrm{wt}_{\mathrm{Pt}}$ on graphitized high surface area carbon noted **Pt/GC**

The starting point for the use of catalyst powders relies on the formulation and dispersion of it in a mixture of ultrapure water, isopropanol (IPA) and ionomer. The proportion of each components differs depending on the application (RDE drop casting and GDE spray coating). All the manipulations of powders containing nanoparticles are done under a laminar-flow nano hood (Safetech) to prevent any dispersion (hence potential breathing) of catalysts nanoparticles by the experimentalist in the laboratory. The powders' weighing is done using an antistatic apparatus on the container, the spatula and the vial to further reduce the risks.

i. RDE inks for the drop casting

In the case of RDE drop-cast method, the inks are prepared as follows: water ($\rho = 18.2\ \mathrm{M\Omega\ cm}$, total organic carbon (TOC) $< 3\ \mathrm{ppb}$) from a Milli-Q system (Millipore, Merck) is put first on the powder to prevent any combustion of the IPA (HPLC grade Fisher Chemical) to reach a volumetric ratio of $H_2O:IPA = 2.5$. A $5\ \%\mathrm{wt}$ Nafion® suspension ($1100\ \mathrm{EW}$, Sigma Aldrich) is then added to act, mainly in RDE as a binding element for the active layer. An ionomer to carbon ratio (I/C) of 0.7 is targeted. The inks are then placed for $30\ \mathrm{min}$ in an ultrasonic bath filled with cold water (*ca.* $10 - 15°\mathrm{C}$). The inks are stored for at least a day before being used. The storage duration is limited to a month in a fridge before the ink is wasted.

ii. GDE's spray on GDL at CEA-LITEN

A first batch of sprayed electrodes are made for the Tanaka commercial catalysts (Pt/VC, PtCo/VC and Pt/GC); it is made in collaboration with the CEA-LITEN for a joint study of low-loaded electrodes (targeting $20\ \mathrm{\mu g\ cm_{geo}^{-2}}$ of platinum) and realised by Clémence Lafforgue (a former postdoctoral researcher in LEPMI/CEA-LITEN) following the experimental protocol summarised here for the sake of gathering all the process. The catalytic inks are prepared by mixing the same component in the same order as mentioned in the previous section. The solution is stirred mechanically using a magnetic bar for $5\ \mathrm{min}$ at a rotating speed of $400\ \mathrm{rpm}$ and then placed in an ultrasonic bath for $30\ \mathrm{min}$ in cold water (refreshed after $15\ \mathrm{min}$). The ionomer dispersion is added afterwards and the final solution is placed under magnetic stirring overnight. For the Vulcan XC72-supported catalysts, the composition of the inks is as follow: $0.5\ \mathrm{g}$ of catalyst powder, $13.9\ \mathrm{g}$ of water, $29\ \mathrm{g}$ of IPA and $0.8\ \mathrm{g}$ of ionomer (to target a I/C mass ratio of 0.7). For the graphitized carbon-supported catalyst, the mass of catalyst powder and ionomer are changed to 0.2 and 0.32 respectively to target an I/C ratio of 0.5. The electrodes are directly sprayed on the chosen GDL (H23C8, Freudenberg) using a Sono-Tek® ExactaCoat equipped with a $120\ \mathrm{kHz}$ Impact nozzle. The heating plate is brought to $80°\mathrm{C}$ and the GDL is hold using the vacuum system. Loadings are measured after the spray with X-ray fluorescence (XRF) and lead to $0.018\ \mathrm{mg_{Pt}\ cm_{geo}^{-2}}$ ($\pm 7\%$), $0.020\ \mathrm{mg_{Pt}\ cm_{geo}^{-2}}$ ($\pm 7\%$) and $0.019\ \mathrm{mg_{Pt}\ cm_{geo}^{-2}}$ ($\pm 8\%$) for Pt/VC, PtCo/VC and Pt/GC, respectively. Each as prepared GDE is then punched to a $3\ \mathrm{mm}$ diameter disk, that is inserted into a ring ($6\ \mathrm{mm}$ outer and $3\ \mathrm{mm}$ inner diameters) of the same GDL with no spray on it.

b) Rotating disk electrode setup

i. Principle of the Thin Film Porous Rotating Disk Electrode

The sheer principle of this method is to prepare a porous, thin-film of catalyst, that requires a very little amount of active material, on a glassy carbon disk (acting as current collector and being almost inactive with the environment and the reaction at stake) embedded in a PTFE cylindrical tip; the whole is screwed on the rotor and dipped in an ultrapure electrolyte (here $0.1\ \mathrm{M}$ $HClO_4$). The reacting gas (O_2) is dissolved in the electrolyte; its solubility being quite small (*ca.* $1\ \mathrm{mmol\ L^{-1}}$) and its diffusion coefficient in a liquid media on the order of $10^{-6}\ \mathrm{cm^2\ s^{-1}}$ [129], this leads to a mass-transport limitation plateau for high oxygen reduction reaction (ORR) overpotentials. In the case of the RDE, mass-transport limitations can be corrected to unveil only the charge transfer kinetic of the reaction of interest, which makes it a powerful and easy technique for electrocatalytic activity determination.

The rotation of the electrode establishes a stationary regime as it controls the thickness of the diffusion layer:

$$\delta_{O_2} = 1.61 * D_{O_2}^{1/3} * \nu^{1/6} * \Omega^{-1/2} \qquad \text{(Eq. II.3.1)}$$

δ_{O_2}, D_{O_2}, ν and Ω being respectively the oxygen diffusion layer thickness, oxygen diffusion coefficient, the electrolyte kinematic viscosity ($\mathrm{cm^2\ s^{-1}}$) and the electrode angular rotation rate ($\mathrm{rad\ s^{-1}}$).

So, in the case of the RDE and its particular convection induced by the rotation of the electrode, the mass-transport kinetics parameter m_{O_2} expression becomes:

$$m_{O_2} = \frac{D_{O_2}}{\delta_{O_2}} = 0.62 * D_{O_2}^{2/3} * \nu^{-1/6} * \Omega^{1/2} \qquad \text{(Eq. II.3.2)}$$

In such conditions, the faradaic current of the ORR at a given potential ($j_{\mathrm{f}}(E)$) is either ruled by the charge transfer limited kinetics of the reaction ($j_{\mathrm{ct}}(E)$) or by the mass-transport kinetics (j_{lim}) depending on the overpotential (respectively low or high), as described by the Koutecky-Levich model (that assumes that the diffusion in the thickness of the active layer is negligible, which is valid for active layer loadings of $20\ \mathrm{\mu g_{Pt} cm_{geo}^{-2}}$):

$$\frac{1}{j_{\mathrm{f}}(E)} = \frac{1}{j_{\mathrm{ct}}(E)} + \frac{1}{j_{\mathrm{lim}}} \qquad \text{(Eq. II.3.3)}$$

In the case of mass-transport limitation, it means that all the species at the vicinity of the electrodes are consumed, fixing the concentration gradient as the diffusion layer thickness is also fixed. In these conditions (valid for high overpotentials), the limiting current density is given by:

$$j_{\mathrm{lim}} = -n * F * C_{\mathrm{O_2}} * m_{\mathrm{O_2}} \qquad \text{(Eq. II.3.4)}$$

Where n is the number of electrons exchanged, F is the Faradaic constant and $C_{\mathrm{O_2}}$ is the oxygen solubility in the electrolyte.

$$j_{\mathrm{lim}} = -0.62 * n * F * C_{\mathrm{O_2}} * D_{\mathrm{O_2}}^{2/3} * \nu^{-1/6} * \Omega^{1/2} \qquad \text{(Eq. II.3.5)}$$

The charge transfer limited current density is then obtained using the Koutecky-Levich correction:

$$j_{\mathrm{ct}}(E) = \frac{j_{\mathrm{f}}(E) * j_{\mathrm{lim}}}{j_{\mathrm{lim}} - j_{\mathrm{f}}(E)} \qquad \text{(Eq. II.3.6)}$$

This charge transfer current density will be used in the following as the way to compare the activity between catalysts. It is reported to the geometric surface of electrode by definition and will be adapted to specific current density (corresponding to the real surface of catalyst used) and mass current density (corresponding to the exact mass of catalyst used).

ii. Preparation of the experimental setup

For RDE experiments, the setup used is a four-electrode glass cell made up of several elements as can been seen on Figure II - 3 - 1.

The RDE stator (OrigaTrod, Origalys) enables a fine control of the rotation speed of the electrode, ruling the mass-transport of oxygen inside the electrolyte. Rotation speeds used: 400 – 900 – 1,600 – 2,500 rpm.

The gas inlet is made of glass, with a PTFE tap that can switch from bubbling gas in the electrolyte during the purge with either Ar (99.999 %, Messer), CO (99.997 %, Messer) or O_2 (99.999 %, Messer) or on top of the electrolyte to prevent signal noise during the electrochemical techniques.

The reference electrode is a home-made reversible hydrogen electrode, renewed for each day of experiments.

The auxiliary electrode (also called fourth electrode) is a simple Pt wire with a small Pt sphere at the end. It is connected to a capacitor bridge in parallel with the reference, to act as a high-frequency noise filter and to accelerate the response time [130].

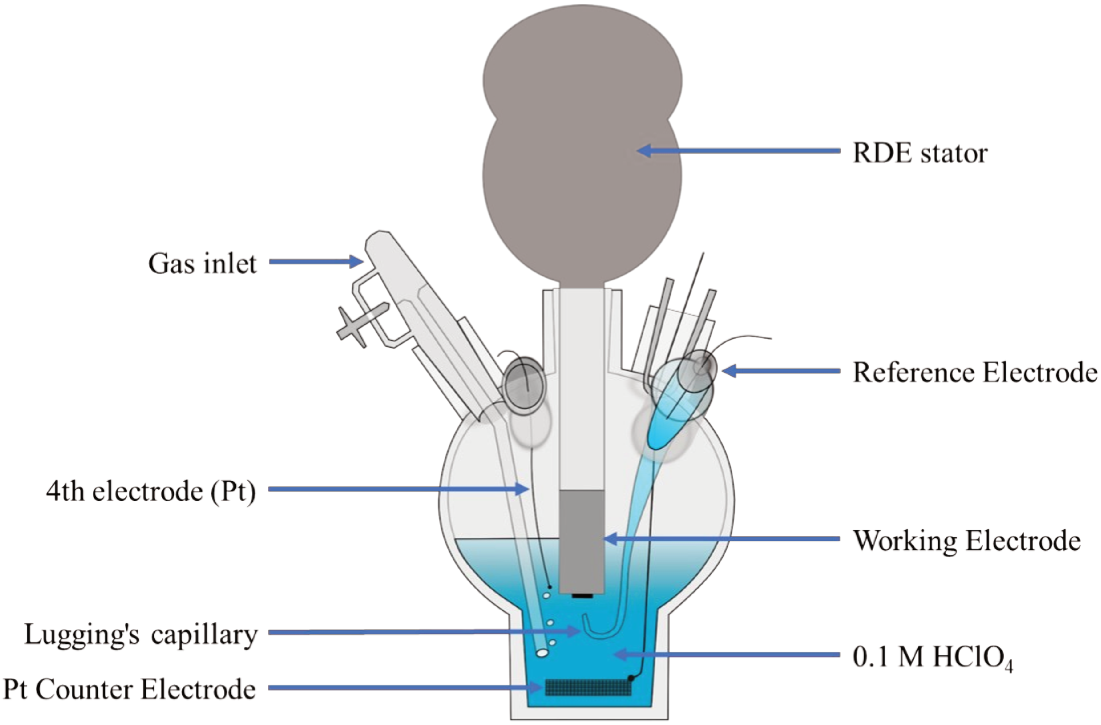

Figure II - 3 - 1: Schematic representation of a four-electrode cell for RDE experiments

The working electrode is made of a PTFE cylinder with a glassy carbon cylinder of $5\ \mathrm{mm}$ ($0.196\ \mathrm{cm}^2$) in the middle. It is on the glassy carbon that the electrocatalytic ink is deposited.

The Luggin's capillary is where the reference electrode is placed into (on the upper part) and the other side of the Luggin is placed as close as possible from the working electrode. There is no current line in the Luggin (the potentiostat is of very high internal resistance >> $10^9\ \Omega$), which makes the potential similar from one side to the other. It also prevents as much as possible the contamination of the working electrolyte with the reference, which is not really the case for RHE reference but rather to avoid oxygen, which would shift its potential.

The electrolyte is a $0.1\ \mathrm{M}$ perchloric acid (70% $HClO_4$, Suprapur Supelco, Merck) prepared in the beginning of each week and lasting a week, at most.

The counter electrode is a platinum mesh with a large surface to avoid any current limitation that would impact the working electrode experiment.

Prior to any experiment, the cell and every glass and PTFE parts are soaked into a mixture of hydrogen peroxide (30% H_2O_2, Chem-Labs) and sulfuric acid (96% H_2SO_4, Roth) to remove any organic pollution. As sulphate anions SO_4^{2-} adsorb specifically on platinum and lower its activity, the cell is thoroughly rinsed at least twice with ultrapure water and boiled for at least 1 hour before a final rinsing to ensure a proper cleanliness.

The glassy carbon electrodes are mirror-polished using diamond paste down to $1\ \mu\mathrm{m}$ and rinsed / ultrasonicated in three successive baths (with intermediate water rinsing) of acetone (Fisher Chemical), a mix water/ethanol (96% EtOH, VWR Chemical) and pure water. To facilitate the deposit of the thin catalyst layer, the tip is placed in an oven at $90°\mathrm{C}$ while the ink is placed in an ultrasonic bath for 5 minutes. The deposition process consists of screwing the tip on a dedicated RDE rotor (facing the roof), to apply a slow rotation rate and to drop-cast an aliquot of $10\ \mu\mathrm{L}$ on the rotating tip. A hot and convective flow of air is generated using a hairdryer to accelerate the drying process of the ink solvents. A whole and uniform coverage of the glassy carbon by the catalyst layer is expected to ensure proper experiment.

c) Gas Diffusion Electrode setup and electrochemical methods

I would like to thank Marine Tregaro (a former LEPMI PhD student) for having introduced and battled with me on the GDE to get the first results on this GDE [131] *at LEPMI; a grateful thank to Prof. Matthias Arenz (Univ. Bern, Switzerland) for having provided the original version of the cell with its schematics, that was in-house modified for the present studies. A warm thank also to Pascal Martin (CEA Grenoble) for his knowledge and his expertise for the development of the GDE schematics as it is used in this work.*

The interest toward the GDE lies on the main shortcoming, whereas intrinsic, of the RDE: the severe mass-transport limitation related to oxygen diffusion in liquid electrolyte. As a matter of potential, $0.85\ \mathrm{V}\ vs.\ \mathrm{RHE}$ is as far as one can try to determine intrinsic activity in RDE before being limited by the diffusion of oxygen (in this case). The low solubility of oxygen fixes the maximum current one can reach to *ca.* $5.5\ \mathrm{mA\ cm_{geo}^{-2}}$ (at $1{,}600\ \mathrm{rpm}$), leading to a complete impossibility to comprehend how the catalyst may work under higher current densities (and hence at lower potential); the extrapolation towards single cell tests often fails roughly when one tries to bridge the great kinetics performance of state-of-the-art electrocatalysts obtained in RDE to their (often disappointing) performance in small PEMFC unit cells [51,132].

The main difference of the GDE compared to RDE lies on the presence of a liquid-gas interface at the level of the active layer of the studied catalyst. On the one hand, the liquid-containing upper part of the cell (made of PTFE) enables a precise control of the potential – similar to what is done in RDE – and the counter electrode is placed in a frit to prevent bubbles of oxygen from nucleating and obstructing the connexion with the working electrode. On the other hand, the gas flow under the electrode directly feeds the active layer, without needing to transport the reactant gas (here O_2) in dissolved state into the electrolyte; this enables both much higher gas concentration and diffusion coefficient, resulting in a - at least – three orders of magnitude higher mass-transport kinetics than in RDE. The GDE setup is made of several elements, as can be seen on Figure II - 3 - 2 and described thereafter:

<u>The reference electrode</u> is a commercial RHE (Gaskatel) which is held and placed as close as possible from the working electrode.

<u>The counter electrode</u> is a large area platinum mesh to enable high oxygen evolution reaction (OER) current densities to provide the electrons to the electrical circuit if large ORR currents are reached at the working electrode.

<u>The working electrode</u> is constituted of a catalyst layer sprayed onto a GDL.

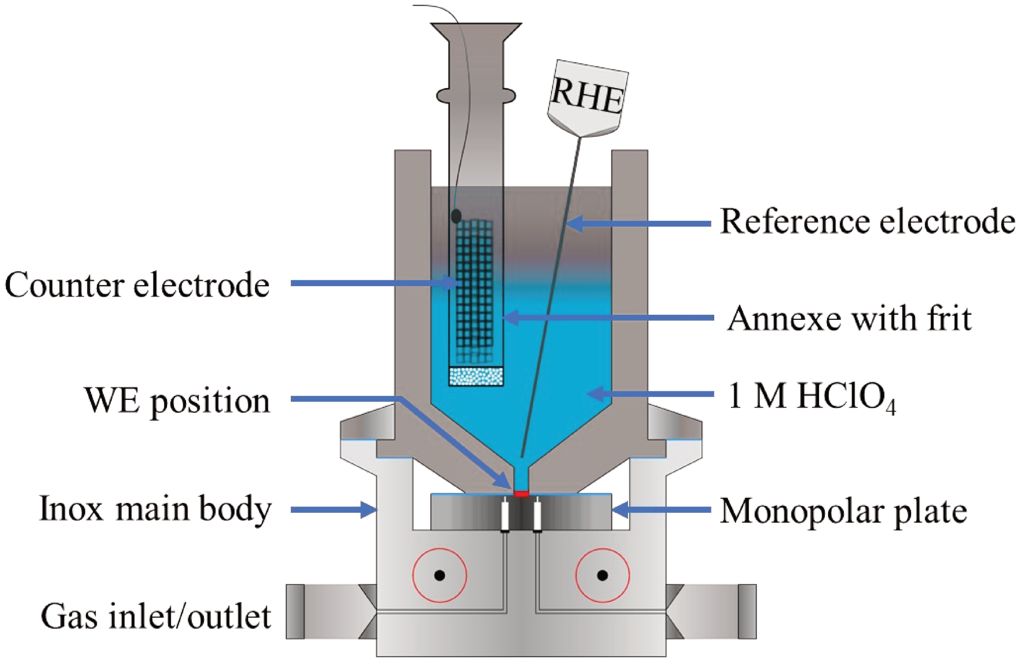

Figure II - 3 - 2: Schematic representation of the Gas Diffusion Electrode cell. Adapted from [133]

The annex frit aims to avoid the nucleation of oxygen bubbles on the surface of the upper PTFE beaker. This would lead to a progressive loss of contact between the working and both the reference and the counter electrode. It also avoids contamination by platinum ions dissolved from the counter electrode.

The electrolyte is a 1 M perchloric acid (70% $HClO_4$, Rotipuran Ultra Roth) aqueous solution, prepared in the beginning of each week and lasting a week. The higher concentration used compared to the RDE is to balance the smaller surface ($0.071\ \mathrm{cm}^2$, *ca.* three times lower than in RDE) to have a reasonable high frequency resistance and therefore reasonable ohmic losses as higher current densities are reached.

The monopolar plate is made of graphite and exhibits three main features: i) a flow field with 10 parallel channels (and 9 lands, 250 µm width each) pattern, ii) an O-ring sealing to ensure the tightness of the gases and iii) PEEK (Polyetheretherketone) rods to guide the positioning of the plate.

The lower body in stainless steel is the main part of the system; it is manufactured with linear heating-fluid channels and gas lines in its core. It is not in contact with the electrolyte.

The gas inlet/outlet as well as the water connection to the inox body of the cell are ensured with push-in inox connectors (LF3000, Parker Legris) to plug the gas and water lines. These are screwed on the inox cell body and enable an easy preparation of the experimental setup.

In a will to increase the reproducibility of the experimental results, I have designed a bench with mass flow controllers (SLA5800 Series, Brooks) manufactured by the company Serv'Instrumentation to set precisely for every experimental technique similar flow rates for every gas used. That way, a similar amount of water is brought to/removed from the electrodes and this eliminates a possible source of error in the understanding afterwards.

d) Electrochemical techniques

For each experiment, performed in RDE and in GDE, the same protocol has been applied and a minimum of 3 electrodes have been tested for each catalyst and each condition studied in the following part of this work. The differences are highlighted in the corresponding subsections. In a more general way, the experimental cells are thermally stabilized at $25°\mathrm{C}$ (RDE and GDE) using a thermostatic bath (F12, Julabo). The realization and acquisition of the electrochemical techniques are done using a Bio-Logic SP-150 or SP-300 potentiostat equipped with a frequency analyser. Before any measurements, the high frequency resistance is determined at the open circuit potential at $100\ \mathrm{kHz}$ with an amplitude of $10\ \mathrm{mV}$. This resistance is dynamically corrected at 85% and post-corrected of the 15% remaining during the data treatment to have (fully) ohmic-drop corrected experiments; with both setups, the uncompensated resistance is *ca.* $3-5\ \Omega$.

Table 1 summarizes the purge time and gases flow rates for the different techniques used for the RDE and the GDE. During the RDE purging periods (a few bubbles per second), an additional rotation of the electrode at $400\ \mathrm{rpm}$ is applied for a better homogeneity in the solution.

Table 1: Time and flow rate of each gas for the RDE (left – in blue) and GDE (right – in red) techniques (liquid electrolyte)

	Break-in	CV $20\ \mathrm{mV\ s^{-1}}$	CO stripping	Pseudo ORR	ORR cycles
Waiting Time (min)	**20 / 10**	**0 / 0**	**5-35 / 3-15**	**0**	**20 / 10**
Gases Flow rate (mL min^{-1})	**50**	**50**	**80**		**60**

i. Break-in and CV

In order to free the catalyst of its oxidised outer layer and of possible organic compounds, 50 potential cycles between 0.05 and $1.23\ \mathrm{V}\ vs.\mathrm{RHE}$ are applied at a scan rate of $500\ \mathrm{mV\ s^{-1}}$ to reveal a clean and stable surface of the electrocatalyst. This number of cycles is enough to reach steady state curve features with very slight evolutions from one cycle to another, and low enough to avoid significant aging of the catalysts. A flow of Ar is required to avoid oxygen reduction current and focus on surface (non-faradaic) processes. A subsequent $3-$ cycles voltammetry sequence at $20\ \mathrm{mV\ s^{-1}}$ is then applied to reduce the intensity of the capacitive current, j_{dl}, of the measured current in order to compare the different catalysts' features.

$$j_{\mathrm{dl}} = C_{\mathrm{dl}} * \frac{\mathrm{d}E}{\mathrm{d}t} \qquad \text{(Eq. II.3.7)}$$

With C_{dl} the double layer capacitance (in F cm^{-2}) and $\frac{\mathrm{d}E}{\mathrm{d}t} = \nu_{\mathrm{b}}$ the scan rate of the CV (in $\mathrm{V\ s^{-1}}$).

ii. CO stripping technique

The CO stripping technique is used as a powerful tool to measure the ECSA of the platinum-based catalysts, both in RDE and GDE. CO is injected in the cells while the potential is held at $0.1\ \mathrm{V}\ vs.\mathrm{RHE}$ for a waiting time adapted to cover all the platinum surface within the active layer ($5 - 3\ \mathrm{min}$ for RDE and GDE, respectively). After another purge to remove all the excess of CO (according to the period noted in Table 1), three successive CVs are performed to: i) oxidize the monolayer of CO adsorbed on the surface and ii) obtain a baseline to correct for all the classical features (hydrogen adsorption/desorption, platinum oxides formation/reduction), letting just the faradaic current corresponding to the electrooxidation of CO. The resulting charge per surface unit of platinum is taken equal to $420\ \mu\mathrm{C}\ \mathrm{cm}_{\mathrm{Pt}}^{-2}$ [134] for the determination of the ECSA. This value might not apply for Pt_3Co and Pt_3Ni alloys studied, but is nevertheless assumed to remain an acceptable value, as demonstrated by Dubau *et al.* [40]. The cycle after the electrooxidation of CO is also used for the determination of the $\mathrm{H}_{\mathrm{upd}}$ ECSA for RDE and GDE as it exhibits a similar electrode state. A charge of $210\ \mu\mathrm{C}\ \mathrm{cm}_{\mathrm{Pt}}^{-2}$ is used in this case.

iii. Oxygen reduction reaction cycles and pseudo-ORR

For all the catalysts studied, the ORR activity is measured by doing CVs with a slow scan rate ($\nu_{\mathrm{b}} = 5\ \mathrm{mV\ s}^{-1}$). The potential limits for this technique are set at 0.2 and $1.05\ \mathrm{V}\ vs.\mathrm{RHE}$. The potential is held at $0.2\ \mathrm{V}\ vs.\mathrm{RHE}$ for $1\ \mathrm{min}$ before the scan starts to reach a study state. The rotation rate of the RDE is fixed at 400, 400, 900, $1{,}600$, $2{,}500$ and $400\ \mathrm{rpm}$ successively under an oxygen-saturated electrolyte and the scan at $1{,}600\ \mathrm{rpm}$ is used for the determination of the intrinsic activity measurement. As the resulting current density is low in RDE, a similar CV (same scan and rotation rates) is performed with an Ar-purged electrolyte, right before to switch to O_2. This way, the correction of the background (mostly capacitive) current can be achieved. In the case of the GDE setup, the electrolyte (on top of the electrode) does not need to be saturated in O_2, rather O_2 is fed to the electrode through the monopolar plate. The same potential window and scan rate are kept alike the RDE measurements. However, 7 cycles are performed to observe the evolution of the current density; for the 25°C study, the current reaches a near-stable state on the 7^{th} cycle. This will be further detailed in the next chapters.

For both setups, the determination of the ORR activity is made on the increasing potential scan (positive sweep).

iv. Galvano Electrochemical Impedance Spectroscopy

In GDE, as higher current densities are reached and the mass-transport being ideally non-limiting, but in practice it is not as straightforward as it is in RDE (being analytically solved and well understood), a succession of impedance spectra is performed at different current densities from $100\ \mathrm{kHz}$ to $1\ \mathrm{Hz}$ with 8 points per decade with a $100\ \mu\mathrm{A}$ amplitude for the $I\ =\ 0\ \mathrm{A}$ spectrum and an amplitude equals to 10% of the steady state point for the other spectra. The maximal current of the impedance sequence is defined regarding the maximum reached current during the ORR cycles.

The impedance spectra are fit using a model from Gaumont [126], which is presented thereafter and is abiding by the following hypotheses:

The oxygen transport is supposed ideal with no concentration gradient (both in the active layer and in the GDL), the electronic resistivity of carbon phase is neglected and the electrode is characterized by its protonic resistivity and double layer capacitance. It is valid in stationary regime for low current densities (R_{p}<< R_{ct}).

$$Z_{\mathrm{ORR}}(f) = R_{\mathrm{HF}} + \frac{R_{\mathrm{p}}}{\sqrt{2i\pi f R_{\mathrm{p}} C_{\mathrm{dl}} + \frac{R_{\mathrm{p}}}{R_{\mathrm{ct}}}}} * \frac{1}{\tanh\,(\sqrt{2i\pi f R_{\mathrm{p}} C_{\mathrm{dl}} + \frac{R_{\mathrm{p}}}{R_{\mathrm{ct}}}}} \qquad \text{(Eq. II.3.8)}$$

Examples of parameter values can be found in Table 2 and the corresponding fits on Figure II - 3 - 3.

Table 2: Parameters extracted from GEIS fit using the transmission line model detailed by Gaumont[126]

	1 mA	10 mA	25 mA	50 mA
R_{HF} ($\Omega\ \mathrm{cm}_{\mathrm{geo}}^{-2}$)	1.21	1.23	1.23	1.22
C_{dl} ($\mathrm{mF\ cm}_{\mathrm{geo}}^{-2}$)	1.2	1.0	1.0	0.9
R_{p} ($\Omega\ \mathrm{cm}_{\mathrm{geo}}^{-2}$)	0.13	0.035	0.031	0.029
R_{ct} ($\Omega\ \mathrm{cm}_{\mathrm{geo}}^{-2}$)	3.68	0.78	0.50	0.51

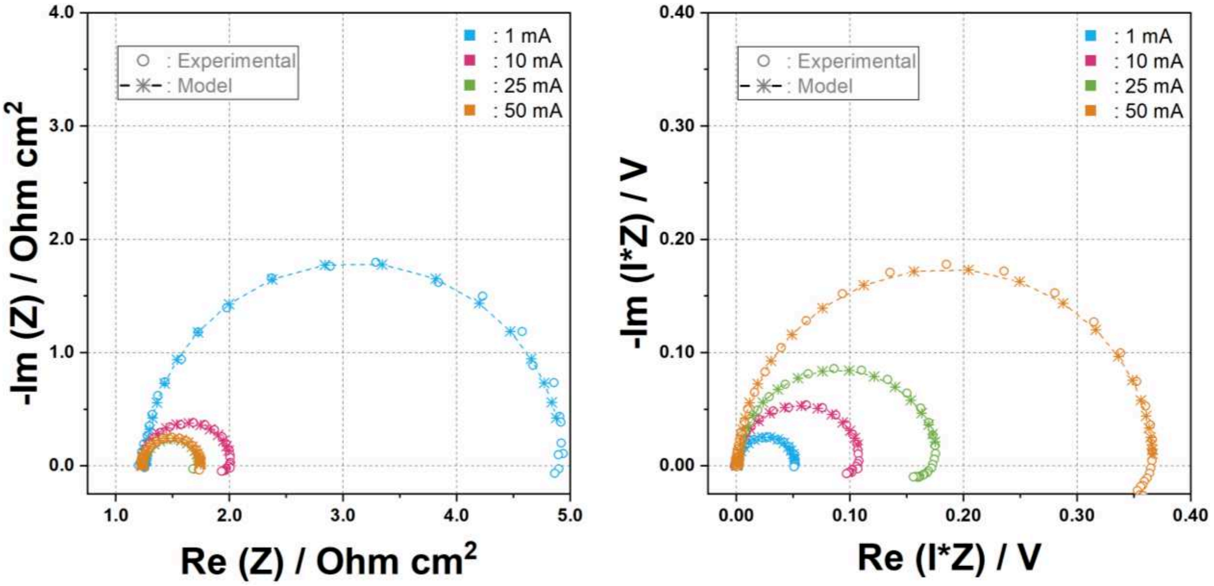

Figure II - 3 - 3: Impedance spectra and fit obtained in GDE half-cell under O_2 flow of $60\ ml\ min^{-1}$at various current in Nyquist plot (left) and Tafel plot (right, with subtraction of R_{HF})

4. *Ex situ* physical and chemical characterizations

To unveil if the catalyst has been oxidized, dissolved, or agglomerated, the use of additional physical and chemical characterizations before and after tests are interesting and very valuable. In this section, electronic microscopies, photonic diffraction and diffusion as well as chemical elemental analysis will be introduced.

For the aging study of membrane-electrodes assemblies, a few preparation steps must be done:

- pulling the GDLs off;
- cutting localised samples (scanning electron microscopy, SEM, Raman spectroscopy);
- anode catalyst layer scrubbing and extraction (transmission electron microscopy, TEM);
- cutting localised samples (X-ray diffraction, XRD, Raman spectroscopy);
- cathode catalyst layer scrubbing and extraction (TEM).

a) Microscopy techniques

As view is the sense one relies the more on, it is particularly appreciable to be able to observe the materials studied during their lifetime. As they are prepared as nanoparticles, it reaches the limit of the optical microscopy observation (being *ca.* $0.2\ \mu\text{m}$) and one must switch to electronic microscopy; electron having a lower wavelength and as such a higher resolution, up to the nanometre, can be reached. Transmission electron microscopy and scanning electron microscopy, schematics presented on Figure II - 4 - 1, have been used in this thesis work because each technique brings its own lot of interesting information [135].

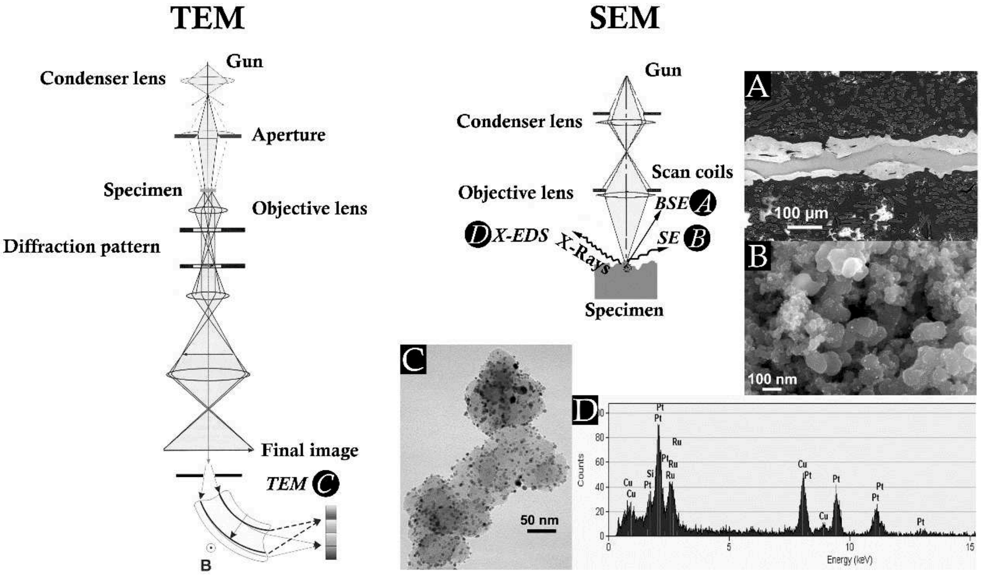

Figure II - 4 - 1: Scheme of TEM and SEM with examples of MEA's images: ***A)*** *SEM BSE mode,* ***B)*** *FEG-SEM SE mode,* ***C)*** *TEM and* ***F)*** *XEDS analysis. Reprinted from Chatenet et al. [135].*

i. Transmission Electron Microscopy (TEM)

Transmission electron microscopy is a technique relying on the particle-wave duality of electrons. Accelerating electrons in a $200\ \mathrm{kV}$ electrical field produces a resulting wavelength of the particle beam of *ca.* $2.5\ \mathrm{pm}$ [136], enabling a theoretical point-to-point observation at the sub-nanometre scale. The electrons are produced with a LaB_6 single crystal source and the beam is further focused using electrostatic and electromagnetic lenses. The focused beam then hit the sample, which has to be thin (*ca.* $100\ \mathrm{nm}$) to enable the transmission of electrons through the materials, creating a surface object of a three-dimensional one. This interaction produces many particles, as depicted in Figure II - 4 - 2; among all of them, mainly transmitted electrons and X-rays are analysed in this work to give information about the size, the shape, the dispersion, and the elemental atomic ratio of the particles.

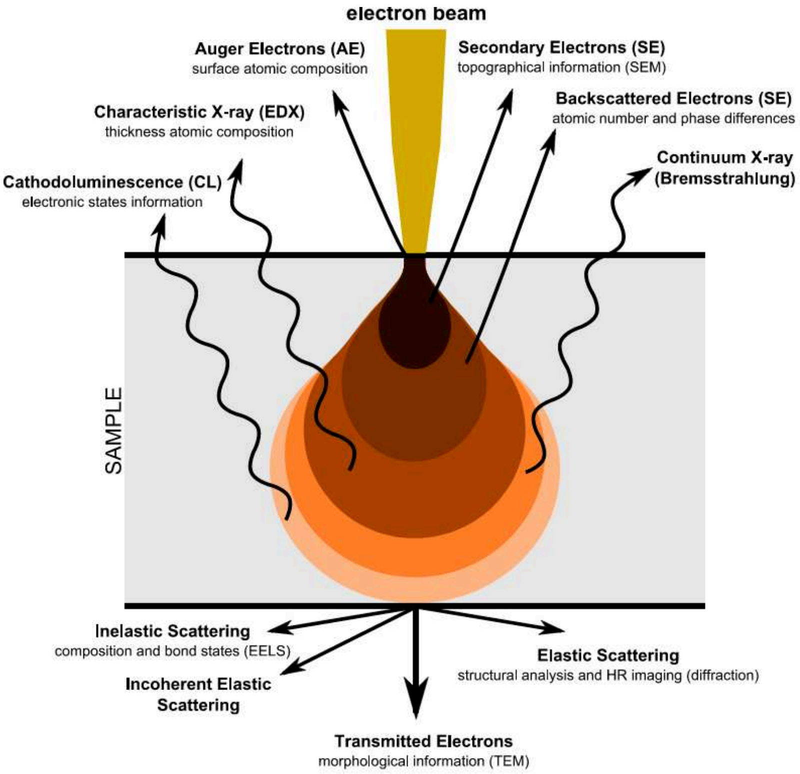

Figure II - 4 - 2: Emissions resulting from the interaction electron beam - sample. Reprinted from [137]

The samples for TEM observations are prepared with specially designed TEM copper grids ($200\ \mathrm{mesh}$, TED PELLA INC.). The first step is to dip the grid several times in pure ethanol, then let it dry for some minutes before dipping it again in pure water. These steps are made to remove the thin protective organic membrane on the grid. After that, the grid is dipped a few times directly in the catalyst powders (for the initial and as received catalytic powder) or droplets of suspensions of isopropanol and aged electrodes catalyst layer’s powders are deposited on it. The suspensions are beforehand agitated and sonicated to break all the possible agglomerate resulting from the scrapping step. The TEM grids are then being stored in a dedicated box, waiting for the observations.

For each grid, a total of 4 areas are investigated at $50\mathrm{k}$ magnification and 4 images are taken for each one of the 4 areas at magnification of $200\mathrm{k}$. To be statistically relevant, at least 200 nanoparticles' Ferret diameters (*i.e.* $\frac{(d_{\max}+d_{\min})}{2}$) are measured using the freeware ImageJ; the (isolated) particle size distribution (PSD) histograms are then plot. Three different equivalent diameters can be calculated using the PSD [138]:

$$\bar{d}_\mathrm{n} = \frac{\sum_{i=1}^{N} x_\mathrm{i} d_\mathrm{i}}{\sum_{i=1}^{N} x_\mathrm{i}} \quad \text{(Eq. II.4.1)}$$

$$\bar{d}_\mathrm{s} = \frac{\sum_{i=1}^{N} x_\mathrm{i} d_\mathrm{i}^3}{\sum_{i=1}^{N} x_\mathrm{i} d_\mathrm{i}^2} \quad \text{(Eq. II.4.2)}$$

$$\bar{d}_\mathrm{v} = \frac{\sum_{i=1}^{N} x_\mathrm{i} d_\mathrm{i}^4}{\sum_{i=1}^{N} x_\mathrm{i} d_\mathrm{i}^3} \quad \text{(Eq. II.4.3)}$$

$\bar{d}_\mathrm{n}$, $\bar{d}_\mathrm{s}$, $\bar{d}_\mathrm{v}$ being respectively the number, surface and volume averaged diameters and x_i the number of particles having a diameter d_i. $\bar{d}_\mathrm{s}$ has the closest meaning to ECSA determined experimentally, as it is influenced by the outer surface of the particles and $\bar{d}_\mathrm{v}$ is significantly alike the diameter that can be found for crystallites using XRD (as the particles/crystals are smaller than $100\ \mathrm{nm}$, further detailed in the Section II-4-b).

X-Ray energy dispersive spectrometry (X-EDS) is also performed to identify locally the elemental composition of the Pt_3Co catalyst after degradation to check if an evolution of the Pt:Co ratio happened while aging.

The TEM observations have been made by Marian Chatenet and the author, the PSD analysis has been fully realised by the author.

ii. Scanning Electron Microscopy (SEM)

In scanning electron microscopy, the electron beam is accelerated at much lower voltage ($10\ \mathrm{kV}$) than in TEM and the observation is made (in this work) mostly on secondary and back scattered electrons; the result leads to topographical and chemical (Z number) information on the sample studied, respectively.

The preparation of the sample differs in two ways: the in-plane or cross-section observation. The in-plane study (of a CCM catalyst layer's surface for instance) needs very small preparation: for conductive sample (like GDL or catalyst layers), the studied surface is put on a carbon tape and a small piece of carbon tape is also put on the periphery of the sample (the membrane not being electron conductive) to enable the evacuation of the electrons and prevent a shift of the image over time during the observation because of a charging surface. The cross-section sample preparation requires the preparation of an epoxy resin to immobilize the observed material. The resin is dried for a full day before being polished (multi-steps) using alumina suspension down to $1\ \mu\mathrm{m}$. The resin block is then put into an oven for half a day at *ca.* $50 - 60^{\circ}\mathrm{C}$ to remove all the water from the small interspace between the sample and the resin (created due to the contraction of the resin while drying during the initial step). When the sample is dried, a silver paint is applied from the top to the bottom of the resin block. After another drying, the final block is put into a vacuum sputter where a carbon rope is lightened to spread small carbon particles on the sample and make its outer surface electron conductive. All the drying steps are respected to avoid any water evaporation when the samples will be in the SEM observation chamber. The SEM used in this work is a Zeiss Ultra 55 FEG-SEM operated at $10\ \mathrm{kV}$ independently of the observation, respectively back scattered electrons, secondary electrons or X-EDS.

Thicknesses of catalysts layers or membranes can be measured thanks to cross-section observations. Images are taken using the Back Scattered Electrons (BSE) detector for the determination of the cathode catalyst layer thickness, as this mode of observation gives a high contrast between high and low Z atoms (such as Pt and C or F, for example). By doing so, there is a high chemical contrast between the catalytic layers (full of Pt) and the membrane (mostly C and F). The images are taken at rather low magnification, to have a long view of the cross-section, but not too low, to limit errors on the measurement of the CL thickness. The measurement of a “mean” thickness is done after integration of all the pixel of the cathode layer for a given width of image, as depicted on Figure II - 4 - 3.

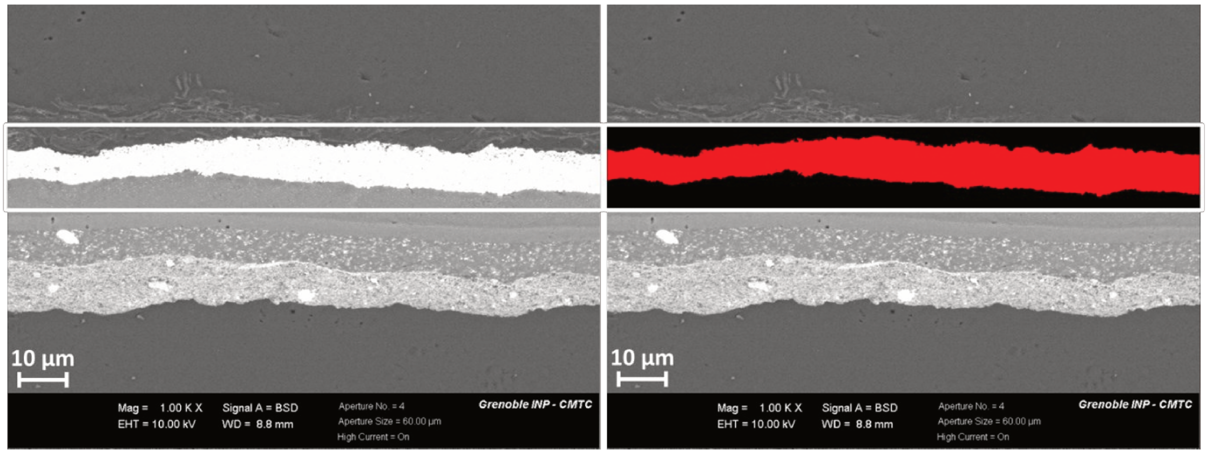

Figure II - 4 - 3: SEM images of a PEMFC MEA's cross-section (left) and selection of the CL's pixels for the estimation of the "mean" thickness (right)

After all these pixels have been integrated, this “pixel area” value is divided by the width of the SEM image. The image scale bar finally gives a relation between the number of pixels measured and a unit length on the image. This leads to a mean thickness, that a perfectly homogeneous catalyst layer would have with no heterogeneities. This method is applied for all three reference MEAs to determine their initial mean thickness.

The samples and SEM observations are performed by the author. A warm thanks to Frederic Charlot and Joëlle Calabro for their trainings on SEM utilisation and samples preparation.

iii. X-ray energy dispersive spectroscopy (X-EDS)

X-rays are emitted during electronic microscopy as a result of the interaction between the electron beam and the sample. These photons have particular energy, depending on the materials they originate from and on the energy of the incident beam. In the case of the heavier atomic number materials studied in this thesis, Platinum Lα and Mα (9.44 and $2.05\ \mathrm{keV}$ respectively) and Cobalt Kα and Lα (6.93 and $0.78\ \mathrm{keV}$ respectively) could enable the discrimination of the desired elements. As the incident beam has an energy of $10\ \mathrm{keV}$, they can theoretically be detected, noting that the Pt Lα has a very low intensity, as well as the Co Kα and that the Co Lα, on the other hand, is too close to the fluorine Kα ($0.68\ \mathrm{keV}$). The acquisition time depends on the area studied; it lasts a few minutes (spectra on points) and can go to a few tenths of minute for elemental mappings on poorly emissive surface.

b) X-ray diffraction (XRD)

X-ray diffraction is a non-destructive and (usually) *ex situ* method widely used in material science to determine the crystallinity, the lattice parameters in case it is indeed crystalline, the existence of alloy with the elemental ratio and more generally the composition of a material. A monochromatic source of X-rays (Cu Kα1, $\lambda = 1.5406$ Å) is oriented in various 2θ angles around the sample and the photons interfere coherently when specific conditions are met, naming the Bragg's conditions:

$$\lambda = 2d_{\mathrm{hkl}}\sin\theta, \tag{Eq. II.4.4}$$

with λ the wavelength of the photons, d_{hkl} the interplanar distance of (hkl) Miller indices planes and θ the angle between the incident beam and the diffracting planes. The X-Rays diffraction peaks are very thin on bulk materials but start to broaden when the particle size is under *ca.* $100\ \mathrm{nm}$ [139], making the determination of the crystallites size (normal to the crystallographic planes) possible using the Scherrer equation [140]:

$$\bar{d}_{\mathrm{XRD}} = \frac{0.9*\lambda}{\mathrm{FWHM}*\cos\theta} \tag{Eq. II.4.5}$$

with, FWHM the full width at half of the maximum intensity of the broaden peak (in radians). The equivalent diameter measured via XRD is an average of the crystallites size of the various planes for which a diffraction peak has been obtained. The values of these parameters are obtained by fitting the (220) Platinum peak on the different diffractograms.

The fit is made using a PsdVoigt1 model which is a linear combination of Gaussian and Lorentzian function, the function equation being:

$$y = y_0 + A\left[m_{\mathrm{u}}\frac{2}{\pi}\frac{w}{4(x-x_{\mathrm{c}})^2+w^2} + (1-m_{\mathrm{u}})\frac{\sqrt{4ln2}}{\sqrt{\pi}w}e^{-\frac{4ln2}{w^2}(x-x_{\mathrm{c}})^2}\right] \qquad \text{(Eq. II.4.6)}$$

With y_0 the baseline of the XRD diagram, x_{c} the abscissa centre of the peak, A the area under the curve, w the full width at half maximum (as previously introduced, also found as FWMH) and m_{u} the shape factor (0 means the fit is a perfect gaussian and 1 the fit is a perfect Lorentzian) of the fit.

Example of fit can be seen on Figure II - 4 - 4 below, with the resulting parameter extracted: $y_0 = 9450$ counts, $x_{\mathrm{c}} = 67.6$ °, $A = 21730$ u. a., $w = 3.64$ ° and $m_{\mathrm{u}} = 0.48$ with a regression coefficient $R^2 = 0.995$.

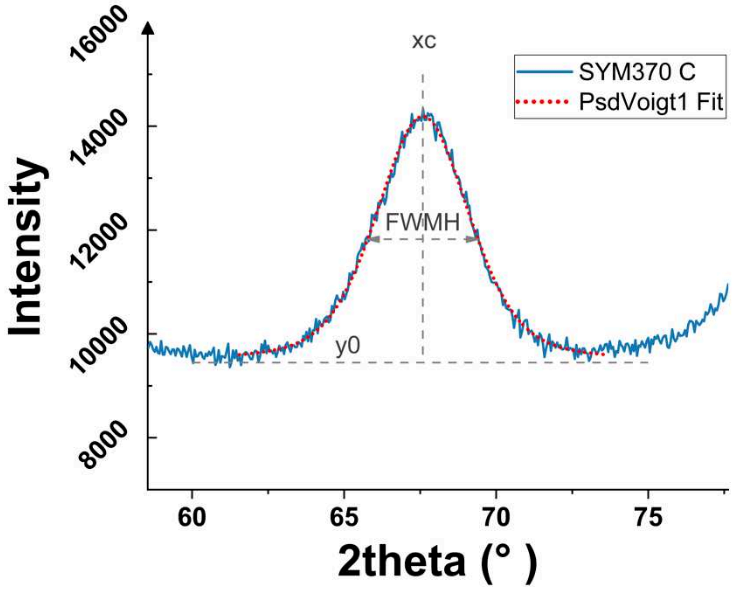

Figure II - 4 - 4: Example of fit using the PsdVoigt1 function on the (220) peak of Pt

The linear combination of these two functions is necessary to balance the possible change of behaviour: with a small mean particle size dispersion, the peak is wider and is better fit using a Lorentzian, while with larger mean particle size dispersion, it is better fit with a Gaussian function.

c) Raman Spectroscopy

In this work, Raman spectroscopy has been used to probe the influence of the degradation protocols on the Pt nanoparticles' carbon support (Vulcan XC-72), widely used in the literature [141] for both platinum based and non-PGM catalysts, being at the RDE [59] or MEA [142–144] level. The spectra are recorded using a Renishaw InVia apparatus used in a backscattering configuration. The materials are excited with a monochromatic light of 532 nm wavelength. To prevent movement of the MEAs under the light, the initial beam is spread on a line for which the resulting power density is much lower than it was for a focalised beam. The spectra are then acquired on a $50\ \mu\mathrm{m}^2$ area and "average spectra" can be obtained in a single measurement. An example of Raman spectrum is proposed on Figure II - 4 - 5 for the cathodic layer outer surface of a pristine MEA.

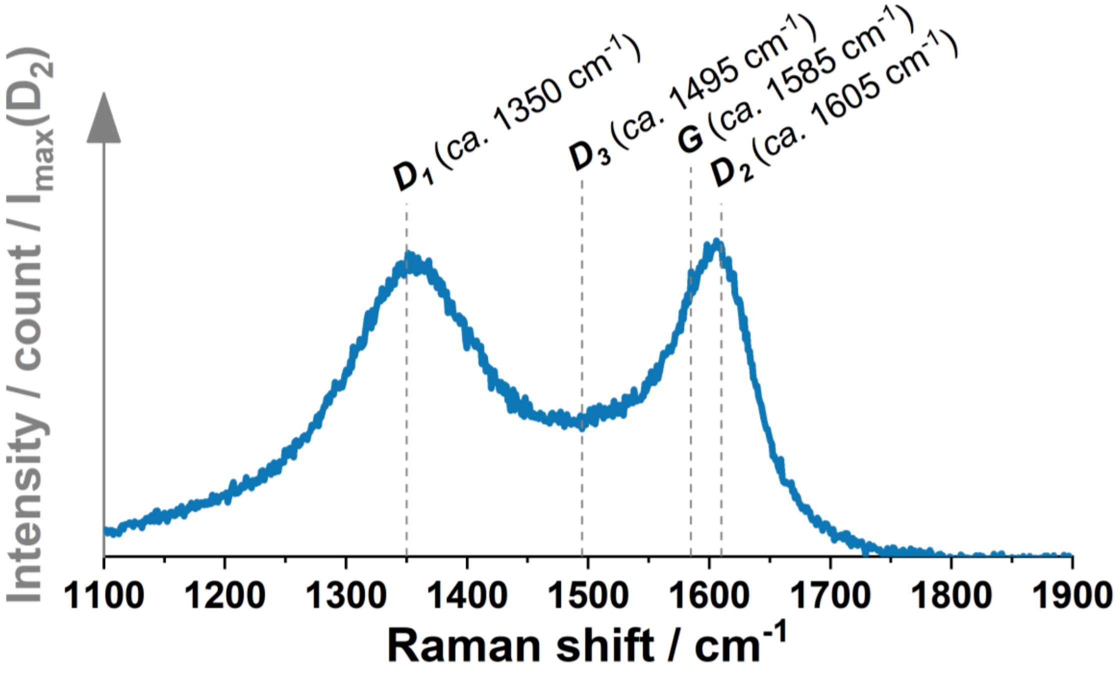

Figure II - 4 - 5: Raman spectrum of a pristine MEA cathode catalyst layer outer surface in the range 1100 - 1900 cm^{-1} using a monochromatic 532 nm light source

On this typical spectrum, several areas of interest can be observed at various Raman shift (difference of frequency from the incident radiation) : the $\mathrm{D_1}$ band (*ca.* $1350\ \mathrm{cm^{-1}}$) and $\mathrm{D_2}$ band (*ca.* $1605\ \mathrm{cm^{-1}}$) correspond to the disordered graphene lattice, the G band (*ca.* $1350\ \mathrm{cm^{-1}}$) is ascribed to the ideal graphite lattice and the $\mathrm{D_3}$ band (*ca.* $1350\ \mathrm{cm^{-1}}$) stands for the amorphous carbon.

All the Raman spectra in this work have been acquired by Michel Mermoux, and analysed (by the author) after normalization by the maximum intensity in the $\mathrm{D_2}$ band region.

d) ICP-MS elemental analysis

Inductively-coupled plasma mass spectrometry (ICP-MS) is a chemical analysis method that enables the quantification of elements by producing a plasma made of rare gas (in this case, Ar) and of a very diluted solution and counting the number of ions received at a specific position on the spectrometer, the trajectory of the ions being controlled by the modification of a magnetic field, so to separate ions with different m/z ratios (m = mass, z = charge). A calibration curve (counts *vs.* concentration) is first prepared using the same supporting solution and by diluting standards of known concentrations. In the case of the ICP-MS, only a few traces (ppb) of element are needed to be detected.

Prior to the ICP-MS quantification, the samples (powders or GDE) are first placed in PTFE tubes (CEM) filled with $10\ \mathrm{mL}$ of aqua regia prepared the day before and let at open air for

$15\ \mathrm{minutes}$ (to limit over pressure). The tubes are then placed in a microwave oven (Mars, CEM) and the temperature is increased to $200°\mathrm{C}$ with a $5°\mathrm{C}\ \mathrm{min}^{-1}$ ramp and is held for $30\ \mathrm{minutes}$. After they have cooled down to ambient temperature, the lixiviated solution is diluted in $40\ \mathrm{mL}$ of ultra-pure water. The vials are weighed before and after the addition of the diluted lixiviated solution in order to have the mass of liquid. The ICP-MS (NexION 2000, Perkin Elmer) gives a concentration (in ppb) of element, knowing the mass of solution and the sample surface leads to the loading of the electrode in g_{Pt} per unit geometric surface in cm^2. All the ICP-MS measurements are performed by Vincent Martin. The mineralization step and the analysis of the data are done by the author.

Chapter III

New way to assess catalyst performance ? A GDE study

This chapter is mainly inspired from the article:

Raphaël Riasse, Clémence Lafforgue, Florent Vandenberghe, Fabrice Micoud, Arnaud Morin, Matthias Arenz, Julien Durst, Marian Chatenet

Benchmarking proton exchange membrane fuel cell cathode catalyst at high current density: A comparison between the rotating disk electrode, the gas diffusion electrode and differential cell,

Journal of Power Sources, Volume 556, 2023, 232491, ISSN 0378-7753,

https://doi.org/10.1016/j.jpowsour.2022.232491.

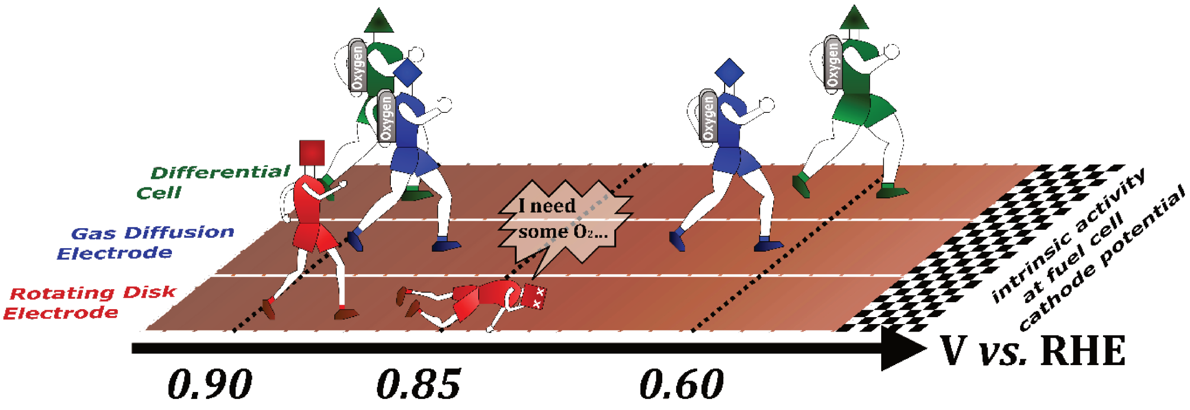

Chapter III. New way to assess catalyst performance ? A GDE study

1. Why is the gas diffusion electrode important and interesting ?

a) Aim of the study

Many catalysts are currently (and have been) developed to improve the stability and intrinsic activity in proton exchange membrane fuel cell (PEMFC) operation, as it is expected to sustain the roadmap of hydrogen vehicles [52]. These catalysts are very needed for the oxygen reduction reaction (ORR), making them a critical component of the PEMFC [6,145]. Most of these materials are synthesized using platinum group metals (PGM); indeed, non-noble catalysts from 3d transition metals are more unstable in acidic environment, and in particular $\mathrm{Fe\text{-}N\text{-}C}$ materials, the most investigated class of non-noble catalysts [146–150]. ORR catalysts synthesized from PGM that exhibit high enhancement factors when compared to classical $\mathrm{Pt/C}$ catalysts are either structurally ordered or structurally disordered carbon-supported catalysts [50]. Some materials from both families have been shown to display higher intrinsic activity than $\mathrm{Pt/C}$ when they are tested in liquid environment (rotating disk electrode); however, they have not been successfully integrated into PEMFC cathode yet, delivering disappointing performances [51]. This raises the question of the relevance of the characterization protocols used to benchmark these advanced catalysts at the laboratory scale: can they really unveil their true performances in real system? The present chapter will answer this important question.

b) Introduction of the experimental setups

Three characterization setups have been used to compare a similar, or at least only slightly modified, experimental protocol to benchmark the intrinsic activity of three different state-of-the-art ORR catalyst materials: platinum $47\ \%\mathrm{wt}_{\mathrm{Pt}}$ on Vulcan carbon, platinum cobalt $46-6\mathrm{wt}\%_{\mathrm{Pt-Co}}$ on Vulcan carbon and platinum $30\ \%\mathrm{wt}_{\mathrm{Pt}}$ on graphitised high surface area carbon. They will all be referred as $\mathrm{Pt/VC}$, $\mathrm{PtCo/VC}$ and $\mathrm{Pt/GC}$, respectively.

i. Rotating disk electrode (RDE)

The rotating disk electrode is the most-widely used setup for the characterization of a catalyst at the laboratory scale, focusing in this work on the ORR activity. Its main particularity (and strong advantage) is that it is really easy to use and has been used for more than thirty years worldwide. It enables the assessment of the performance of a catalyst in very clean conditions with less than $50\ \mathrm{mg}$ of catalyst powder. This is interesting because for novel synthesis routes, it is often complicated to produce more than a few mg, which is an amount *ca.* an order of magnitude (at least) below what is necessary to produce electrodes for PEMFC single cell studies. Preparing inks for RDE study is rather simple, as only a good suspension of the catalyst powder is expected, the acid liquid electrolyte mainly ensuring the transport of protons in the very thin active layer prepared ($20\ \mu g_{Pt}\ cm_{geo}^{-2}$, resulting in micron or submicron active layer) where no layer effect is expected. This is far away from the intensive work one must perform to prepare active layers appropriate to a single catalyst in PEMFC [151–153]. The RDE methodology has been progressively improved over the years, resulting in a fairly robust and well accepted protocol, that enables to benchmark with a good reproducibility the Pt-based ORR electrocatalysts [154–156], both in terms of initial activity and accelerated stress tests measurements.

However, in the case of the ORR, it involves a gaseous reactant (here O_2). While in a fuel cell O_2 (from air) is transported to the catalyst|ionomer interface through flow channels and gas diffusion media, for the RDE, this reactant must be dissolved in the liquid electrolyte, leading to a small solubility ($ca.\ 1\ \mathrm{mmol\ L^{-1}}$) and reduced diffusion coefficient by three orders of magnitude (to $ca.\ 10^{-6}\ \mathrm{cm^2\ s^{-1}}$) [129]. As a result of these two phenomena, the O_2 transport is roughly four decades slower in RDE than it is in a real PEMFC system. This is the reason why severe diffusion-convection mass-transport limitation is intrinsic to the RDE technique for ORR catalysts studies. The corresponding current obtained in absolute value is on the order of $5.5\ \mathrm{mA\ cm_{geo}^{-2}}$ at a rotation speed of $1{,}600$ revolution per minute (rpm), the conditions in which the DOE suggests to perform kinetics ORR measurements in RDE. As a matter of fact, this current is at least three orders of magnitude smaller than current densities observed in PEMFC single cell cathodes. Of course, as explained in Chapter II, it is possible to correct the mass-transport limitation as well as the ohmic drop of the RDE data, but this correction is imprecise and not viable for potential below $0.85\ \mathrm{V}$ versus the reversible hydrogen electrode reference (RHE). (too close to the limiting plateau). The RDE can therefore only enable a reliable catalytic activity assessment above this potential limit, which is then out of the working range for PEMFC cathodes. Thus, RDE can only provide intrinsic activity measurements for ORR catalysts outside the potential region of interest for PEMFC and at much lower current densities than in a real system. If extrapolations are made to predict the behaviour of an electrocatalyst, it is, of course, a large source of uncertainty, putting into question the relevance of the RDE to benchmark PEMFC cathode catalysts. The group of Gasteiger investigated the advantages and drawbacks of RDE characterizations and compared it to PEMFC characterizations [157]. It concluded stating that RDE indeed suffers limitations that forbid to forecast a catalyst behaviour in PEMFC, as well as PEMFC is also not trivial and straightforward to benchmark catalysts.

ii. Gas Diffusion Electrode (GDE)

As the scientific community has become more aware of the RDE limitations, solutions have been proposed to move on to other experimental devices. In the early 2000s, the group of Grenoble innovated with the gas diffusion electrode, which was applied to benchmark PEMFC cathode catalysts [158,159], relying on former works in the field of phosphoric acid fuel cell catalysis [160,161]. Though an order of magnitude (or so) larger current than in RDE were obtained, the first GDE setup used by Antoine et al. did not prevent mass-transport limitations completely, as the GDE was easily flooded [158,159]. Another group at the imperial college of London, under the direction of Anthony Kucernak has tried to understand the kinetics of fast reaction in three electrodes liquid electrolyte environment, with for example the floating electrode setup [162–165]. This setup has been tried and the results presented [166] but they have not been deepened as it was hard to avoid electrode flooding related to the absence of convective flux at the vicinity of the electrode. In order to resolve this limitation, Arenz *et al.* and Wilkinson *et al.* did recently revisit the GDE system; more specifically, they added gas channels to feed the gas reactant to the active layer with a convective flux, thus resulting in the absence of flooding of the active layer at room temperature experimental conditions [167–169]. This enables to use these three-electrode setups at higher current densities than previously observed in RDE for the ORR, making possible the observation of the intrinsic catalyst activity in the relevant potential range of PEMFC after correction of the ohmic drop and assuming that mass-transports of reactant gas and protons are both negligible. These studies started in the mid-2010s and from then on, papers reporting these GDEs setups have grown numerous, going from catalysts studies to CO reactivity understanding and even used to assess the catalysts stability [170–174]. A few years ago, one multi-lab paper on this topic was aimed to compare the different GDE systems [175]. It delivered the message that each experimental setup comes with its own advantages and drawbacks, so the GDE setups cannot deliver universal information (at least without initial care). The setup used in this chapter is a setup resembling that of Arenz in the university of Bern and aims to set conditions in which the GDE could be considered a reliable tool for intrinsic ORR kinetics measurements. The GDE Pt-loading is kept similar to that in RDE, $20\ \mu\mathrm{g}_{\mathrm{Pt}}\ \mathrm{cm}_{\mathrm{geo}}^{-2}$, so to minimize any layer effect in the thickness of the cathode (and avoid protons and O_2 transport limitation as much as possible).

iii. Differential cell (DC)

To determine to what extent the GDE results obtained can be significantly used to predict the behaviour of the catalysts in real operation in a fuel cell, a third experimental setup is used. It is a small unit PEMFC of $ca.\ 1.8\ \mathrm{cm}^2$ geometric active area, the so-called differential cell from CEA Grenoble (also used in ref. [128,176]), which is operated in conditions for which mass-transport should be as less limiting as possible. The gas is fed with high stoichiometric coefficient to ensure a homogeneous repartition on the surface of the active layer, with a negligible depletion of the gas quantity from the inlet to the outlet of the cell. The flow channels of the cell are parallel, rather similar to the ones of the GDE. The cathode Pt-loading will be kept similar to that in RDE, $20\ \mu\mathrm{g}_{\mathrm{Pt}}\ \mathrm{cm}_{\mathrm{geo}}^{-2}$, minimizing layer effects in the thickness of the cathode.

The electrodes were prepared by Clemence Lafforgue at CEA Grenoble by ultrasonic spray deposition on $250\ \mu\mathrm{m}$ PTFE sheets, following the same protocol as described in the GDE's spray on GDL at CEA-LITEN section of chapter II for the inks' preparation and utilization. The anodic catalytic layers are prepared using a doctor blade automatic film coater (Elcometer) on

PTFE sheets as well, which are immobilized on a plate heated at 60°C; a platinum loading of $0.1\ \mathrm{mg_{Pt}\ cm_{geo}^{-2}}$ is targeted. Before hot-transferring on NR115 Nafion® membranes (130 $\mu\mathrm{m}$ thick), the platinum loading is evaluated using X-ray fluorescence (XRF) measurements: $0.019\ \mathrm{mg_{Pt}\ cm_{geo}^{-2}}$ ($\pm$ 8 % of local aerial loading on the catalyst layer), $0.020\ \mathrm{mg_{Pt}\ cm_{geo}^{-2}}$ ($\pm$ 8 %) and $0.018\ \mathrm{mg_{Pt}\ cm_{geo}^{-2}}$ ($\pm$ 8 %) are measured for the $\mathrm{Pt/VC}$, $\mathrm{PtCo/VC}$ and $\mathrm{Pt/GC}$ active layers, respectively. The hot-transfer step is realised for 10 min at 1 MPa and 160°C. A thick membrane was chosen to mitigate the effect of $\mathrm{H_2}$ cross-over that could severely impact such low-loaded cells for the electrochemically active surface area (ECSA) and ORR measurements at the cathode. The MEA are prepared by pressing the catalyst coated membrane (CCM) prepared with SGL 22BB gas diffusion layers (GDL) on each side as well as 150 $\mu\mathrm{m}$ thick polytetrafluoroethylene (PTFE) gaskets. Despite the ink formulation and deposition process were the same, the substrate (GDL H23C8 with MPL for the GDE and PTFE sheet for DC) and hot-transfer process are different. A systemic study of the impact on the catalyst layer for both GDE and decal-transfer CCM was not performed during this work: differences for both types of electrodes are awaited, but not known.

The electrochemical characterizations in DC were performed by Clemence Lafforgue at CEA Grenoble, as well, but will be detailed here briefly for the sake of simplicity for the compilation and discussion of results with RDE and GDE that can already be found in Chapter II. Experimental section.

The experimental protocol is sequenced as follow:

- **<u>Break-in:</u>** Chronoamperometry (CA) at $0.1\ \mathrm{V}$ for 30 min (for $\mathrm{Pt/VC}$ and $\mathrm{PtCo/VC}$) or 90 min (for $\mathrm{Pt/GC}$) at 80°C under $\mathrm{H_2/O_2}$ flow ($38\ \mathrm{NL\ h^{-1}}$ and $18.8\ \mathrm{NL\ h^{-1}}$ respectively) at 80 % relative humidity and a total pressure of 1.34 bara on both sides.
- **<u>ECSA measurements:</u>** Cyclic voltammetries (CV) from $U = 0.1\ \mathrm{V}$ to $U = 1.2\ \mathrm{V}$ at 20, 50, 100 and 200 $\mathrm{mV\ s^{-1}}$ at $T = 30$°C and 100 % RH under $\mathrm{H_2/N_2}$ flows ($38\ \mathrm{NL\ h^{-1}}$ and $95\ \mathrm{NL\ h^{-1}}$ respectively).
- **<u>ORR activity measurements:</u>** Staircase potentiostatic electrochemical impedance spectroscopy (SPEIS) at $T = 30$°C, 100 % RH, under $\mathrm{H_2/O_2}$ flow ($38\ \mathrm{NL\ h^{-1}}$ and $18.8\ \mathrm{NL\ h^{-1}}$ respectively) and atmospheric pressure. 16 voltage steps of 50 mV with a duration of 3 s from $U = \mathrm{OCV}$ (open circuit voltage) to $U = 0.1\ \mathrm{V}$. After each step, the impedance is acquired from 50 kHz to 1 kHz. This is done twice and the backward step of the second cycle is used.

For the SPEIS data sets, values of the current, voltage and high frequency resistance are taken to obtain cell voltages corrected from both ohmic drop and $\mathrm{H_2}$ cross-over. To have points regularly spaced in the $0.95 - 0.6\ \mathrm{V}$ voltage range, a linear regression is made between the IR-corrected points, which is especially needed below 0.8 V. For the 0.95 V current value, the first point of the SPEIS technique is taken. Finally, for the 0.9 V point, a linear regression is done using the current values of the three highest voltages to measure Tafel slopes. This point is obtained from the closest experimental point using the mean Tafel slope.

As a brief reminder of this subsection, schemes of the setups and interfaces as well as summary of the main points of each setup are presented on Figure III - 1 - 1.

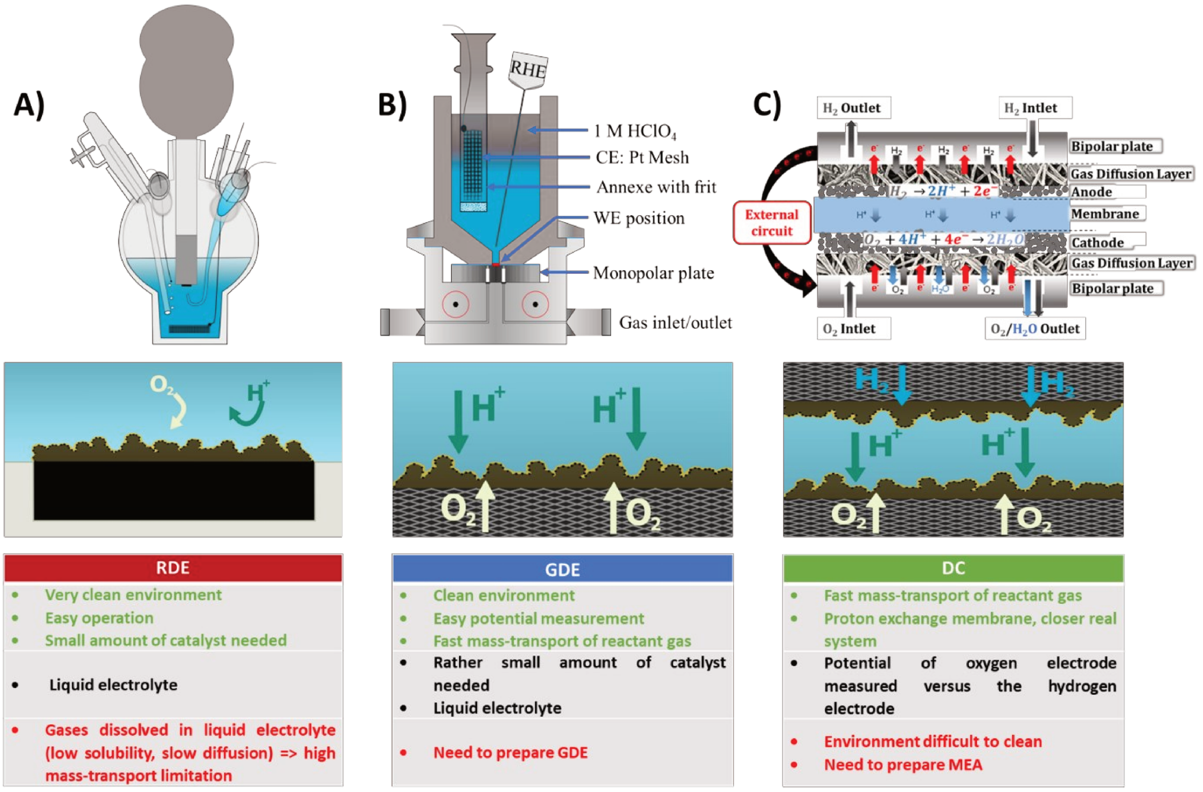

RDE	GDE	DC
Very clean environment Easy operation Small amount of catalyst needed	Clean environment Easy potential measurement Fast mass-transport of reactant gas	Fast mass-transport of reactant gas Proton exchange membrane, closer real system
Liquid electrolyte	Rather small amount of catalyst needed Liquid electrolyte	Potential of oxygen electrode measured versus the hydrogen electrode
Gases dissolved in liquid electrolyte (low solubility, slow diffusion) => high mass-transport limitation	Need to prepare GDE	Environment difficult to clean Need to prepare MEA

*Figure III - 1 - 1: Summary of all three setups' environment with their advantages and drawbacks. **A)** RDE, **B)** GDE and **C)** DC. Reprinted from [133]*

2. Intrinsic activity study using the RDE, the GDE and the DC setups on three commercial catalysts

a) Physicochemical properties of the three ORR catalysts

To start the story of this benchmark, a quick overview of the physicochemical features (shape, size, composition) of the three catalysts studied with these three setups is presented. They are very common commercial catalysts, and were chosen because they are popular in many studies within the literature. Pt on Vulcan carbon (Pt/VC) can be considered as a reference catalyst often used to compare the activity of new and state-of-the-art catalysts, PtCo on Vulcan carbon (PtCo/VC) represents the working field on alloyed catalysts to improve their intrinsic activity [38,45,46] and Pt on graphitized carbon (Pt/GC) highlights the change in carbon support done to increase the durability of catalyst nanoparticles, as it is one major degradation route of these types of materials [59,143] (see Chapter I. General context of the thesis : the Proton Exchange Membrane Fuel Cells). The transmission electron microscope (TEM) pictures of Figure III - 2 - 1 show that the Pt/VC catalyst is made of small and very agglomerated nanoparticles, mostly arranged in 2D flat rafts at the surface of the carbon support. The $\mathrm{PtCo/VC}$ is made of nanoparticles of Pt_3Co average composition, with essentially spherical-shape, that are isolated and of larger diameters than that of $\mathrm{Pt/VC}$. The last catalyst, $\mathrm{Pt/GC}$, is made of nanoparticles rather similar to the ones of $\mathrm{PtCo/VC}$ as they are spherical and rather isolated on the carbon support, despite its smaller developed surface (*ca.* $120\ \mathrm{m}^2\ \mathrm{g}_\mathrm{C}^{-1}$ for GC instead of $ca. 250\ \mathrm{m}^2\ \mathrm{g}_\mathrm{C}^{-1}$ for Vulcan XC72), but their average size is intermediate between $\mathrm{Pt/VC}$ and $\mathrm{PtCo/VC}$.

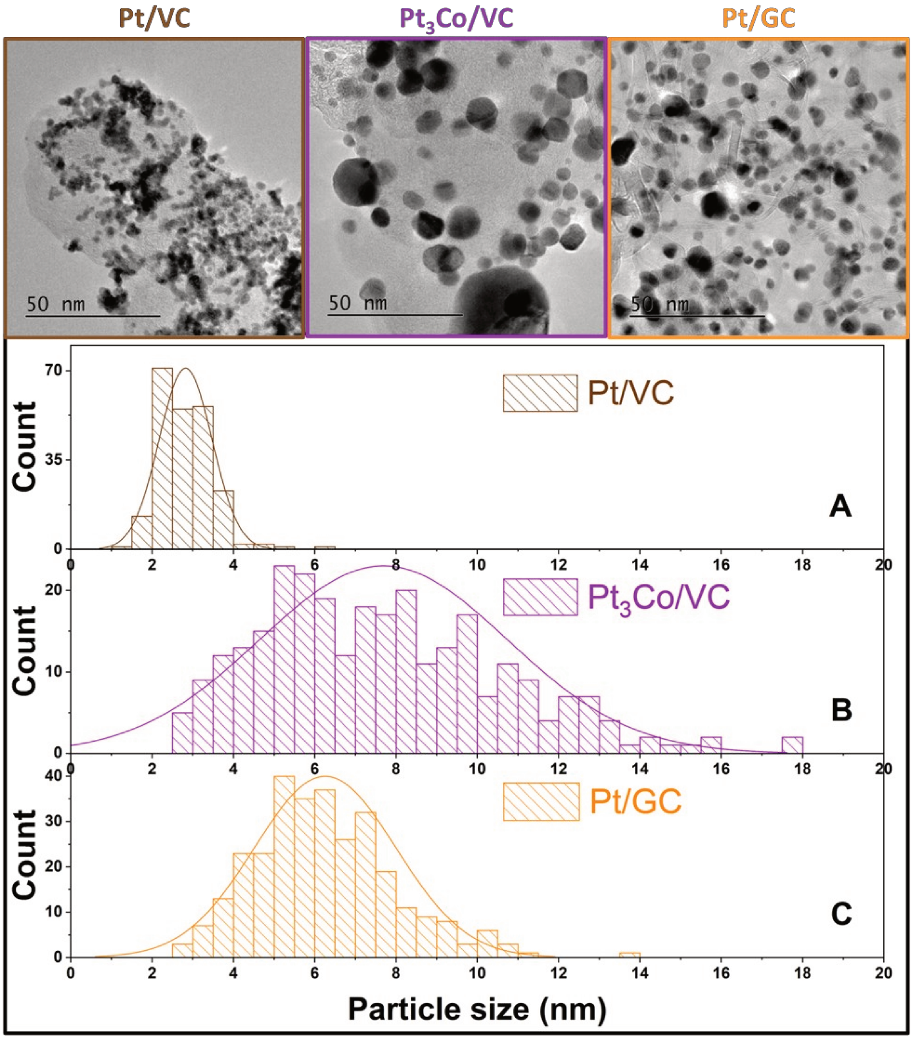

*Figure III - 2 - 1: TEM pictures and particle size distribution histograms of isolated nanoparticles of **A)** the Pt/VC (brown), **B)** the Pt_3Co/VC (purple) and **C)** the Pt/GC (orange) catalysts*

From these TEM images, particle size distribution (PSD) have been drawn, as described in Chapter II. The number-averaged particle sizes are 2.8, 6.3 and $8.3\ \mathrm{nm}$ for $\mathrm{Pt/VC}$, $\mathrm{Pt/GC}$ and $\mathrm{PtCo/VC}$ respectively. The theoretical surface areas that can be calculated from these diameters lead to 100, 44 and $34\ \mathrm{m}_\mathrm{Pt}^2\ \mathrm{g}_\mathrm{Pt}^{-1}$, following the same order. These values are only calculated considering the mean diameter determined from the PSD and do not consider the agglomeration degree of the particles. For example, in the case of the $\mathrm{Pt/VC}$ catalyst, the formation of flat rafts by agglomeration of the nanoparticles leads to a decrease in the effective surface area of the material. This would be very difficult to quantify only relying on TEM images.

To briefly have a look at the microscopic feature of the tested electrodes, Figure III - 2 - 2 presents three top surface SEM images of a $\mathrm{PtCo/VC}$ electrode not tested using the backscattered electron (BSE) detector (Z contrast but no topological information) and one cross-section. As can be seen, having very homogeneous surface is difficult at such low loading ($20\ \mu\mathrm{g_{Pt}}\ \mathrm{cm_{geo}^{-2}}$) with the spray deposition technique but an active layer thickness of $ca.\,0.5 - 1\ \mu\mathrm{m}$ is estimated from these images, considering heterogeneity of the surface at some area. Microscopic spheres deposited on the electrode were observed (bottom-left image on Figure III - 2 - 2). As scanning electron microscope (SEM) images in cross-section only gives very local information, XRF and inductively coupled plasma mass spectrometer (ICP-MS) measurements, which give a sample-large result and therefore hold larger statistical relevance, are the ones used to estimate the average Pt loading (no estimation comes from layer thickness measurement in SEM).

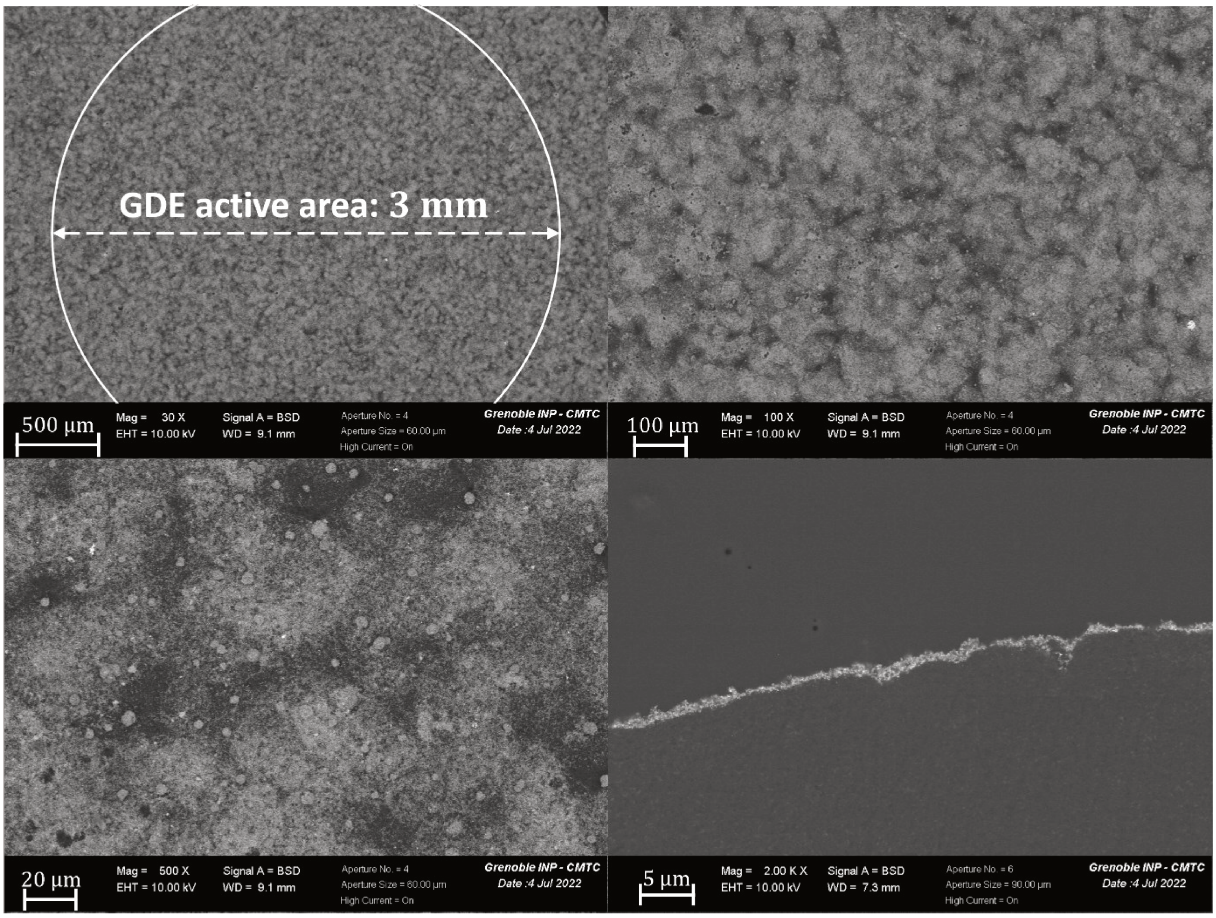

Figure III - 2 - 2: Surface SEM images of a PtCo/VC sprayed GDE at different magnifications with a BSE detector. Bottom right picture is a cross-section of the electrode

The ICP-MS measurements were made for the GDE following the procedure developed in Chapter II. The quantification of the amount of platinum (the mean value) and the errors (standard deviation) are calculated using all three tested electrodes for each catalyst. The as-determined loadings (calculated using the geometric area of the electrodes, $0.071\ \mathrm{cm^2}$) are $0.021\ \mathrm{mg_{Pt}}\ \mathrm{cm_{geo}^{-2}}$ ($\pm 2\ \%$), $0.020\ \mathrm{mg_{Pt}}\ \mathrm{cm_{geo}^{-2}}$ ($\pm 3\ \%$) and $0.018\ \mathrm{mg_{Pt}}\ \mathrm{cm_{geo}^{-2}}$ ($\pm 3\ \%$). These loadings were used in the following to determine the mass activity in GDE, while XRF measurements were used for DC measurements as it would have been more complicated to perform ICP-MS on studied electrodes without loss.

b) Determination of the ECSA: influence of the working electrode environment

In this work, experiments are done using low electrodes loadings to access the intrinsic activity of the studied catalysts. To that goal, it is expected that no limitations are at stake, in particular no “active layer effects”, *i.e.* no consequent mass-transport limitations occurring in the active layer, which would happen with thick active layers [129,171]. However, as the $\mathrm{Pt/GC}$ catalyst is less loaded than the others ($30\%\mathrm{wt_{Pt}}$ instead of $45-50\%\mathrm{wt_{Pt}}$), the same electrode loading is reached for slightly thicker active layer; it is posited that this is still thin enough (< 1 µm) to prevent these limitations as much as possible in the thickness of the electrode. Moreover, the three setups (RDE, GDE and DC) are fundamentally different by the nature of the (working) electrode environments and the way reactant are fed to the active layer (mass-transport of protons, water and oxygen). This difference also applies to the potential control the experimentalist has on the system: the RDE and GDE are three-electrode setups, which enable access to the potential of the working electrode, while the DC is a two-electrode setup, for which the potential of the working electrode is always intrinsically linked to the one of the counter electrode (even though the conditions in which the DC is operated shall guarantee that the hydrogen electrode is not limiting, should it be in $\mathrm{H_2/N_2}$ or in $\mathrm{H_2/O_2}$ conditions). Due to all these differences, these experimental environments induce non-negligible differences when it comes to the determination of the ECSA. In a liquid environment (RDE and GDE), the electrolyte can (in principle) easily access every particle of the catalyst layer. The thin film produced when preparing the RDE electrode is more likely to be fully flooded, at least when the carbon support used is not too hydrophobic (which is the case for Vulcan carbon); this is a bit more speculative in the case of the graphitised carbon used for the $\mathrm{Pt/GC}$ catalyst, even if the presence of the ionomer can slightly improve its hydrophilicity. It starts to be more complicated with the GDE, which is believed to be in a state in between the fully-flooded and the dry conditions. Indeed, the active layer deposited on the gas diffusion layer is supposed to be flooded, because it is in direct contact with the liquid electrolyte on top of it, but the other side, at the interface with the GDL, is assumed to be hydrophobic enough and subjected to a high gas flow. This should result in a dry catalyst layer|gas diffusion layer interface. The GDE active layer should then be sufficiently hydrated to have a good proton accessibility from the electrolyte, and well accessed by the gaseous reactant on the other side, overall resulting in as-low-as-possible mass-transport limitation from protons and $\mathrm{O_2}$. This can be realised due to the small thickness of the active layer and of the experimental conditions chosen, as will be demonstrated hereafter. Higher temperatures or a different GDL could induce a different behaviour with the active layer hydration. It is no wonder why, up-to-date, every groups working with the GDE setup still use the same GDL (H23C8, Freudenberg) [133,149,174,177,178]. However, these particular operating conditions lead to very different $\mathrm{O_2}$ activity (partial pressure of gaseous species, $ca.$ 1 bar for pure gases) from that experienced in liquid electrolyte (the solubility of $\mathrm{O_2}$ and $\mathrm{H_2}$ in aqueous electrolytes in RDE measurements is *ca*. 10 $^{-3}$ mol L^{-1}). This of course modifies the equilibrium potentials at stake, which is especially the case for hydrogen reactions. Producing molecular hydrogen (and so, a rather small quantity of it) in a mix environment of liquid electrolyte and a high flow of nitrogen gas instead of a fully liquid one lead to a smaller activity for the dihydrogen (an activity of $ca.\ 10^{-3}$ mol L^{-1} in flooded liquid electrolyte, the RDE, *i.e*. an activity of *ca*. 10^{-3} for H_2), and so in the present case, 90 mV earlier onset for the hydrogen evolution reaction. This value can, on the other hand, help to estimate the activity of hydrogen in this environment. On Figure III - 2 - 3, one can see the cyclic voltammograms for RDE and GDE during CO stripping measurements. For each catalyst, the low vertex potential value applied in the hydrogen under potential deposition ($\mathrm{H_{upd}}$) region ($0.05\ \mathrm{V}\ vs.\mathrm{RHE}$) seems to not be appropriate for the measurement of the ECSA using the $\mathrm{H_{upd}}$ method due to a very early onset of the hydrogen evolution reaction (HER). The shape of the RDE and GDE curves are therefore very different in the $\mathrm{H_{upd}}$ region, with the experimental difference of HER onset of 90 mV mentioned above.

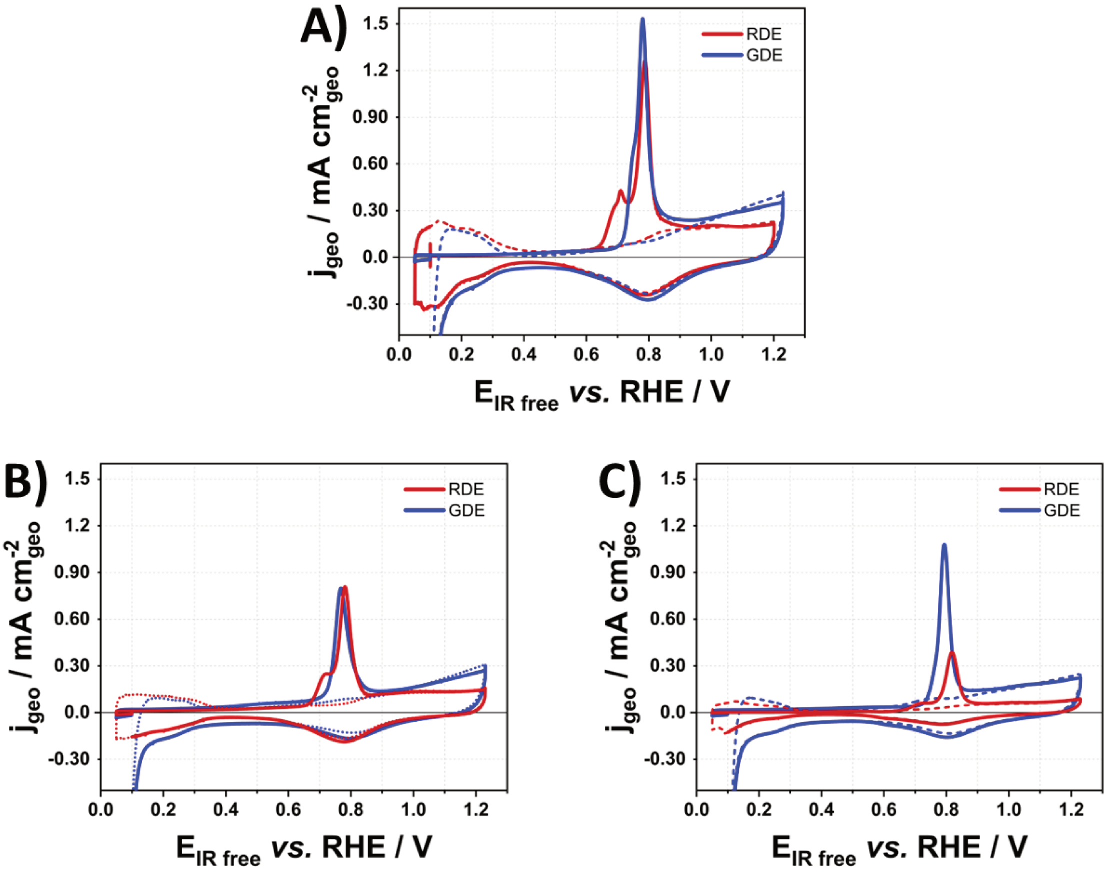

Figure III - 2 - 3: CO stripping cyclic voltammetries at 20 mV s^{-1} using the RDE and GDE setups performed under inert atmosphere (Ar) after adsorption of CO at 0.1 V vs. RHE for all three catalysts: ***A)*** *Pt/VC,* ***B)*** *Pt_3Co/VC and* ***C)*** *Pt/GC. Potentials are ohmic-drop corrected*

Figure III - 2 - 3 makes clear that a different HER/HOR (hydrogen oxidation reaction) equilibrium potential exists for the $\mathrm{Pt}|$gas phase+liquid interface compared to the $\mathrm{Pt}|$liquid interface; the upward displacement of the effective potential at which the hydrogen evolution reaction takes place in GDE (and PEMFC) [179] surely leads to a miscalculation of the ECSA in GDE using the $\mathrm{H_{upd}}$ methodology. Gilman et al. indeed reported the formation of molecular $\mathrm{H_2}$ at positive RHE potentials, which contribution is higher as the scan rate decreases, leading to a miscalculation of the $\mathrm{H_{upd}}$ charge [180]. This will be further discussed hereafter. From Figure III - 2 - 3, one can see that the CO electrooxidation peak is also different for both setups as observed in the work of Tregaro [131]. One specificity of the RDE data is the pre-peak of CO oxidation, attributed to agglomerated nanoparticles [181]. This is well detected for $\mathrm{Pt/VC}$ and $\mathrm{PtCo/VC}$ catalysts in RDE setup but only slightly observed for the $\mathrm{Pt/VC}$ catalyst when the GDE setup is used, with a very small shoulder. This means that the experimental setup also influences the electrochemical response of the catalyst itself, despite having similar active layers. This may be a way to assess the hydration of the electrode, being not as flooded in GDE than in RDE configuration; this would slow down a bit the $\mathrm{OH_{ads}}$ formation on carbon support, that can initiate at lower potential this reaction in fully flooded conditions. This however does not change the peak potential of the CO electrooxidation, being dependent on the scan rate and the catalyst mean particle size [181,182]. However, the CO stripping aspect for $\mathrm{Pt/GC}$ catalyst is very surprising. It seems that, in addition to a different peak position for the CO oxidation, even the capacitive current is different between the RDE and GDE experiments. The spray technique must result in better dispersed and less agglomerated active layers for the evaluation of this catalyst, for which ink formulation and dispersion to prepare RDE tips was difficult, due to the high hydrophobicity of its carbon support. It is also possible that, despite our care, the $\mathrm{Pt/GC}$ active layer was not fully wetted by the electrolyte in RDE, owing to the large hydrophobicity of the GC.

For the DC evaluation of the ECSA, it was not feasible to use the CO stripping method, leaving only the $\mathrm{H_{upd}}$ as the only mean of ECSA measurement. Therefore, multiple scan rates were used to perform cyclic voltammetries, as presented in Figure III - 2 - 4, to choose the optimal scan rate for the $\mathrm{H_{upd}}$ ECSA measurement.

As can be seen on the CVs, for all catalysts, those measured at 100 and $200\ \mathrm{mV\ s^{-1}}$ possess a peak in the low voltage region during the anodic scan. This is attributed to $\mathrm{H_2}$ formed during the non-negligible HER witnessed in the cathodic scan; at high voltage scan rate, the $\mathrm{H_2}$ formed does not have the time to diffuse out of the active layer and a fraction of it can be oxidized as soon as the voltage is increased during the following anodic scan. This faradaic oxidation current adds to the capacitive current related to the desorption of protons and leads to an overestimation of the $\mathrm{H_{upd}}$ charge. On the contrary, for low voltage scan rates, it is possible that impurities, which are difficult to remove in PEMFC conditions, do bias the measurements; although they have been stripped of the surface at high cell voltages, they have time to diffuse back to the catalytic sites when the potential is in the $\mathrm{H_{upd}}$ range. As a result, in this study, the intermediate case of $50\ \mathrm{mV\ s^{-1}}$ seems a good compromise between these effects and was selected for the evaluation of the ECSA.

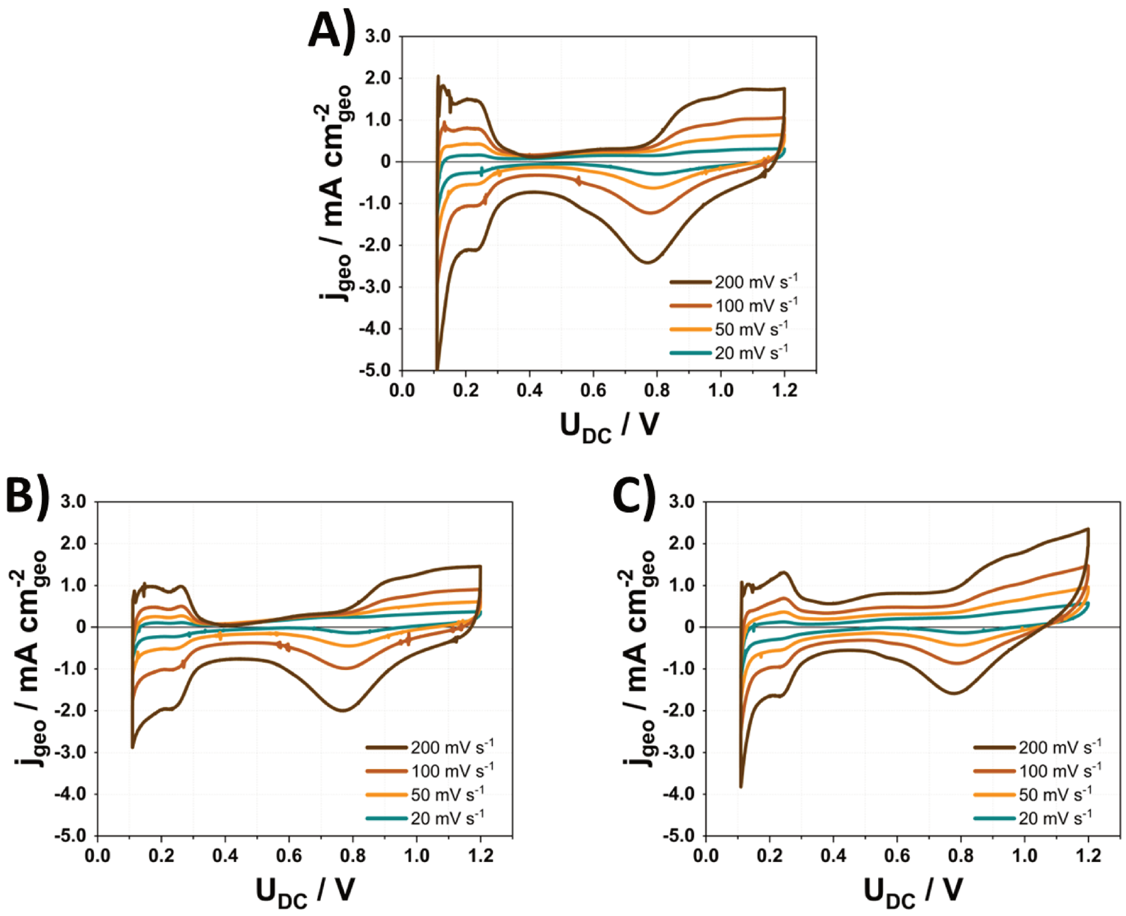

Figure III - 2 - 4: Cyclic voltammetries performed under inert atmosphere (N_2) in DC environment for a single electrode of each catalyst at different voltage scan rates for ***A)*** *Pt/VC,* ***B)*** *Pt_3Co/VC and* ***C)*** *Pt/GC. The CVs are corrected of the H_2 cross-over.*

Figure III - 2 - 5 summarises the results obtained for the different ways to calculate the ECSA for the three setups and three catalysts. For a given catalyst (here Pt/VC), it is clear that the difference previously observed on the CO stripping voltammetries for the RDE and GDE setups also applies to the DC setup (Figure III - 2 - 5). In GDE and DC, both setups with active layers partially in the gas phase, the voltammograms exhibit the same trend: H_2 evolves at more positive potential/cell voltage than in RDE. Additionally, the onset potential observed for the HER in GDE is similar to the one observed in DC, leading to two conclusions: (i) the GDE uses a true reference (commercial RHE), validating the fact that the hydrogen electrode in DC can be considered as a robust reference in the tested conditions, and (ii) the degree of humidification and value of protons/hydrogen activities influence this onset potential; this further proves that the active layer in GDE is not flooded but has a rather similar humidity as the DC. Having that in mind, H_{upd} measurements should be made with a higher low-vertex potential in GDE and DC, which would however lead to an under-estimation of the ECSA measured by this method. This conclusion and voltammograms aspect also apply to PtCo/VC and will be later presented. For the determination of the ECSA, the CO oxidation coulometry is a more reliable method; it gives very similar results for the RDE and GDE setups. It is then clear, looking at Figure III - 2 - 5, that the ECSA values determined using the CO stripping technique and the $\mathrm{H_{upd}}$ one are within the error bars for the RDE but differ significantly for the GDE and DC.

The case of Pt/GC is peculiar, with two noticeable issues. The first one is related to its catalyst layer preparation (as previously mentioned). The technique usually employed for catalyst layer preparation is not well adapted for such a graphitised and hydrophobic carbon, leading to issues with the reproducibility of the ink deposition; this creates non-homogeneous and incomplete active layers with regions of local thinner or thicker active layer. The second is related to the hydrophobic nature of the carbon support, which is therefore less intruded by the liquid electrolyte. This could lead to some “dry” active layer area, even in RDE environment, *i.e*. not accessible to the electrolyte and of the protons, resulting to an underestimation of ECSA both with the $\mathrm{H_{upd}}$ and CO stripping methods. This is well observed on Figure III - 2 - 5 for which Pt/GC is the only catalyst exhibiting lower ECSA in liquid electrolyte.

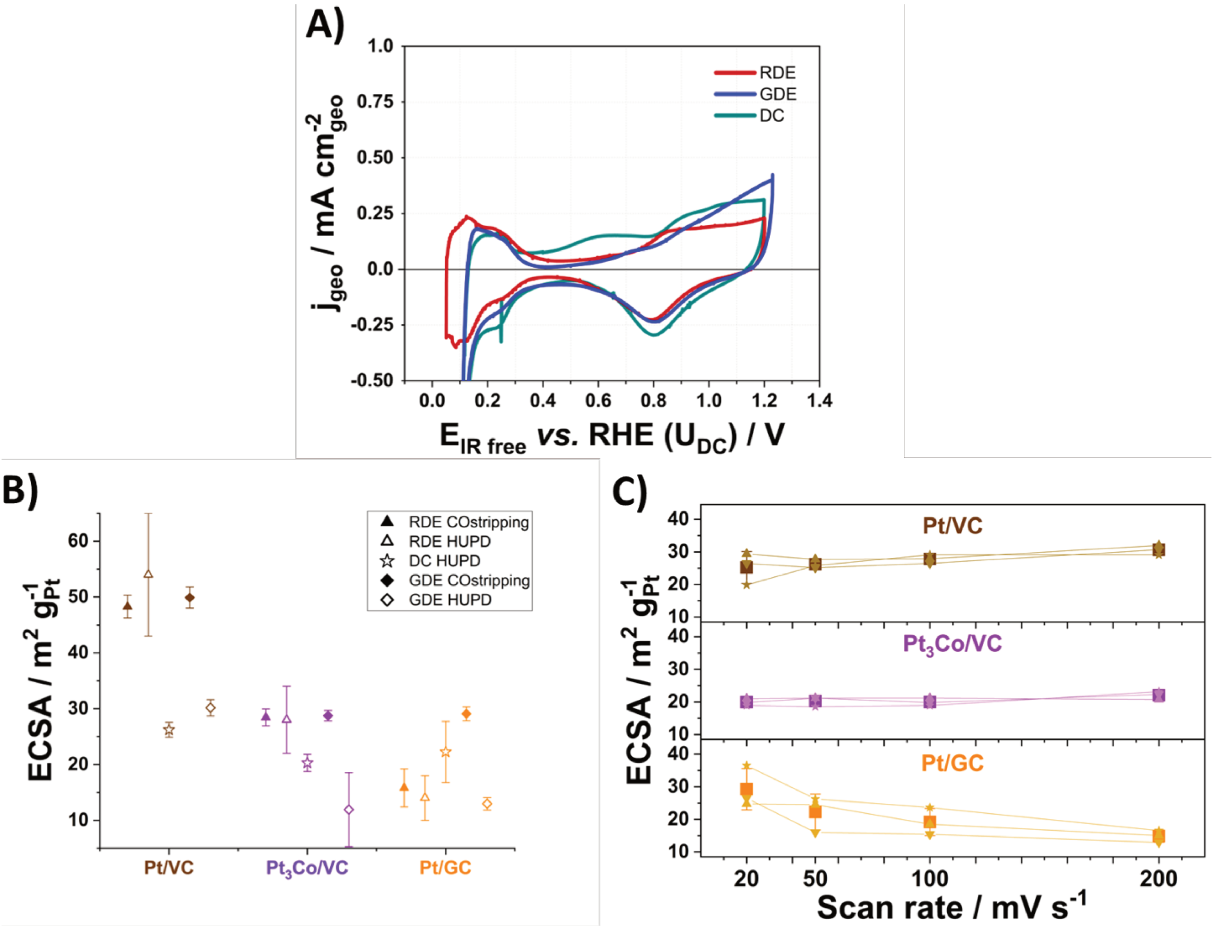

Figure III - 2 - 5: ***A)*** *CV obtained with Pt catalyst under inert atmosphere with the RDE (red), GDE (blue) and DC (green) setups;* ***B)*** *ECSA values determined using CO stripping and* H_{upd} *methods for the three setups and the three catalysts and* ***C)*** *Evolution of the ECSA determined via* H_{upd} *at different voltage scan rates for the DC setup for Pt/VC (brown), PtCo/VC (purple) and Pt/GC (orange)*

For the $\mathrm{H_{upd}}$ measured in DC, the choice of an intermediate voltage scan rate account for small variations of the ECSA measured for both Vulcan-supported catalysts and in the same range as the GDE measurements, despite being lower than that determined using CO stripping. Knowing that, it is reasonable to assume that the active area determined in DC is an underestimation of the real ECSA, having in mind that ECSA ($\mathrm{H_{upd}}$) < ECSA (CO stripping) in GDE. However, the decreased ECSA obtained for the $\mathrm{Pt/GC}$ catalyst when increasing the voltage scan rate (Figure III - 2 - 5) could be related to the uneven repartition of the water in the active layer volume, leading to proton accessibility issues.

To conclude, the ECSA values for all catalysts will be assessed by CO stripping for RDE and GDE, and $\mathrm{H_{upd}}$ at $50\ \mathrm{mV\ s^{-1}}$ for DC.

c) Determination of the intrinsic ORR activity: influence of the working electrode environment

Having the ECSA values for all catalysts in all three environments studied (CO stripping for RDE and GDE, $\mathrm{H_{upd}}$ at $50\ \mathrm{mV\ s^{-1}}$ for DC), the ORR performance of these catalysts can be accessed and compared using the geometric, the specific surfaces (leading to the specific activity, SA) and the mass (leading to the mass activity, MA) of catalysts. The ORR kinetic activity measurement is based on measured and corrected (ohmic drop for all and hydrogen cross-over for DC) polarization curves in the three setups. The study will go by comparing the different setup catalyst by catalyst before gathering all the results.

The ORR measurements of RDE, GDE and DC are gathered in different graphical views presented in Figure III - 2 - 6 for the $\mathrm{Pt/VC}$ catalyst, to begin with. The **A)** geometric and **B)** specific current densities polarizations curves are displayed and the first observation that can be made is that the RDE geometric current density for the ORR is way inferior to those measured in GDE or DC. This is explained by the 3 to 4 decades slower mass-transport kinetics of oxygen in the liquid environment compared to the gas phase, leading to dramatically low mass-transport limited current. This is no surprise and was the reason to evaluate the GDE setup to start with. The second observation made is related to the reproducibility of the results. Indeed, not talking about the RDE, but for gaseous electrodes, the GDE has much larger error bars than the DC measurements. This is related to the influence of local heterogeneities much more impacting for very small geometric surface areas ($0.071\ \mathrm{cm^2}$ in GDE *vs.* $1.8\ \mathrm{cm^2}$ in DC). Small heterogeneities on the active layer surface will impact more the GDE measurements than the DC ones. In both cases though, the geometric current density evolution seems rather similar for high electrode potentials/cell voltages, but a clear separation is seen as soon as the potential goes under $0.7\ \mathrm{V}\ vs.\ \mathrm{RHE}$, the current being lower for the GDE. The reason for that is still unclear and can be attributed to increasing oxygen mass-transport limitation related to a possible progressive flooding of the active layer, the production of water coming with the reduction of oxygen in acidic media. It is very unlikely that the limitation comes from a protonic mass-transport limitation as (i) there should be more acid electrolyte (hence more protons) in the active layer in GDE and (ii) the Nafion® ionomer distribution should be the same due to similar ink formulation and deposition parameters for GDE and DC. It can however not be excluded that DC electrodes have better ionomer distribution thanks to the hot-pressing step. This will be later discussed by the use of impedance spectra performed along the polarization curves in GDE.

Additionally, the differences between ECSA measured using the $\mathrm{H_{upd}}$ in DC and CO stripping in RDE/GDE would lead to a significant gap between the specific current densities (j_{spe}). However, even assuming a similar ECSA for both GDE and DC, the geometric current densities measured show that in the range $0.8 - 0.6\ \mathrm{V}$, the GDE fails to match the DC measured current. Whatever these bias and differences, the Tafel plots representing the specific activities for this catalyst are very well overlapping in the $0.9 - 0.8\ \mathrm{V}\ vs.\ \mathrm{RHE}$ range. This means that any setup used is relevant for the measurement of intrinsic ORR activity for the $\mathrm{Pt/VC}$ catalyst in these conditions ($25°\mathrm{C}$, fully hydrated gases or $0.1\ \mathrm{M}$ liquid electrolyte in the high potential region). This also applies for the mass activity measured: the RDE, GDE and DC do compare rather well in this “high” potential range, with this time a high tendency for the DC to underestimate the MA for the high cell voltages (see explanation below). In addition, the GDE and DC seem to give quite similar results until $0.7\ \mathrm{V}\ vs.\ \mathrm{RHE}$, the GDE hence being much more adapted than RDE to assess intrinsic ORR kinetics at high currents/low potentials.

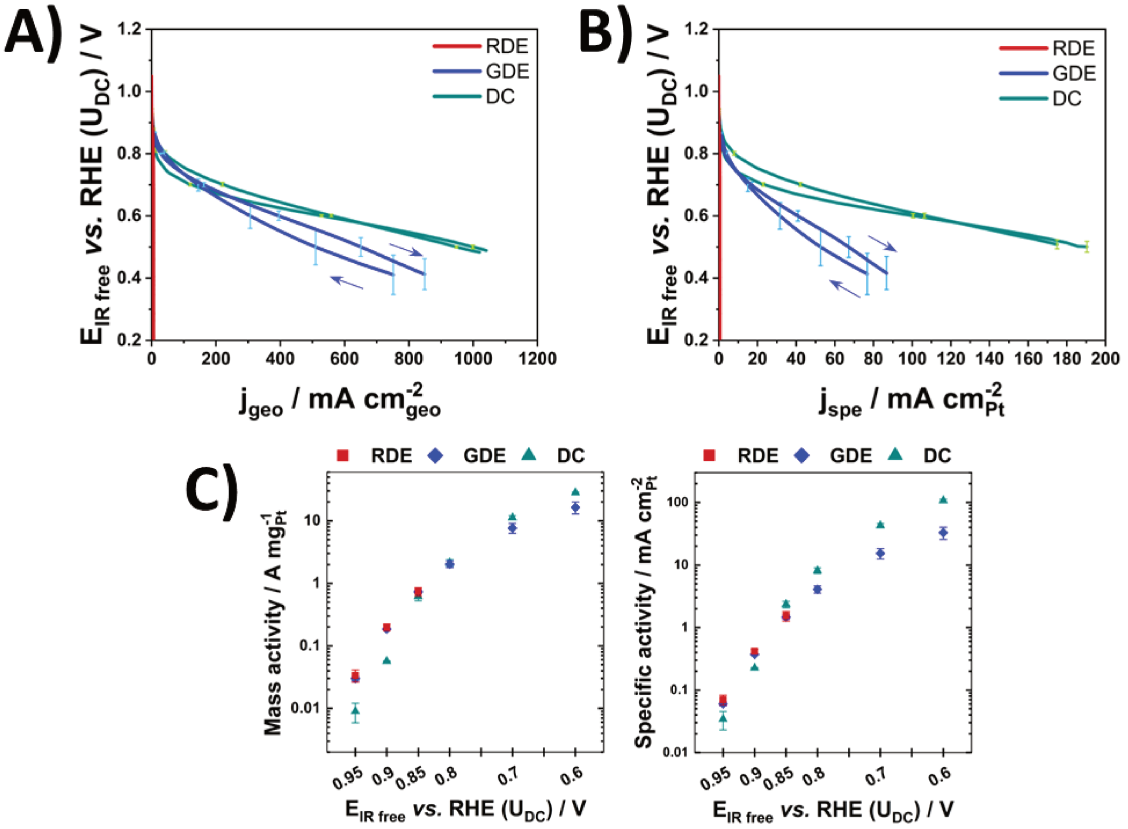

Figure III - 2 - 6: Experimental results obtained with the Pt/VC catalyst. ***A)*** *Mean polarization curves with respect to the geometric surface of the electrodes,* ***B)*** *Mean polarization curves with respect to the chosen ECSA,* ***C)*** *Tafel plots summarizing the mass and specific activities at different potentials and cell voltages. Same colour code for experimental setups as in previous figures (red, blue and green for RDE, GDE and DC respectively)*

All the techniques come with their own advantages and drawbacks: the Tafel plots show, for the high cell voltages/electrode potentials region, that the DC measurements lead to lower current densities, both being expressed by the catalyst mass (in a pronounced manner) or specific area (to a smaller extent). This is linked to the $\mathrm{H_2}$ cross-over that is intrinsically related to the DC configuration. The $\mathrm{H_2}$ flow that crosses the membrane can afterward be oxidised at the cathode, lowering the net reduction current as well as decreasing the open circuit voltage of the cell. The use of a $130\ \mu\mathrm{m}$ thick membrane planned to limit this phenomenon cannot prevent it totally. This leads to difficulties in measuring correctly currents at high cell voltages in DC. With no surprise, in the case of the RDE, it is the other way around: there is no possible measurement of the intrinsic activity for the ORR below $0.85\ \mathrm{V}\ vs.\mathrm{RHE}$ as it starts to be severely mass-transport limited. For the GDE and DC, the difference in the voltage/potential region under 0.7 V can be explained by difference in water management. The current produced in the first case is $ca.55\ \mathrm{mA}$ while it is $ca.1.9\ \mathrm{A}$, 35 times higher. The heat production is (much) more important for the DC, which possibly frees some flooded active sites due to thermal effect. This is coherent with the hysteresis observed on the DC polarization curves: the current for the increasing voltage scan is higher than for the decreasing voltage scan.

Tafel slopes can be determined using the discretized points of the Tafel plots presenting the specific current densities (Figure III - 2 - 6 for $\mathrm{Pt/VC}$ and related figures for $\mathrm{PtCo/VC}$ and $\mathrm{Pt/GC}$). For the "high potential region" (between 0.9 and $0.8\ \mathrm{V}\ vs.\mathrm{RHE}$), the values of the Tafel slopes are close to $90\ \mathrm{mV\ dec^{-1}}$ in RDE and GDE but only $64\ \mathrm{mV\ dec^{-1}}$ in DC. For the low potential region (0.8 to $0.6\ \mathrm{V}\ vs.\mathrm{RHE}$), they are closer to 170 for DC and $210\ \mathrm{mV\ dec^{-1}}$ in GDE, the measurement being not possible for RDE. This is not in agreement with earlier reports on these materials [129,183]. These values support the idea that not only charge-transfer kinetics governs the measurements for all setups (even with the Koutecky-Levich correction in RDE that should correct mass-transport and all experimental efforts to avoid it in GDE and DC) or that the Butler-Volmer kinetics does not apply anymore at so large currents. This hypothesis will not be debated further here, but will be the object of a forthcoming PhD in LEPMI.

The trend observed for the bimetallic $\mathrm{PtCo/VC}$ catalyst is rather similar to the $\mathrm{Pt/VC}$ previously presented, as displayed on Figure III - 2 - 7. Indeed, RDE still exhibits several decades lower geometric current densities than GDE and DC and a better reproducibility is observed for the DC measurements when compared to the GDE ones. Nevertheless, the geometric and specific current densities measured are closer to one another for this catalyst, on the full range of potential/cell voltage. The issues regarding the measurements of ECSA in DC environment still results in higher difference in specific activity (Figure III - 2 - 7) determination between GDE and DC. However, the difference in ECSA is not sufficient to explain this difference, as the ratio between the ECSA in GDE and DC is equal to 1.5, whereas the difference in the activity measurements in the "low potential region" (0.8 to $0.6\ \mathrm{V}\ vs.\mathrm{RHE}$) is of a factor 2. This agrees with the previous finding that another non-negligible limitation but not related to the nature of the catalyst (as it was observed for both $\mathrm{Pt/VC}$ and $\mathrm{PtCo/VC}$) must be at stake and should be deeper investigated. Another possibility may be the difference in the geometric electrode size and thermal management between the GDE and DC. The DC electrode has a 25 times higher surface and thus higher platinum mass, leading to much higher currents that produce more heat. Also contrary to the GDE, the DC does not have a bulk of liquid electrolyte on top of the working electrode: this leads to a larger local thermal gradient produced in DC. These thermal management heterogeneities may have an impact and lead to experimental discrepancies on the measured activities. Additionally, the hysteresis observed for the $\mathrm{Pt/VC}$ catalyst is much less present for $\mathrm{PtCo/VC}$, if not absent. This hysteresis was attributed to water produced at high current density, which is still the case here, with even higher current density than for $\mathrm{Pt/VC}$. The assumption of only accounting this hysteresis for water production and flooding of the active site is therefore not valid anymore.

For this catalyst, the Tafel plots comparison of the ORR activities for all three setups (Figure III - 2 - 7) do not match as well as observed for $\mathrm{Pt/VC}$. Quite surprisingly, the activities measured in RDE (thus, at high potentials) are lower than that in GDE and DC.

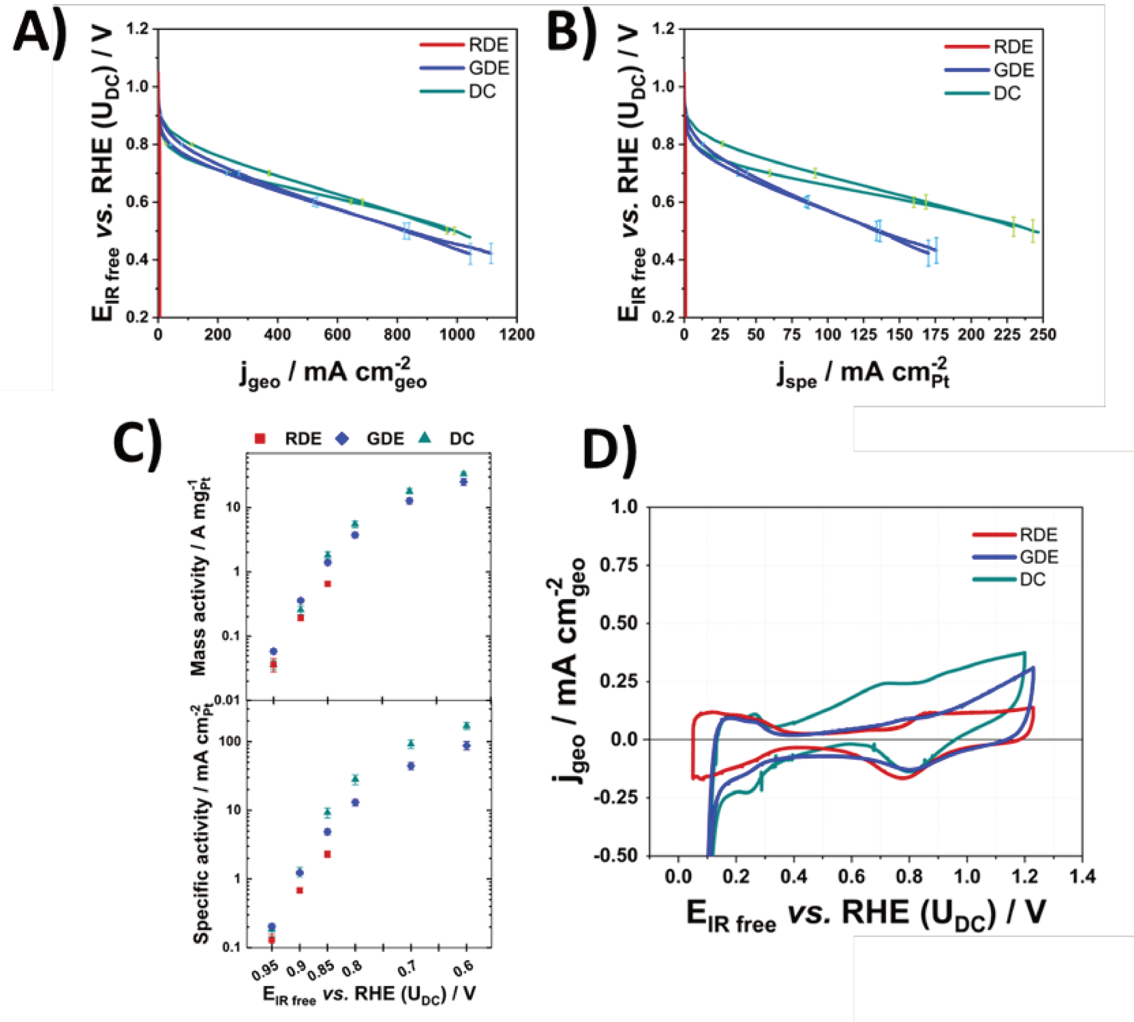

Figure III - 2 - 7: *Experimental results obtained with the PtCo/VC catalyst.* ***A)*** *Mean polarization curves with respect to the geometric surface of the electrodes,* ***B)*** *Mean polarization curves with respect to the chosen ECSA,* ***C)*** *Tafel plots summarizing the mass and specific activities at different potentials and cell voltages.* ***D)*** *CV at 20 mV* s^{-1} *with respect to the geometric surface of the electrodes. Same colour code as previously used*

This lower RDE activity can neither be attributed to the cleanliness of the experimental setup (DC being assumed to be the worst case and RDE, cleaned in Caro's acid to remove all impurities, the best one), nor to the liquid environment (shared with the GDE). However, it is expected that more active catalysts are more limited by mass-transport of reactants; so, the reactant should be depleted much faster for $\mathrm{PtCo/VC}$ than for $\mathrm{Pt/VC}$ (for example) at a given overpotential, due to higher current densities (Faraday's Law) per unit surface of material, resulting in a lower concentration of reactant at the vicinity of the active site; setups enabling higher reactant mass-transport (such as GDE and DC) would be less prone to such limitation, therefore explaining this result. The evolution of the current density follows a similar slope for both RDE and GDE, close to $95\ \mathrm{mV\,dec^{-1}}$ and a smaller slope for DC of *ca.* $75\ \mathrm{mV\,dec^{-1}}$ (similar to previous finding on $\mathrm{Pt/VC}$).

The current density in RDE and GDE should evolve in the same way, despite the RDE having a smaller starting point, believed to originate from the partial pressure of oxygen species/activity near the active sites. The GDE leading to higher activities than the RDE is nonetheless a proof that the GDE (i) yields good-enough cleanliness, with no detrimental poisoning of the active sites and (ii) its data can be considered less mass-transport limited compared to RDE data, even after the Koutecky-Levich correction of mass-transport for the latter. The high potentials Tafel slopes of $\mathrm{PtCo/VC}$ match the ones found for $\mathrm{Pt/VC}$, but the slopes determined for the low potential region are significantly higher and close to $240\ \mathrm{mV\,dec^{-1}}$. This value is twice the slope one can expect for the ORR reaction kinetics on platinum at such potentials in the realm of Butler-Volmer kinetics [21] and this likely shows that the mass-transport limitation cannot be considered non-negligible, even for the thin active layers considered here [183]: at least for this part of the curve, there is something more altering the measured kinetics value. This could be attributed to the volumic aspect of the active layer, as proposed by Gaumont *et al.* [126]. However, despite these differences, one can notice the agreement found for the mass activity of both GDE and DC (Figure III - 2 - 7): in the potential range of a real system ($0.9-0.6\ \mathrm{V}\ vs.\,\mathrm{RHE}$), both setups lead to comparable intrinsic activity measurements.

The $\mathrm{PtCo/VC}$ was chosen as a bimetallic catalyst, which usually promises higher intrinsic activity in RDE at high potentials ($0.95-0.9\ \mathrm{V}\ vs.\,\mathrm{RHE}$), but with serious doubts on its ability to maintain this improvement factor to the relevant range of potential for the PEMFC ($0.9-0.6\ \mathrm{V}\ vs.\,\mathrm{RHE}$). Figure III - 2 - 8 presents the improvement factors (IF) of $\mathrm{PtCo/VC}$ and $\mathrm{Pt/GC}$ reported to the reference $\mathrm{Pt/VC}$ used. They are calculated using both the specific activities (left-hand side graphs) and mass activities (right-hand side graphs). On the top graphs of this figure, related to the $\mathrm{PtCo/VC}$ catalyst's IF, it is shocking to see that the small (for SA) or poor (for MA) IF awaited at high electrode potentials in RDE are way underestimated in comparison to when the catalyst is tested using gas flow setups. In addition, these IF are almost constant in GDE and vary very significantly for the DC. In any case, on the whole range of potentials/cell voltages, $\mathrm{PtCo/VC}$ yields better intrinsic ORR kinetics than the reference $\mathrm{Pt/VC}$, which was not possible to tell using only the RDE setup; the advantage of $\mathrm{PtCo/VC}$ over $\mathrm{Pt/VC}$ rather monotonously decreases with the electrode potential, between 0.9 and $0.6\ \mathrm{V}\ vs.\,\mathrm{RHE}$. The decrease in the IF with the electrode potential (more important in DC) suggests a possible change in the alloyed or reference catalysts during the experiment. The higher IF measured at high cell voltages can be attributed to the smallest oxide coverage of $PtCo/VC$ at high potentials. The specific activity is of great interest to understand the ORR kinetics, but mass activity is still what matters for cost-effectiveness of the real system, because it translates directly the quantity of catalyst that has to be integrated to match the desired power density targeted, which is more relevant for industrials. In this case, the MA IF of $PtCo/VC$ is still superior to 1 as the measurements in GDE and DC show, confirming its interest for practical use.

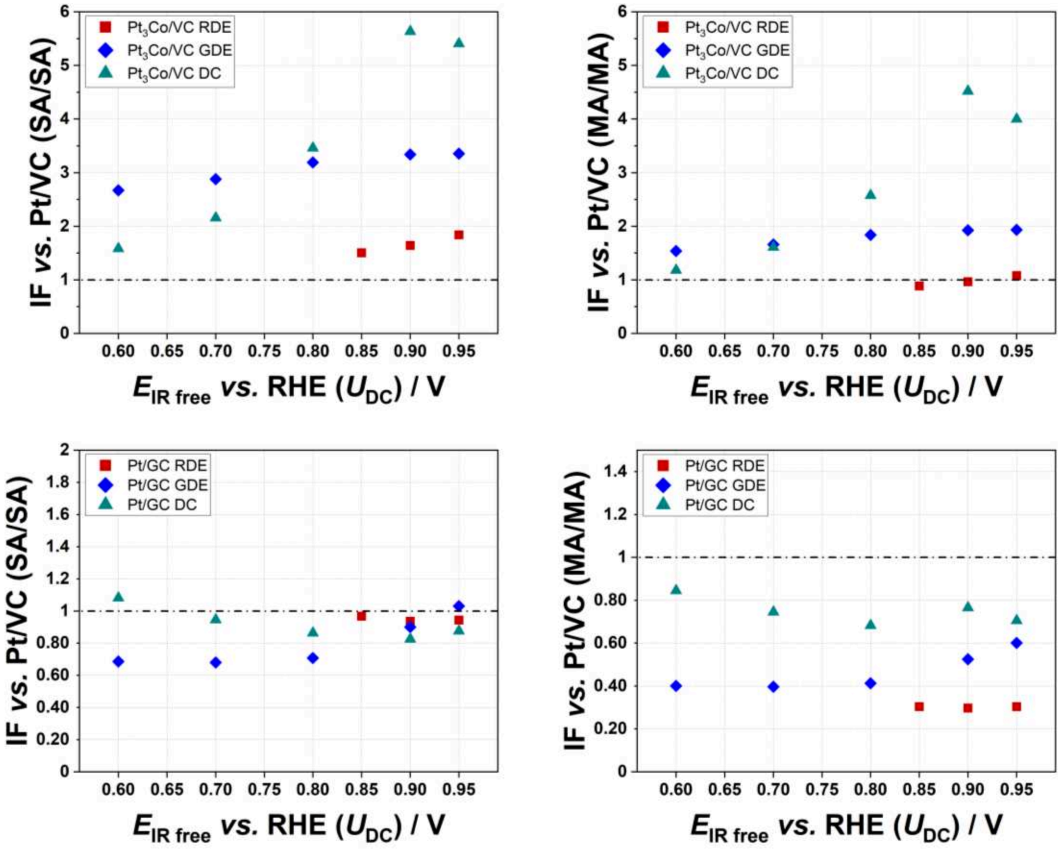

Figure III - 2 - 8: Improvement factors relative to the Pt/VC catalyst for all three setups measured via specific activities (top-left) and mass activities (top-right) ratio for the Pt₃Co/VC catalyst and specific activities (bottom-left) and mass activities (bottom-right) ratio for the Pt/GC catalyst.

Finally, Figure III - 2 - 9 presents the results obtained for the Pt supported on graphitized carbon. Despite the shape of the RDE curves being similar for this catalyst as it was for the two others, highly limited by mass-transport of oxygen, one can see a huge gap between GDE and DC. The difference displayed for these two setups polarization curves is, for this catalyst, much bigger than it was for Pt/VC (see above). The explanation that can be put forth to explain these differences on the whole range of potential studied is once again the water management, believed to be linked to the tremendously different nature of this carbon support. Indeed, the shape observed for the polarization curves is rather similar to the one obtained for Pt/VC, but with a very different shape between the upward and backward scans (despite having a very good experimental reproducibility). This catalyst reaches the lowest maximum current density among the three catalysts and it appears that the time spent at high potential plays a beneficial role on the performance. Indeed, starting from low potentials, the upward scan has lower performance compared to the downward cycle. Moreover, the open circuit voltage is known to be drastically drying, which should have helped to remove water accumulated (produced during the 1-minute waiting period prior to the upward scan) in the pores of the carbon. These findings tend to point out that studying this type of carbon support with liquid electrolyte leads to many discrepancies in the experimental results, related to the bad contact (RDE) or flooding (GDE) of the active layer. The Tafel plots however show that for high electrode potentials, there is still a good match for all three setups on the evaluation of the intrinsic ORR activity.

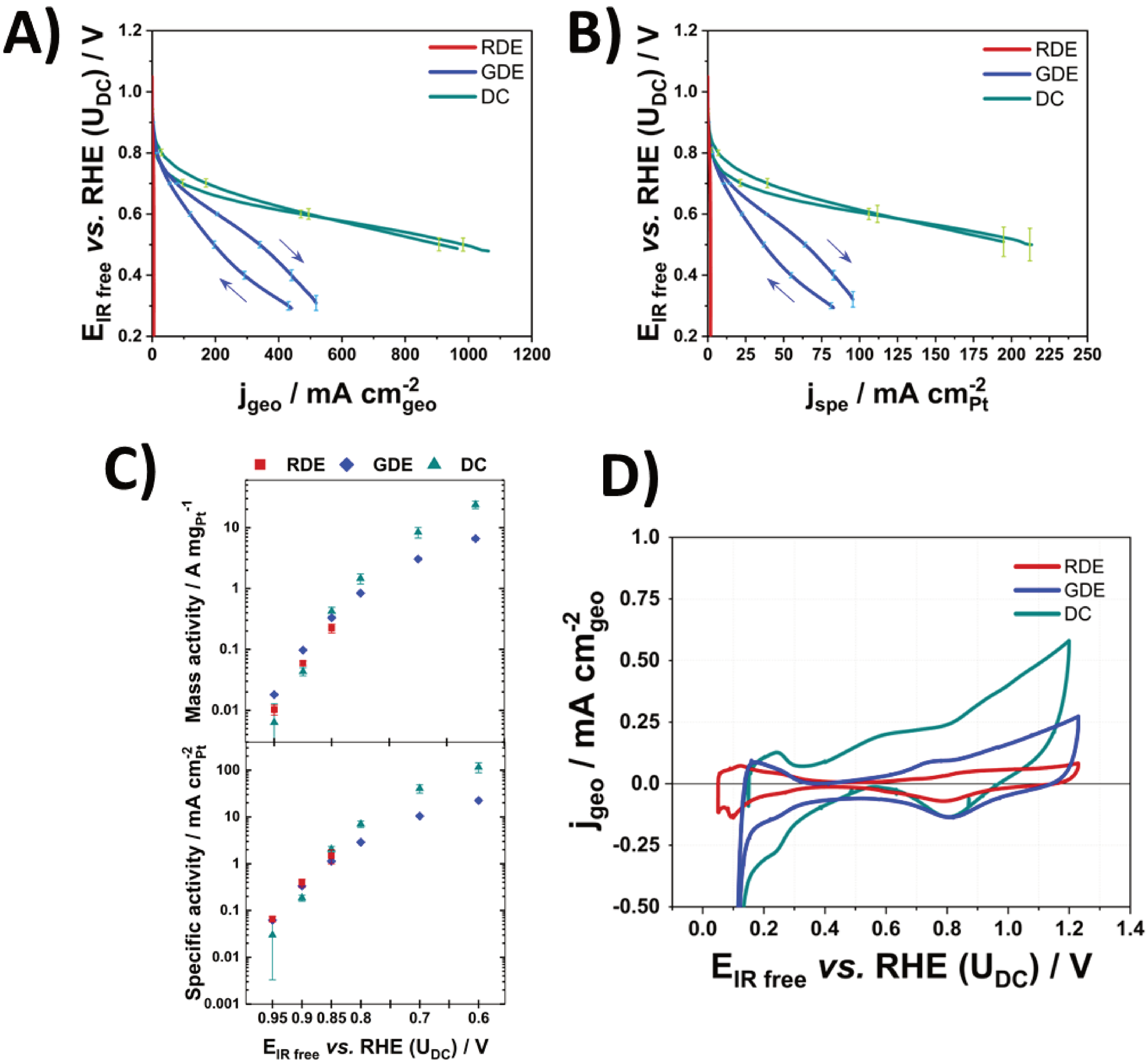

Figure III - 2 - 9: Experimental results obtained for Pt/GC catalyst. ***A)*** *Mean polarization curves with respect to the geometric surface of the electrodes,* ***B)*** *Mean polarization curves with respect to the chosen ECSA,* ***C)*** *Tafel plots summarizing the mass and specific results at different potentials and cell voltages and* ***D)*** *CV at 20 mV s^{-1} with respect to the geometric surface of the electrodes. Same color code as for the previous figures.*

The interesting point, looking at all the results obtained in the high potential region, is that RDE results found for each catalyst at least transpose to the other setup or even get better.

This means that it should be possible to keep the improvement factors measured in RDE if one integrates catalysts in low-loaded electrodes, on model active layers and experimental setups such as GDE and DC. However, it will never be able to translate the critical moment when the performance starts to be limited by mass-transport, as it was not present (PtCo/VC), starting to appear (Pt/VC) or detrimental (Pt/GC) in GDE and absolutely unpredictable in RDE when limitations occur as low as 0.85 V vs. RHE. This extrapolation also relies on the value of the Tafel slope (which obviously changes below 0.85 V *vs.* RHE) and the nature of the catalyst more than on the carbon support: the best overlap is observed for both Pt/VC and Pt/GC while PtCo/VC exhibited the highest differences in this region. This gap is not explained by the difference in ECSA as it is, for the PtCo/VC, the closest among the three catalysts. Figure III - 2 - 8 also presented the discrepancy between both single metallic catalysts: the Pt/GC maintains its SA to the level of Pt/VC, but its mass activity is detrimentally lower and falls down for all three setups to half (in GDE) or even a third (RDE) of that of Pt/VC. However, the SA IFs are close to 1 for all setups for the Pt/GC catalyst, implying that each active site works near-similarly for Pt/VC and for Pt/GC. The MA IF for Pt/GC being way below 1 means that the structure, size, agglomeration, carbon support of this catalyst hinder its good mass performance. This trend is very pronounced for RDE and tends to stabilize moving to the GDE and finally the DC setup: the presence of water in the vicinity of the electrode environment decreases in that sequence, being less and less impacting for the catalyst.

Figure III - 2 - 10, related to DC characterizations, highlights this phenomenon: the gap between both single metal platinum catalysts almost vanishes. A similar behavior is observed on the whole scanned range of cell voltage for the Pt catalysts, offering a good prospective of comparison for similar catalysts composition (in terms of catalytic particles) as it seems to depend mainly on the nature of the metal and not much on the nature of the carbon support. The PtCo/VC alloyed material (which has not been acid leached) is not on par with the two others, and its improvement factor over the pure Pt/C samples is significant on the whole polarization curve (from 0.9 to 0.5 V).

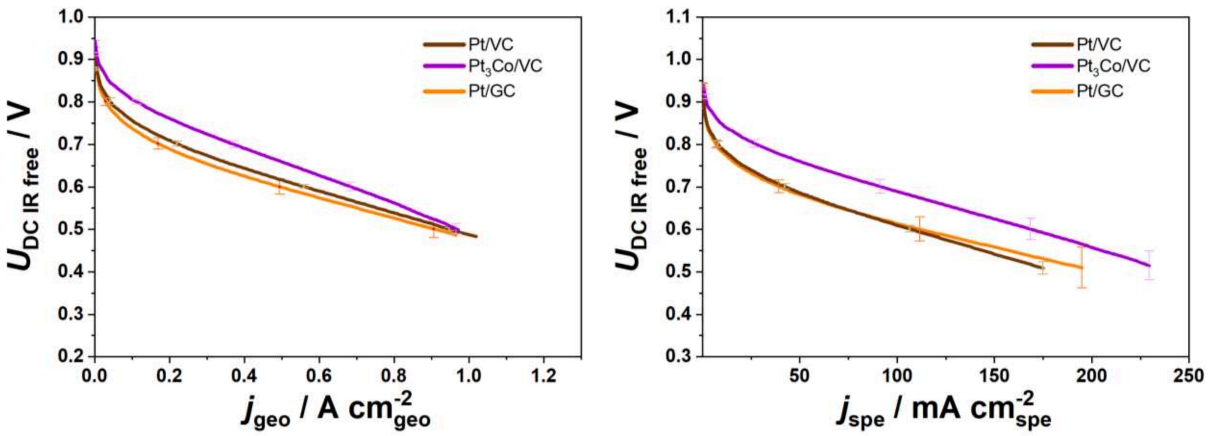

Figure III - 2 - 10: Mean polarization curves in DC environment for all three catalysts with respect to the geometric current density (left) and the specific current density (right), H_{upd} related ECSA taken at 50 mV s^{-1}.

3. Impedance spectra analysis in GDE setup

Galvanostatic electrochemical impedance spectroscopy (GEIS) spectra were measured along the polarization curves performed in the GDE setup for all three electrodes tested for all three catalysts. These spectra were studied using the transmission line model from Gaumont [126], that includes a possible mass-transport issue of the protons in the active layer (but none from the oxygen in the active layer[3]):

$$Z_{\mathrm{ORR}}(f) = R_{\mathrm{HF}} + \frac{R_{\mathrm{p}}}{\sqrt{2i\pi f R_{\mathrm{p}} C_{\mathrm{dl}} + \frac{R_{\mathrm{p}}}{R_{\mathrm{ct}}}}} * \frac{1}{\tanh\sqrt{2i\pi f R_{\mathrm{p}} C_{\mathrm{dl}} + \frac{R_{\mathrm{p}}}{R_{\mathrm{ct}}}}} \qquad \text{(Eq. III.3.1)}$$

With R_{HF} the high frequency resistance, related to the conductivity of the electrolyte and of the current collection, C_{dl} the double layer capacitance, intrinsic property related to the nature of the electrode in contact with the electrolyte, R_{p} the proton transport resistivity in the thickness of the electrode, related to the accessibility of the active sites by proton and R_{ct} the charge transfer resistance, translating the faradaic reaction happening here (the ORR). The idea is to perform a proof by contradiction, to see if it is reasonable to consider mass-transport limitations or not in GDE; as tricky as it might be, this will maybe give some tip on the physical conditions in the active layer.

The impedance spectra measured in the case of the $\mathrm{Pt/VC}$ catalyst are presented in Figure III - 3 - 1. For the very low current density ($1\ \mathrm{mA} \Leftrightarrow 14\ \mathrm{mA\ cm_{geo}^{-2}}$), the spectra are well overlapping for all the electrodes, but starting at $10\ \mathrm{mA}$ ($\Leftrightarrow 140\ \mathrm{mA\ cm_{geo}^{-2}}$), difference starts to appear with, for one electrode, a decrease of the high frequency resistance. This also accompanies more important inductive phenomena at low frequencies (the frequency decreasing when reading the impedance spectrum from left to right). This phenomenon, often observed when performing low frequencies impedance spectra in GDE and DC systems, is attributed to water transport in a non-fully wet ionomer or intermediate adsorbed species relaxation [159,184,185].

---

[3] The assumption seems reasonable in this case, the studied active layers being very thin

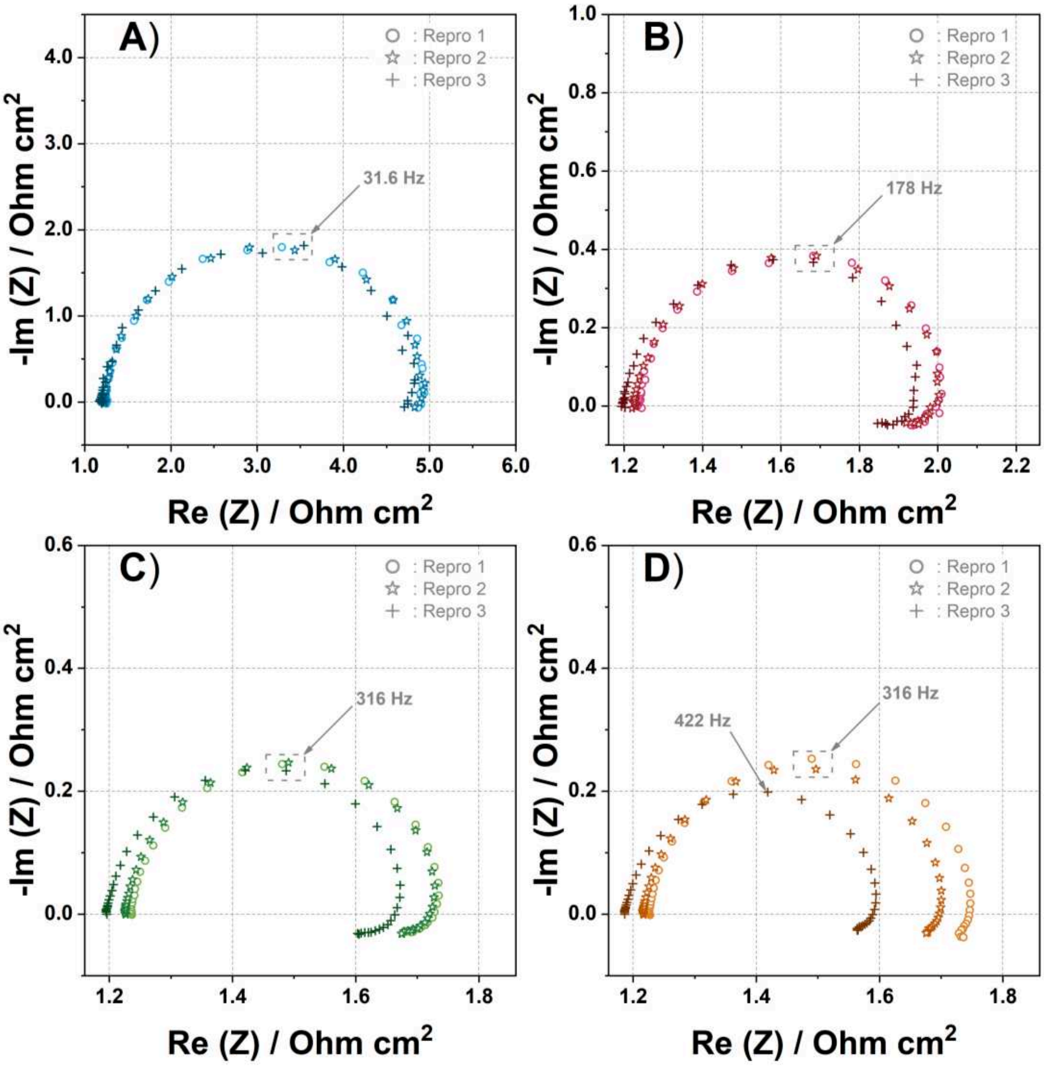

Figure III - 3 - 1: Galvanostatic electrochemical impedance spectra measured under an O_2 flow of 60 mL min^{-1} for all electrodes tested for the Pt/VC catalyst at ***A)*** *1 mA,* ***B)*** *10 mA,* ***C)*** *25 mA and* ***D)*** *50 mA. The symbols represent the different electrodes tested.*

The impedance spectra of the reproduction 1 of the experiment for this catalyst will be kept for further work, as it is overlapping with reproduction 2 almost until the highest current density tested. Figure III - 3 - 2 gathers the corresponding spectra as well as the fit realized using the model of Gaumont. For this simple catalyst on model active layers of $20\ \mu\mathrm{g_{Pt}cm_{geo}^{-2}}$, the fits are good, even if not taking the low-frequency inductive loop into account. However, it is clear by looking at the high frequency region (left-hand side on the graphs) that no obvious 45°-slopes are observed on the spectra. This is also verified with the extracted values of R_p, which do not have a huge weight on the fit aspect: $R_\mathrm{p} = 0.05 \pm 0.02\ \Omega\ \mathrm{cm_{geo}^2}$. An estimation of the proton resistance parameter is made, using the active layer thickness ($0.5\ \mu\mathrm{m}$), the conductivity of the ionomer (taken as $0.1\ \mathrm{S\ cm^{-1}}$) and the volumic ratio of ionomer in the electrode (between 0.4 and 0.64). This leads to a value of $ca.\ 0.3\ \mathrm{m\Omega\ cm_{geo}^2}$, two orders of magnitude lower than the value found using the fit. Moreover, this value of resistance would result of pure proton transport in ionomer, but in GDE, it is expected that water or electrolyte is present on top of the layer, increasing the conductivity in the active layer. The parameter extracted from the fit is therefore not impacting (shape of the spectra) and far from theoretical value. Also, no real observation of double semi-circles can be made on these impedance spectra, as diffusion of oxygen would have appeared as a low frequency loop in addition to the charge transfer loop, more likely for the diffusion of oxygen in liquid water formed or in ionomer.

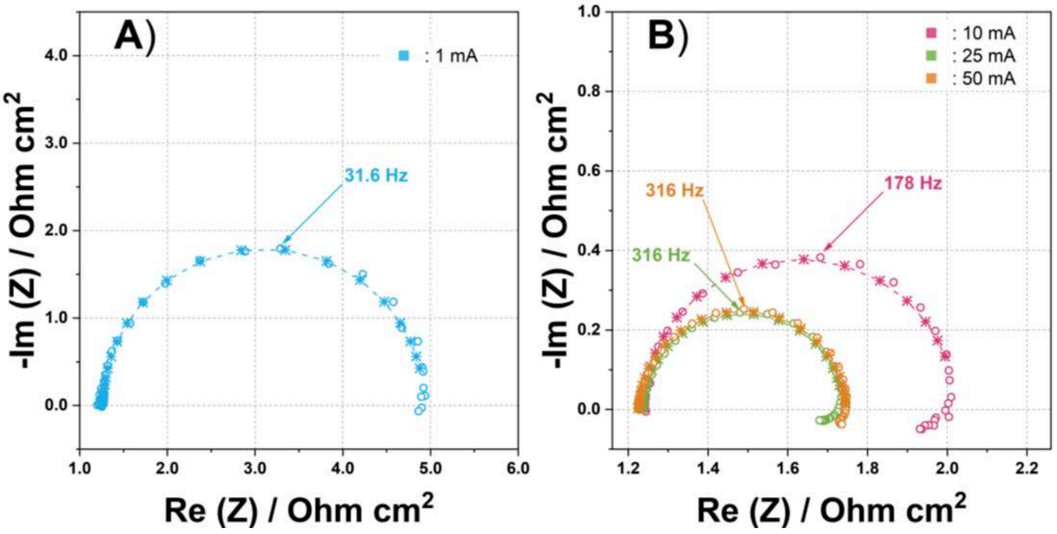

*Figure III - 3 - 2: Experimental and fitted impedance spectra for the Pt/VC reproduction 1 electrode at **A)** 1 mA and **B)** 10, 25 and 50 mA.*

This is rather confusing, as the difference observed between the GDE and DC polarization curves could suggest that mass-transport limitations happen in GDE. Moreover, if one takes a look at the apex frequency (frequency at the maximum of the semi-circle), it is similar for both the 25 and $50\ \text{mA}$ impedance spectra. As the apex frequency is the same and the double layer capacitance is not supposed to change with the current density, it leads to a similar charge transfer resistance: $R_{\text{ct}} = 0.49 \pm 0.02\ \Omega\ \text{cm}^2_{\text{geo}}$ and $R_{\text{ct}} = 0.46 \pm 0.06\ \Omega\ \text{cm}^2_{\text{geo}}$. This trend is not compatible with the imposed twice-higher current; a diminution of the charge transfer resistance would have been expected, instead, at least in the frame of a Butler-Volmer kinetics. It is still always possible that a concomitant increase of a diffusion resistance for the transport of oxygen would have compensated the decrease in charge transfer resistance, but in this case, it is not possible to validate this assumption either.

It is complicated to find a similar behaviour for all three tested electrodes of PtCo/VC. Indeed, as can be seen on Figure III - 3 - 3, other than the 1 mA spectra, they all differ, with their own specificity. However, the spectra still exhibit some interesting aspect such as the absence of 45°-slopes at high frequencies, attesting that, for this catalyst with this setup and at these current densities (from 14 to $700\ \text{mA}\ \text{cm}^2_{\text{geo}}$), no limitation by the transport of protons seems to happen; this observation is in adequation with the results for the Pt/VC GDE, that bares the same carbon support. Despite having similar apex frequencies, the 25 and 50 mA spectra do not overlap in this case, as shown on Figure III - 3 - 4. This raises the point of the selectivity of such observations: would it depend on the nature of the catalyst or the experimental conditions? This question remains open.

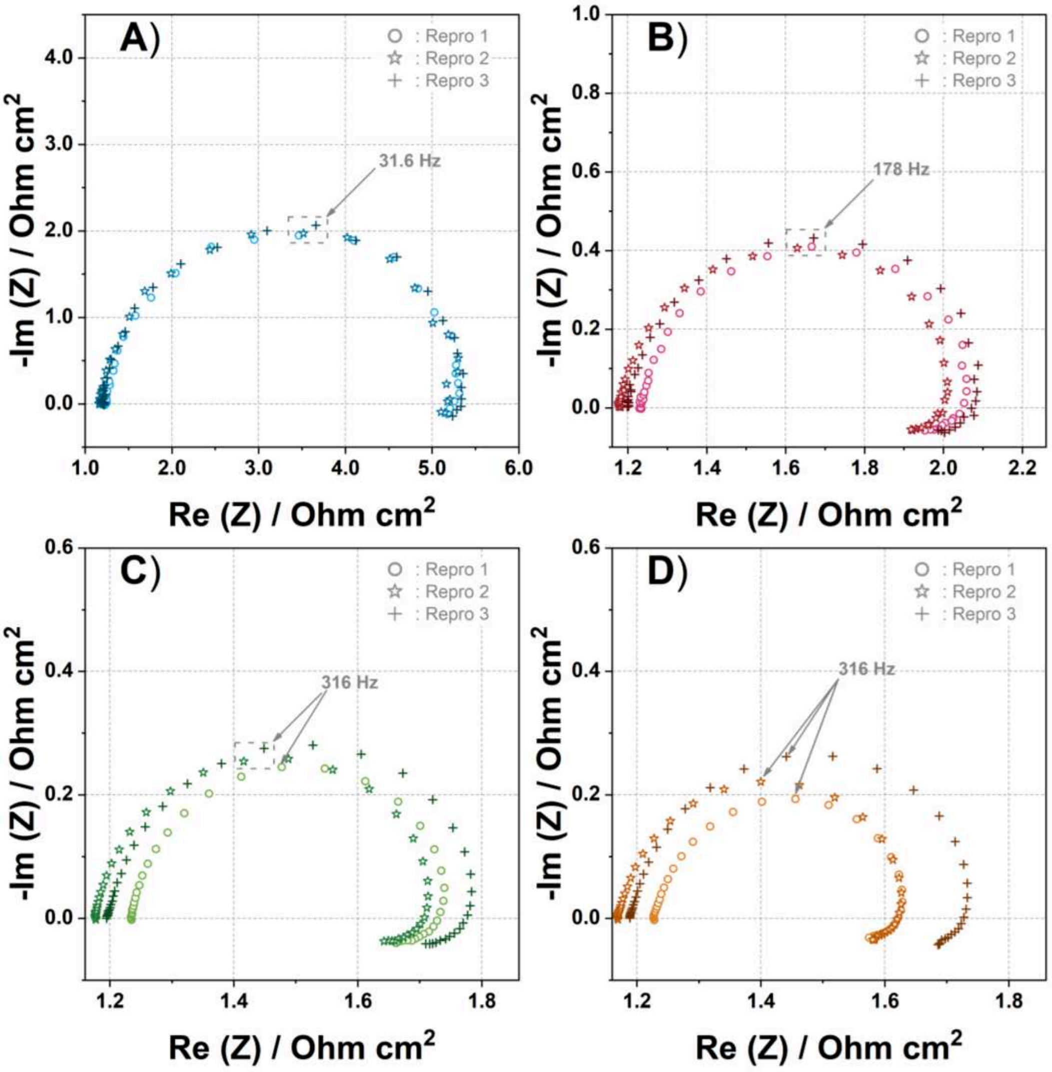

*Figure III - 3 - 3: Galvanostatic electrochemical impedance spectra measured under an O_2 flow of 60 mL min^{-1} for all electrodes tested for the PtCo/VC catalyst at **A)** 1 mA, **B)** 10 mA, **C)** 25 mA and **D)** 50 mA. The symbols represent the different electrodes tested.*

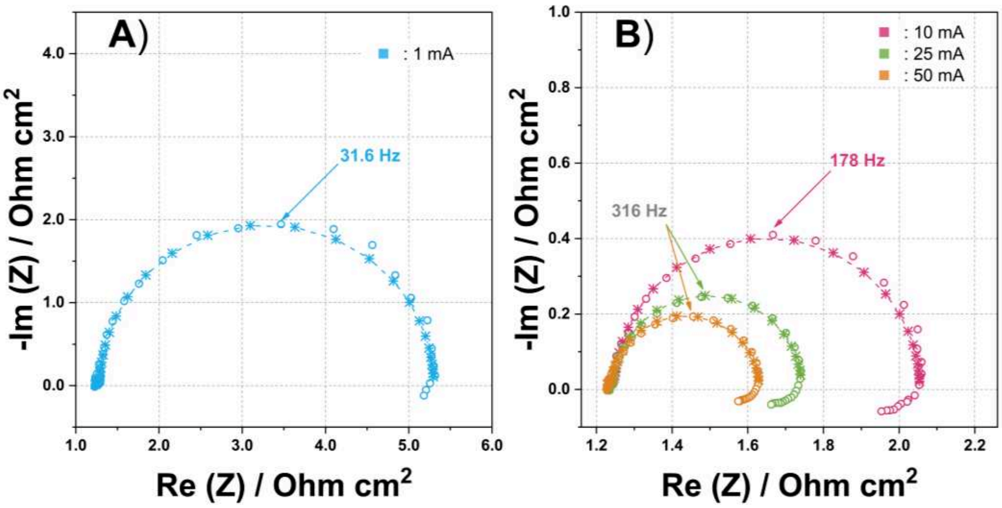

*Figure III - 3 - 4: Experimental and fitted impedance spectra for the PtCo/VC reproduction 1 electrode at **A)** 1 mA and **B)** 10, 25 and 50 mA.*

The more important discrepancies observed among the three catalysts during the reproducibility measurements go to the Pt/GC catalyst. In a very curious manner, this catalyst has a better polarization curves reproducibility than the Pt/VC catalyst, but the observed impedance spectra along this curve (that stopped with the $350\ \mathrm{mA\ cm^{2}_{geo}}$ spectrum), gathered in Figure III - 3 - 5, do present significant differences in this intermediate current density region. This can be explained as the polarization curves slope in this region varies a lot, with this strange shape observed on Figure III - 2 - 9. The few differences noted in this region imply changes in the polarization resistance, being the point at which the impedance goes at very low frequencies.

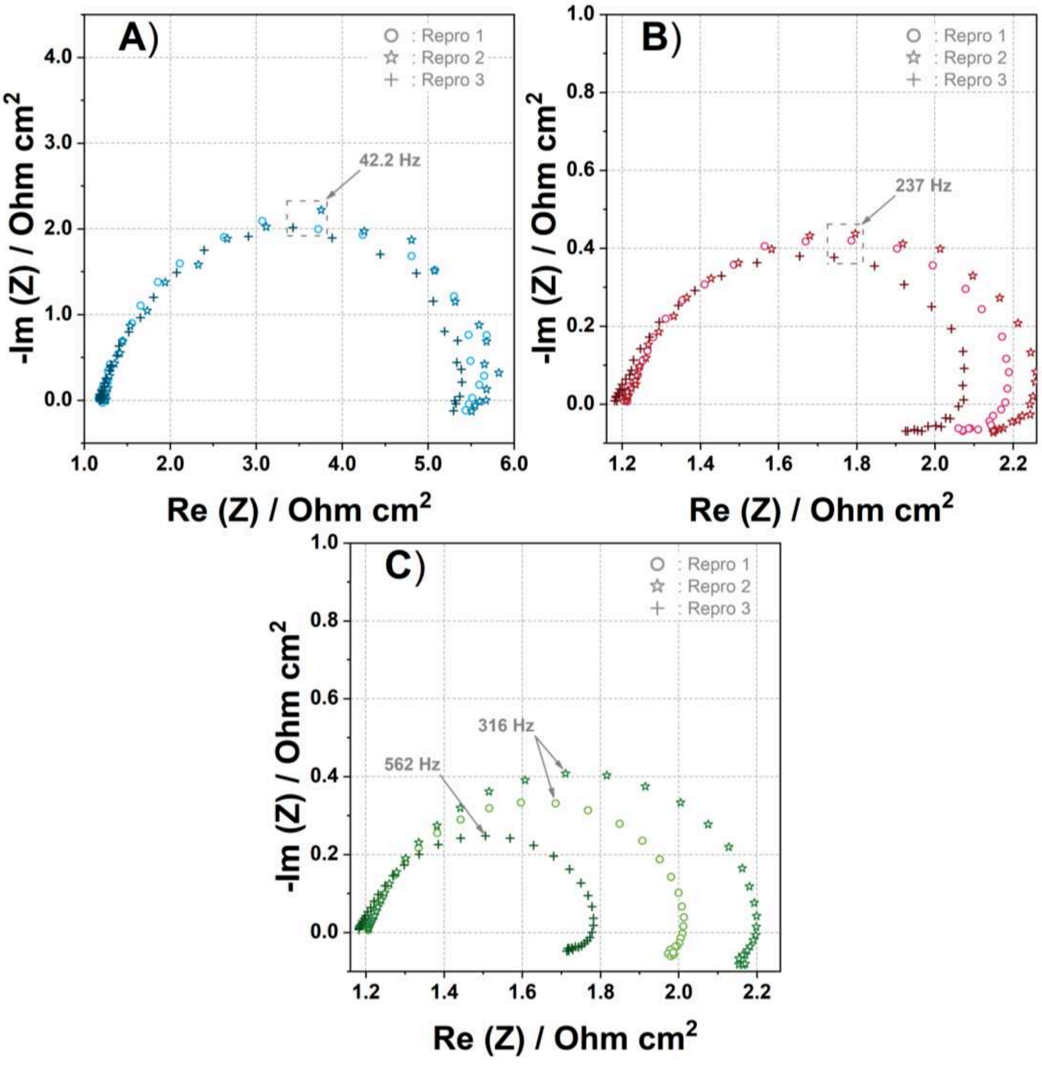

Figure III - 3 - 5: Galvanostatic electrochemical impedance spectra measured under an O_2 flow of 60 mL min^{-1} for all electrodes tested for the Pt/GC catalyst at ***A)*** *1 mA,* ***B)*** *10 mA and* ***C)*** *25 mA. The symbols represent the different electrodes tested.*

It was also really complicated to apply the model to this catalyst. In fact, the high frequency region does not present a 45°-slope, but a non-negligible slope, nevertheless. This could be the result of a non-ideal distribution of the double layer of the electrode, originating from heterogeneities in the plane of the electrode, of the ionomer dispersion for example, that lead to a constant phase element (CPE) behaviour (or to uneven catalyst layer thickness). This non-ideal behaviour was not tested, rather the protonic resistance and double layer capacitance were fixed and the charge transfer resistance was modified by hand to match as much as possible the aspect of the spectra. Another possibility would have been to consider the Pt/GC to have the same charge transfer resistance as the Pt/VC catalyst, both being monometallic platinum catalysts supported on carbon materials, and to vary the double layer capacitance and protonic resistance. The latter case was unsuccessful, so the first case was kept.

The classical fit for Pt/VC and PtCo/VC and the hand-adjustment made for Pt/GC resulted in the following and last results, presented on Figure III - 3 - 6. As previously mentioned, the simulated impedances of the Pt/GC are poorly valid in the high and mid frequency region, with a too big impact of the protonic resistance (imposed from the model) and a CPE-like behaviour of the experimental data. It is rather difficult to determine the absence or the presence of mass-transport limitations from these observations.

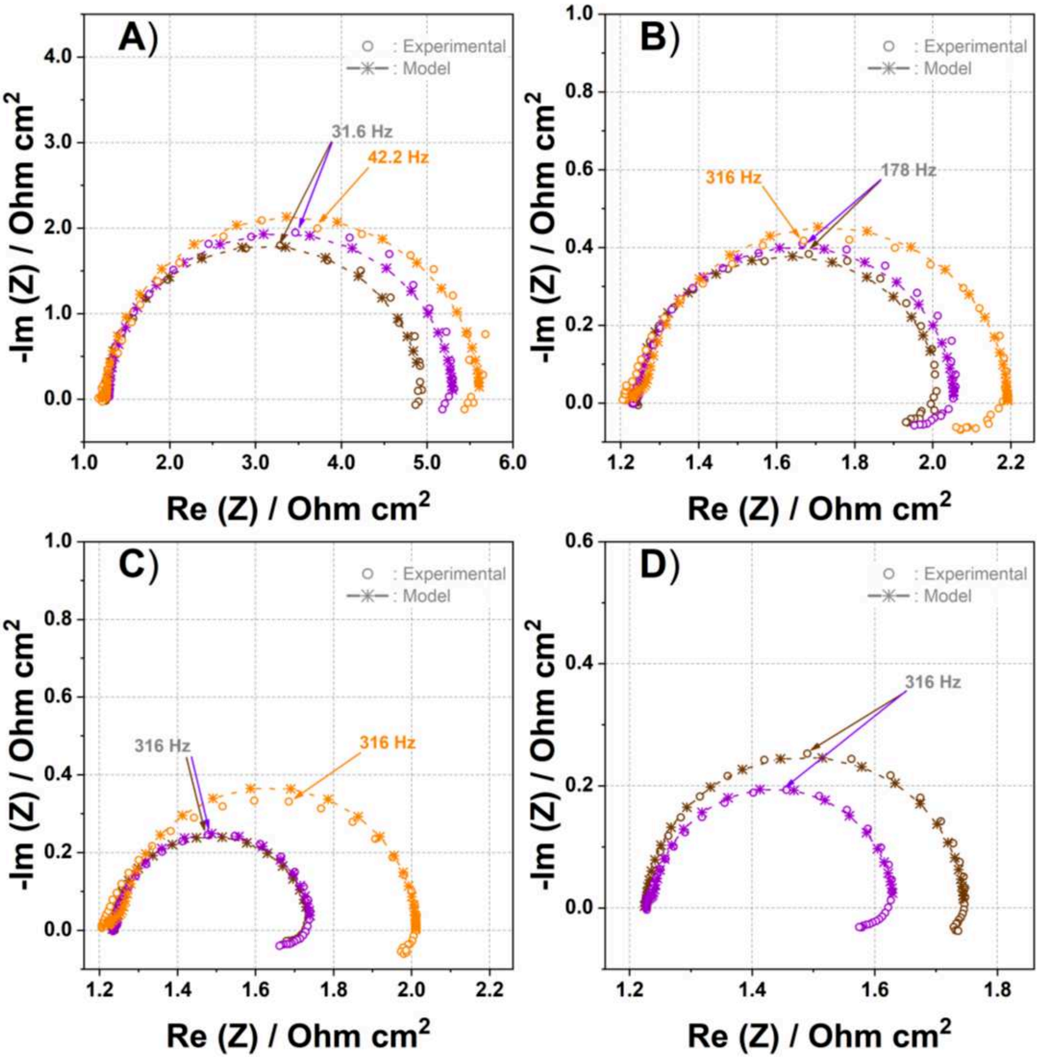

Figure III - 3 - 6: Galvanostatic electrochemical impedance spectra measured under an O_2 flow of 60 mL min^{-1} for all catalyst at A) 1 mA, B) 10 mA, C) 25 mA and D) 50 mA. The colours representing a catalyst with Pt/VC in brown, PtCo/VC in purple and Pt/GC in orange.

4. Discussion

This work aimed to compare three of the most used characterization setups of the literature: the rotating disk electrode (RDE), the gas diffusion electrode (GDE) and the differential cell (DC). The idea was to understand whether these systems all enable to access the intrinsic (ohmic-drop and mass-transport free) ORR activity of carbon-supported Pt-based catalyst. The considered electrolyte and cell environments, from fully liquid (RDE), to a liquid|gas interface (GDE) and finally to a fully-hydrated polymer|gas interface possibly in presence of liquid water (DC), lead to different mass-transport mechanisms for the protons, oxygen and water. Three commercial catalysts were compared, which are all very popular in the PEMFC community, and their activities are summarized in Table 3 for each experimental setup.

To perform the experiments, low-loaded electrodes were prepared ($20\ \mu g_{Pt} cm_{geo}^{-2}$) with the idea to minimize (or even suppress) as much as possible the mass-transport limitation in the thickness of the active layer; this should avoid any non-kinetics effect at the catalyst surface and facilitate the determination of the intrinsic activity of the materials studied for the ORR. An as similar as possible active layer production process was used for both the GDE and DC electrodes, to avoid any active layer effect and prevent experimental discrepancies not related to the catalyst itself: the same spray technique was used for the active layers' elaboration, with the same ink formulation recipe and protocol, to have the same particle dispersion and the most adapted process (catalyst coated backing for GDE and hot-transfer on membrane for DC). As for the distribution of the protonic conducting ionomer in the active layer, studies on the impact of the hot-transfer process might be achieved to better understand the changes in the active layer protonic resistivity. It was demonstrated in the lights of the experimental results that each setup comes with its own peculiarities (advantages and drawbacks), that will - in addition - depend on the nature of the catalysts investigated.

The hydrophobicity of the catalyst is an important parameter to be considered, as it strongly influences its interactions with the environment, in particular in presence of liquid electrolyte. This is mainly observed for the interaction of $\mathrm{Pt/GC}$ with the liquid electrolyte in RDE configuration: this renders the ECSA determination trickier for $\mathrm{Pt/GC}$ than for the two Vulcan XC72-supported catalysts (displaying different values for CO and $\mathrm{H_{upd}}$ ECSAs in RDE), because aggregates of $\mathrm{Pt/GC}$ + ionomer may be surrounded but not intruded by liquid water, leading to smaller than expected ECSA in liquid electrolyte (especially in RDE and to some extent GDE). The effect is also somewhat detrimental in DC, the geometric ORR current density being smaller than expected, owing to difficulties for $\mathrm{O_2}$ to reach the core of these aggregates, hence depreciating the measured mass activity.

Table III - 1: Recap chart of all mass (top of the cell) and specific (bottom of the cell) activities for each catalyst and each experimental setup on the whole range of studied potentials

MA (A mg^{-1}_{Pt}) SA (mA cm^{-2}_{Pt})	**Pt/VC - TEC10V50E**			**PtCo/VC - TEC36V52**			**Pt/GC - TEC10EA30E-HT**		
Potential	**RDE**	**GDE**	**DC**	**RDE**	**GDE**	**DC**	**RDE**	**GDE**	**DC**
0.95	0.034 ± 0.007 0.07 ± 0.01	0.030 ± 0.003 0.060 ± 0.005	0.009 ± 0.003 0.034 ± 0.011	0.036 ± 0.009 0.13 ± 0.03	0.058 ± 0.005 0.203 ± 0.013	0.036 ± 0.006 0.19 ± 0.04	0.010 ± 0.002 0.066 ± 0.009	0.018 ± 0.001 0.062 ± 0.001	0.006 ± 0.006 0.03 ± 0.03
0.9	0.20 ± 0.02 0.41 ± 0.04	0.186 ± 0.002 0.372 ± 0.006	0.057 ± 0.001 0.226 ± 0.004	0.19 ± 0.02 0.68 ± 0.06	0.36 ± 0.03 1.24 ± 0.09	0.26 ± 0.04 1.3 ± 0.2	0.059 ± 0.006 0.39 ± 0.08	0.098 ± 0.004 0.335 ± 0.009	0.043 ± 0.007 0.19 ± 0.03
0.85	0.7 ± 0.1 1.5 ± 0.3	0.73 ± 0.05 1.5 ± 0.1	0.62 ± 0.09 2.3 ± 0.3	0.65 ± 0.06 2.3 ± 0.2	1.4 ± 0.1 4.9 ± 0.4	1.8 ± 0.2 9.3 ± 1.6	0.22 ± 0.04 1.5 ± 0.5	0.33 ± 0.01 1.14 ± 0.03	0.42 ± 0.07 2.0 ± 0.3
0.8	X	2.0 ± 0.3 4.1 ± 0.5	2.1 ± 0.3 8.2 ± 0.9	X	3.7 ± 0.4 13.0 ± 1.4	5.5 ± 0.7 28.2 ± 4.7	X	0.84 ± 0.04 2.89 ± 0.07	1.5 ± 0.3 7.0 ± 1.1
0.7	X	7.7 ± 1.4 15.4 ± 2.9	11.2 ± 0.8 42.9 ± 3.1	X	12.7 ± 1.3 44 ± 5	18.1 ± 1.7 93 ± 13	X	3.0 ± 0.2 10.5 ± 0.2	8.4 ± 1.7 40.6 ± 8.4
0.6	X	16.4 ± 3.4 32.9 ± 7.3	28.1 ± 0.8 107.4 ± 5.8	X	25.2 ± 3.0 88 ± 12	33.2 ± 2.3 170 ± 20	X	6.6 ± 0.4 22.6 ± 0.6	23.8 ± 3.3 116 ± 28

The high gas flows used to remove traces of oxygen from the cathode side of the gas diffusion electrodes (GDE and DC), necessary to prevent any oxygen reduction current for a clean integration of the $\mathrm{H_{upd}}$ region, implies a thermodynamical displacement of the equilibrium potential of the HOR/HER (the activity of protons and hydrogen is not the same in the gas-ionomer phase than in liquid-electrolyte-ionomer phase), leading to higher hydrogen evolution reaction current at similar electrode potential ($vs.\,\mathrm{RHE}$) / cell voltage. The HER onset is around $130\ \mathrm{mV}\ vs.\,\mathrm{RHE}$ in GDE and DC, compared to $50\ \mathrm{mV}\ vs.\,\mathrm{RHE}$ in the case of the RDE. As a result of this, the CV to measure $\mathrm{H_{upd}}$ in GDE and DC must be plotted with a more positive value of the lower vertex potential than in RDE (otherwise, the CV is significantly biased by HER/HOR currents), which renders very questionable the ECSA determination (at the higher low-vertex potential in GDE and DC, one is not sure to complete the $\mathrm{H_{upd}}$ layer). So, the $\mathrm{H_{upd}}$ methodology may underestimate the ECSA measured in GDE and DC. CO-stripping gives a much more reproducible ECSA evaluation between RDE and GDE, but is usually awkward in DC (and was not performed here). In the end, it was chosen to evaluate the ECSA of the three catalysts by CO-stripping (RDE and GDE) and $\mathrm{H_{upd}}$ at $50\ \mathrm{mV\,s^{-1}}$ (DC), choices which are believed to be the "lesser incorrect" to establish a fair comparison of these materials in this study. Another possibility would have been to try to strongly reduce or even shut down the nitrogen flow before the experiment as it is made in some studies [120,122,186,187], which is supposed to enable better measurements of the ECSA using the $\mathrm{H_{upd}}$ in DC. However, due to the low cathode loadings, it is possible that traces of oxygen in the inlet pipes or dead volumes of the system would have impacted the small capacitive current that results from the $\mathrm{H_{upd}}$ adsorption/desorption on these very low-loaded Pt-based active layers (an issue which is usually not encountered in the literature, with active layers loaded above $100\ \mathrm{\mu g_{Pt}\ cm_{geo}^{-2}}$).

The current densities with respect to the geometric and specific surfaces were studied on the relevant range of potentials for the RDE, GDE and DC setups. These potential ranges where the measurements can be performed may vary from one setup to the other.

- RDE. The mass-transport kinetics of oxygen is much slower in liquid electrolyte, due to the small solubility and diffusivity of oxygen in liquids. This prevents any measurement of the ORR activity below $0.85\ \mathrm{V}\ vs.\,\mathrm{RHE}$ in RDE, because the current density is fully mass-transport limited and cannot be corrected using the Koutecky-Levich model (and any other model). So RDE measurements of the ORR activity are only viable in the range $0.85 - 0.95\ \mathrm{V}\ vs.\,\mathrm{RHE}$.
- GDE. Having $\mathrm{O_2}$ gas that can diffuse from the back side of the GDE (the front side being in contact with the liquid electrolyte) enables to promote much faster mass-transport in the GDE than in the RDE case. ORR kinetics can be more reliably measured in the full range of relevant potential of a PEMFC cathode: $0.6 - 0.95\ \mathrm{V}\ vs.\,\mathrm{RHE}$. However, flooding of the active layer might still occur, especially at large current densities.
- DC. The DC is hindered by the unavoidable $\mathrm{H_2}$ crossover, that results in smaller open circuit voltages than in the two previous setups and prevents reliable measurements of the ORR activities above $0.9\ \mathrm{V}\ vs.\,\mathrm{RHE}$. However, below this potential/cell voltage value, the mass-transport is faster than in the previous cases, leading to (usually) better

performance, especially at very high current densities/low cell voltage/cathode potential (typically below $0.7\ \mathrm{V}\ vs.\ \mathrm{RHE}$).

Following the work of Ly *et al.* [51], it was feared that the improvement factor observed in RDE for the $\mathrm{PtCo/VC}$ electrocatalyst ($ca.\ 1.5-2$ over the $\mathrm{Pt/VC}$ electrocatalyst) falls down to lower extent in GDE and especially in DC. However, the results presented here showed that even higher improvement factors are observed for the two latter experimental setups, respectively 3 and 4 in average on the potential range of the RDE. This shows that the disappointing results shown by Ly *et al.* (coming from many groups on the planet), *i.e*. PEMFC performance being largely lower than anticipated from the RDE predictions, are not explained by the fact the RDE measures an artificially high intrinsic activity that is not reproduced in PEMFC, but rather that the worse performances in PEMFC originate from electrode effects and not to intrinsic catalytic effects. Herein, by using on purpose very low-loaded Pt-based active layers, full hydration and high $\mathrm{O_2}$ stoichiometries in GDE and DC, the mass-transport issues that are usual in real PEMFC conditions (from $\mathrm{H^+}$ and/or $\mathrm{O_2}$ transport) are not so encountered, and the intrinsic activity of the catalysts can be measured appropriately. This was further investigated in GDE using electrochemical impedance spectroscopy on the studied low-loaded electrodes for all three catalysts, that were quite well reproduced using a simple transmission line model. No 45°-slopes were observed at high frequency regions, in adequation with the small thickness of the electrode, letting the author thinks that proton transport is not limiting. Concerning the transport of oxygen, as no real proof were possibly extracted neither to validate nor to invalidate mass-transport limitations, it can be imagined that a small fraction of the active layer might be flooded, with no clue to determine its volumic fraction. The reason why the GDE still fails to match the DC performance at very large current densities (potential below $0.7\ \mathrm{V}\ vs.\ \mathrm{RHE}$) can be attributed to the flooding generated by the production of water, due to the ORR, that cannot be counterbalanced by significant heating of the GDE|electrolyte interface; in a DC, heating is more likely at high current density, rendering the issue of water flooding less probable.

Anyhow, the GDE appears as a very good compromise between the RDE and the DC, enabling relevant intrinsic ORR kinetics measurements in a wide potential region ($0.7-0.95\ \mathrm{V}\ vs.\ \mathrm{RHE}$). Armed with this device, it was shown that catalysts that were postulated “good” in RDE at high potential/low current densities keep their promises in GDE and DC at lower potential/high current densities, leaving hope that, with proper PEMFC electrode engineering, advanced ORR catalysts will be successfully implemented in PEMFC cathodes.

5. Conclusion

This work compared the rotating disk electrode (RDE), the gas diffusion electrode (GDE) and the differential cell (DC) to measure the intrinsic (ohmic-drop and mass-transport free) ORR activity of popular carbon-supported Pt-based catalysts. The differences in specific and mass activities observed are related to the fundamental nature of each setup. On the one hand, the RDE enables high cleanliness in the measurements and operation with minimal amounts of catalyst material, but is very limited by mass-transport, leading to the possible determination of the intrinsic activities of the catalyst on a very narrow potential range, towards high electrode potentials/low current densities. On the other hand, GDE is less clean than RDE but much more than DC and is less limited by mass-transport than RDE, enabling the determination of ORR kinetics parameters down to lower potential values (higher current densities), which is more compatible with the range of interest for PEMFC operation (0.95 to $0.7\ \mathrm{V}\ vs.\mathrm{RHE}$). Though measurements are possible below $0.7\ \mathrm{V}\ vs.\mathrm{RHE}$, the device starts to be limited, likely by electrode flooding hence O_2 mass-transport, which questions the apparent surface/fraction of catalyst really accessed by O_2. For the DC, although it is limited by the hydrogen crossover and (possibly) short-circuit currents and suffers from a lower cleanliness, which render difficult ORR measurements at high potentials, it works in high stoichiometry conditions, the pressure can be regulated to have better water removal and is more adapted for low cell voltage operation; in practice, the DC enables satisfactory “kinetics” measurements in the range 0.85 to $0.6\,\mathrm{V}\ vs.\mathrm{RHE}$. So, all these systems have their own advantages and drawbacks and are very complementary if one wants to cartography the intrinsic ORR properties of a given catalyst.

Moreover, all devices enable a meaningful comparison of state-of-the-art carbon-supported Pt-based catalysts, and the study shows that the improvement factors observed in RDE are essentially maintained in GDE and DC, at least if the gas diffusion electrodes (catalyst layers) are prepared in the same way.

Finally, this study highlights the possibility to compare the results obtained in RDE to those obtained in GDE and DC, at least until $0.85\ \mathrm{V}\ vs.\mathrm{RHE}$ as lowest potential value, regardless of the nature of the catalyst considered (within the ones studied herein). The GDE appears as a nice intermediate tool between the RDE and DC, enabling high current density measurements with low platinum loadings and without requiring the use of important amounts of catalyst powder or of a complex and costly lab auxiliary as the one needed for DC tests. However, it remains to be confirmed whether carrying out measurements at higher temperature is possible, which is going on in the group of Arenz, with an improved design of their GDE setup [188]. The rise in pressure would prevent issues faced when working without membrane at higher temperatures. The DC is also a very useful tool to investigate more in detail all the issues related to the integration of complex catalysts, such as the ink formulation and its effect on the electrode performance; it is therefore a nice complement to the RDE and GDE to tailor active layers/electrodes for practical applications.

Chapter IV

Degradation study of Pt_3Co catalytic layer in 25 cm² PEMFC setup

A segmented cell and material study

Chapter IV. Degradation of Pt_3Co catalytic layers in 25 cm² Proton Exchange Membrane Fuel Cell setup – A segmented cell and material study

Pt_3Co on Vulcan carbon (VC) has been demonstrated in the previous chapter to be the best oxygen reduction reaction (ORR) catalyst among the tested ones. This result was expected in the rotating disk electrode (RDE) configuration (the literature made this predictable), and was confirmed in the gas diffusion electrode (GDE) and the differential cell (DC) setups, in conditions where the mass-transport limitation is much less an issue. This means that the intrinsic activity of Pt_3Co/VC is way superior to those of Pt/VC and Pt/GC (graphitized carbon) in conditions close to those of the cathode in real proton exchange membrane fuel cell (PEMFC) operation. The next step in the study of a catalyst is the integration in bigger PEMFC single cell cathode, to test corresponding membrane electrodes assemblies (MEA) under more realistic fluidic, thermal and hygrometric conditions, and in particular to assess whether the good ORR activity maintains in the long-term. To that goal, this chapter focuses on the study of Pt_3Co/VC stability in "technical cell"; different accelerated stress tests (AST) have been tested following the protocols established by the US DoE, which are schematized on Figure IV - 1 - 1.

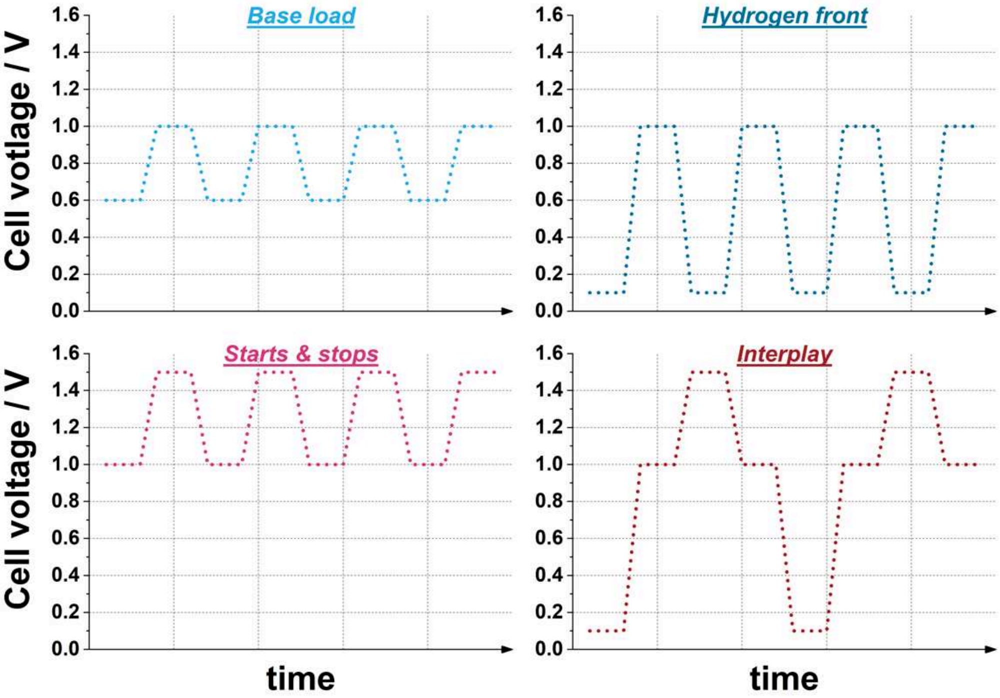

Figure IV - 1 - 1: Representative schematics of accelerated stress tests applied in this study. Left-hand side are protocols developed by the US DoE, right-hand side graphs are additional protocols used.

These protocols, consisting of small steps of $t = 3$ s resting time at different cell voltage, are performed under an inert H_2/N_2 atmosphere at 80°C and almost 100% RH. The *Base-Load* protocol represents the natural variations of the cell voltage in the working range of a PEMFC, between 0.6 and $1\ \mathrm{V}$, and aims to accelerate the degradation that may happen during most of the working time of the cell. The *Starts & Stops* sequence, between 1 and $1.5\ \mathrm{V}$, highlights the occurrence of high cell voltage when a hydrogen front forms at the anode during the system start-ups and shutdowns [113,189–191]. On another view angle, if hydrogen is not purged at the anode (to prevent the creation of the front, hence mitigate start-up/shutdown issues), but rather let inside the anode, it will homogeneously diffuse from the anode side to the cathode side, leading to a temporary decrease of the cathode catalyst layer potential (to *ca.* $0.1\ \mathrm{V}$); the *Hydrogen front* sequence (between 0.1 and $1\ \mathrm{V}$) is used to simulate this phenomenon. The final protocol studied is a mix of these different protocols, to have an overview of the aging when every possible mechanism is considered. This latter protocol is called *Interplay*; its potential sequence (between $0.1,\ 1, 1.5$ and then $1\ \mathrm{V}$) is believed to represent the interactions of the different phenomena most likely to happen in the real life of a cell.

1. Physicochemical characterizations of the as-prepared electrodes

The Pt_3Co/VC catalyst has been integrated into several MEAs with different cathode catalyst loadings (Table IV - 1**)**. All these MEAs were characterized at the beginning of test and after $30{,}000$ cycles for the *base-load*, the *starts & stops* and the *hydrogen front* and $15{,}000$ cycles for the *interplay*, leading to $60{,}000$ voltage steps experienced by the MEAs for all the protocols.

Table IV - 1: Summary of the cathode platinum loading and accelerated stress test protocols used for each electrode.

MEA name	Cathode catalyst layer loading ($\mathrm{mg_{Pt}\ cm_{geo}^{-2}}$)	AST protocol
SYM364A	0.57	*Base-load*
SYM365A	0.51	*Base-load*
SYM373A	0.34	*Base-load*
SYM374A	0.43	*Base-load*
SYM374B	0.43	*Hydrogen front*
SYM375A	0.42	*Starts & stops*
SYM375B	0.42	*Interplay*

Cathodes with similar catalyst loading are used to study the influence of the different accelerated stress test protocols (SYM374A, SYM374B, SYM375A and SYM375B); the impact of different cathode catalyst layer loading is analysed using the *base-load* protocol (SYM364A, SYM365A, SYM373A and SYM374A).

To perform this study, electrochemical methods are coupled with physicochemical analyses to access the catalyst material properties at the beginning of test and end of test (BoT and EoT, respectively). As some of these techniques are destructive (scanning electron microscopy, SEM, transmission electron microscopy, TEM and Raman are used here), they are applied on reference MEAs, named SYMX-C, which were prepared at the same time as the tested SYMX-A or SYMX-B electrodes (similar batches). These non-tested MEAs are assumed to have the same initial state as their tested homologues.

a) Observation using electronic microscopy

Electronic microscopy is performed to have structural and visual observations of the different reference MEAs, that have not been assembled nor tested electrochemically. On the one hand, scanning electron microscopy is used to have access to "microscopic features", like the catalyst layer (CL) thickness evolution and possible cracks or platinum bands formation in the membrane. Transmission electron microscopy, on the other hand, is used to analyse the "nanoscopic feature" of the catalyst; particle size distribution (PSD) of the pristine and aged catalysts, as well as the nanoparticles shape/extent of agglomeration, to better understand the aging mechanisms at stake.

i. Scanning electron microscopy

SEM pictures were acquired in backscattered electron (BSE) detector mode; this mode enables Z contrast, leading to better visualization of the cathode catalyst layer|membrane and cathode catalyst layer|epoxy resin interfaces, hence the reliable measurement of the cathode catalyst layer thickness (and membrane and anode thicknesses) in post-treatment after imaging. Figure IV - 1 - 2 displays representative SEM images of the reference MEAs used for the active layer thickness measurement. No particular defect has been found on these reference MEAs during the SEM observations, by wandering along the $1-1.5$ centimetre-long sample in each case. This still only gives really local information on the deposition process. From these images, the cathode catalyst layer thickness was measured (see Scanning Electron Microscopy (SEM) in chapter II for details on the measurements); its evolution with the estimated catalyst loading is drawn on Figure IV - 1 - 3.

The catalyst layer thicknesses correlate rather well to the cathode platinum loadings for the reference MEAs, leading to a regression coefficient $R^2 = 0.9947$. The linear coefficient found to relate both measures is consistent with previous findings on catalyst layers made with Vulcan carbon-supported nanoparticles, leading to either $0.5\ \mu\mathrm{m}$ for $20\ \mu\mathrm{g_{Pt}\ cm_{geo}^{-2}}$ found in the GDE study (chapter III, Physicochemical properties of the three ORR catalysts) and $ca.\,10\ \mu\mathrm{m}$ for electrodes studied in the literature at similar loadings $(0.4\ \mu\mathrm{g_{Pt}cm_{geo}^{-2}})$ [92,119,192]. An observation that can be made, however, is the increasing error made when increasing the cathode catalyst loading using this average pixel surfacing on ImageJ. To the author belief, it can be attributed either to heterogeneities in the spray deposition process or in the position of the catalyst coated membrane (CCM) while taking the SEM images: if the

CCM is slightly curved, this will lead in a non-perpendicular cross-sectional view of the active layer, increasing visually its thickness.

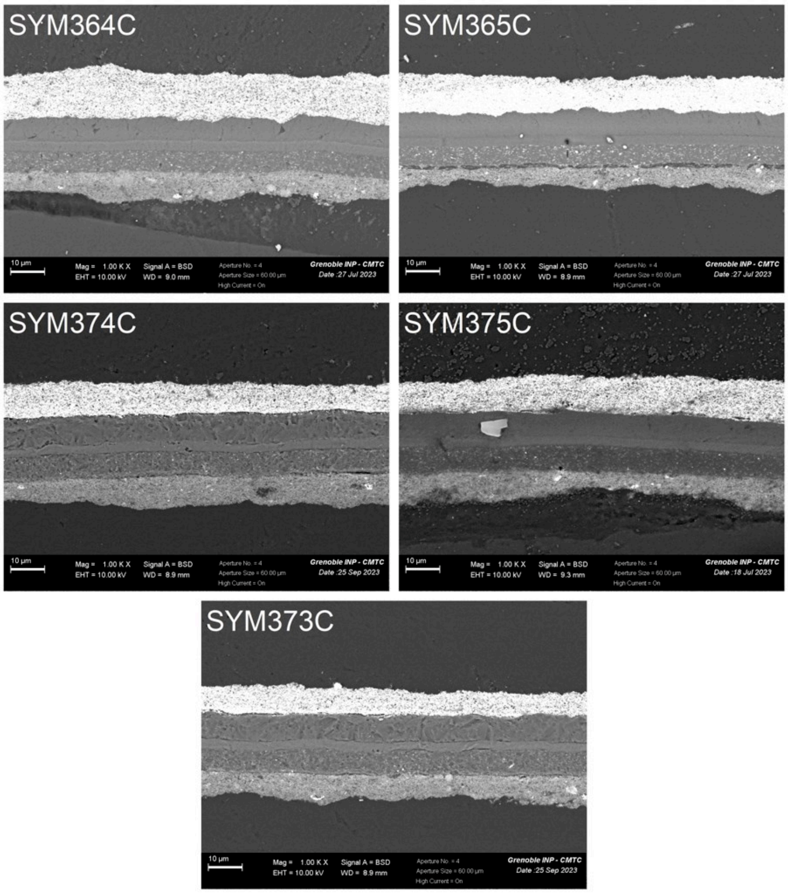

Figure IV - 1 - 2: SEM images of the Pt_3Co reference MEAs of the different batch used in the voltage cycling degradation study.

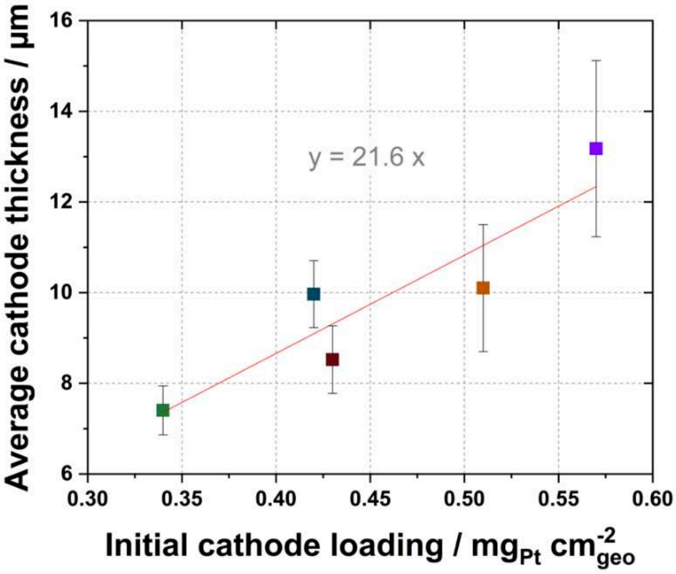

Figure IV - 1 - 3: Evolution of the cathode catalyst layer thickness of the reference MEAs as a function of the estimated cathode platinum loading.

ii. Transmission electron microscopy

After the microscopic scale observed using SEM imaging, the nanoscale is investigated to determine the PSDs of the catalyst powder and pristine sprayed catalyst layer. The TEM grid was prepared using the SYM374C electrode, for which it is believed that the catalyst particles size, shape and repartition on the carbon support are fully representative of any pristine catalyst layers, independently on the electrode batch and on the catalyst layer loadings; indeed, the ink formulation, deposition, drying and MEA processing were always kept identical for all the MEAs tested. Figure IV - 1 - 4 presents the PSD histograms as well as the corresponding TEM micrographs of the Pt_3Co/VC catalyst, in its powder state and after creation of a cathode catalyst layer on a MEA; the latter data gives an idea of the aspect of the catalyst before any degradation happens upon electrochemical operation of the MEAs. It nevertheless seems, from these PSDs and TEM micrographs, that already after the spray deposition of the active layers, there is a visible impact of the preparation method on the size and repartition of the alloyed catalyst nanoparticles. This can be explained, and has been previously observed in the literature, by leaching of Co atoms at the surface of the particles during the ink formulation and spray, as it was the case for Ni atoms [41,193]. This further confirms that simple catalytic ink formulation, storing and handling is enough to already (minorly) affect the texture and (for Pt-Co alloys) composition of the Pt-Co/C nanoparticles [194]. This can explain the slight negative shift and narrowing of the catalyst particle size distribution. Other than that, it seems the particles are, in both cases, well dispersed and not much agglomerated at the surface of the carbon support.

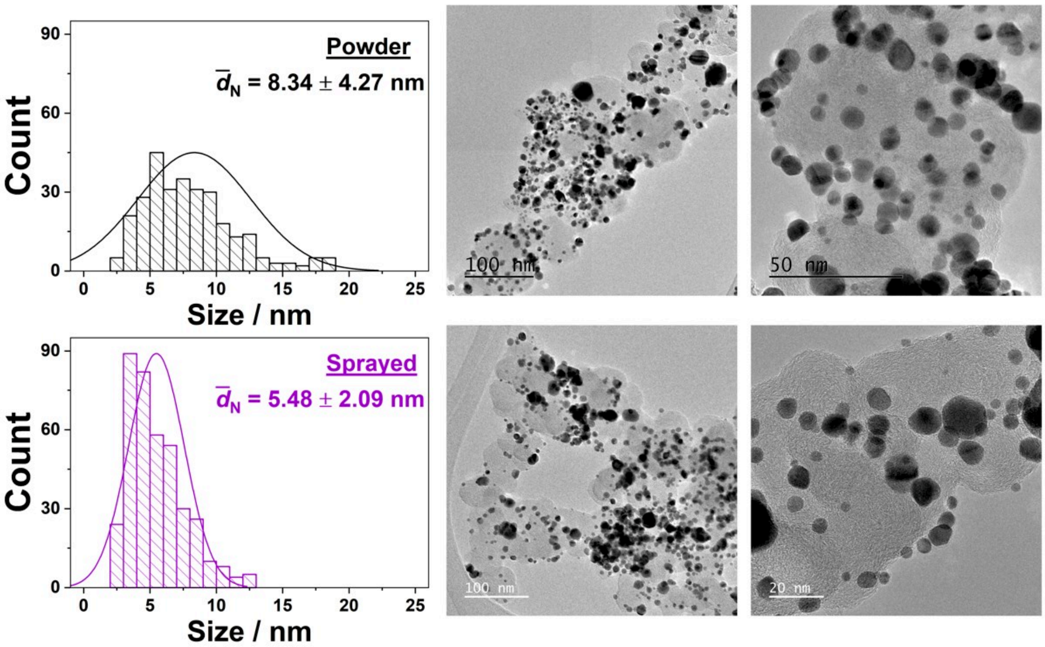

Figure IV - 1 - 4: Particles size distribution and TEM pictures of the PtCo/VC powder (top) and reference MEA (bottom)

To be more specific on the possible chemical composition changes, the $\frac{\%\text{at Pt}}{\%\text{at Pt}+\%\text{at Co}}$ ratio obtained from X-ray energy dispersive spectroscopy (X-EDS) performed during the TEM analysis is $73 \pm 1\%$ of platinum atoms for the sprayed catalyst in the pristine MEA, a value that is very close to the 75% expected for a non-leached Pt_3Co catalyst (which was found for the initial powder using inductively coupled plasma-mass spectrometer, ICP-MS). This is then rather intriguing at first sight, as it would mean that the nanoparticles mean size decreased but without leaching of Co atoms, which was supposed to happen during the ink formulation process. However, one must keep in mind that X-EDS is a global chemical analysis, sensitive to both alloyed Co (metallic state in the Pt-Co nanoparticles) and to Co^{x+} ions or oxides that could be present and adsorbed on the Vulcan XC72 carbon surface or dissolved in the ionomer after leaching in the (Nafion®-containing, hence acidic) ink. Here, it is likely that all Co metal, Co^{x+} ions and oxides were kept in the volume of the cathode active layer (which had not been operated), explaining this absence of decrease of the overall Co-content in the cathode; this does not mean that the Co metal fraction in the Pt-Co/C nanoparticles has not changed upon MEA elaboration. Dubau *et al.* noted similar bias with X-EDS measurements of new/used Pt-Co-based MEAs [100,195]. In any case, it is wise to add that if Co dissolution happens in the ink and MEA elaboration, this shall be restricted to the very surface of the nanoparticles, hence making potential changes of the bulk Pt:Co ratio small for the sprayed nanoparticles versus their initial (powder) state.

b) X-Ray Diffraction footprint of the reference MEAs

The X-Ray diffraction (XRD) technique is applied to the reference MEAs and on the catalyst powder to determine: (i) the peaks position, characteristic of the lattice parameter, which can be used to determine the atomic fraction of Co in the lattice of platinum and (ii) the crystallite size of the Pt_3Co alloy, using the Scherrer law [140]. If any change of the alloy composition occurs, the position of the peak observed on the XRD spectra will be modified following the Bragg's relation:

$$\lambda = 2d_{\mathrm{hkl}}\sin\theta \qquad \text{(Eq. IV.1.1)}$$

As λ, the wavelength of the incident photons, is a constant, if the composition of the alloy changes, the lattice parameter (a linear combination depending on the atomic fraction of each element and their respective lattice parameter, as told by the Vegard's law) will either increase (due to a loss of Co and a return towards a full platinum matrix) or decrease (if more alloying element – Co - is added into the alloying matrix). The interplanar distance will then increase, leading to smaller angles ($\sin(\theta)$ increasing monotonically with θ in the range $[0, \frac{\pi}{2}]$) for the diffraction peaks. On Figure IV - 1 - 5 the diffraction diagrams of the reference MEAs match almost perfectly the one of the Pt_3Co powder. The crystallite size extracted using the Scherrer formula and fit on the (220) peak (as defined in chapter II, X-ray diffraction (XRD))gives homogeneous values of $ca.$ 13 nm. This confirms the near-absence of variation of the Pt:Co ratio determined by TEM X-EDS presented before. Combining the TEM X-EDS and

XRD data, one can conclude that the initial state of the MEAs used in this study is still very close to the initial Pt_3Co alloy; the ink formulation and spray deposition affect to a minor extent the chemistry of the Pt-Co nanoparticles.

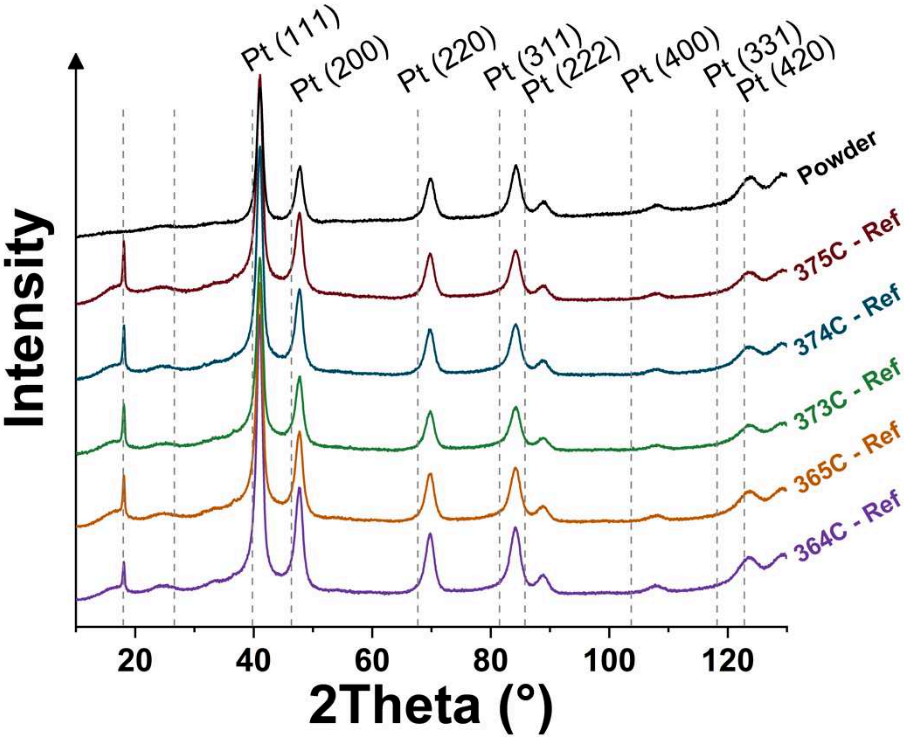

Figure IV - 1 - 5: X-ray diffraction diagrams of the catalyst pristine powder and of the different reference MEAs

c) Raman spectroscopy of the reference cathode catalyst layers

Considering the carbon support is the same for all the cathodes studied in this chapter, only one pristine (not tested) cathode (SYM373-C) among the reference MEAs has been analysed in Raman spectroscopy. The sample was prepared as detailed in chapter II – Experimental Section. The intensity of the whole spectrum is normalised by the maximal intensity of the G-D_2 convoluted band and is taken in this very case at the $1605\,\mathrm{cm}^{-1}$ wave number (corresponding, if alone, to the D_2 band). This spectrum of the outer layer of the active layer, proposed on Figure IV - 1 - 6, will be the reference with all the other spectra coming from the aged electrodes. It is mainly disordered with very little graphite vibrational mode, as can be seen with the absence of a thin peak at $1580 - 1585\ \mathrm{cm}^{-1}$: instead, it is fused into one large band with the D_2 disordered peak. This means that the carbon black (Vulcan XC72) is not graphitized, as expected [59,194], hereby confirming the previous XRD observations.

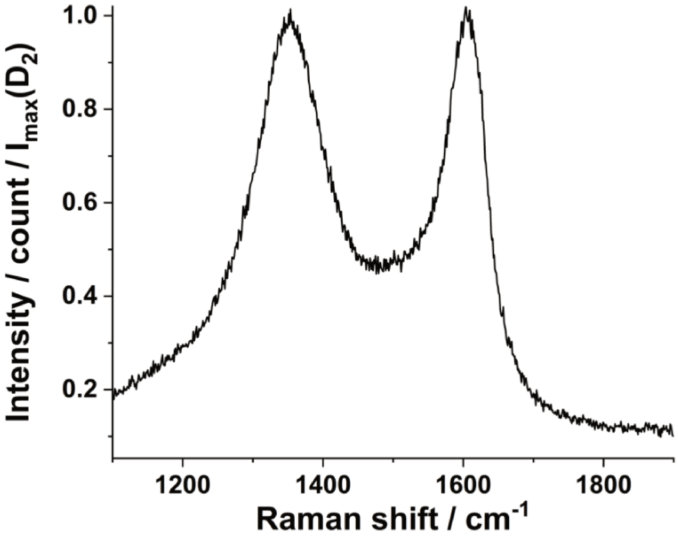

Figure IV - 1 - 6: Raman spectrum of the cathode catalyst layer of SYM373-C

2. Comparison of the electrochemical behaviour of the tested MEAs before and after their respective ASTs

In this study, performed at LEMTA in Nancy, the protocol has been designed to be really simple and straightforward to implement: it follows the sequence presented in Figure IV - 2 - 1. This protocol starts by in-house conditioning, beginning of test performance determination and characterizations under H_2/N_2, these three steps being the initial characterizations. Then, the chosen AST is implemented (*cf*. Figure IV - 1 - 1). After it, the conditioning is done again before end of test performance and characterizations (exactly the same methodologies and procedures than the initial characterizations). The entirety of the performance and characterizations are done under hydrogen, air and nitrogen flows with 50% relative humidity, the accelerated stress test being the only step performed at $100\%\ \mathrm{RH}$. The in-house conditioning is using humidity cycling to activate the active layer, by alternating the cell voltage between $0.6\ \mathrm{V}$, OCV and $0.3\ \mathrm{V}$ with respectively steps of 45, 30 and $60\ \mathrm{s}$ to have different current densities and thus a succession of drying, normal and wet conditions.

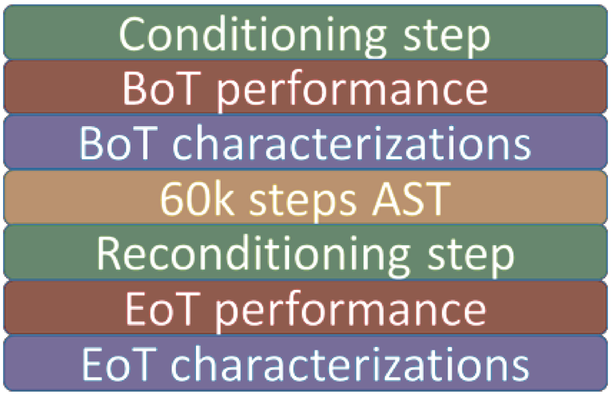

Figure IV - 2 - 1: Testing sequence of the AST degradation study on Pt_3Co MEAs cathode

It was not possible to perform measurements under oxygen, so in the rest of this Pt_3Co/VC degradation study, the only oxidant gas used will be air for the performance measurements. The hardware used here was a segmented cell of $25\ \mathrm{cm}^2$ with the cathode current collecting plate being split in 20 segments, the anode being non-segmented. Segment n°1 is located at the air/nitrogen inlet (on top of the anode hydrogen outlet) and the segment n°20 is located at the air/nitrogen outlet (on top of the anode hydrogen inlet) and the position of the different segments is described more on Figure II - 2 - 1.

a) Determination of the well-being of the tested electrodes using the conditioning step

All the MEAs chosen for the study (summarized in Table IV - 1) are firstly subjected to the conditioning step, as detailed in the previous sections. The duration of the conditioning step is $ca.\,2\ \mathrm{hours}$ and the last step is taken to analyse the maximum current density that can produce the MEAs. Once the AST is finished, the MEA conditioning is done another time, to reach steady state performance and similar conditions / environment for all the electrodes after their respective aging procedure. This repeated conditioning step is mandatory, owing to the different aging sequences applied: without re-conditioning, this might have led to different electrode, catalyst or membrane states, that could have affected the end of test measurements. The performance of the final step at 0.3 V for two examples of electrodes before and after their aging procedure are presented in Figure IV - 2 - 2. The performances are given following a colour bar to visually highlight the difference between BoT and EoT. The bars have the same ordinate scales and the greater bars stand for the BoT, while the smaller ones stand for the EoT post conditioning $0.3\ \mathrm{V}$ step.

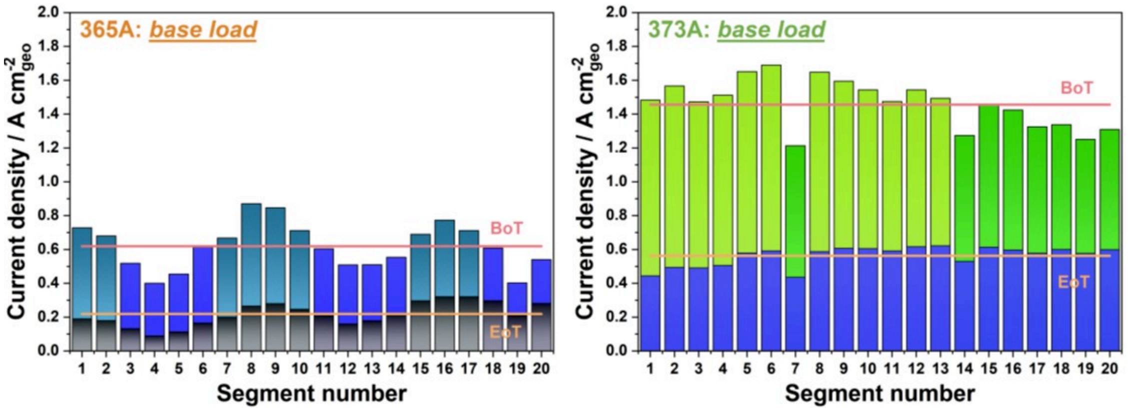

Figure IV - 2 - 2: H_2/air performance at the last 0.3 V step of the conditioning before and after the base-load AST for SYM365A (left) and SYM373A (right) MEAs. The geometric current is measured on a 20th of the total MEA surface to give the geometric current density on a given segment. Top line is the overall BoT current measured while bottom line is the overall EoT current. The colour scale is a tool to appreciate visually the possible heterogeneity.

As can be seen on this figure, a very useful property of the segmented cell is that it can give access to local MEA performance. A first observation is that, despite MEA SYM365A has higher cathode catalyst loading ($0.51\ \mu g_{Pt}\ cm_{geo}^{-2}$) than SYM373A ($0.34\ \mu g_{Pt}\ cm_{geo}^{-2}$), they exhibit very different overall performance from each other, as depicted by the horizontal lines (the top one being the BoT, the bottom the EoT). Moreover, SYM365A has locally very reduced performance compared to SYM373A and much more heterogeneous performance: half of the segments work significantly less than the other half, already at beginning of test. One should note that all MEAs are positioned on the same side (here, the right of the MEA when looking at it from top with air inlet on the left and hydrogen inlet on the right). Furthermore, the maximum performance of the 20 segments for MEA SYM365A at BoT do not even reach $1\ A\ cm_{geo}^{-2}$, which is roughly a half of these for SYM373A, which denotes that the SYM365A MEA suffers severe initial performance issues. However, SEM and TEM imaging as well as XRD did not reveal any major issue on the SYM365C reference MEA. So, it was decided that this MEA will not be further investigated.

The other MEAs were not suffering this bias; Figure IV - 2 - 3 gathers all the end of conditioning data for all further studied MEAs. Horizontal lines on this graph represent the mean current value of the MEAs measured in BoT (top line) and EoT (bottom line). This mean value indicates that the initial performance of SYM374A and SYM374B are very similar and, decreasing the platinum loading of the cathode (SYM373A) leads to slightly smaller performance. Concerning the SYM375 batch, the platinum loading is supposed to be similar but the initial performance is 20% lower than expected. Furthermore, if the platinum loading is increased, the performance was supposed to increase as well, but this was not found for SYM364A, which have also 20% lower performance. These differences will try to be delt with in the following.

A feature which is visible on several MEAs (SYM373A, SYM374B, SYM375A and SYM375B) must be explained. The segment n°7 (as well as segment n°14 but to a smaller extent) on these MEAs has always lower performance. This is not related to the active layer behaviour (for example resulting from local damage created during the hot-pressing step[4]), but it is rather related to the contact with the current collector of the segmented plate. Indeed, for these two segments, the resistance of the connection between the gas diffusion layer (GDL), the flow field and current collector to the acquisition board is bigger, which implies higher ohmic drop and lower performance locally. This was further demonstrated by testing a MEA flipped from 180° in plane, to compare the initial performance and the performance after the rotation. Due to the geometry of the segmented cell, by doing so, the area under segment n°7 goes under segment n°14 (and inversely), but this will still work as segment n°14 (and the mirror situation for segment n°14 that is now n°7) has not similar resistance/performance decrease. This shows that the local performance stayed the same despite the flip of the MEA, attesting the hardware issue more than a defect on the MEA.

---

[4] Once the hot-pressing step has been done, all the MEAs were marked to position them in the same orientation they were during the hot-pressing.

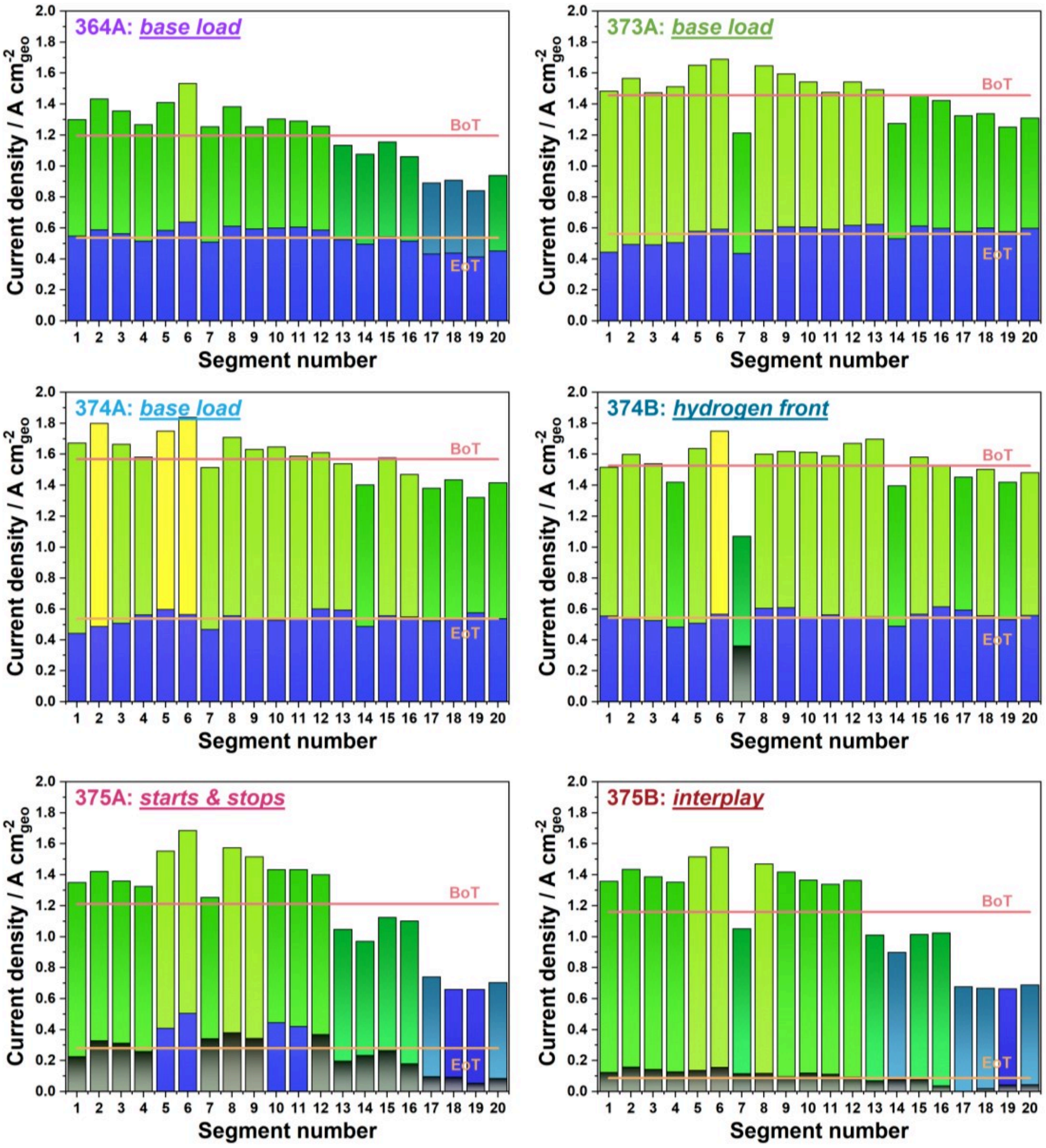

Figure IV - 2 - 3: H_2/air performance at the last 0.3 V step of the conditioning before and after the base-load AST for all tested MEAs. The name of the MEA and the AST underwent are specified on each bar graphs. Top line is the overall BoT current measured while bottom line is the overall EoT current. The colour scale is a tool to appreciate visually the possible heterogeneity.

This bias being explained, on a more general point of view, it appears that in these conditions (atmospheric outlet pressure, stoichiometric coefficients of 1.5/3 on the hydrogen and air sides respectively), the BoT performance are rather uniform from the inlet to the outlet of the cell, except for SYM375A and SYM375B, that exhibit lower current densities for the air outlet segments row. This is not related to any lack or heterogeneity of the active materials at the surface of the MEA, detailed measurements of the local electrochemically active surface area (ECSA) being presented in Figure A - 1 in the Annexes. For some reasons, still unknown, mass-transport issues happened at the end of the air channels, maybe water flooding, but the current density repartition was not homogeneous at the beginning of the conditioning either. The behaviour of both SYM375A and SYM375B does not seem to be related to the cathode catalyst loading, as they have the same loading as SYM374A and SYM374B. Additionally, it would be awkward to attribute that difference to the hot-pressing process, as it was kept similar for all the electrode batches.

If one now takes a proper look at the EoT re-conditioning performance, some points can be outlined. Firstly, after $30\mathrm{k}$ cycles of the different aging test, all the MEAs have been quite a lot affected by their respective AST, leading to maximum EoT performance of $0.6\ \mathrm{A\ cm_{geo}^{-2}}$ and a $ca.\ 50\%$ loss of geometric current density. Secondly, *base-load* and *hydrogen front* AST seem to have a similar impact on the performance loss experienced by the MEA, as attested by the SYM374A and SYM374B MEAs; in addition, these ASTs lead to more homogeneous performance at EoT than it was at BoT. Thirdly, $30\mathrm{k}$ cycles of the *starts & stops* and *interplay* protocols have a disastrous impact on the performance of the tested MEAs. In order to analyse the impact of the ASTs, the different losses of the MEAs are gathered in Figure IV - 2 - 4.

This graph translates well the visual impression from Figure IV - 2 - 3, with the effect of the different AST observed just after the conditioning. For all three *base-load* aged MEAs, no obvious impact of the loading can be seen. The mean losses of geometric current density at 0.3 V are essentially within the error bars for the medium and lower cathode catalyst loading: $65.6 \pm 4.1\%$ $(0.43\ \mathrm{mg_{Pt}cm_{geo}^{-2}})$ and $61.3 \pm 4.8\%$ $(0.34\ \mathrm{mg_{Pt}cm_{geo}^{-2}})$, and only the higher cathode catalyst loading, seems to show slightly less pronounced degradations of the geometric current density at 0.3 V: $54.9 \pm 3.1\%$ $(0.57\ \mathrm{mg_{Pt}cm_{geo}^{-2}})$, but the authors would not make this a marked trend (at least for now).

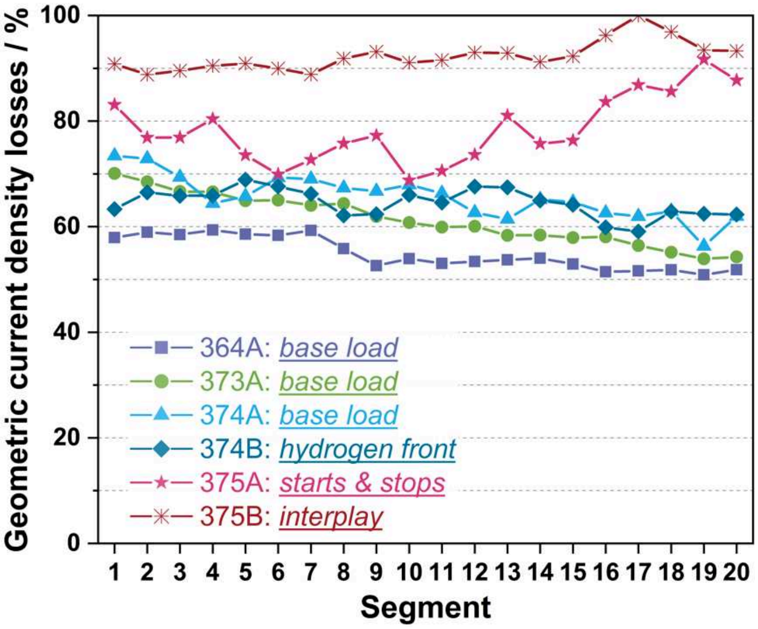

Figure IV - 2 - 4: Geometric current density losses for the different aged MEAs calculated with the difference between BoT and EoT last conditioning step at 0.3 V

The *hydrogen front* protocol has a similar mean value of geometric current density losses (65.6%) than the *base-load* one $(65.6\%$, taken from SYM374A as it has the same cathode loading), but the degradation is less varying from one segment to another, with the lowest standard deviation observed of 2.7% on the whole segments.

There is no surprise for the *starts & stops* and the *interplay*: they were believed to be the more severely impacting ASTs, and indeed revealed geometric current density losses of $ca. 80\%$ for the former and more than 90% for the latter, well beyond the values monitored for the *base-load* and *hydrogen front* ASTs. It is clear that these two ASTs are very degrading compared to the *base-load* and *hydrogen front*.

b) Effect of the AST on the cyclic voltammograms and electrochemically active surface areas

For the determination of the electrochemically active surface area, two cyclic voltammograms (CV) are performed between 0.1 et $0.7\ \mathrm{V}$ under $\mathrm{H_2/N_2}$ atmosphere at voltage scan rate of $50\ \mathrm{mV\ s^{-1}}$. The nitrogen flow is interrupted just before the start of the first CV to prevent effect from molecular hydrogen displacement and earlier hydrogen evolution reaction, which could false the measurement of the ECSA via the hydrogen under potential deposition ($\mathrm{H_{upd}}$) method (see Chapter III. New way to assess catalyst performance ? A GDE study). The ECSA is determined in the $\mathrm{H_{upd}}$ region, by applying a linear regression correction approach. As can be seen on Figure IV - 2 - 5, the global curve (green dashed curve) and the curve calculated by adding the local current for all the segments (black curve) both reveal the presence of consequent hydrogen cross-over and short-circuit resistance, which can be observed on the mean offset of the curve and on the slope of the double layer capacitive current region (between 0.4 and $0.7\ \mathrm{V}$).

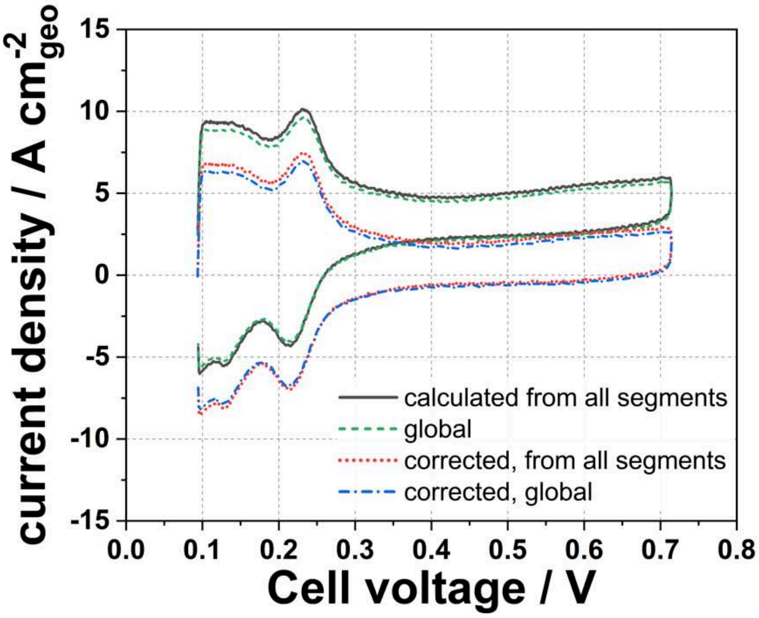

Figure IV - 2 - 5: Cyclic voltammogram under H_2/N_2 between 0.1 and 0.7 V at 150 mV s^{-1} for the SYM373A MEA at BoT. Curves calculated are sum of the current of the 20 segments. Correction is made from hydrogen cross-over and short-circuit resistance

A linear regression is made in the $0.4 - 0.5\ \mathrm{V}$ region and is extrapolated in the $\mathrm{H_{upd}}$ region before integrating the area to measure the charge of protons desorption. This is also done for the adsorption charge (negative scan). The ECSA given in this chapter will be the mean value of the adsorption and desorption charges, measured with a linear regression correction of the background. The red dot and blue dashed-dot voltammograms presented on Figure IV - 2 - 5 are corrected from hydrogen cross-over and short-circuit resistance, these values resulting from permeation current measurement (voltage hold for $3\ \mathrm{min}$ at 0.3, 0.4, 0.5, 0.6 and $0.7\ \mathrm{V}$). As this method is not working for every segment due to instabilities and noise in the current measurement, the linear regression technique is kept for the measurement of the ECSA, though.

These voltammograms show that only slight discrepancies can be noticed between the global measured current and the current calculated as the sum of all the segments current. In the rest of this chapter, independently on the calculated value of the ECSA, it is assumed that these values will be similar. The (very slight, here neglected) difference between both calculated and global curves is ascribed to hardware artefacts.

After correction of the hydrogen cross-over and of the short-circuit resistance, cyclic voltammograms of several electrodes are presented on Figure IV - 2 - 6. On this graph, SYM374A (EoT) and SYM375B (BoT and EoT) are not shown. This is explained by two reasons: (i) hardware issue led to a non-measured permeation which prevent the correction for the EoT SYM374A CV of both latter parameters, rendering the comparison with the other MEAs tricky and that (ii) detrimental current instabilities have been observed during the CVs of the SYM375B electrode at BoT and EoT. As these current instabilities are too detrimental to retrieve the results, it will be assumed that the initial ECSA and CV of SYM375B match the ones of SYM375A (same loading, same batch). Figure IV - 2 - 6 shows that the CVs aspect match at the beginning of test, differences being noticed in the intensity in the $\mathrm{H_{upd}}$ region and the double layer region, matching the difference in cathode catalyst loading: SYM364A and SYM373A have respectively the higher and lower loadings and thus respectively the higher and lower $\mathrm{H_{upd}}$ areas and double layer currents. After 30k aging cycles, there has been some significant changes on the CVs, that are not identical among the different MEAs (Figure IV - 2 - 6 B). To take a proper look and better understand the mechanisms at stake, this figure is separated in Figure IV - 2 - 6 C), showing the BoT and EoT curves for SYM374B to represent the AST performed under $1\ \mathrm{V}$ (the *base-load* and the *hydrogen front* ASTs) and Figure IV - 2 - 6 D) showing the BoT and EoT curves of SYM375A to represent the AST performed over $1\ \mathrm{V}$ (*starts & stops* and *interplay* ASTs).

On Figure IV - 2 - 6 C) (for the ASTs under $1\ \mathrm{V}$), it appears that the only visible impact the aging had on the CVs aspect is related to the decrease of current/area in the $\mathrm{H_{upd}}$ region. On Figure IV - 2 - 6 D), for the ASTs performed over $1\ \mathrm{V}$, in addition to a similar (or even more pronounced) decrease of the $\mathrm{H_{upd}}$ area, functionalization of the carbon support starts to be observed in the voltage region over $0.6\ \mathrm{V}$; this observation matches findings from Castanheira *et al.*, that incursions to voltage over $1\ \mathrm{V}$ are very damaging to the carbon support [59].

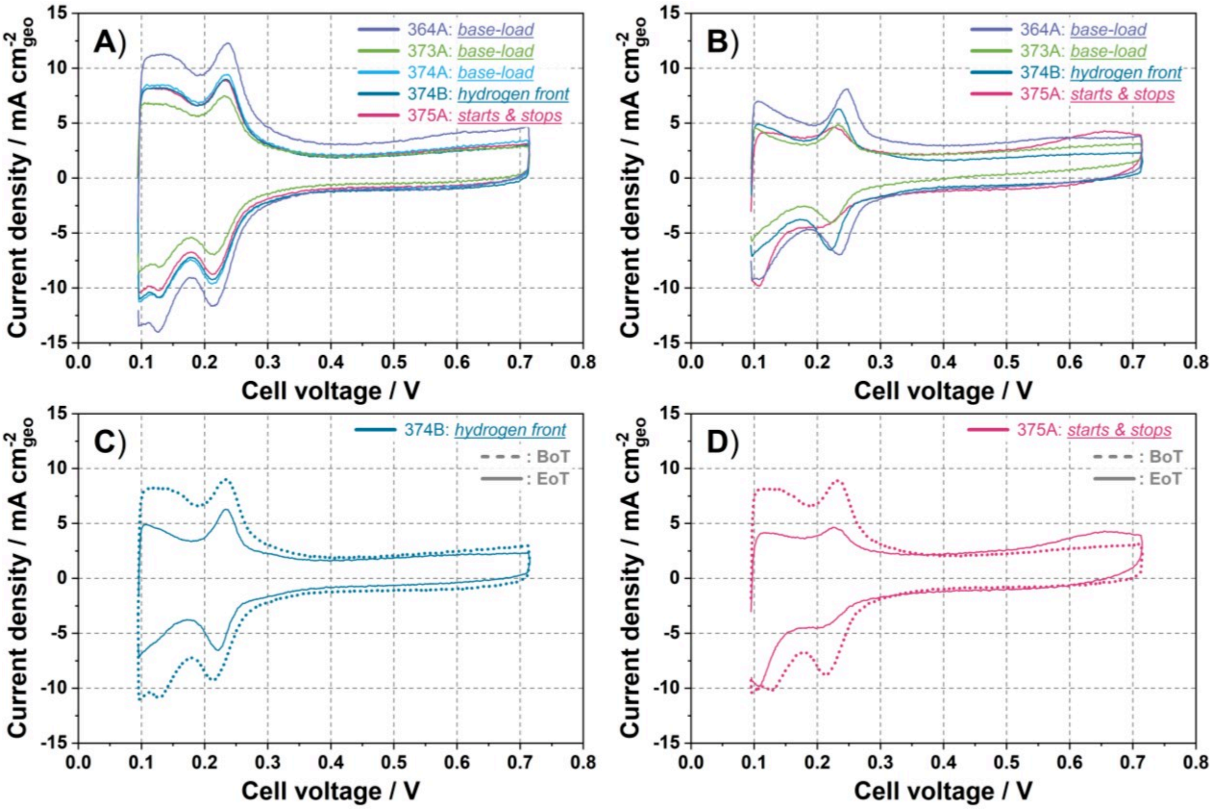

Figure IV - 2 - 6: Cyclic voltammograms under H_2/N_2 corrected with the permeation method. ***A)*** *Beginning of Test CVs for some MEAs,* ***B)*** *End of Test CVs for some MEAs,* ***C)*** *BoT and EoT CV for SYM374B MEA and* ***D)*** *BoT and EoT CV for SYM375A*

Figure IV - 2 - 7 gathers the results of the ECSA losses, calculated from the measurement of the $\mathrm{H_{upd}}$ adsorption and desorption charges on the CVs of Figure IV - 2 - 6. The initial values of ECSA are in agreement with the values found for low-loaded electrodes in the chapter III: Determination of the ECSA: influence of the working electrode environment (for the GDE and DC tests). The higher ECSA measured here compared to the use of the $\mathrm{H_{upd}}$ method in DC can be explained by the absence of nitrogen flow while recording the CVs, avoiding the detrimental shift of the hydrogen evolution reaction (HER) onset which was at stake in the DC measurements. On the graph, the ECSA values for the MEAs are sorted from higher (left) to lower (right) catalyst loadings. The comparison between the values measured with the global current recorded and the values measured with the different segments for each electrode is made (empty square and cross markers, respectively). With a reasonable error and confirmed on four MEAs, the sum of the segments ECSA lead to a similar ECSA value than that determined with the global current measured. As such, the SYM374B initial ECSA can be determined, even despite the load saturated at $2\ \mathrm{A}$ during the CV and preventing a proper acquisition of the CV.

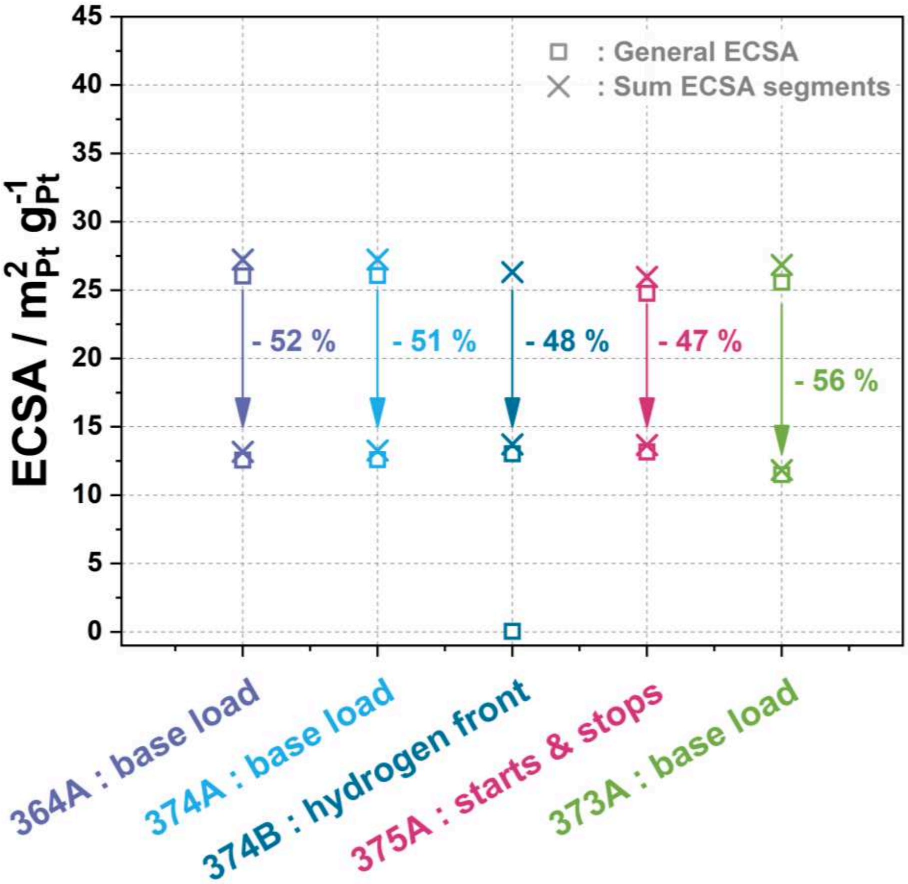

Figure IV - 2 - 7: ECSA determined via the adsorption and desorption of protons in the H_{upd} *region, before and after ASTs for all tested MEAs. The ECSA is reported to the initial mass of platinum in the active layer.*

Regarding the evolution of the ECSA and quite surprisingly, it appears that neither the AST, nor the cathode catalyst loading have a real impact on the way the ECSA decreases upon aging: roughly 50% ECSA loss is measured in all cases at EoT. The ECSA loss, a marker very frequently taken to benchmark catalysts stability/durability behaviour [196], does therefore not seem to be really relevant here. This statement will be further discussed in the following.

c) Different performance losses upon the AST

After the determination of the active surface, performance losses are dealt with. On Figure IV - 2 - 8, polarization curves performed at 1 bara and 50% RH are plotted at BoT and EoT. The beginning of test curves are rather overlapping for current densities below $0.75\ \mathrm{A\ cm_{geo}^{-2}}$, denoting a good high voltage reproducibility for all MEAs. Differences only appear between SYM364A, SYM375A and SYM375B and the other MEAs for higher current densities. This agrees with the current densities observed during the conditioning step at $0.3\ \mathrm{V}$ on Figure IV - 2 - 3: there seems to be mass-transport issues for the 4 last segments near the air outlet for these MEAs, that translate into the decreased voltage at large current density, observed here for SYM364A, SYM375A and SYM375B.

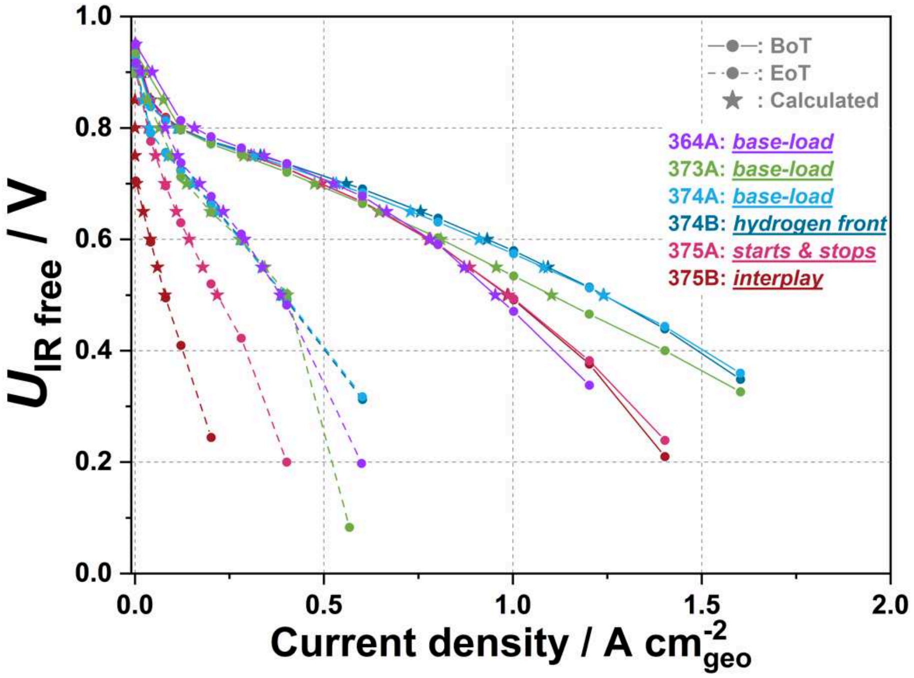

Figure IV - 2 - 8: Polarization curves measured at BoT and EoT, 1 bara, 50% RH, 80°C, st 3 air / 1.5 hydrogen for all tested electrodes

After the aging, three different behaviours appeared: (i) MEAs aged in *base-load* and *hydrogen front* (thus AST below $1\ \mathrm{V}$) come all together and have similar end of test performance, (ii) *starts & stops* has more significant impact on the performance decrease on the whole voltage range and (iii) the *interplay* AST seems to be even more detrimental to the EoT performance. To go further in the analysis, all the MEAs aged under $1\ \mathrm{V}$ are gathered together on the top graph of Figure IV - 2 - 9 and the MEAs aged over $1\ \mathrm{V}$ are gathered on the bottom graph of this figure.

Figure IV - 2 - 9 (top) makes very clear that the EoT performance of the cells aged under $1\ \mathrm{V}$ overlap very well on the whole range of voltage. As both initial and aged performance are overlapping, one can confidently conclude that there is no major (if any) influence of the cathode catalyst loading on the extent of degradations, as well as no visible impact of the lower voltage boundary on the electrochemical performance decay ($0.1\ \mathrm{V}$ for *hydrogen front* and $0.6\ \mathrm{V}$ for *base-load*).

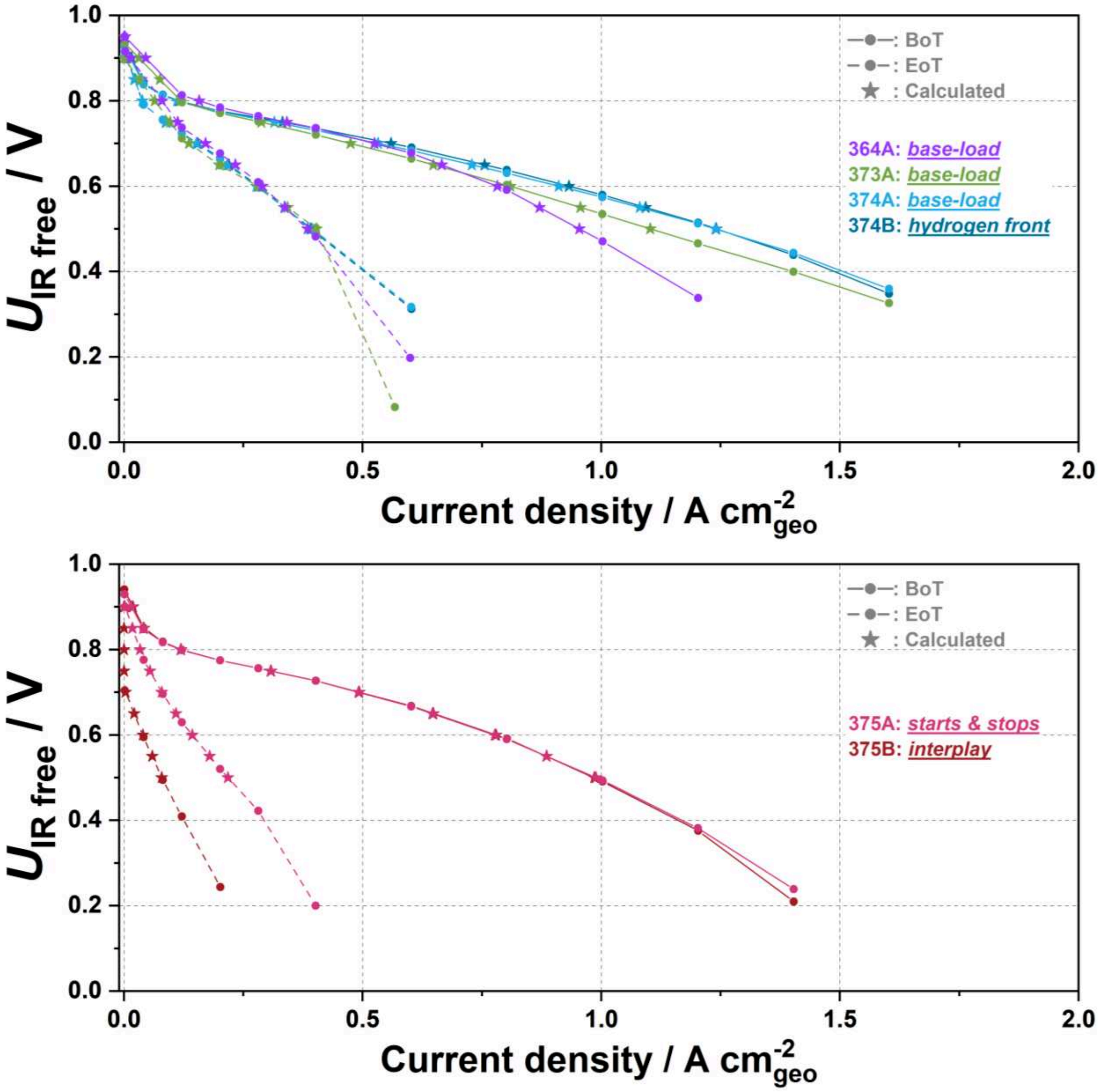

Figure IV - 2 - 9: Polarization curves measured at BoT and EoT for the electrode aged under 1 V (top) and over 1 V (bottom). The measurements were performed at 80°C, 50 % RH and 1 bara with stoichiometric coefficients of 3 and 1.5 respectively for air and hydrogen

On the contrary, for the AST over 1 V (Figure IV - 2 - 9 (bottom)), the effect of the protocols seems much more impacting for the MEAs (with losses of current density at a given voltage *ca.* 2-4 times larger at EoT for the *starts & stop* and *interplay* ASTs, respectively, than for the *base-load* and *hydrogen front* ASTs). Furthermore, the *interplay* AST seems the most degrading, as it even affects the open circuit voltage (OCV) at EoT, being lower than 0.8 V.

For all polarization curves, star markers are calculated points at fixed voltage (from 0.8 to 0.5 V) determined using a linear interpolation between the measured points of the polarization curves. The geometric current density losses are determined using these calculated points to get the variation of these losses along the voltage range of interest for practical PEMFC operation and in which a linear regression between points is not totally absurd. This evolution is displayed in Figure IV - 2 - 10.

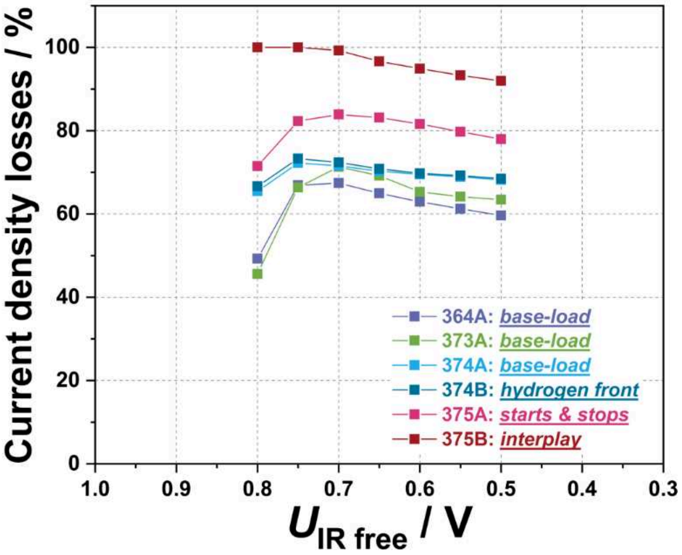

Figure IV - 2 - 10: Evolution of the geometric current density losses as a function of the cell voltage. Experimental conditions were 80°C, 50% RH, 1 bara and stoichiometric coefficient of 3 and 1.5 respectively for air and hydrogen. Points were determined using a linear regression between the polarization curves points.

For the *base-load* and *hydrogen front* aging protocols, the values calculated in the whole range from 0.8 to $0.6\ \mathrm{V}$ agree well with the losses determined in the conditioning step of $ca.\ 60-65\%$ at $0.3\ \mathrm{V}$; only the points calculated at 0.8 V make exception for MEAs 364A and 373A (which will not be commented here). This again points to the absence of relation between the losses of current density and both the cathode catalyst loading and the lower voltage boundary, when the MEAs did not experience voltages above 1 V. On the contrary, the current density losses calculated for the *starts & stops* and *interplay* ASTs amount to 80 and close to 100%, respectively, on the whole cell voltage working range denoting for the extremely damaging incursions to cell voltages above 1 V for the cathode catalyst layer.

3. Post-degradation physicochemical characterization of the aged electrodes

Once the MEAs AST and EoT characterizations are done, the cells are dismounted and the MEAs are stored until *post mortem* physicochemical characterizations are performed. These observations, despite being not destructive in essence (such as the XRD) still needs in practice to scrap the anode catalyst layer to avoid its contribution[5]. Pieces of MEAs are then coated in epoxy resin for SEM observations, the cathode catalyst layer is scrapped at some other place to prepare TEM grids and Raman is done by immobilizing a piece of MEA on a slide using carbon tape to prevent MEA/membrane undulation (local drying related to the heat brought by the beam) and awkward beam focus.

---

[5] It is assumed here that the anode and membrane are not degraded in the conditions of these AST, which is reasonable for tests performed under H_2/N_2 configuration: the anode potential likely remained very close to $0\ \mathrm{V}\ vs.\ \mathrm{RHE}$ no H_2O_2 (hence no radical) should have form in these conditions.

a) Observation using electronic microscopy: *post-mortem* study

i. Scanning electron microscopy

Post mortem SEM analyses are performed in a similar way as presented in the chapter II: Scanning Electron Microscopy (SEM) for the analysis of the cathode catalyst layer thickness, by BSE detector mode imaging (Figure IV - 3 - 1). From these, the cathode active layer thickness can be calculated (Figure IV - 3 - 2).

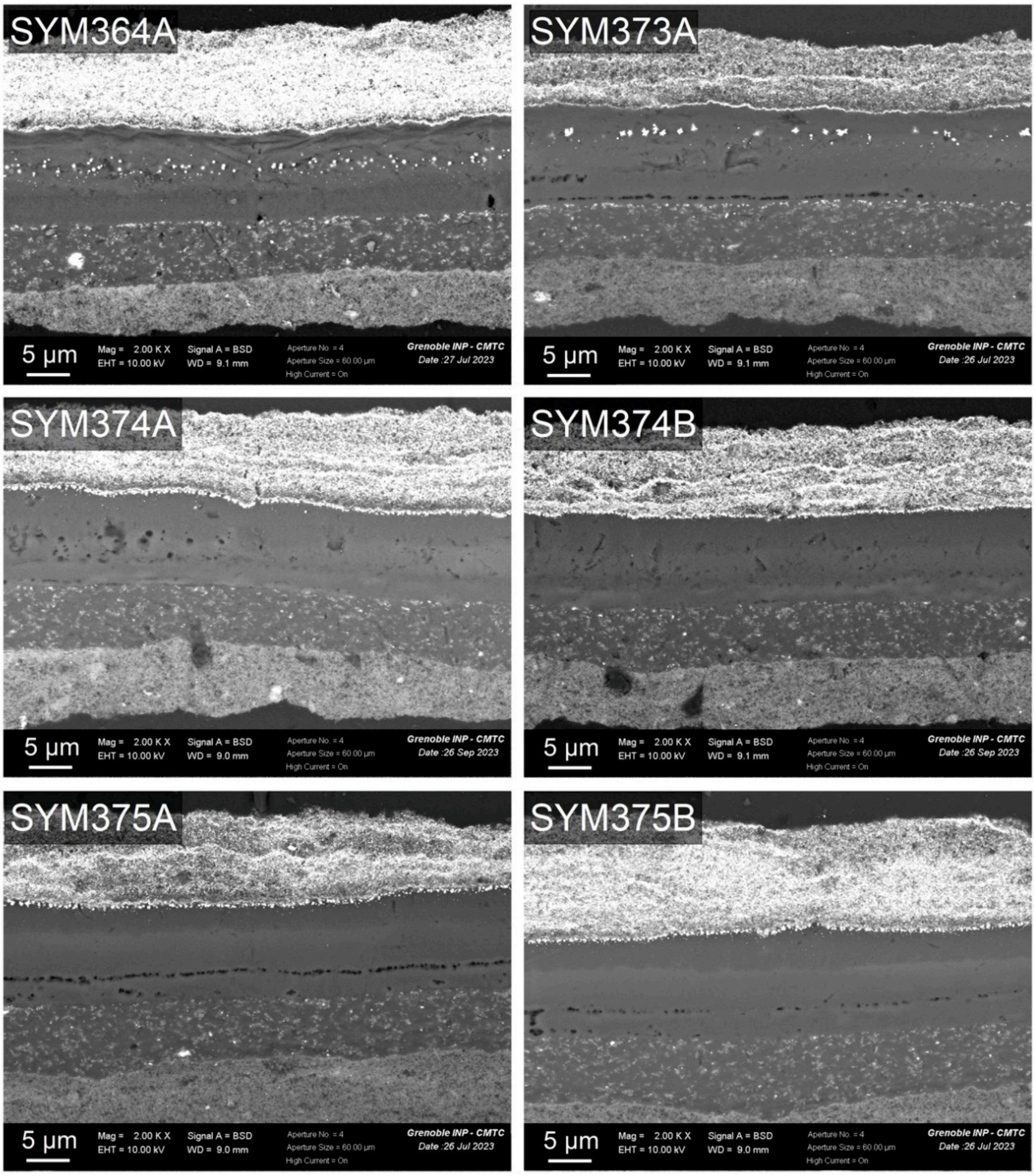

Figure IV - 3 - 1: SEM images of the Pt_3Co aged MEAs after the different AST protocols. SYM364A, SYM373A and SYM374A were aged with the base-load protocol. SYM374B, SYM375A and SYM375B were aged with the hydrogen front, the starts & stops and the interplay protocols respectively.

From the values of Figure IV - 3 - 2, aged MEAs all have similar active layer thickness than their reference (pristine) counterparts. This result was expected for the *base-load* and *hydrogen front* ASTs as they are not supposed to impact the carbon support via carbon corrosion [59]. However, this is quite surprising for the *starts & stops* and the *interplay* ASTs not to observe any change in the active layer thickness. One possible explanation to this absence of remarkable diminution of the cathodes thickness can be the fraction of active layer affected by such mechanism, which would result in a small and not pronounced enough decrease to get out the error bars. It was therefore demonstrated by Makharia *et al.* that even a small weight loss of carbon ($ca. 5-10\%$) is enough to cause important mass-transport losses [190]. Additionally, surface functionalization (the first step of carbon corrosion) can be enough to alter the ORR performance by rendering the active layer more hydrophilic, hence prone to flooding.

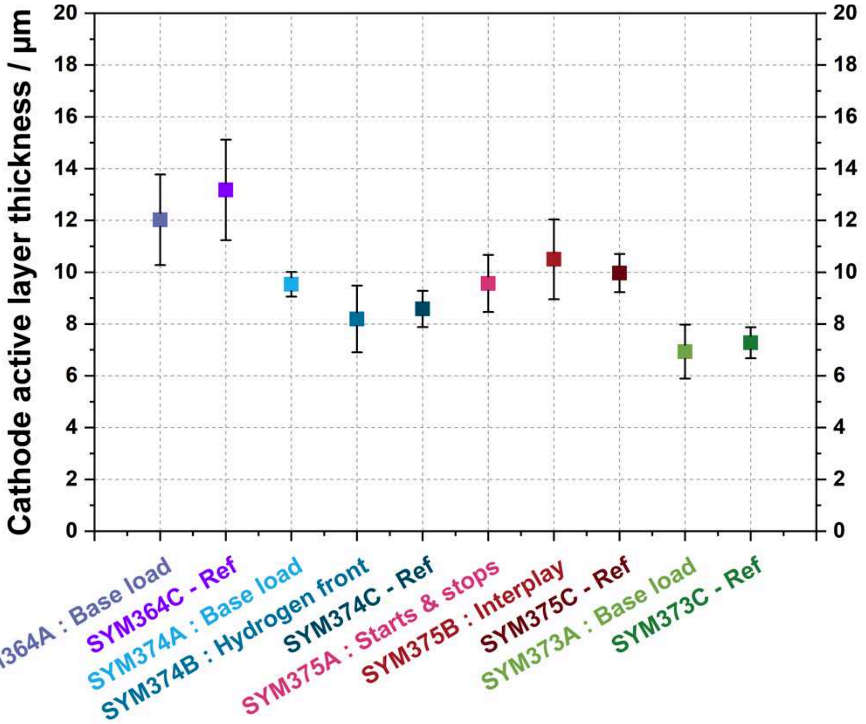

Figure IV - 3 - 2: Cathode catalyst layer thickness measurements for the aged and reference MEAs using the pixel average method

Looking more closely at the SEM images of Figure IV - 3 - 1 shall enable to better understand, visually, some of the mechanisms at stake. The pieces of MEAs were taken at the same location for the different aged MEAs.

Starting with the electrodes aged between 0.6 and $1\ \mathrm{V}$ with the *base-load* protocol, it is questioning to observe the formation of huge platinum particles in the proton exchange membrane (PEM) for SYM364A and SYM373A but not for SYM374A. This indicates that the mechanism of dissolution/redeposition of platinum in the PEM is happening here, as cycling in this voltage range implies both cathodic and anodic dissolution of platinum, a well-studied aging process [173,197]. The cross-over of hydrogen in the PEM renders possible the reduction of these ionic species, forming this band of platinum particles. However, the absence of platinum band for the SYM374A electrode is rather strange as it was exposed to the same AST protocol and thus same voltage cycling in a voltage range where the oxidation of platinum is always observed. This observation also stands for SYM374B, aged between 0.1 and $1\ \mathrm{V}$, that would make this dissolution/redeposition possible but, here again, no platinum band is observed. The SEM observation was repeated at another location but no Pt band was found in the membrane either. A common feature for these four MEAs is the dense line present at the interface between the cathode catalyst layer and the PEM. The nature of this line will be further developed and discussed in the next paragraph.

To continue with the two last aged MEAs, SYM375A and B, they both do not present any visible platinum band in their membrane. This can be understood in the case of the *starts & stops* AST (for SYM375A), as the voltage is cycled between 1 and $1.5\ \mathrm{V}$: platinum is always protected by an oxide layer in these conditions [198], and therefore less prone to dissolution. Dissolution of platinum should however be possible for the *interplay* AST, as the voltage is cycled down to $0.1\ \mathrm{V}$, resulting in both high anodic and cathodic sweep that favour the formation of platinum ionic species.

Finally, a stratification of the cathode active layer has appeared on several images (SYM373A and SYM375A for example), with lower brightness, revealing some more intense lines in the whole catalyst layer thickness that suggest local accumulation of platinum within the cathode active layer.

Higher magnification images on Figure IV - 3 - 3 give the possibility to better analyse the previous observations. Two different kinds of cathode|membrane interface are distinguished by looking at the two top images (left SYM373A for *base-load* and SYM375A for *starts & stops*): platinum particles have segregated at the interface, resulting in a higher local intensity of the backscattered electrons; these particles are still a part of the cathode for the *base-load* AST, whereas for the *starts & stops* aged MEA, the particles (apparently bigger) are for some of them completely disconnected of the active layer, as if they “fell” in the membrane due to corrosion of their carbon support (after having formed in the cathode active layer at the interface with the membrane) or if they have directly nucleated/grown in the membrane (following reduction by H_2 crossing-over); the author cannot choose the best scenario, so far, both being equally possible in his mind. In the case of SYM374A and SYM374B, bigger particles are observed at this same interface between the cathode and the membrane; the absence of the platinum band (which is well observed for SYM373A) may be explained by a much higher densification of this interfacial agglomeration of platinum.

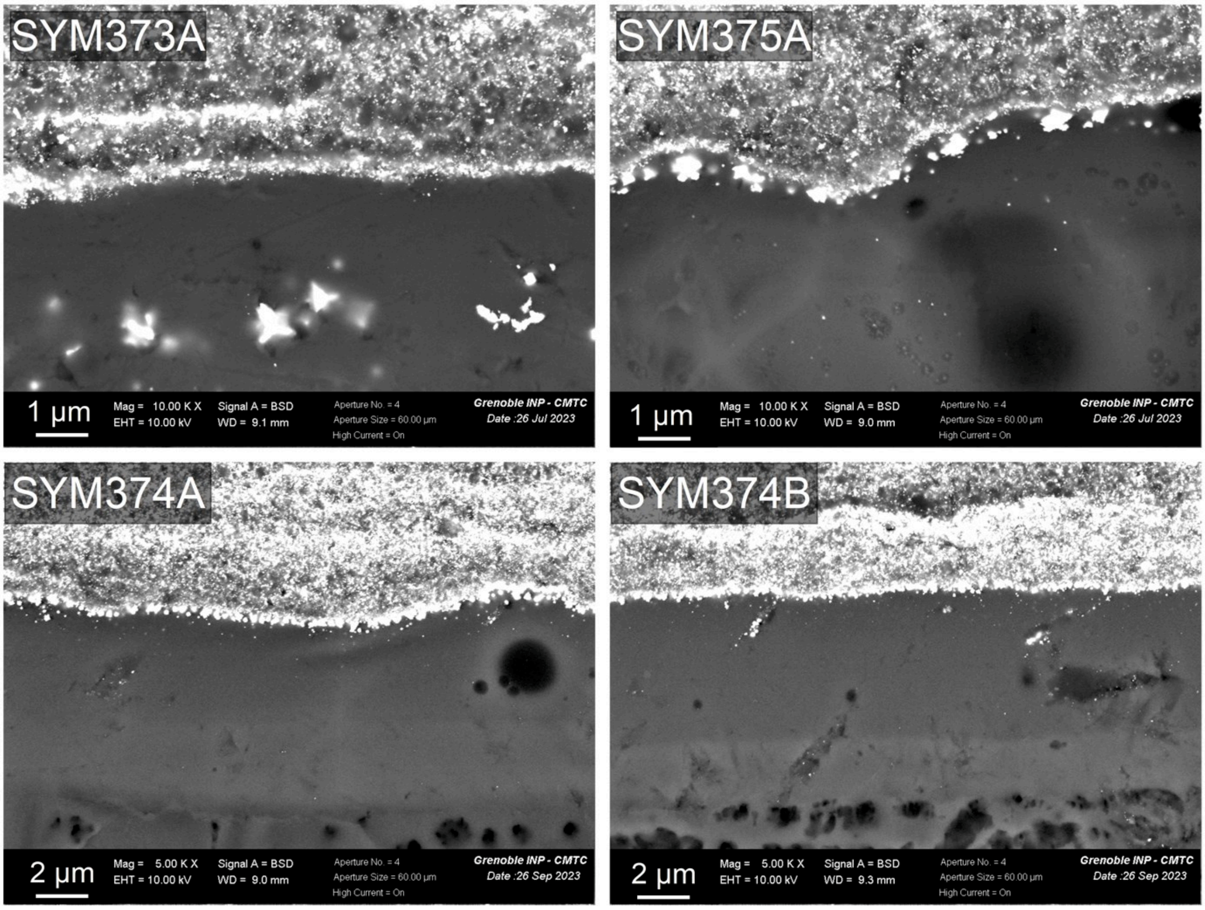

Figure IV - 3 - 3: SEM images of the Pt$_3$Co aged MEAs after the different AST protocols. Both images on the left (SYM373A and SYM374A) are MEAs aged with the base-load protocol. SYM375A and SYM374B (on the right) were aged with the starts & stops and the hydrogen front protocols respectively.

ii. Transmission electron microscopy

Switching from the microscale of the scanning electron microscopy to the nanoscale observation with the transmission electron microscopy, particles size distributions were measured for each aged MEAs on at least 175 particles taken on 16 representative images. The PSDs histograms of the cathode catalysts are presented in Figure IV - 3 - 4 for the different tested MEAs, in addition to the powder and sprayed references. Reasonably similar mean particle sizes (10.7, 11.7 and $10.8\ \mathrm{nm}$, respectively, for the SYM364A, SYM373A and SYM374A MEAs) can be calculated from these PSD histograms for the three MEAs aged following the *base-load* protocol. Also, for these MEA PSD histograms, the dispersion is really wide, with standard deviation of $ca.\ 4.5\ \mathrm{nm}$, much wider than for the references' PSDs. The *base-load* AST is the one that leads to the biggest growth of the isolated nanoparticles (particle agglomerates or gigantic nanoparticles are not taken into consideration for the PSD measurements). The *hydrogen front* particle size analysis results in mean particle size of $8.9\ \mathrm{nm}$, with a dispersion of $3.1\ \mathrm{nm}$.This more moderated increase of the particle size cannot be verified to originate from more important Co atoms dissolution, as the X-EDS performed is sensitive to metallic, oxide but also ionic forms of Co. In fact, the mean atomic percentages determined in TEM X-EDS on 4 grains of carbon at lower magnification for both *base-load* and *hydrogen front* are in all case 80% of Pt atoms and 20% of Co atoms, resulting in a slight decrease of the Co content when compared with the sprayed ratio of 75% and 25% determined for respectively Pt and Co atomic percentages.

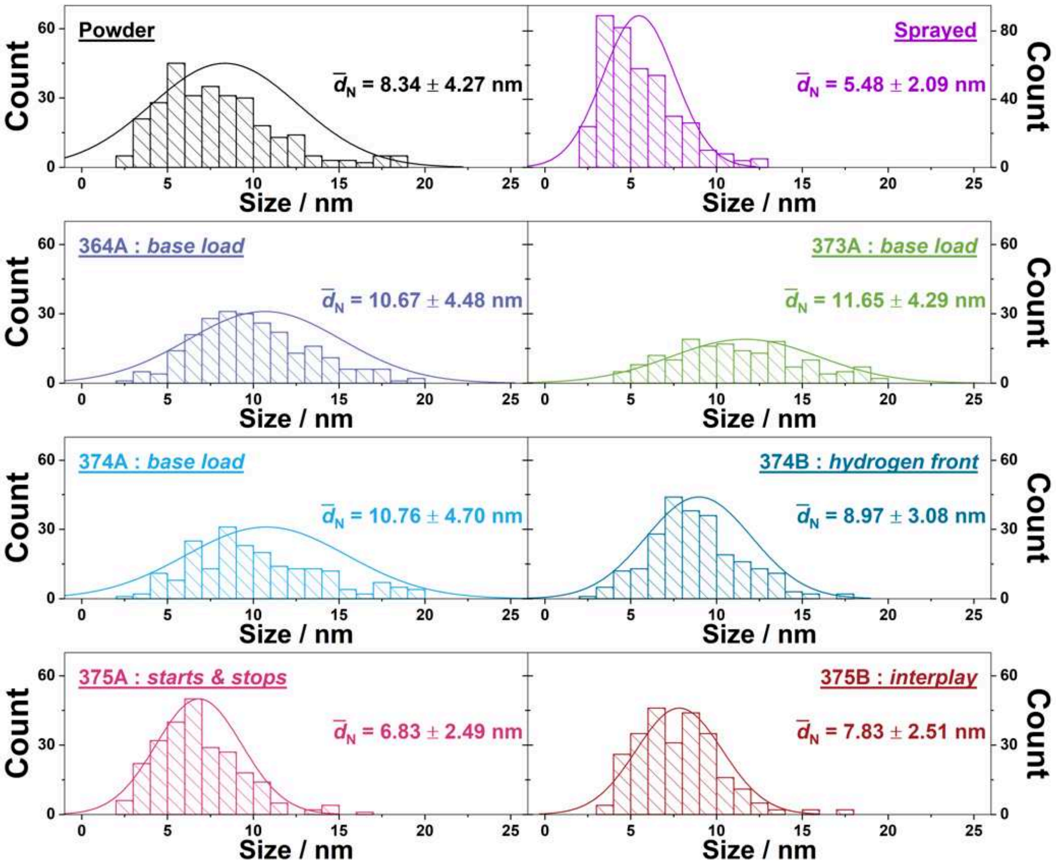

Figure IV - 3 - 4: Particle size distribution histograms of the powder, sprayed references and of the aged MEAs. The counting was performed on the scratch cathode catalyst layer powder. A minimum of 175 isolated particles on 16 images were used to have reasonable statistics.

For the AST protocols involving excursion over 1 V, even lower particle size mean diameters are measured after aging, with 6.8 ± 2.5 nm and 7.8 ± 2.5 nm for the *starts & stops* and the *interplay* AST, respectively. In the former case, the high voltages at which the catalyst is permanently confronted (1 – 1.5 V) leads to the formation of a shell of platinum oxide, which likely prevents platinum dissolution and (even more) redeposition, limiting the dissolution of small particles at the expense of bigger ones (Ostwald ripening) and related particles growth. Another possible phenomenon could be the consumption of the water present in the active layer due to water electrolysis and carbon corrosion, both reactions being likely to happen at 1.5 V; dryer conditions would prevent the diffusion of Pt and thus the Ostwald ripening mechanism. In consequence, the mean diameter measured at EoT for the *starts & stops* AST is the closest one to the initial mean diameter measured on reference MEAs powder (5.5 ± 2.1 nm). As the *interplay* name says, this AST protocol is in-between the *hydrogen front*/*base-*

load and the *starts & stops* protocols and this gives intermediate mean particle diameter of $7.8 \pm 2.5\ \mathrm{nm}$. All the different AST protocols have their own influence on the increase and size distribution of the nanoparticle's diameter; the particles growth varies in the following sequence: *base-load* > *hydrogen front* > *interplay* > *starts & stops*.

However, this kind of analysis, as previously said, only focuses on the fraction of isolated (and round-shaped) nanoparticles, which are not the only objects found when looking at the nanoscale of the catalyst. On Figure IV - 3 - 5, presence of agglomerates and non-spherical particles is well seen on every TEM micrograph. These images were taken on areas believed to be (to the naked eye and to the author's belief) the most damaged ones among each grain observed. As one can see, big particles and agglomerates are present for the *base-load* and *hydrogen front* TEM images, but the carbon shape has not much changed and many platinum particles are still visible on top of it. For the ASTs over $1\ \mathrm{V}$, however, detrimental impact is observed on the carbon particles, which seem to have reduced in size, while very few platinum particles remain present on it. Among the two ASTs over 1 V, the *interplay* seems to have the most deleterious effect on the shape of the carbon support, as particles only supported in the ionomer are visible. The extent of Pt particles agglomeration can therefore be ranged as follows: *base-load* ≤ *hydrogen front* << *starts & stops* ≤ *interplay*.

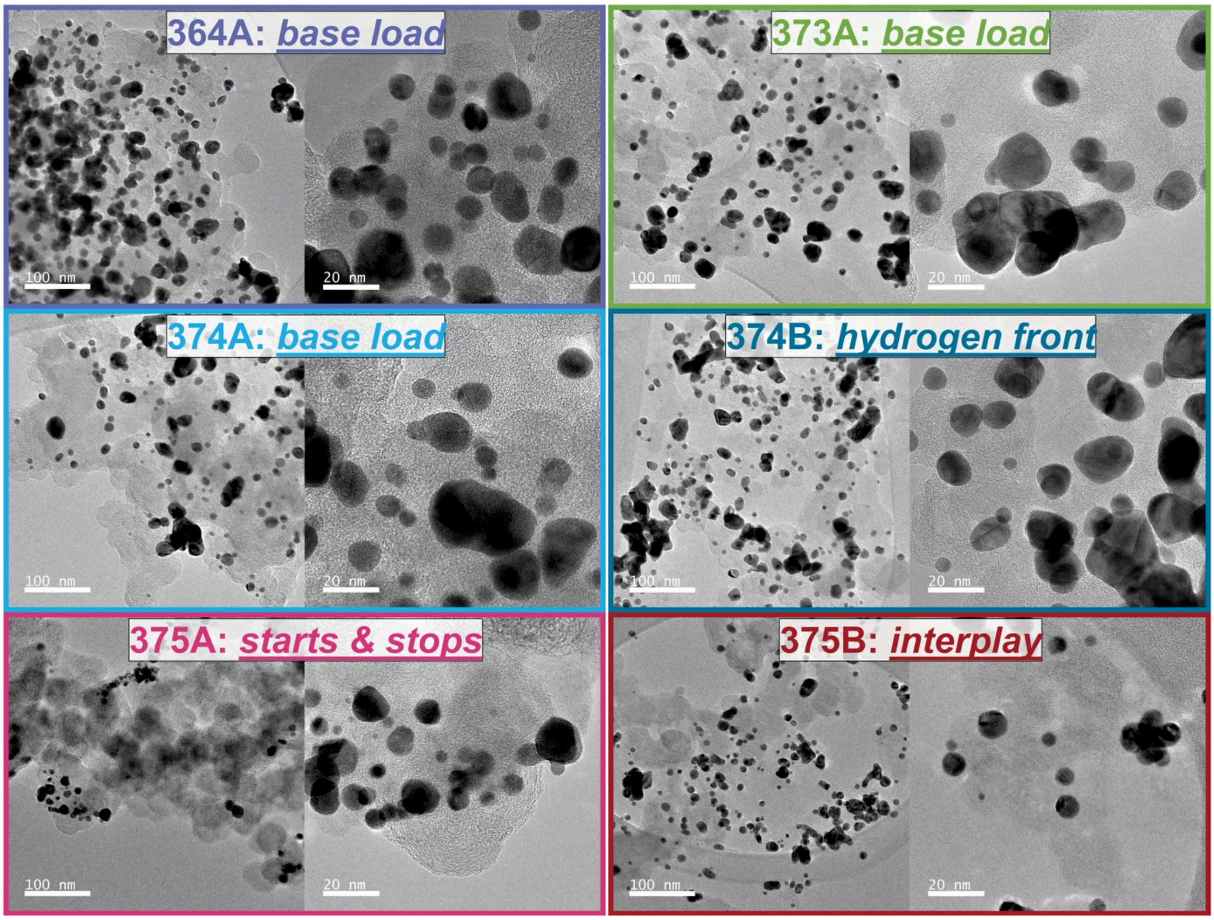

*Figure IV - 3 - 5: TEM micrographs obtained at *50k (left) and *200k (right) magnification for all MEAs after aging.*

b) De-alloying observed using X-Ray diffraction diagrams

Post mortem diffractograms are added to those of reference MEAs (presented in the beginning of this chapter) on Figure IV - 3 - 6: important deviations from the pristine active layers are observed, displaying a (at least partial) return to a full platinum lattice for the aged catalyst layers. For all the aged MEAs, formation of a pure platinum crystalline structure of similar nature (cubic face centred) coexisting with the original Pt$_3$Co structure is evidenced. This is very well observed with the appearance of peaks at the same position as the angle markers for the platinum crystalline structure. These platinum peaks are very thin, implying that the platinum crystallites that are formed are rather big, and visually bigger than the Pt$_3$Co initial crystallites. The apparition of peaks at $2\theta \approx 26°$ and $2\theta \approx 52°$ is ascribed to carbon (002) and (004) crystalline orientations. The origin of these peaks is unclear, but the author posits that it could be related to (partial) transfer of (some of) the microporous layer (MPL) to the surface of the cathode catalyst layer during the removal of the GDL that has occurred for SYM375A and SYM375B, the only two aged electrodes presenting such features. Indeed, degradation of the carbon support during the AST was not marked (no real active layer thickness change), and could not have led to such major “formation” of graphitized carbon.

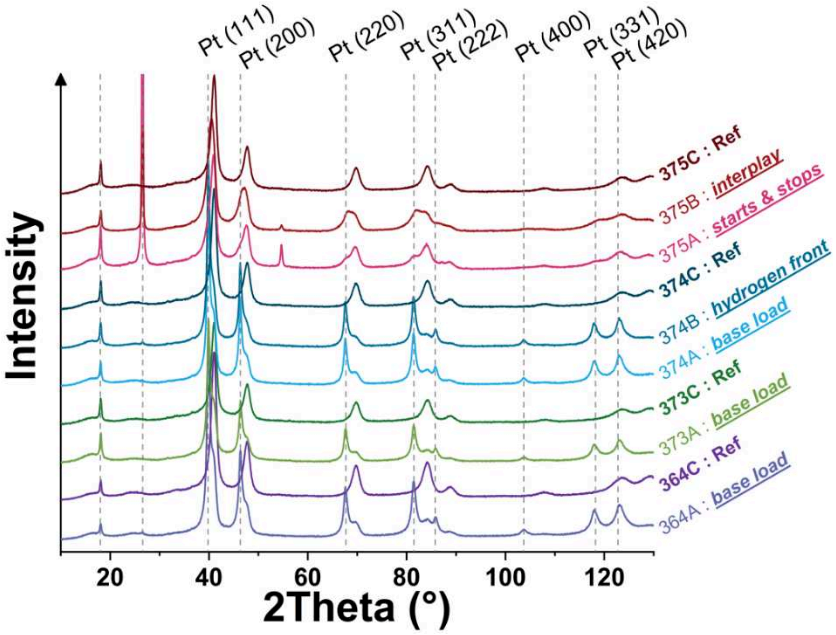

Figure IV - 3 - 6: X-ray diffraction diagrams of the catalyst reference MEAs and of all the aged MEAs

A zoom is made on the (220) peak, as it is the more adapted to use mono or multi-peaks fitting on it without the necessity to create more than two contributions. The peaks are fit using the same procedure as for the reference MEAs, with the PsdVoigt linear combination of Gaussian and Lorentzian. The results are presented in Figure IV - 3 - 7, where there is a clear trend for the ASTs under $1\ \mathrm{V}$, and a different one for the ASTs over $1\ \mathrm{V}$.

On the one hand, it is visually clear that for both the *base-load* and the *hydrogen front* aging protocols, thin peak at the position of pure Pt (220) appears and the Pt$_3$Co (220) peak suffers a decrease in intensity and broadens. After deconvolution of the two peaks and utilisation of the Scherrer Law, small decrease in the crystallite size of the Pt_3Co by $ca. 14\%$ is calculated (from 12.8 to $ca. 11$ nm). Big platinum crystallites are formed, ranging from 22 nm for the SYM364A electrode with the heaviest loading to reach its maximum at 26 nm with SYM374B. No clear correlation can be seen from the evolution of this Pt (220) crystallite size, at least not depending on the catalyst loading of the active layer. It can however be noted that both the higher Pt (220) and the lower Pt_3Co (220) crystallite sizes are observed for the *hydrogen front* aged MEA (SYM374B): this could be a sign that a more important leaching of Co or more important platinum loss is likely happening during this aging protocol.

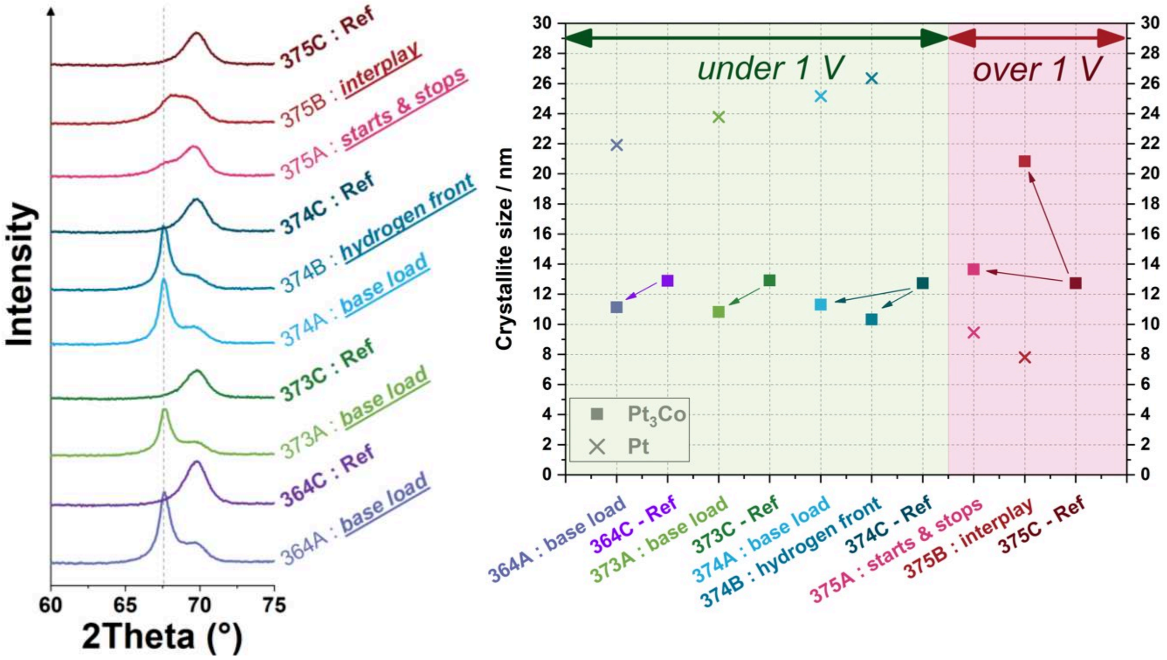

Figure IV - 3 - 7: Aspect of the (220) crystallographic orientation on the reference and aged MEA's diffraction diagrams (left) and crystallite size for the (220) orientation for all MEAs (right).

On the other hand, if one takes a look at the behaviour of the MEAs aged with upper voltage boundary over 1 V, the trend is totally different. In this case, no Pt (220) peak as clear as for the *base-load* and *hydrogen front* is observed: a shouldering is visible for the *starts & stops* AST, though, and a peak almost exhibiting a plateau is seen for the *interplay* AST. In both cases, wider Pt (220) peaks are measured, corresponding to smaller crystallite size, of 9.5 and 7.8 nm for *starts & stops* and *interplay*, respectively. A slight increase of the Pt_3Co (220) crystallite size is witnessed for the former AST as compared with the reference MEA, while a huge increase of this crystallite size is measured for the latter AST. The increase of the crystallite size of Pt_3Co is possible if one considers a mechanism of crystallite migration and coalescence, that can probably happen with a small part of dissolution and redeposition to form a pure platinum crystalline phase; in this regard, the low vertex potential value of the *interplay* AST, renders more likely the growth of very large Pt_3Co nanoparticles. For the *starts & stops* AST, it seems that the dissolution is predominant and no sign of Pt_3Co crystallites migration and coalescence is found.

c) Raman spectroscopy: comparison with the reference cathode catalyst layers

Similarly to all the other physicochemical analyses, end of life Raman spectroscopy is also done on the aged MEAs, with the expectation to observe change in the carbon material of the active layer, possibly related to the AST applied. Raman spectra are separated in two groups, depending on the upper voltage limit (which separate the *base-load* and *hydrogen front* on one hand and *starts & stops* and *interplay* on the other hand). Figure IV - 3 - 8 (left) shows no change in the Raman spectra (normalized by the intensity of the D_2 band, at $ca. 1605\ \mathrm{cm}^{-1}$) for the *base-load* and *hydrogen front* ASTs. This result can either be linked to the absence of impact of the carbon support of the active layer in the cycling between 0.1 or $0.6\ \mathrm{V}$ to $1\ \mathrm{V}$, or to the analysis depth. Raman spectroscopy is related to the inelastic scattering of light in a material; so, using a light in the wavelength of the visible ($532\ \mathrm{nm}$) means that dark materials will absorb this light, leading to small penetration in the material (black materials like PEMFC catalysts are typical of this). In that case, only the outer extreme surface (several 10 nm) of the active layer is probed via Raman spectroscopy and not the $ca. 10\ \mu\mathrm{m}$ of the cathode active layer. Here, Raman was performed on the MPL side of the active layer, and one cannot exclude that, if the membrane|active layer side had been observed, changes in the Raman spectra would have been put into evidence. The situation is completely different for the AST over $1\ \mathrm{V}$: modification of the D_1 band ($ca. 1350\ \mathrm{cm}^{-1}$) and of the G band are observed. In fact, the SYM375B spectrum (*interplay* AST) has similar position and intensity of the D_3 band ($ca. 1495\ \mathrm{cm}^{-1}$), corresponding to the amorphous carbon, but modification of the left side of the D_2 band, which stands for increased disorder of the graphitic lattice and graphene layer edges. This is quite unexpected, as one would expect corrosion of the amorphous phase (and therefore the D_3 band) as well. It was therefore observed by Castanheira *et al.* that oxidation of the amorphous phase and creation of defects from the graphite phase can result in similar Raman spectra, despite presence of carbon corrosion as witnessed by DEMS measurements [59]. For the *starts & stops* AST, the spectrum is much different: (i) similar position of the D_1 band than SYM375B, (ii) apparition of a thin peak corresponding to the G band at $1585\ \mathrm{cm}^{-1}$, which stands for the ideal graphitic domain and (iii) decrease in the intensity ratio between D_2 and D_3. The apparition of this G band of much higher intensity on such a poorly graphitised carbon support electrode is an artefact coming from the transfer of the MPL layer on the cathode catalyst layer which was unavoidable during the focus of the Raman monochromatic light on the surface of the sample. Transfer of this graphitic structure of the GDL microporous layer agrees with the previous finding of the X-rays diffraction. In any case, the fact that the MPL was transferred is an indirect sign of harsher carbon corrosion for this MEA, in line with the more aggressive conditions experienced (above 1 V), and this goes in line with the larger changes of the Raman spectra for the MEAs aged with incursions above 1 V.

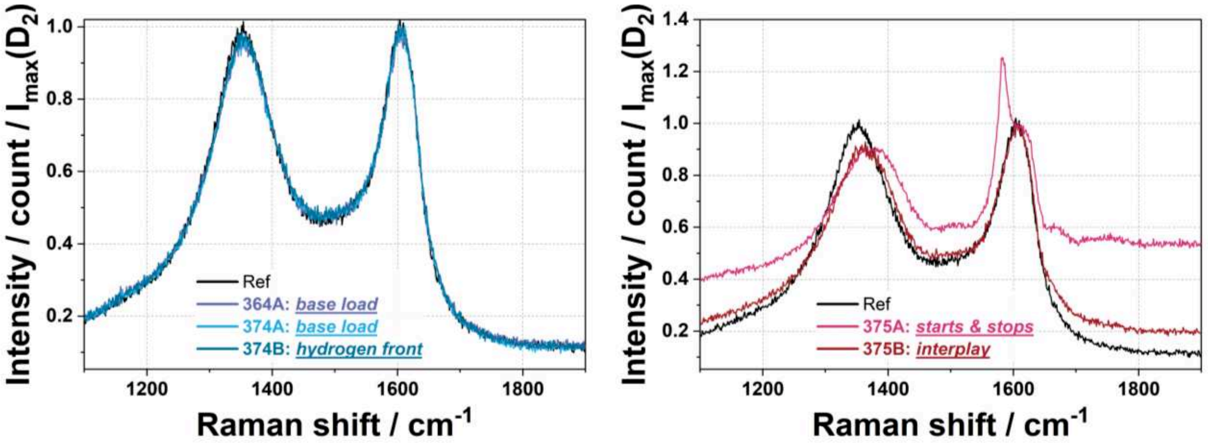

Figure IV - 3 - 8: Raman spectra of the aged electrodes separated by the upper voltage limit: 1 V and 1.5 V respectively on the left and right side

4. Discussion

The results presented in the previous parts of the chapter show that it is relevant to separate the different accelerated stress tests protocols (and thus MEAs) in two groups as a function of the upper voltage boundary experienced: the AST under $1\ \mathrm{V}$ (*base-load* and *hydrogen front*) and the AST over $1\ \mathrm{V}$ (*starts & stops* and *interplay*).

To begin with, after $60{,}000$ voltage steps ($30{,}000$ cycles for all AST except $15{,}000$ cycles for the *interplay* that has 4 steps per cycle instead of 2 steps per cycle), all the MEAs studied here have lost roughly half of their electrochemically active surface area, but the explanation of this rather constant ECSA loss differs from one AST to the other (see below). The performance decay seems a more reliable marker of degradation, with much higher values of current density losses found at given voltage, these values differing with the nature of AST at stake: $60 - 65\%$ and $80 - 90\%$, measured for the ASTs under $1\ \mathrm{V}$ and the ASTs over $1\ \mathrm{V}$, respectively. Combining these two figures shows that the decrease in performance cannot be solely explained by the decrease of ECSA and therefore by the variation in ECSA. These performance losses were demonstrated to be rather constant on the cell surface (*cf.* Figure IV - 2 - 4) as well as constant in the voltage range $0.8 - 0.5\ \mathrm{V}$ (Figure IV - 2 - 10). For both AST groups, the reason of these higher performance losses vary a little and is developed in the following paragraphs.

For the ASTs under $1\ \mathrm{V}$, dealloying of the Pt_3Co initial catalyst happens, as demonstrated by the decrease in Pt_3Co crystallite size observed on the X-rays diffractograms and by the calculated ratio between Pt and Co atoms: the initial ratio determined by X-EDS analysis was the expected $Pt_{0.75}Co_{0.25}$ atomic fraction and this value evolved to $Pt_{0.80}Co_{0.20}$ (equivalent to a Pt_4Co, not existing as a crystal) or $Pt_{0.84}Co_{0.16}$ (*ca*. Pt_5Co) in average. These values were found on different MEAs and for a given MEA, it was dependant on the area studied, which is believed to originate from a possible heterogeneity of aging in the thickness of the active layer, especially for the high-loaded electrode (SYM364A). However, these calculated proportions are more informative as chemical analysis and do not provide representative information of the real crystalline structure. Nevertheless, this leaching of Co atoms and formation of Pt crystallites leads to a decrease in the intrinsic activity of the catalyst, in line with the findings of the previous chapter: Pt_3Co/VC exhibits higher performance for the ORR than Pt/VC. The absence of active layer thinning and the overlapping Raman spectra of the aged and reference MEAs indicate that the carbon support has not been majorly corroded during the aging process. This is well seen on the TEM micrographs, with no visible impact on the surface and texture of the carbon particles. From these micrographs also, one can notice that agglomeration of the catalyst nanoparticles has happened in a non-negligible extent, especially when the MEAs experienced voltages of $0.1\ \mathrm{V}$ (*hydrogen front*). In addition, platinum is lost via dissolution and redeposition in the membrane due to hydrogen cross-over, forming a nicely observed big platinum band of apparent (for some of them) micrometre-size objects (Figure IV - 3 - 3). In summary, many concomitant degradation mechanisms intervened in the aging process of this group of electrodes, with platinum dissolution/redeposition in the ionomer/membrane, dissolution of Co atoms from the catalyst particles and crystallites migration was also observed on TEM pictures.

For the ASTs over $1\ \mathrm{V}$, the performance losses are more important but the mechanisms are also different. As observed on the cyclic voltammograms (Figure IV - 2 - 6), functionalization of the carbon support is occurring with the appearance of an oxide formation feature between $0.6 - 0.7\ \mathrm{V}$, which is the initial sign of carbon corrosion. In agreement with this observation, the Raman spectra show slight modification of the D_1 band, confirming that functionalization/corrosion of the carbon support happened, even if it is not consequent enough to result in significant thinning of the cathode catalyst layer. It is however observed on SEM images, focusing on the cathode|membrane interface, that some catalyst particles are not supported by the carbon anymore in this region, showing that the carbon corrosion could be heterogeneous in the thickness of the cathode and more prevalent/fast at the cathode|membrane interface than in the cathode centre of cathode|MPL interface. In addition, the rather high voltage conditions of these tests make platinum to be almost completely oxidized, and therefore not much prone to dissolve and redeposit (either thanks to the hydrogen cross-over, or to low potential excursion in the *interplay* AST). The consideration of the water consumption due to water splitting and carbon corrosion also account for a lower mobility of the ions in the active layer. So, one can conclude that these particles have more likely lost their carbon support than originate from a major dissolution/redeposition mechanism (even if this mechanism cannot be totally excluded, in particular for the *interplay* AST). Additionally, the X-rays diffraction diagrams show the formation of small platinum particles (much smaller than the particles observed at the cathode/PEM interface) as well as an increase in the Pt_3Co crystallite size. This can be explained if migration/coalescence of the particles happens. The increase in size is higher for the *interplay* protocol, maybe due to higher voltage range scanned used as a driving force for the particle migration at the surface of the carbon support.

Additionally, the study of the cathode catalyst layer platinum loading influence has shown no difference in behaviour for the three MEAs aged with the *base-load* AST. This is, in conditions where only low ($\leq 0.12\ \mathrm{A\ cm_{geo}^{-2}}$) capacitive current ($\mathrm{H_2/N_2}$ gas configuration) is produced, related to the absence of not impacting mass-transport in the thickness of the active layer. This resulted in rather homogeneous performance losses for electrodes aged with a similar AST protocol, independently on their platinum loading. Another phenomenon which could explain the higher performance losses compared to the ECSA losses, despite it was not studied here, is related to the Co atoms leaching, which leads to the increase of the protonic resistance [100,105] due to contamination of the membrane/ionomer by this cation. This phenomenon would have possibly been observed via the use of impedance spectroscopy under $\mathrm{H_2/N_2}$ gas configuration performed in the $0.2 - 0.4\ \mathrm{V}$ voltage range.

5. Conclusion

This study was aimed to understand the performance stability of a Pt_3Co/VC catalyst integrated in highly-loaded PEMFC cathode. To that goal, several MEAs were produced via the spray deposition technique and tested in a segmented cell at the LEMTA. Four different accelerated stress tests that derivate from the US DoE recommendations were investigated: (i) *base-load* (2 steps: $0.6 - 1\ \mathrm{V}$) representing most of the working time of the cell in "conventional" operation, (ii) *hydrogen front* (2 steps: $0.1 - 1\ \mathrm{V}$) mimicking the diffusion of hydrogen from the anode to the cathode after the cell is shut down (also called depolarization), (iii) *starts & stops* (2 steps: $1 - 1.5\ \mathrm{V}$) simulates the temporary formation of a hydrogen front at the anode, raising the cathode potential in the opposite side of the H_2-starved region and (iv) *interplay* (4 steps: $1 - 1.5 - 1 - 0.1\ \mathrm{V}$) tested to apprehend the interaction of all previous mechanisms altogether. Three different loadings were subjected to a similar AST (*base-load*) to see if there was an effect of the cathode catalyst layer loading on the durability of the MEAs. In addition to these durability tests, in-house conditioning based on humidity cycling are performed to have homogeneous initial electrode state, cyclic voltammograms and permeation measurements under inert atmosphere are done to access the electrochemically active surface area and some other cell parameters (hydrogen cross-over and short-circuit resistance) further used for the correction of the CVs. The performance of these cells are assessed using hydrogen/air flows, the segmented cell enabling to access the local performance and active area, if needed.

In the light of these tests, no impact of the cathode active layer loading was found to reduce or increase the degradation rate of the performance on *base-load* AST. In the voltage range scanned, the performance losses accounted for $60 - 65\%$ of the initial performance, and this was similar for the *base-load* and *hydrogen front* ASTs. Both ASTs led to a similar 50% loss of ECSA, attributed to Ostwald ripening coupled with migration/agglomeration of the catalyst particle at the surface of the carbon support. The difference between the ECSA and performance losses can be ascribed to decreased ORR intrinsic kinetics, due to Co atoms leaching from the Pt-Co alloy. The presence of a platinum band in the PEM points toward a widely-observed platinum dissolution into ions and redeposition in the membrane by the H_2

crossing-over. This platinum band was however missing for some MEAs after aging, and the reason why is still unclear.

Accelerated stress tests going to higher cell voltages (*starts & stops* and *interplay*) revealed much higher performance losses, despite having the same ECSA decrease (for the *starts & stops* AST at least). Carbon support functionalization and oxidation was shown to happen in larger extent in this case, as well as crystallites migration and coalescence, leading to the formation of bigger $Pt_{1-x}Co_x$ crystallites. No platinum band in the membrane was observed, as the platinum of the catalyst particles is believed to be protected by an oxide layer and less prone to dissolve in these conditions. Ostwald ripening was indeed not as much present, as particle size distribution measured from TEM micrographs show poor increase of the isolated particles size. However, agglomeration was more consequent, in result of harsher carbon functionalization/corrosion at the high potential values experienced, and related metal/oxide nanoparticles migration/collision.

Chapter V

Potentiostatic degradations study of 25 cm² unit PEMFC MEAs

Chapter V. Potentiostatic degradations study of 25 cm² unit PEMFC MEAs

According to the literature [107,199], comparing the real performance/durability of state-of-the-art membrane electrodes assembly (MEA) materials is a complex task, owing to the absence of unifying ageing protocols, and to the variety of the experimental conditions used to qualify proton exchange membrane fuel cells (PEMFC). In particular, if one wants to guarantee performances at end-of-life (*e.g.* 100 kW for the stack after *ca.* 5000 h of operation), it is still difficult to predict what should be the initial performances desired for the MEA. In addition, because the MEA performances degrade versus operating time, the fuel cell would likely operate in degraded mode initially, in abnormal operating conditions (*e.g.* higher cell voltage and lower current density than the targeted nominal operating regime of the PEMFC stack), and this can be detrimental to the MEA materials long-term durability. To evaluate whether such initial abnormal (degraded) operating conditions impact the durability of the MEA, this chapter evaluates the materials degradations and electrochemical loss of performance of $25\,\mathrm{cm}^2$ unit PEMFC MEAs that have been operated mostly under potentiostatic regime, over a broad cell voltage (assimilated to the cathode potential range), from 0.85 to $0.60\ \mathrm{V}$ for roughly 700 hours.

In order to understand the influence of cell holding voltages and possible detrimental operating conditions on the core materials of single cell PEMFC, several hundreds of hours of operation under hydrogen/air conditions are performed. As studied materials, six MEAs of rather homogeneous cathode platinum loadings were produced via the spray-deposition technique, integrating a classical commercial Pt/VC (Vulcan carbon) catalyst ($47\ \%\mathrm{wt}_{\mathrm{Pt}}$ TEC10V50E from Tanaka Kikinzoku Kogyo, TKK). The idea was to use a simple commercial platinum catalyst with spherical-shaped monometallic nanoparticles to limit the effect related to alloying, ordering or disordering properties of state-of-the-art bimetallic catalysts, which would induce more parameters in the equation. Cathode loadings of $ca.\ 0.4\ \mathrm{mg_{Pt}\ cm_{geo}^{-2}}$ are used as intermediate loadings for light duty (target closer to $0.2\ \mathrm{mg_{Pt}\ cm_{geo}^{-2}}$) and heavy duty ($0.4 - 0.6\ \mathrm{mg_{Pt}\ cm_{geo}^{-2}}$) vehicles.

The experimental protocol was designed with a will to limit as much as possible the number of voltage cycles experienced by the MEAs. As such, the conditioning (single voltage step at $0.6\ \mathrm{V}$ for $2\ \mathrm{hours}$), the polarization curves (2 cyclic voltammograms, CV, between open circuit voltage, OCV and $0.54\ \mathrm{V}$) and the $\mathrm{H_2/N_2}$ characterizations (5 cycles between 0.05 and $0.94\ \mathrm{V}$ for three voltage scan rates, 6 chronoamperometry, CA, steps) are made so that only a few and reasonable amount of voltage cycles are necessary to extract interesting and meaningful information on the state of the catalyst or of the membrane, core materials of the MEAs. Most of the working time of the cells is spent at constant voltage operation to reveal to the greatest possible extent the influence of the cell voltage on the aging process.

1. Physicochemical characterizations of the as-prepared electrodes

A total of $6\ \mathrm{MEAs}$, all based on 47 wt% Pt/Vulcan XC72 catalyst (Pt/VC), have been tested at various cell voltages, ranging from 0.85 to $0.60\ \mathrm{V}$ to better understand and estimate the impact of the cell voltage working point on the degradation of the cathode active layer (and of the membrane). All the MEAs were similar by the nature of their core components (anode, membrane, cathode, gas diffusion layers (GDL) and gaskets) and the anode loadings. Table V - 1 gathers the chosen cell voltage held for the potentiostatic steps and the initial cathode catalytic layers loading, determined via weighing of the electrode after the spray deposition process.

Table V - 1: Summary of the potentiostatic – aged electrodes

MEA's name	**Cell voltage held (V)**	**Cathode catalytic layer loading ($\mathbf{mg_{Pt}cm_{geo}^{-2}}$)**
SYM370-A	0.70	0.38
SYM370-B	0.85	0.38
SYM371-A	0.85	0.42
SYM371-B	0.60	0.42
SYM372-A	0.80	0.42
SYM372-B	0.60	0.42

Several physicochemical analyses have been performed post-test on these MEAs and compared to those performed for identical MEAs at initial state (named SYM37X-C): MEAs were prepared with $18 \times 6\ \mathrm{cm}^2$ membranes that were cut in three pieces (namely A, B and C). The SYM37X-C MEAs have neither been hot-pressed nor electrochemically tested; as such, they give in this study the initial fingerprints for each batch of MEAs (at non-degraded, *i.e.* pristine state). They will also be referred to as Reference MEA. This comparison between aged and initial MEAs will be used to follow whether these conditions are harmful (or not) to their core materials, in particular the cathode active layer and the membrane. Scanning electron microscopy (SEM) is used to measure the thickness of cathode active layers and probe the existence of cracks and delamination within or between the layers; transmission electron microscopy (TEM) was used to observe the Pt/C cathode catalyst particle size distribution (PSD), while X-rays diffraction (XRD) and Raman spectroscopy respectively give information of the Pt crystallized phase and graphitic - amorphous carbon phases.

As a reminder, the aging protocol follows several steps that are repeated a certain number of times (Figure V - 1 - 1) to reach the desired test duration. After the conditioning step, beginning of test (BoT) performance and characterizations are performed before starting the aging at constant voltage. The procedure comprises several breaks for hardware management, such as refilling of the humidifiers (no gas flow, cell at the open circuit voltage, atmospheric pressure). The aging is then restarted at the appropriate potentiostatic step to reach either 7, 14 and then 7 days again, where sets of intermediate (Interm1 and 2) and end of test (EoT) $\mathrm{H_2/N_2}$ and performance characterizations are performed. Due to the tests' conditions (small number of cycles, rather high $\mathrm{H_2}$ stoichiometric coefficient), it is more likely that the anode (i) potential stays close to $0 - 0.1\ \mathrm{V}$ versus the reversible hydrogen electrode (RHE) and (ii) does not suffer a lot, and so is believed to not degrade. Small amount of intermediate characterizations was placed in the experimental protocol to avoid additional and non-negligible degradations [123]. As such, the cell voltage will also be considered very close to the cathode potential value (expressed in V *vs.* RHE).

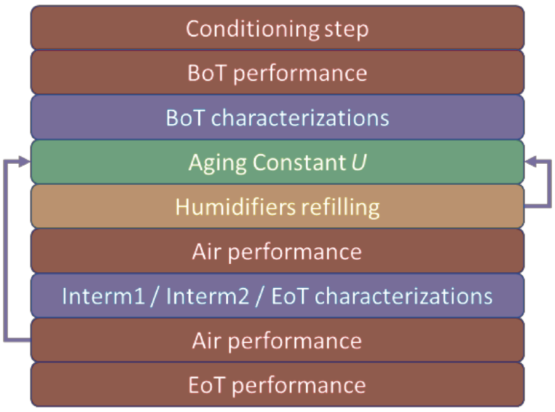

Figure V - 1 - 1: Sequencing of the cell lifetime for potentiostatic degradation

Hereafter, the physicochemical fingerprints of the reference MEAs will be firstly analysed using these physicochemical techniques mentioned above. Secondly, the electrochemical analysis of the MEAs made in the course (prior, during and after) of the single cell aging tests will be detailed. Thirdly, a comparison between the physicochemical response of the reference and aged MEAs will be done, and all these results will finally be discussed afterwards, so as to draw conclusions about the study.

a) Observation using electronic microscopy

i. Scanning electron microscopy

Small pieces of reference MEAs $(1 \times 1.5\ \mathrm{cm^2})$ have been cut and placed in epoxy resin (following the method described in chapter II: Scanning Electron Microscopy (SEM)). Examples of SEM images for the three reference MEAs are proposed on Figure V - 1 - 2. For example, the mean thickness of SYM372-C obtained on a minimum of 4 different images, each one spaced with a distance of a few hundred of micrometres, is $11.1 \pm 1.6\ \mu\mathrm{m}$. With an estimated loading of $0.42\ \mathrm{mg_{Pt}cm_{geo}^{-2}}$, this is rather coherent with previous findings of $20\ \mu\mathrm{g_{Pt}cm_{geo}^{-2}}$ with thickness of $ca.\, 0.5\ \mu\mathrm{m}$ presented in chapter III: Physicochemical properties of the three ORR catalysts as well as in the literature [92].

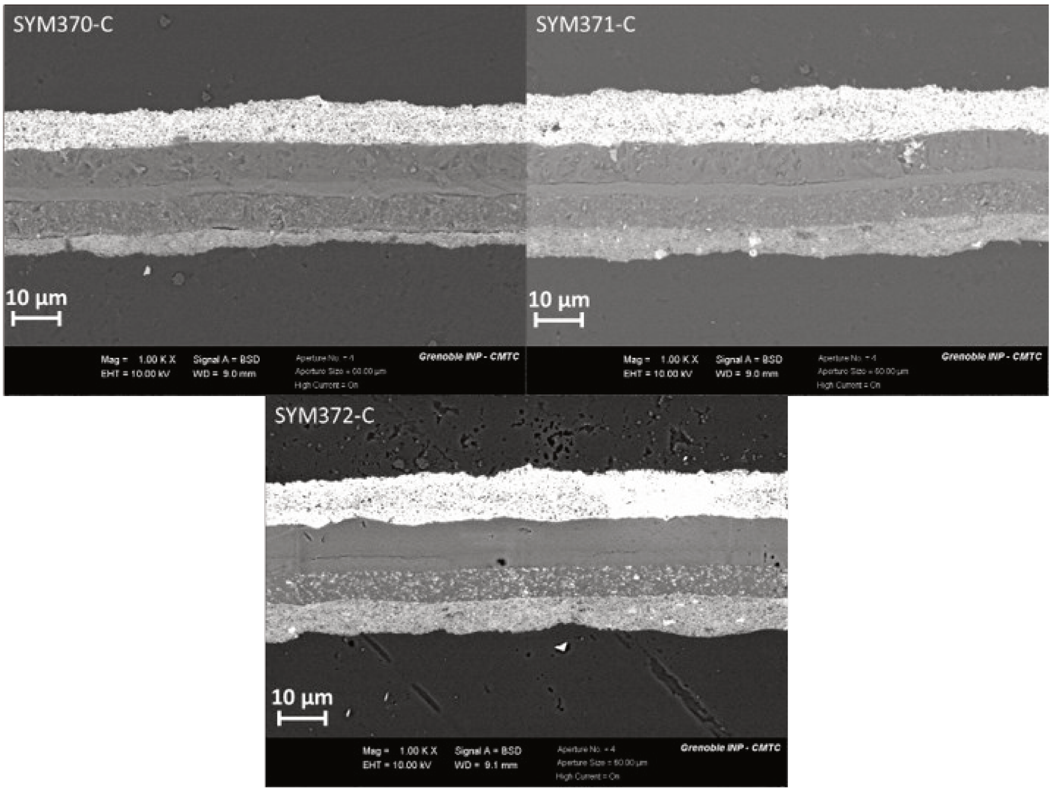

Figure V - 1 - 2: SEM images of the SYM370-C (top left), SYM371-C (top right) and SYM 372-C (bottom) reference MEAs

These SEM images enable to witness that the membrane used (Gore 775.15) has platinum inside one of its sides (each separated with the reinforcement in the middle). The presence of platinum particles in the proton exchange membrane (PEM) is aimed to limit the cross-over of O_2 and H_2 through the membrane, and therefore to mitigate H_2O_2 (hydrogen peroxide) formation. The latter likely follows partial reduction of oxygen (typically on H-covered Pt surfaces) or direct catalytic conversion of H_2 and O_2 on a catalyst surface and can further lead to $HO_2\bullet$ or $HO\bullet$ radicals created by H_2O_2 decomposition, the production of these radicals being lethal for membrane, leading to the formation of $R-O\bullet$ that will further destroy the membrane chains [200–203] in an avalanche sequence. Although this platinum additive is supposed to be present on the cathode side, for all the MEAs studied here, the membrane was flipped, so that the platinum additive is on the anode side. This enables the observation of possible platinum crystallites formation in the membrane, following the degradation of the cathode in the conditions of the test [95], the position of this so-called platinum band being closer to the cathode in technical PEMFC conditions as those experienced herein [95,96,192].

At the initial state of life for pristine MEA, there is no platinum particle in the cathode side of the membrane (upper part of the PEM on the images). On the anode side (on the other side of the reinforcement), a dense band of platinum particles can be observed, resulting from a mixture of platinum on carbon powder mixed with the ionomer constitutive of the membrane during the fabrication process.

ii. Transmission electron microscopy

The TEM grids are prepared as described in chapter II for the powder and active layer analyses. The particle size distribution of the commercial Pt/VC powder and of the as-sprayed reference SYM370C electrode are displayed on Figure V - 1 - 3. From the isolated nanoparticles, the distribution of the size for both the initial powder and the sprayed active layer are completely similar and within the error bar of one another. The micrographs are also really similar, when looking at the materials at initial stage (powder) and after ink formulation, spray deposition process and MEA storage; these processes have not affected the texture of the catalyst in the active layer compared to its pristine state in the commercial powder (in opposition to the slight changes seen in the previous chapter for the Pt_3Co/VC catalyst, associated to Co leaching into the ink). The isolated nanoparticles of the MEAs have very small mean diameters ($\overline{d}_\mathrm{n}$ = $2.94\ \mathrm{nm}$) and a narrow size dispersion. The mean volume-average diameter $\overline{d}_\mathrm{v}$ is slightly bigger: 3.26 nm. However, this kind of evaluation is blurred by the high extent of nanoparticles agglomeration in track-like structures. The awaited electrochemically active surface area (ECSA) expected from such a small mean particle size is *ca*. $100\ \mathrm{m}^2_\mathrm{Pt}\ \mathrm{g}^{-1}_\mathrm{Pt}$, but this overall large extent of agglomeration shall result in smaller effective value in PEM single cell. Comparing the $\overline{d}_\mathrm{v}$ value and the one obtained using X-Ray diffraction ($\overline{d}_\mathrm{XRD}$) will enable to confirm so (see next paragraphs).

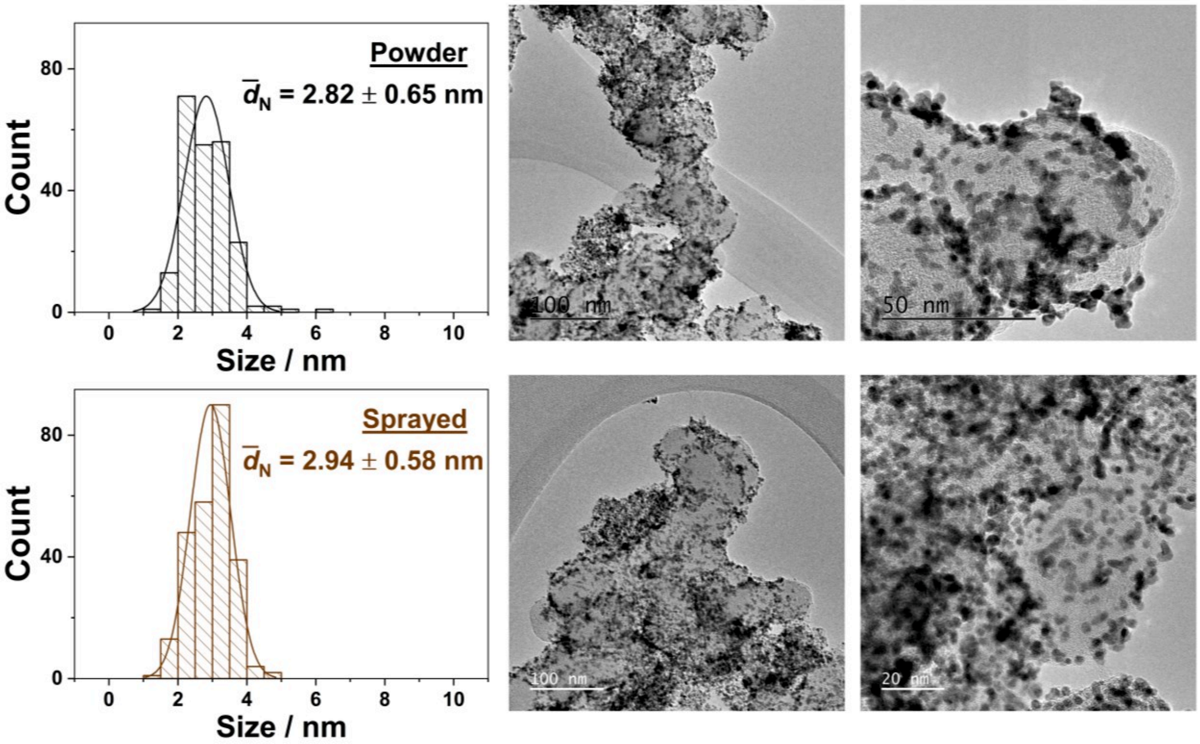

Figure V - 1 - 3: Particles size distribution histograms and TEM pictures of the Pt/VC powder (top) and reference MEA (bottom)

Although these microscopy observations are interesting, one must keep in mind that they are nevertheless very local, hence cannot give global information relative to the MEA (or its electrodes). It was well demonstrated in the literature that degradations are heterogeneous in the thickness of the electrode [92]. Yet, the experience of the team in PEMFC degradation studies and the comparison to literature data gives confidence on the statistical relevance of these images. Of course, crossed-information provided by more global techniques (XRD and Raman) will be of great help to confirm (or not) if the observed features are representative to the whole surface of the MEA (and of the electrodes).

b) X-Ray diffraction footprint of the reference MEAs

The catalyst being constituted of metallic nanoparticles supported on carbon black, it is possible to use X-ray diffraction as a powerful tool to identify its crystalline state (size of crystalline domains, presence of alloyed or segregated phases); XRD can also indicate the level of crystallinity of the carbon black substrate. Figure V - 1 - 4 gives the initial diffraction diagrams of the reference MEAs that will be used to compare with the aged ones. Only one group of diffraction peaks is observed (that of the Pt lattice), with peaks that are rather broad, an indication of rather small crystallite sizes. There is almost no diffraction peak or band corresponding to the graphitic domain of carbon at $2\theta = 26.5°$ [204] that would be characteristic of the graphitic domain of the Vulcan XC72 carbon. This means the Vulcan XC72 carbon support has very thin graphite crystallites (in the (002) direction), which was expected (this kind of carbon support is very well documented in the literature for many of its properties and known to be poorly graphitic and rather highly defective) [59,194,205,155,206,207].

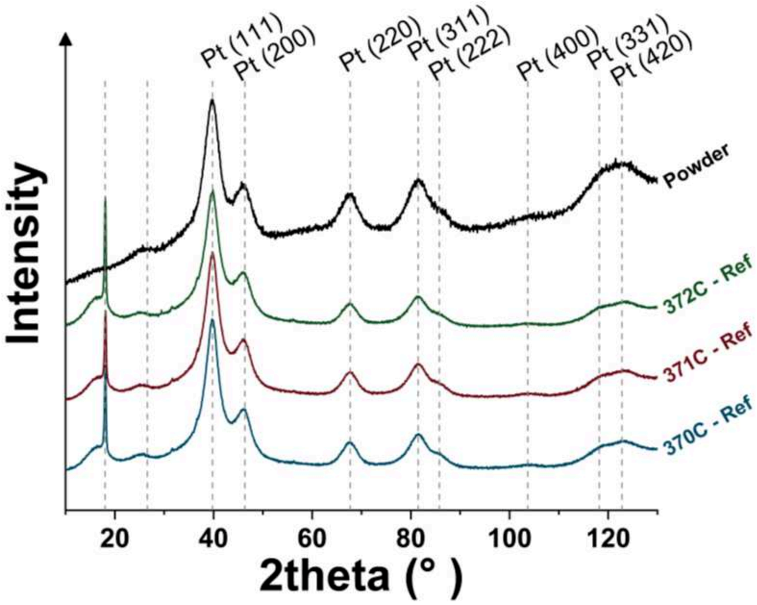

Figure V - 1 - 4: X-Rays diffraction diagrams of the catalyst powder and of the three reference Pt/C cathodes

The different crystallographic orientations of platinum are noted on Figure V - 1 - 4, as well as the diffractograms of the catalyst powder and the three reference MEAs. For the references, all three diagrams fit one to another rather perfectly and of most things, fit with the catalyst powder diagram, indicating that no issue nor (crystallized) pollutions are present on the cathodes. It is taken as granted for the aged electrode as well, which would have exhibited similar diffractograms at their initial stage. Moreover, as the diffraction diagrams show, there is only one single peak for each reflection, as clear for the (220) crystallographic orientation peak. This peak being not biased by neighbour orientations, is therefore chosen to fit and extract interesting parameter such as the crystallites mean diameter: $\overline{d}_{\mathrm{XRD}}$. In the following, we will consider that $\overline{d}_{\mathrm{XRD}}$ can be compared with the volume-averaged Pt nanoparticles diameter determined in TEM, written $\overline{d}_{\mathrm{v}}$.

The fit is made using a PsdVoigt1 model, as explained thoroughly in chapter II: X-ray diffraction (XRD). Using this PsdVoigt1 function, the mean crystallite size $\overline{d}_{\mathrm{XRD}}$ can be evaluated as 5.7, 5.8 and $5.7\ \mathrm{nm}$ for SYM370-C, SYM371-C and SYM372-C respectively. This is rather interesting because one would have expected a larger value if the larger Pt particles present in the membrane had been probed by the X-ray beam during the measurement due to the particle size one can observe on the SEM pictures displayed on Figure V - 1 - 2. This validates the choice to position the Pt-containing side of the membrane towards the anode, and means that any growth of Pt particles upon aging at the cathode should be noticeable without bias by the presence of this platinum band into the anode side of the membrane (except if another Pt band forms in the membrane owing to cathode aging – see previous chapter). These $\overline{d}_{\mathrm{XRD}}$ measurements also attest that the catalyst layers share a similar initial state regarding the particle mean volume-averaged diameter, signing the reproducibility of the MEAs preparation and homogeneity of the mother Pt/C catalyst. One notes that $\overline{d}_{\mathrm{XRD}}$ is almost twice the previously discussed value of $\overline{d}_{\mathrm{V}}$ (from TEM particle size distribution). This is related to the fact that the XRD is sensible to all the particles present in the powder/active layer, while only the isolated ones were taken into account in TEM. The two techniques are complementary: XRD does neither allow to estimate the particle size distribution nor if the smallest particles are affected. Hence, if the degradation leads to a change of the size, agglomeration, and dispersion of the particles, this will be detected by *post mortem* analyses using both XRD and TEM.

c) Raman spectroscopy of the reference cathode catalyst layers

Considering the carbon support is the same for all the cathodes studied in this thesis, only one pristine (not tested) cathode (SYM372-C) among the reference MEAs has been analysed in Raman spectroscopy (Figure V - 1 - 5). The sample was prepared as detailed in Chapter II – Experimental Section. The intensity of the spectrum is normalised by the maximal intensity of the G-D_2 convoluted band (at $1605\ \mathrm{cm}^{-1}$) that corresponds, if alone, to the D_2 band.

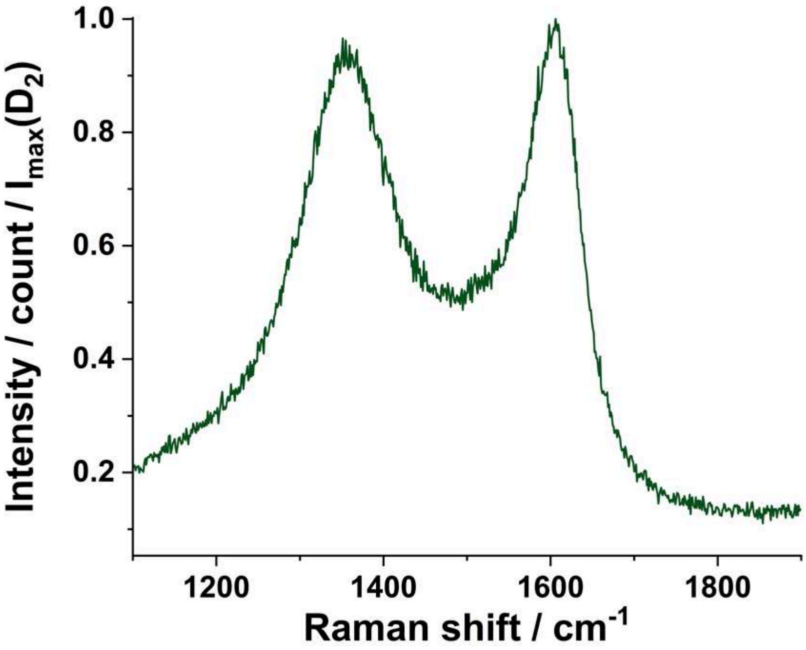

Figure V - 1 - 5: Raman spectrum of the cathode catalyst layer of SYM372-C

This spectrum of the outer layer of the active layer will be the reference with all the other spectra coming from the aged electrode. It is mainly disordered with very few graphite vibrational mode as can be seen with the absence of a thin peak at $1580 - 1585\ \mathrm{cm^{-1}}$: instead, it is fused into one large band with the D_2 disordered peak. This means that the carbon black (Vulcan XC72) is not graphitized, as expected [59,194], again confirming XRD observations.

2. Electrochemical behaviours during lifetime of the cells

This section presents the electrochemical results obtained for all the tested electrodes as a function of the time and the degradation voltage (which are referred in Table V - 1). The cells were operated at $80\ ^{\circ}\mathrm{C}$ and $1.5\ \mathrm{barr}$, in co-flow configuration with minimal flow rates of 400 and $200\ \mathrm{mL\ min^{-1}}$ (for air and hydrogen respectively) with gases at $50\ \%$ RH and using stoichiometric coefficients (over these flows values) of 1.5 on each side.

Due to experimental issue with OCV electrochemical impedance (a drawback of the test-bench used), a mean high frequency resistance has been used to correct all the electrochemical results from the ohmic drop. This high frequency resistance was calculated using the impedance performed at $0.60\ \mathrm{V}$ during the conditioning step, taking the least variating point at the highest frequency. This leads to a mean value $R_{\mathrm{HF}} = 35 \pm 2\ \mathrm{m\Omega\ cm^2_{geo}}$, using data from all the MEAs tested. The very small standard variation between the values measured validates the relevance of this average value of R_{HF}. All the following results will be developed as a function of the degradation time and of the cathode potential (assimilated as the cell voltage), starting with the experiments performed under H_2/N_2, then with the performance obtained with the different electrodes.

a) H_2 cross-over and short-circuit resistance: is the PEM affected by the potentiostatic test?

As it will have an impact in the forthcoming subsections, it is interesting to begin this study with the quantification of the membrane state of health, which is defined here by the hydrogen cross-over coming from the anode (measured by the hydrogen cross-over current density, $j_{\mathrm{cross-over}}^{\mathrm{H_2}}$) as well as the short-circuit resistance (R_{sc}). The hydrogen cross-over current density is proportional to the $\mathrm{H_2}$ flux through the membrane; upon reaching the positive electrode (the PEMFC cathode in "normal" operation), this H_2 is oxidised at the Pt/VC catalyst surface; as the hydrogen oxidation reaction (HOR) is very fast on Pt surfaces, the current measured is limited by the H_2 mass-transport. Figure V - 2 - 1 shows the evolution of $j_{\mathrm{cross-over}}^{\mathrm{H_2}}$ during potentiostatic steps, ranging from 0.3 to $0.7\ \mathrm{V}$.

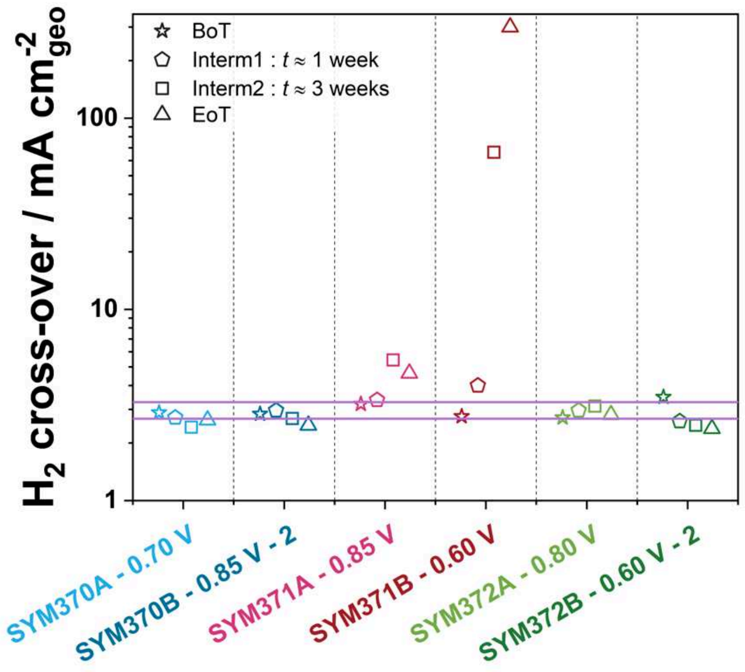

Figure V - 2 - 1: Evolution of the hydrogen cross-over current density for the different characterizations along the lifetime of the MEAs for all 6 studied electrodes

On this figure, is plotted the mean value and error bar of the hydrogen cross-over current density for the BoT, determined with the value of each studied electrode (2 horizontal purple lines). It is equal to $3.0\ \pm 0.3\ \mathrm{mA\ cm_{geo}^{-2}}$ (in agreement with the literature [208,209]) and most electrodes stay within this range during all their lifetime (from left to right: from BoT to EoT, for each electrode). An exception is the SYM371B–0.60V electrode, for which one notices a tremendous increase between characterizations Interm1 and Interm2, $j_{\mathrm{cross-over}}^{\mathrm{H_2}}$ reaching $66\ \mathrm{mA\ cm_{geo}^{-2}}$ after Interm2 and $300\ \mathrm{mA\ cm_{geo}^{-2}}$ at end of test. To a much smaller extent, electrode SYM371A-0.85V also shows an increase of $j_{\mathrm{cross-over}}^{\mathrm{H_2}}$, the others showing stable values over the whole durability test. These electrodes were further tested at the LEMTA with an infra-red (IR) camera positioned at $1\ \mathrm{m}$ from the cell (composed of a serpentine flow field on the anode side on which is screwed a plexiglass frame to hold the observed MEA). A small flow of hydrogen is put at the anode inlet (bottom right corner on the picture of Figure V - 2 - 2 thereafter) and the cathode side is let "breathing" at open air; if H_2 cross-over locally proceeds, H_2 will react with O_2 from air at the cathode catalyst surface, leading to local increase of temperature which will be detected by the IR camera. The last IR thermography pictures taken are presented for both SYM371A-0.85V (left) and SYM371B-0.60V (right). For the first electrode, nothing can be seen on the IR picture, meaning no hole is present on the surface of the MEA. The green pixels in the centre of the frame (and of the MEA) represent the hotter areas due to the combustion of hydrogen which was able to "cross" the membrane and react with the ambient air. For all the electrodes during the observation, the bottom right corner (easily seen on left picture) is always greener than the rest of the MEA, independently of the electrode and is thus considered as an artifact (maybe a small gap that lets either hydrogen go or air come in). Due to this observation, it was concluded that no pinhole appeared on the surface of the membrane for SYM371A-0.85V, despite its slight increase of the hydrogen cross-over oxidation current value. For the other electrode, namely SYM371B-0.60V, the IR picture confirmed that a crack of *ca.* $2-3\ \mathrm{cm}$ appeared over the aging tests, responsible for the high cross-over current observed during the experiment at LEPMI.

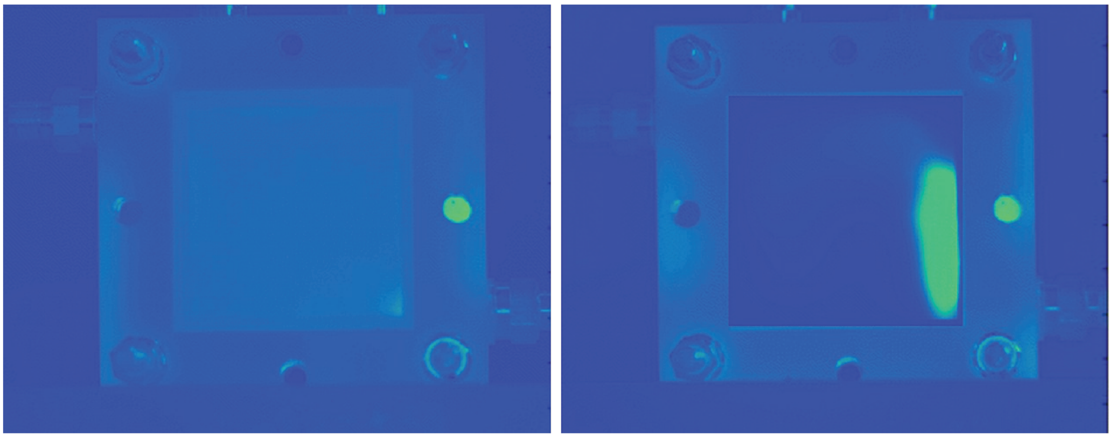

Figure V - 2 - 2: Pictures taken by infrared observation of the aged SYM371A-0.85V (left) and SYM371B-0.60V (right) MEAs in breathing configuration

The small variations of the hydrogen current measured for the other electrodes (smaller than for electrode SYM371A-0.85V, which showed no hole in IR thermography) - within the error bar of the initial measured current, indicate that no weakening of the membrane has appeared during the aging, regardless of the potentiostatic hold potential of the cathode.

The second parameter studied with the potentiostatic hold under $\mathrm{H_2/N_2}$ is the short-circuit resistance R_{sc}. This resistance most likely gives information on the proximity of carbon grain from both side of the membrane: the closer the carbon grains, the lower the resistance. It can therefore give information on possible thinning of the membrane or defect on the initial/aged

MEAs. Figure V - 2 - 3 shows the evolution of this resistance for each electrode from BoT to EoT. It is more complicated to find correlations here between the voltage of degradation and the evolution of R_{sc}. From an overall point of view, this resistance tends to decrease as the electrode ages but not strictly (as demonstrate SYM371A-0.85V and SYM371B-0.60V), which would imply an easiest way for current to pass through the membrane as time passes by. Furthermore, and quite unrelated to the degradation voltage, the SYMX-A denominated electrodes have always lower initial R_{sc} than the SYMX-B electrodes. During the hot-pressing of the electrodes, two different sets of metallic plates were used to alternate the preparation of the MEA (one used as the other is cooling down). It is possible that the repartition of the pressure was not as homogeneous for both sets of plates, leading to membranes which were not strictly compressed in the same way. This is, to the author's knowledge, not very well documented in the literature. There is no way to confirm this, but the effect does not seem overwhelming, anyways. The working time tends to uniformize all the intern architecture of the MEA, toward a R_{sc} value between $170 - 260\ \Omega\ \mathrm{cm}^2_{\mathrm{geo}}$.

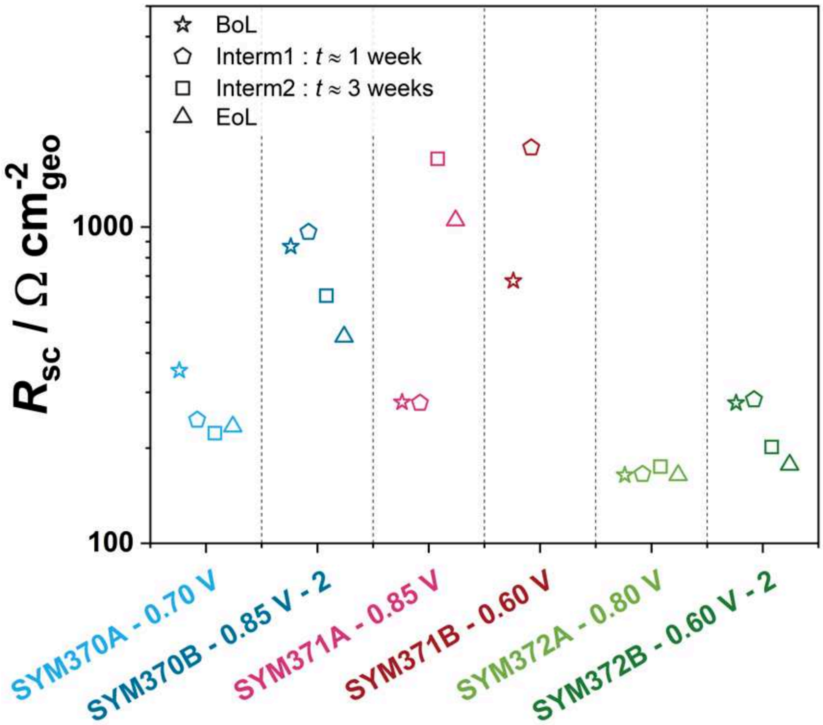

Figure V - 2 - 3: Evolution of R_{SC}, the short-circuit resistance for all the aged electrode during their lifetime

b) H_2/N_2 Cyclic voltammetry: impact on platinum in the active layer

The values of R_{sc} and hydrogen cross-over previously obtained are used to correct the cyclic voltammetries performed under $\mathrm{H_2/N_2}$ to evaluate the hydrogen underpotential deposition ($\mathrm{H_{upd}}$) features of the catalyst layers. More specifically, all the CVs are corrected by the measured value for each electrode at the corresponding working time following the equation:

$$j_{\mathrm{corr}} = j_{\mathrm{measured}} - j^{\mathrm{H_2}}_{\mathrm{cross-over}} - \frac{U_{\mathrm{IR\,free}}}{R_{\mathrm{sc}}} \qquad \text{(Eq. V.2.1)}$$

with j_{measured} the experimentally measured current density (in $\mathrm{mA\,cm^{-2}_{geo}}$), $j^{\mathrm{H_2}}_{\mathrm{cross-over}}$ the hydrogen cross-over current density (in $\mathrm{mA\,cm^{-2}_{geo}}$) and R_{sc} the short-circuit resistance (in $\Omega\,\mathrm{cm^{2}_{geo}}$) both determined with potentiostatic steps and linear regression (see chapter II: Chronoamperometry (CA) for more detailed information) and $U_{\mathrm{IR\,free}}$ the cell voltage corrected from the ohmic drop using j_{measured}.

The effect and validation of the correction are presented with Figure V - 2 - 4, that presents CVs along the lifetime of the electrode SYM372B-0.60V-2 with (dash lines) and without (lines) correction.

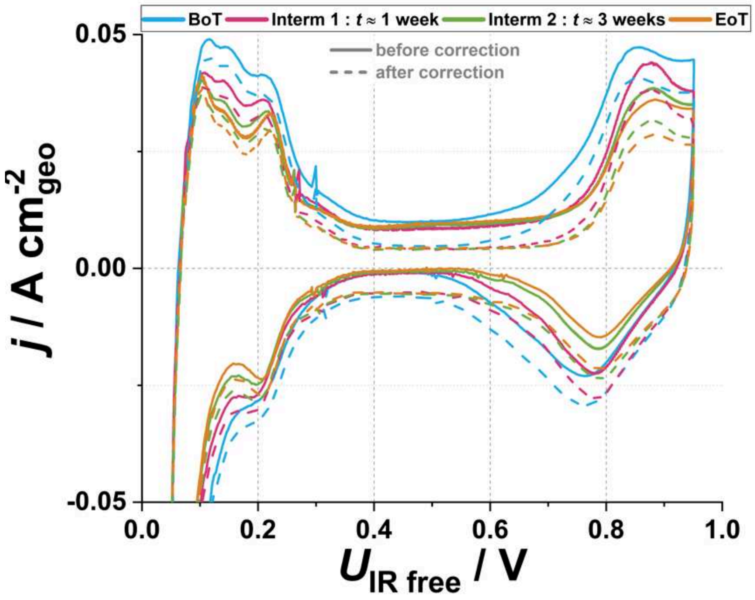

Figure V - 2 - 4: H_2/N_2 CVs performed at 150 mV s^{-1} with (dash lines) and without (lines) correction of the hydrogen cross-over and R_{sc}

This correction will help better apprehending the differences in the CVs that appear through the life of the cells, that were more or less disordered before due to different cross-over current or short-circuit resistance.

If one reconsiders the organisation of the different electrodes presented in Table V - 1 in a different manner to apprehend better the aging cell voltage chosen for each, it leads to the order drawn on Figure V - 2 - 5 presented below, ranging from the higher to the lower voltage.

With regards to this ranking, two groups of electrodes are made: the electrodes aged at voltage/potential for which platinum-oxides cannot be reduced (above $0.80\ \mathrm{V}$) and the electrodes where platinum is supposed to stay (at least partially) metallic (below $0.70\ \mathrm{V}$). These electrodes will be plotted together for each aging duration to moderate the number of graphs, more graphs will be available in Figure A - 2.

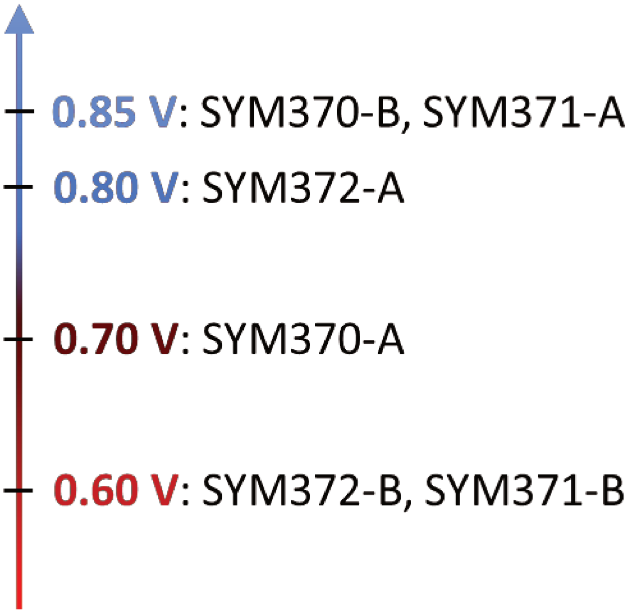

Figure V - 2 - 5: Summary of the cell voltages ranking

To begin with, Figure V - 2 - 6 exhibits the shape of the BoT electrodes after conditioning. All the CVs displayed are the fifth and last cycle performed at this scan rate. The six electrodes' curves are similar after correction; five peaks can be identified (vertical dotted grey lines) and will be used to witness the evolution of the electrodes state along their life. Three of these peaks are in the $\mathrm{H_{upd}}$ region, observed at 0.113, 0.146 and $0.211\ \mathrm{V}$ with a reasonable error of 2, 1 and $3\ \mathrm{mV}$ respectively.

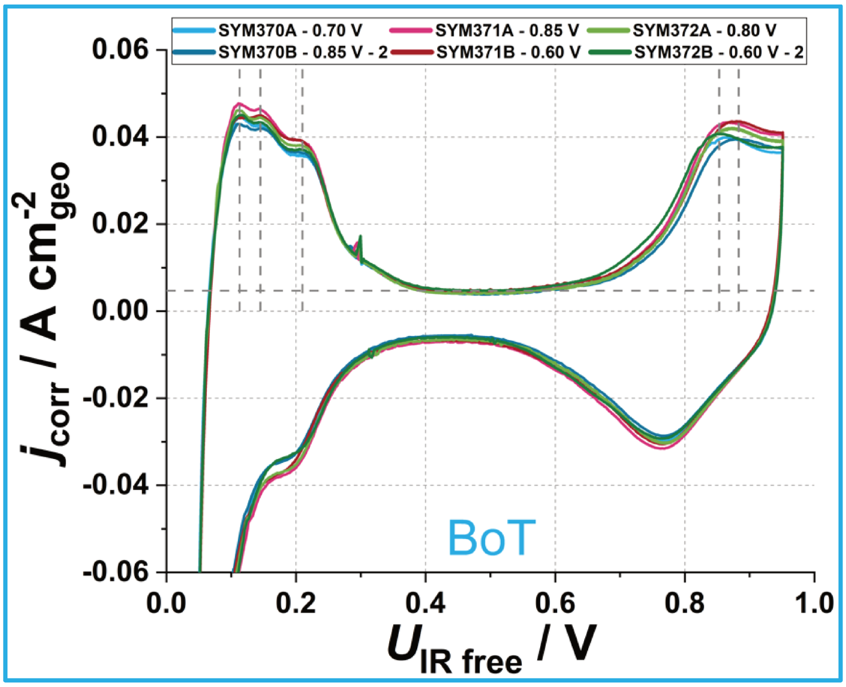

Figure V - 2 - 6: 5th CV performed at 150 mV s^{-1} for each cathode (positive electrode of the MEA) after the conditioning step at their beginning of test

A fast observation gives us decreasing peak current intensities when looking from low to high voltage. The two others are the peaks of the oxidation/reduction of the platinum oxides, located respectively at 0.866 and $0.766\ \mathrm{V}$. The voltage at which the reduction peak is observed is similar for all the electrodes with a measured error of $2\ \mathrm{mV}$, contrary to the oxidation peak which is not very uniform for the six electrodes: the two vertical dashed lines indicate the voltage window in which the peak is observed (the dashed lines being both the lowest and the highest voltage). This peak can be approximately located at $0.867 \pm 0.011\ \mathrm{V}$. An experimental artifact is observed slightly under $0.3\ \mathrm{V}$, that creates a small peak (a single point); it is believed to be related to the potentiostat and will not be further investigated.

The corrected CVs during the initial, intermediate and final characterizations are gathered in Figure V - 2 - 7 and separated in two groups, the high voltage (above $0.80\ \mathrm{V}$, left side) and low voltage (below $0.70\ \mathrm{V}$, right side) groups. After the first week of degradation, the CVs of both the high and low voltage electrodes seem rather unaffected from an overall point of view. Yet, if we take a closer look at the voltages at which the first two peaks in the $\mathrm{H_{upd}}$ region are observed, they moved towards lower voltages and this change in voltage is also true for the reduction peak of platinum oxides which moved positive. Given the incertitude, it is less possible to assume the probable variation of the platinum oxide formation peaks voltage.

These observations apply also after $t = 3\ \text{weeks}$ and $t = 1\ \text{month}$ of experiment, except that a shift of voltage is present for the SYM371A-0.85V during the Interm2 characterizations batch. In this case, all the $\mathrm{H_{upd}}$ peaks are shifted positive, even the reduction one during the backward voltage scan, the oxidation and reduction peaks voltages of platinum oxide stay similar. These subtle changes of peak potential point towards a growth of the Pt particles [95,97], that seems progressive in the course of the test, regardless of the voltage applied.

The third peak of the $\mathrm{H_{upd}}$ region is interesting to separate the two aging regimes. Along the degradation at high potential (left graph on Figure V - 2 - 7), it appears that it does not change (exception made for the strangely shifted SYM371-A at Interm2 stage, not taken into account for the mean and error voltages) and stays at $211 \pm 3\ \mathrm{mV}$, $209 \pm 1\ \mathrm{mV}$, $211 \pm 1\ \mathrm{mV}$ and $212 \pm 2\ \mathrm{mV}$. What is more interesting is that for voltage degradation below $0.70\ \mathrm{V}$, this peak voltage increases slightly with the aging duration (from the initial $211 \pm 3\ \mathrm{mV}$ to $220 \pm 2\ \mathrm{mV}$ after a month).

Another observation is related to the peaks current relative position: at the initial stage, the current was decreasing for increasing voltage peak in the $\mathrm{H_{upd}}$ region, starting with the highest current for the lowest voltage located peak to the lowest intensity peak at the highest voltage position. This is also depending on the aging voltage. As can be seen on the EoT graphs on the bottom of Figure V - 2 - 7, the third peak in the $\mathrm{H_{upd}}$ region is either the highest (left) or lowest (right) intensity peak and reaches, respectively, a steady state or keeps on decreasing. Assuming that each peak observed is characteristic of a crystallographic orientation, it seems that the voltage at which the electrode is maintained influences the aging mechanism at stake. It is however not easy to attribute $\mathrm{H_{upd}}$ peaks to particular crystallographic orientation.

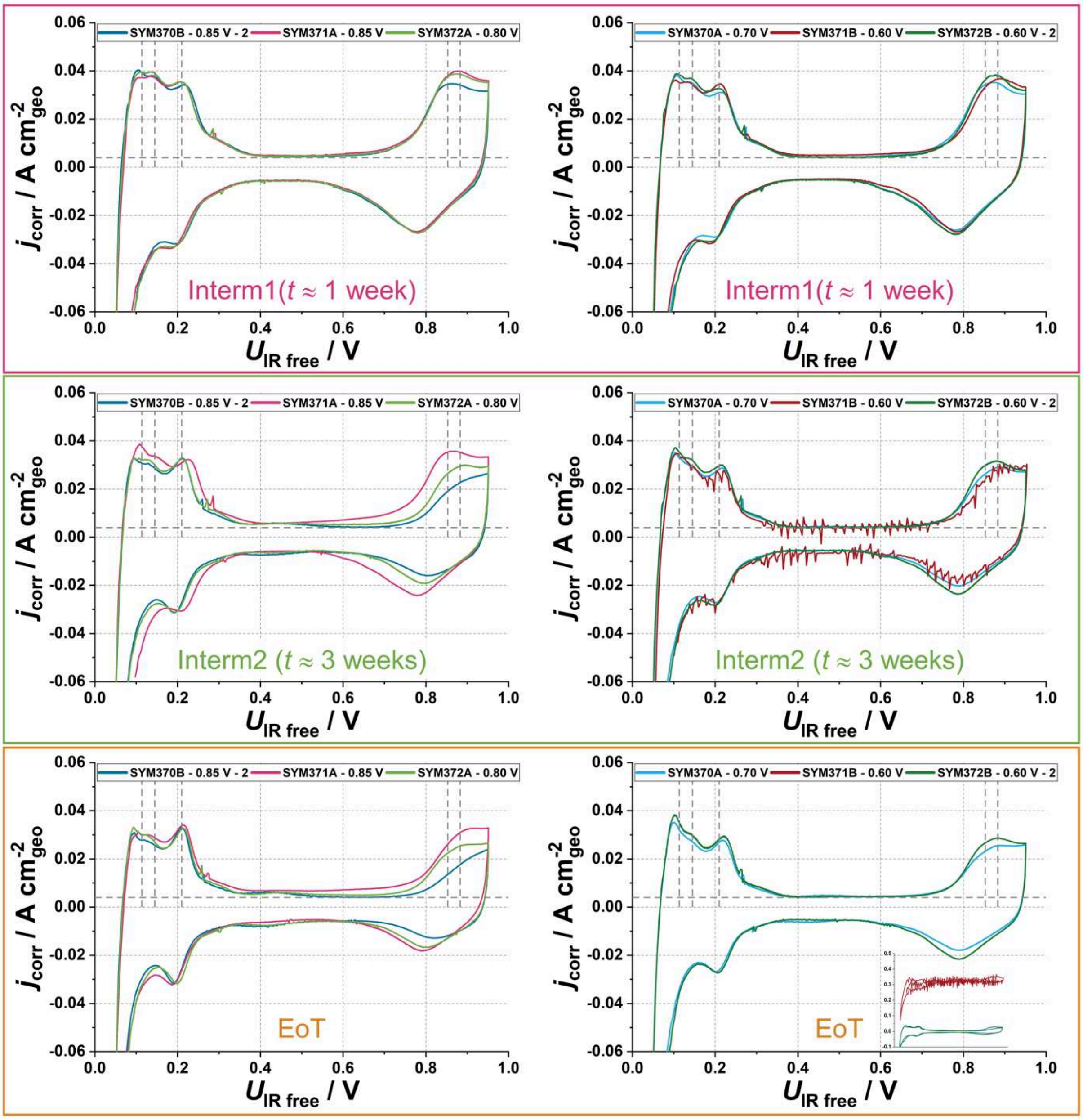

Figure V - 2 - 7: Evolution of the CVs under H_2/N_2 for the electrodes aged at voltage higher than 0.80 V (left) and lower than 0.70 V (right), CVs performed at 150 mV s^{-1}

Indeed if one would use a simple linear combination of monocrystals $\mathrm{H_{upd}}$ region signature peaks, for the catalyst studied here, it would lead to (111) and (110) facets [30]. It was however demonstrated and admitted that single metallic nanoparticles are cubo-octahedron revealing hexagonal (111) facets connected with 3 similar facets and 3 square (100) facets, presenting (110) edges [210]. This difference in the peak alteration may influence the shape of the aged particles, therefore it will be interesting to observe them in high resolution TEM (HRTEM) to verify this assumption, which has not been made when writing this thesis.

As represented on the right-hand Interm2 and EoT graphs, the noised dark red curve of SYM371B-0.60V has suffered the impact of the previously-observed crack on its membrane, making the hydrogen presence at the cathode side detrimental for the characterisation. It was still possible to correct from the oxidation current in the Interm2 stage but no longer possible at EoT, owing to the too large difference between the capacitive current of the CVs and of the hydrogen oxidation faradaic current, leading to a flattening of the curve at EoT stage. It was therefore no longer possible to determine the peak position, except for the lowest voltage of the $\mathrm{H_{upd}}$ peak.

Still looking at the Interm2 and EoT stages for both aging groups, it appears that a couple of wide oxidoreduction peaks between 0.35 and $0.50\ \mathrm{V}$ is forming, attributed to the functionalization of the carbon. As one would expect, this couple of peaks is more evident after aging at the highest voltages and is least present for the low aging voltage group. Also, it seems the high aging voltages impact the formation of platinum oxide, as the peak tends to disappear with the aging duration. On the contrary, when looking at the low aging voltages, a linear part in the platinum oxide formation is more pronounced and tends to let two peaks appear in that region, that could be attributed to $\mathrm{Pt-OH}$ and $\mathrm{Pt-O}$ formation, from low to high voltage respectively.

Figure V - 2 - 8 gathers the measurements of the ECSA (divided by the initial cathode platinum loading, similar to a roughness factor) of the electrodes at each of the four characterizations (BoT, Interm1, Interm2 and EoT); this enables to monitor the evolution of the active area and thus of the platinum nanoparticles size or quantity in the active layer.

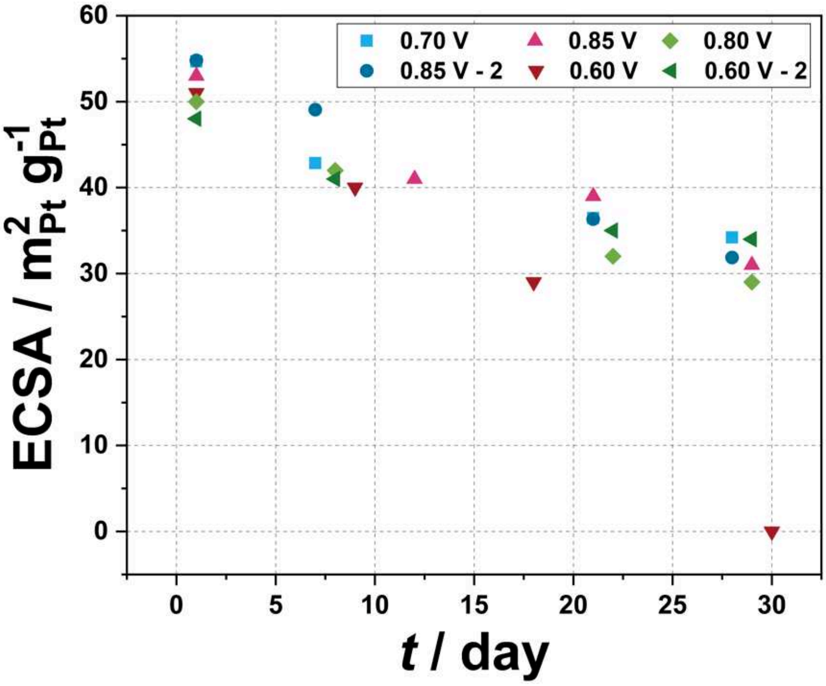

Figure V - 2 - 8: Evolution of the cathode ECSA with the aging time for each aging voltage applied. The ECSA is reported to the initial mass of platinum in the active layer.

With regards to the dispersion of the initial active surface values, it is not possible to confirm by looking at the ECSA that different aging mechanisms are at stake: the decrease of ECSA versus time of test seems rather similar whatever the voltage value in the potentiostatic holds, in agreement with the work of Castanheira *et al.* [211]. Also, the number of points (therefore, of characterizations along the lifetime of the electrodes) is too small to try to claim with certitude a linear (or more complex) decrease trend for the different aging tests; however, it seems that the decrease of the ECSA is initially faster and then slows down. In the case of the SYM371B-0.60V (0.60 V on Figure V - 2 - 8), only the first two points are to be considered, the third being measured with a very noisy CV (shown on Figure V - 2 - 7 Interm2 right graph after correction) thus not very reliable and greatly affected by the crack formation. One conclusion is, to be certain, that all the catalyst layers are affected by their aging test and suffer between 40 and 45% decrease of their developed surface in only one month of experiment. This was a surprise, and the cell voltage applied makes very little difference in the trends. Once again, ECSA does not seem to be a very good marker of degradation (see Chapter IV. Degradation of Pt_3Co catalytic layers in 25 cm² Proton Exchange Membrane Fuel Cell setup – A segmented cell and material study).

These observations make sure that the cathode catalyst layer is deeply affected by the cell voltage, therefore cathode potential, at which the electrode is polarized during its functioning. In addition to the information provided thanks to H_2/N_2 CVs, further insights into the effects of the potentiostatic degradation tests will be given by the current evolution while holding voltage during degradation and during the performance measurements.

c) Decrease of the reduction current produced during the lifetime of the cells

The potentiostatic degradation test was designed to better understand the aging (and possibly the heterogeneity of aging) of the different interfaces and materials at the static various functional regimes a real system may experience; to be more specific, the effect of the cell voltage (cathode potential) was explored on an unprecedented large domain, from 0.6 to 0.85 V in single PEMFC cell. In these conditions, a major difference with more common aging procedures at fixed current density encountered in the literature is the very large difference in current densities observed during the degradation test. Figure V - 2 - 9 shows the very different current densities obtained under hydrogen-air flows with stoichiometric coefficients of 1.5 on each side, in the case the minimal gas flows of $400\ \mathrm{mL\ min^{-1}}$ of air and $210\ \mathrm{mL\ min^{-1}}$ of hydrogen were not sufficient. On the one hand, these gas flows were fixed rather high to ensure, as much as possible the stability of the measured current. In the case of the high cell voltage (0.80 V) with initial current of $0.1\ \mathrm{mA\ cm_{geo}^{-2}}$, this constant flow leads to air stoichiometric coefficients of 10 at the beginning of test and 20 at the end of test, the current being roughly divided by 2 during the aging test. For the 0.85 V tests, for which the current density is even smaller, these high stoichiometric coefficients ensure the stability of the signal (during the cells operation with the used test bench, the current oscillated periodically with a triangle aspect; the reason behind this behaviour is still unclear but if the gas flows were to follow the current variation to correct the stoichiometry, it would have led to uncontrolled instabilities that the author wanted to prevent). On the other hand, such high gas flows surely have an impact on the water contained in the layers.

Of course, in addition to the effect of the gas stoichiometries, the cathode producing a very different current at these different cell voltages, hence a very different amount of water versus time, it has for sure an influence on the hydration of the ionomer of the active layers and of the membrane.

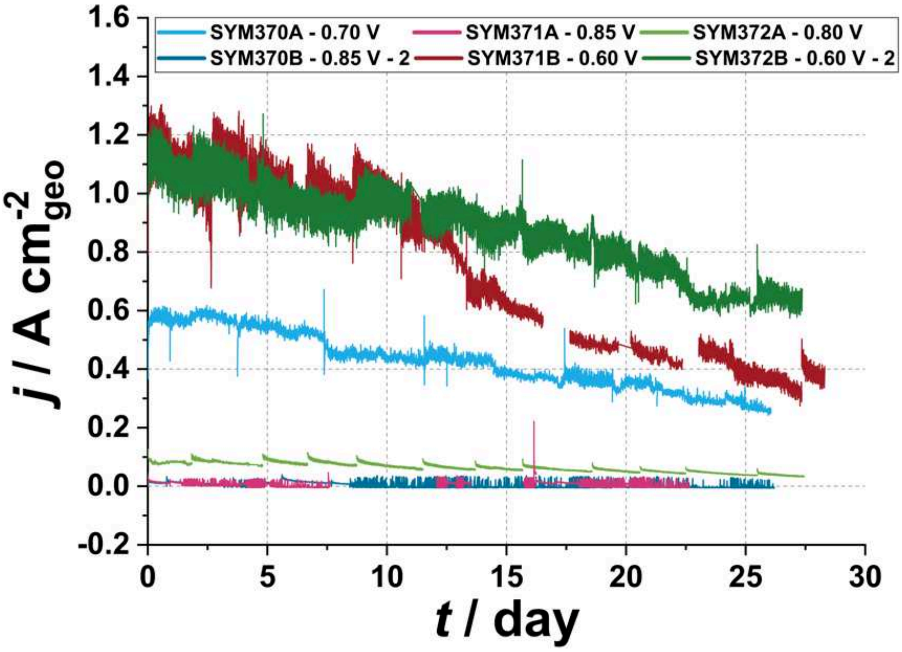

Figure V - 2 - 9: Evolution of the reduction current measured during the potentiostatic degradation steps

Staring at the current densities' evolution on Figure V - 2 - 9 in more details, it appears that for two electrodes taken from two sets (the SYM371B-0.60V and SYM372B-0.60V-2 electrodes), similar current densities were produced at beginning of test, which is a good point for the reproducibility of the experiment. Moreover, it is easy to determine the moment at which the crack appeared in SYM371B-0.60V, approximately $12 - 13\ \mathrm{days}$, which is between Interm1 and Interm2 characterizations, in accordance with the CVs observations in the previous subsection. For each MEA tested, the current densities decrease to half of their initial value in a little less than a month, independently on the aging voltage chosen (in agreement with the near-similar loss of ECSA for all cathodes). In the case of the electrodes aged at $0.85\ \mathrm{V}$, the current densities obtained are very low at the beginning of test and very rapidly fall to zero (probably following the decrease of short-circuit resistance and increase of H_2 cross-over current monitored and detailed above) accompanied with electrical noise. This noise is not believed to result from electrochemical reaction as it is much higher than the $2 - 5\ \mathrm{mA\ cm_{geo}^{-2}}$ hydrogen oxidation current resulting from the cross-over. The voltage was nevertheless held for as long as required for the aging of the electrodes.

There is no real observation of current reversible losses except for the SYM372A-0.80V and the SYM372B-0.60V-2 electrodes (respectively light and dark green on graph). For the first electrode, it is easily seen that every refill of the cell and restart of the aging is done at a higher current than the previous steady state. For the latter electrode, it can be seen after the Interm1 characterisation (taking place at $t = 7\ \mathrm{days}$) that the current density increased slightly. The study of the polarization curves for the performance determination before and after the characterization will give more information on the performance losses and possible reversible losses existence.

d) Polarization curves: loss of performance over time

All the presented polarization curves are performed with a stoichiometric coefficient of 1.5 on each side with similar minimal gas flows as previously detailed: $400\ \mathrm{mL\ min^{-1}}$ of air and $210\ \mathrm{mL\ min^{-1}}$ of hydrogen. Each curve is the first cycle upward scan, which has been corrected of the ohmic drop. Figure V - 2 - 10 presents all the beginnings of test of the different electrodes in a corrected cell voltage *vs.* geometric current density coordinate system. On the one hand, all the electrodes are not exhibiting the same initial performance but are rather reproducible for a similar batch (SYM370A-0.70V and SYM370B-0.85V-2 as well as SYM372A-0.80V and SYM372B-0.60V-2) with identical kinetics region (above $0.80\ \mathrm{V}$) current densities; an exception to this observation is made for the SYM371 batch. On the other hand, all the electrodes have instabilities in the mass-transport region, starting below $0.70\ \mathrm{V}$. It was decided to not go down to $0.55\ \mathrm{V}$ (without correction) due to the increasing presence of such measurement variations and noises. The difference in this voltage region for a given batch, MEAs SYMX-A presenting better transport properties, corresponds well with the smaller short-circuit resistance observed (discussed with Figure V - 2 - 3). This is ascribed also to a possible imbalance in the hot-pressing step for the SYMX-B MEAs. However, it is noted that for similar active layer platinum loading (SYM371 and SYM372 batches), the reproducibility of the polarization curves is rather satisfying.

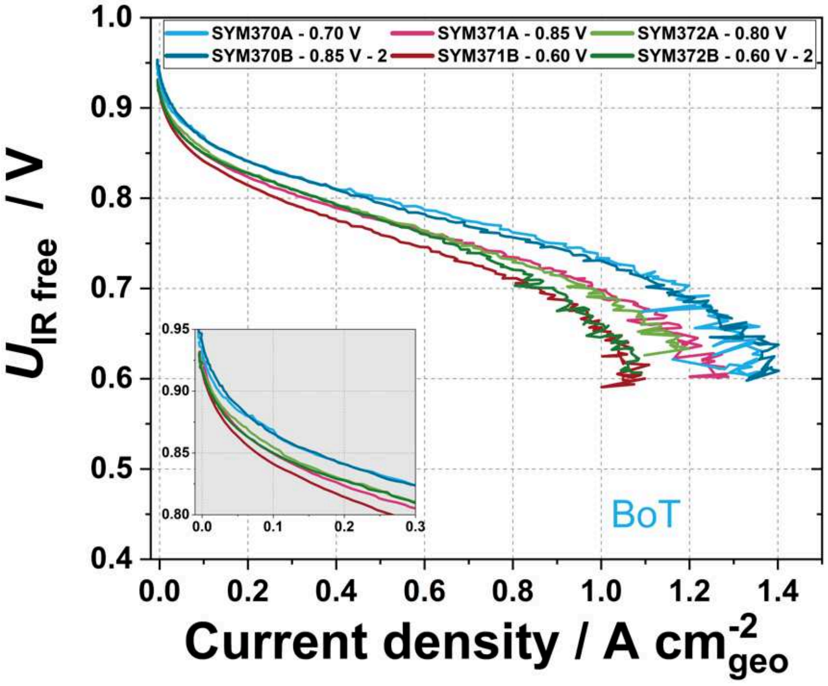

Figure V - 2 - 10: Beginning of test polarization curves under H_2-Air flows at 1.5 stoichiometric coefficient, 10 mV s^{-1} scan rate and 80°C. The curves are acquired just after the end of the conditioning step

Other experimental conditions were also studied to understand the aspect of the curves presented in the previous figure and are shown on Figure V - 2 - 11.

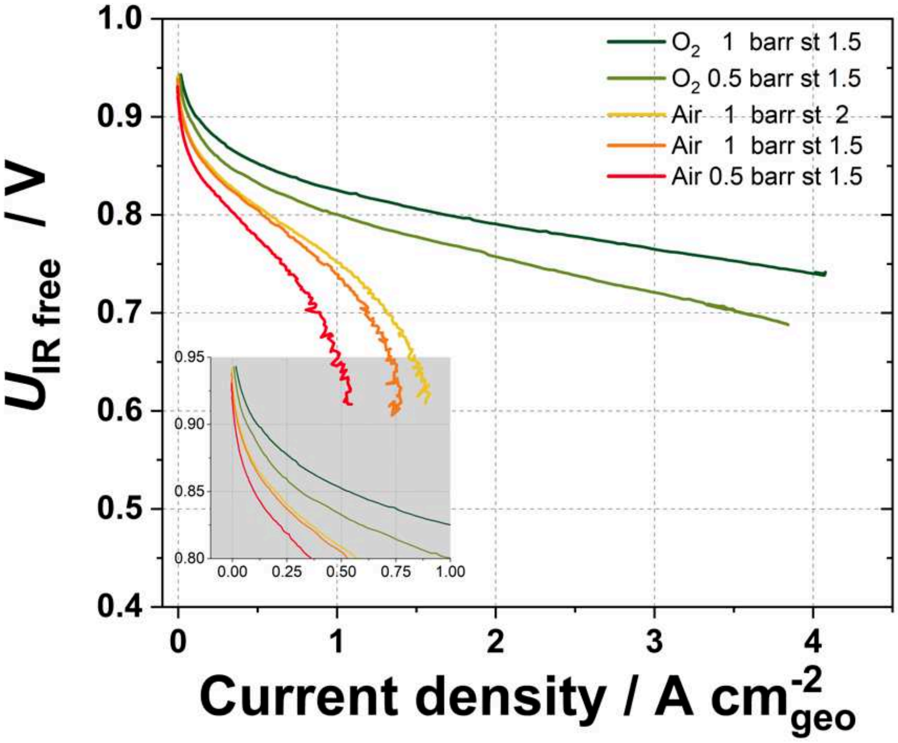

Figure V - 2 - 11: Influence of the cathodic gas on the performance at the beginning of test of SYM372B-0.60V-2. Polarization curves performed at 10 mV s^{-1} and 80°C

On Figure V - 2 - 11, one can remark that the performance at both low and high current densities are naturally very dependent on the gas nature, pressure and stoichiometric coefficient used for the cathodic inlet gas, as documented in the literature [212]. In the case of this study, a focus is made on the performance at low overpressure, low stoichiometric coefficients and using air instead of oxygen, with the idea to have access to performance in conditions that are as close as possible to a real automotive system. The presence of this mass-transport limitation at high current densities will give information on the state of the active layer, whether it is modified or not. Also, if the gas is switched from air to oxygen (yellow-red to green curves), there is no mass-transport limitations observed - even for stoichiometric coefficients of 1.5 - occurring at cell voltage below $0.70\ \mathrm{V}$ as previously observed for the initial curves of all the electrodes fed with air; this demonstrates the initial wellbeing of the electrode.

Assuming that the initial electrodes are all performing properly, the electrodes are separated in two groups to be further analysed, as for the $\mathrm{H_2/N_2}$ characterizations study: the high voltage aging group (with SYM370B-0.85V-2, SYM371A-0.85V and SYM372A-0.80V) and the low voltage aging group (with SYM370A-0.70V, SYM371B-0.60V and SYM372B-0.60V-2). The performance assessment of all the electrodes for the four different characterizations along the lifetime of the cells are gathered in Figure V - 2 - 12. Many things can be observed and, for the sake of clarity, the analysis will be done first for the high voltage group and then for the low voltage group.

From BoT to EoT, the curves are drastically changed by the aging procedure at high cell voltage. The performance is decreasing in both the low and high current densities for all three electrodes (note the absence of SYM371A-0.85V in the Interm2 graph is, because the characterization between $t = 10$ days to EoT could not be made for this electrode – technical issue). On the four graphs, the mass-transport limiting region at high current densities progressively disappears and the curves become linear after a very slow kinetic exponential part. The curves of the SYM370B-0.85V-2 electrode denote very different changes than for the two others, leading to two comments: firstly, even if SYM371A-0.85V aged at the same cell voltage, there was a heating issue during its aging, leading the cell temperature to fall down to $25°\mathrm{C}$, slowing down the degradation of the active layer; secondly, SYM372A-0.80V aged at lower cell voltage and suffered less geometric current density losses from the aging test, having better performance at EoT than SYM370B-0.85V-2. This let us believe that the voltage has an additional influence on the rate of degradation other than just the temperature. Also, SYM370B-0.85V-2 had a higher initial ECSA: this can explain that its performance falls much faster, hence closing the gap with SYM372A-0.80V before Interm2, thus more or less in $t = 21$ days; indeed, the roughness factor is known to majorly impact the degradation rate [122]. Moreover, despite having a high impact on the performance, the degradations that occur at high voltages are not totally irreversible, seen on the Interm1, Interm2 and EoT left-hand graphs: there is always, for each electrode, a non-negligible regain of performance after the $\mathrm{H_2/N_2}$ characterization, as depicted by the dashed lines curves, both in the low and high current density regions. This can be explained by a possible reduction of the platinum oxide by the 15 CVs (at three different scan rates, still present in the protocol even if only part of them are shown in this manuscript) performed in these conditions, that increases the kinetics activity of the active layer (Pt needs to be reduced to catalyse the oxygen reduction reaction, ORR). However, it is not possible to exclude that such regeneration of the active layer is not coupled with a platinum removal on the outer layers of the platinum nanoparticles.

For the low cell voltage aging group, some of the previously-made observations are different. Indeed, by simply looking at the maximum current density obtained for SYM370A-0.70V and SYM372B-0.60V-2 on the right-hand graphs, $1.0\ \mathrm{A\ cm_{geo}^{-2}}$ is still reached after $t = 30$ days, which is significantly better than the $0.7 - 0.8\ \mathrm{A\ cm_{geo}^{-2}}$ obtained for the high voltage group. As well, the low current density region is decreasing much slower. These two observations enable to posit that the cathode active layer degradation is less significant at potentiostatic operation at low cell voltage, in agreement with the almost total absence of reversible degradations noted. Indeed, on Interm1 and EoT graphs, the pre and post characterizations polarization curves are overlapping quite well. This latter fact can be explained by the aging voltages (0.6 and $0.7\ \mathrm{V}$ for SYM372B and SYM370A respectively), that are below the platinum reduction peak voltage of $0.75\ \mathrm{V}$ observed during the CVs under $\mathrm{H_2/N_2}$. However, the Interm2 graph shows a high regain in current density in the high current density region, so a possible oxidation of the active layer may still be possible, but at a much slower rate than for the higher voltage aging group.

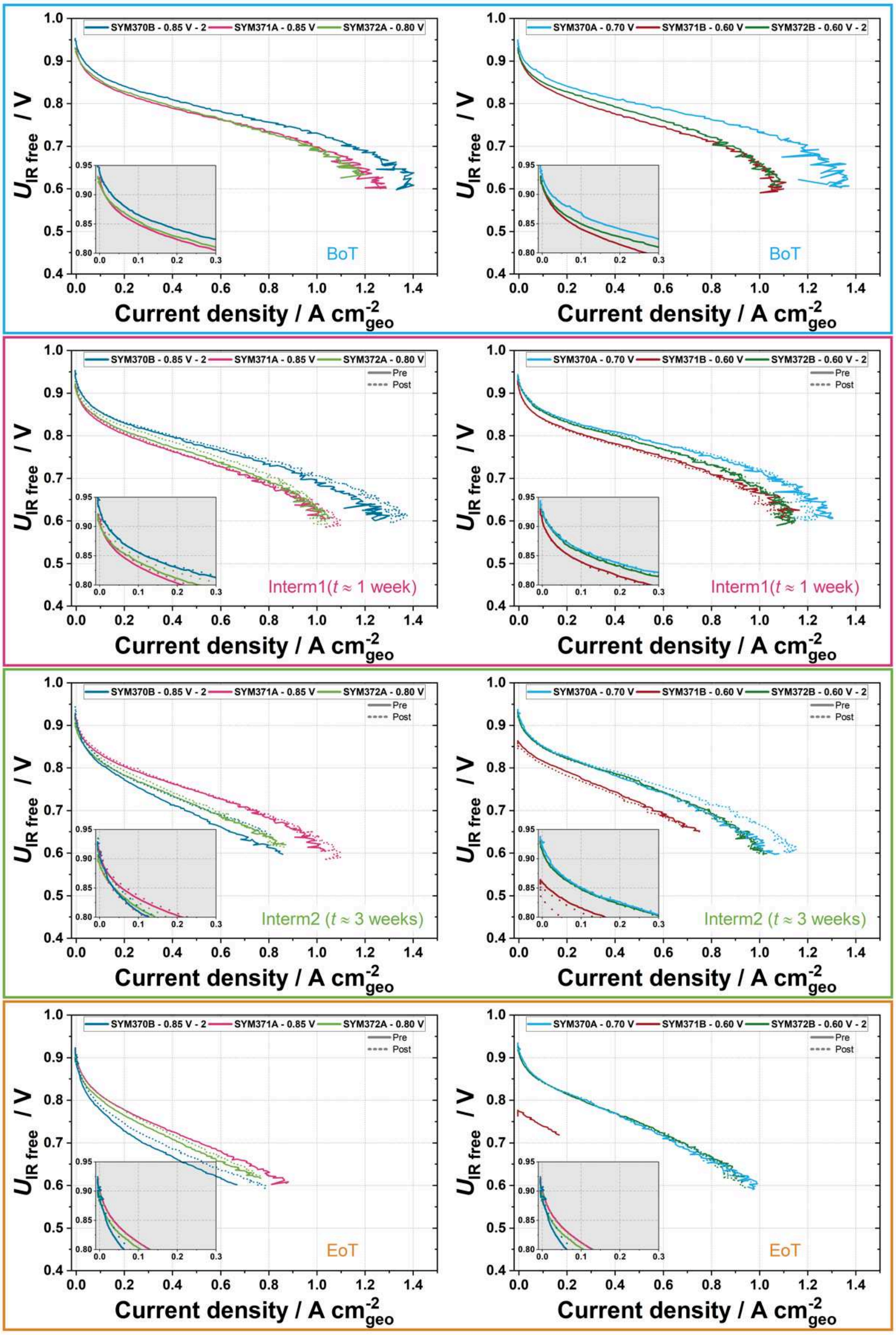

Figure V - 2 - 12: Polarization curves of the high voltage (left) and low voltage (right) aging groups at the different characterization time for all the tested electrodes, from beginning of test (blue, top), intermediate 1 (dark pink, second), intermediate 2 (light green, third) and end of test (orange, bottom). Polarization curves pre (line) and post (dashed line) characterizations are made. The polarization curves are performed at 10 mV s^{-1} and 80°C under a 1.5 stoichiometric gas flow of air at 0.5 barr.

On the contrary, there are some similarities with this first studied group. In fact, the noise and mass-transport limitations observed at the BoT in the high current density region tends to disappear progressively as the aging goes on, leaving linear-shaped curves. The electrode SYM370A-0.70V is also closing very rapidly the gap with SYM372B-0.60V-2, maybe due here again to the difference in initial ECSA: the higher the surface area, the larger the number of active sites prone to (fast) degradations.

The curves of the SYM371B-0.60V electrode are completely ravaged by the crack appearing between Interm1 and Interm2: the OCV is decreasing, and the voltage control starts to be difficult, as it is shown by the lower voltage limit. This marks the withdrawal of the two last points possibly obtained with this electrode. However, the first two can still be used for the analysis.

To finalize this analysis, all the geometric current densities for the four different characterization states are calculated with a linear regression between the two closest points; this way, the current densities at 0.90, 0.85, 0.80 and 0.70 V can be calculated for the pre and post characterization polarization curves. With all those points and for each voltage and electrode, a linear regression is made (the pre and post characterization making a mean of the current density at each degradation state) to obtain the geometric current density losses along the degradation; the corresponding results are gathered in Figure V - 2 - 13.

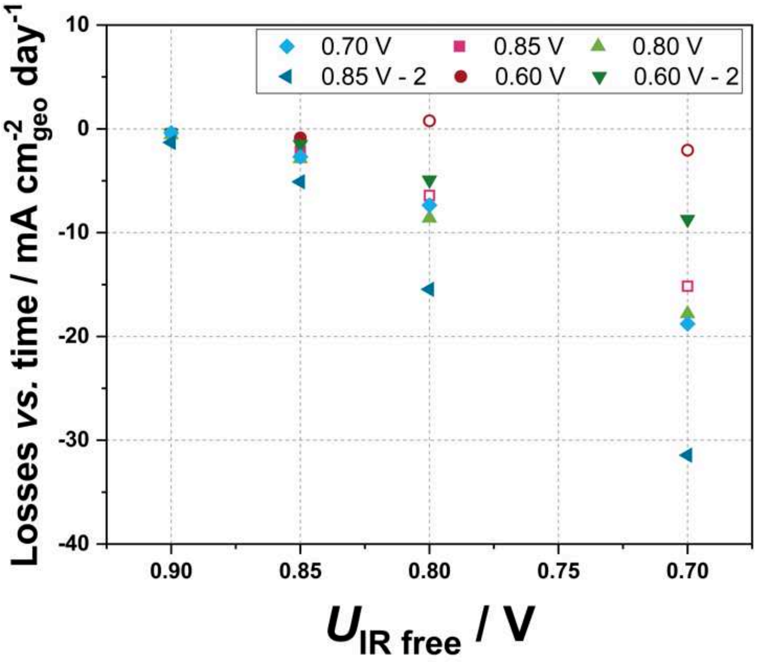

Figure V - 2 - 13: Current density losses with the aging duration for four different voltages for all the aged electrodes. The open symbols are calculated points with experimental issues

The relative position of each point is the same for each voltage, leading to the following order of geometric current density losses, from the biggest losses to the smallest: SYM370B, SYM370A and SYM372A, SYM371A, SYM372B and SYM371B, translated in term of aging voltages as 0.85, 0.70 and 0.80, 0.85, 0.60 and 0.60 V.

The electrodes ECSA presenting no difference except from initial error bars, it is assumed to be similar at a given time for every electrode. This leads to a similar ranking in terms of specific current density losses than it is for the geometric current density, SYM370B-0.85V-2 being always the more impacted one on the whole range of voltage while for high cell voltages, all the other electrodes seem to have the same decrease of $3\,\mu\mathrm{A\,cm_{Pt}^{-2}\,day^{-1}}$, $10\,\mu\mathrm{A\,cm_{Pt}^{-2}\,day^{-1}}$ and $25\,\mu\mathrm{A\,cm_{Pt}^{-2}\,day^{-1}}$ at 0.9, 0.85 and $0.8\,\mathrm{V}$ respectively. The only difference appears for the losses at 0.70 V, similarly to what is observed on Figure V - 2 - 13.

3. Post-degradation physicochemical characterizations of the aged electrodes

After degradation, the electrodes are cut into several pieces to prepare samples for the different analyses as done in the first section of this chapter. All the aged electrodes are then studied using SEM, XRD and Raman spectroscopy.

a) Observation using electronic microscopy: *post mortem* study

i. Scanning electron microscopy

The cathode catalyst layers are analysed as presented in Scanning Electron Microscopy (SEM) and previously done in the beginning of this chapter to average the thickness of the layers on multiple areas. These end of test measurements are shown in Figure V - 3 - 1. There is no clear change of the thickness of the cathode catalyst layer (nor of the anode one) by taking into consideration the error bars, whatever the MEA investigated. For steady state operation, it was found that the carbon corrosion reaction (which would imply modification of the active layer thickness) depends on several parameters such as: the electrode potential, the temperature [112] and the platinum loading on the carbon support [114]. Kinetically, the carbon functionalization/corrosion is favoured as the potential goes up but is also catalysed by platinum metal. These two phenomena are however contradictory, which would explain the results presented here: for 0.70 and $0.80\,\mathrm{V}$ aging tests (SYM370A and SYM372A), Pt is partially oxidized and the carbon functionalization has an average rate (more reduced Pt and slower COR at $0.70\,\mathrm{V}$, more oxidized Pt and faster carbon oxidation reaction (COR) rate at $0.80\,\mathrm{V}$), leading to a small thinning of both active layers by Pt-assisted carbon corrosion. On the contrary, at $0.60\,\mathrm{V}$, despite having reduced platinum, the COR kinetics is too low to form consequent amounts of carbon surface groups that Pt could oxidize, while at $0.85\,\mathrm{V}$, the totally oxidised Pt cannot assist the carbon support corrosion, which is intrinsically not fast enough to be significant alone.

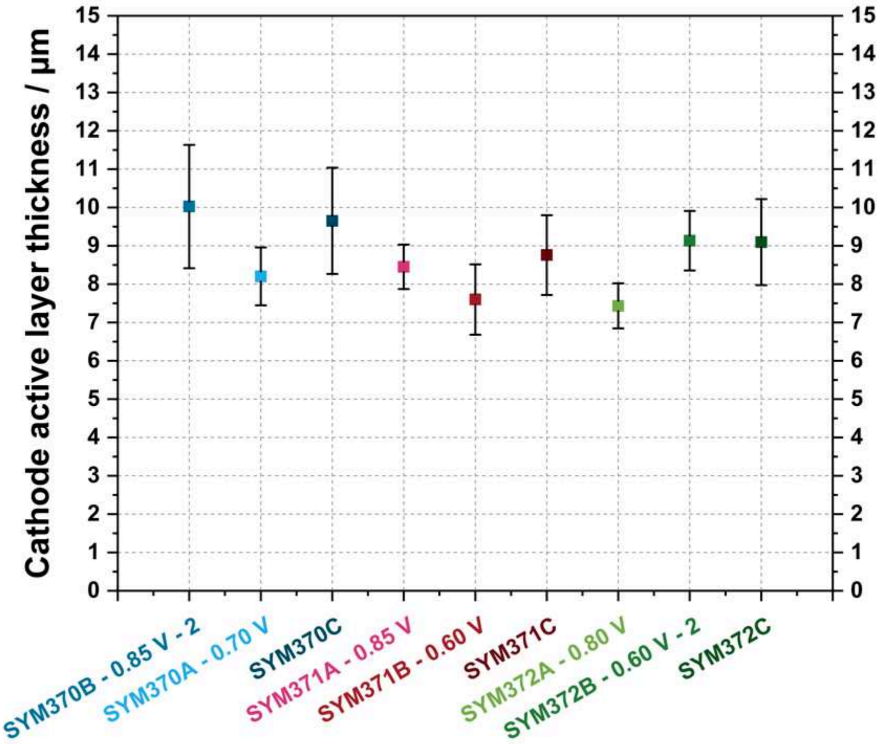

Figure V - 3 - 1: Average cathode active layers thickness for all the aged and reference MEAs using the pixel average method

Pictures taken on the cathode side of the membrane with backscattered electrons (BSE) detector are displayed in Figure V - 3 - 2; they highlight the presence of platinum particles inside the membrane. It is recalled here that, due to the deposition of the active layer on the opposite side of the platinum-enriched membrane, the membrane side of the cathode at the beginning of test was totally free of platinum. Not a single MEA is free from particles but the size and the quantity of these particles differ slightly from one MEA to another. The electrodes are sorted vertically by batch (SYM370 on top, SYM371 in the middle and SYM372 in the bottom) and the high voltage aging group electrodes are put on the left side while the low voltage ones are put on the right side. By doing so, it is easier to notice that for a given batch, the higher the aging voltage, the larger the number of particles and the bigger their apparent size. However, there is no apparent link between the aging voltage and the dispersion and position of the platinum particles in the membrane, which are very close to the cathode active layer in the case of SYM372A-0.80V and seem more distant in the case of the SYM370B-0.85V-2 electrode. This has evidently to do with the different fluidics conditions in which these MEAs operated [96], which will be further discussed below.

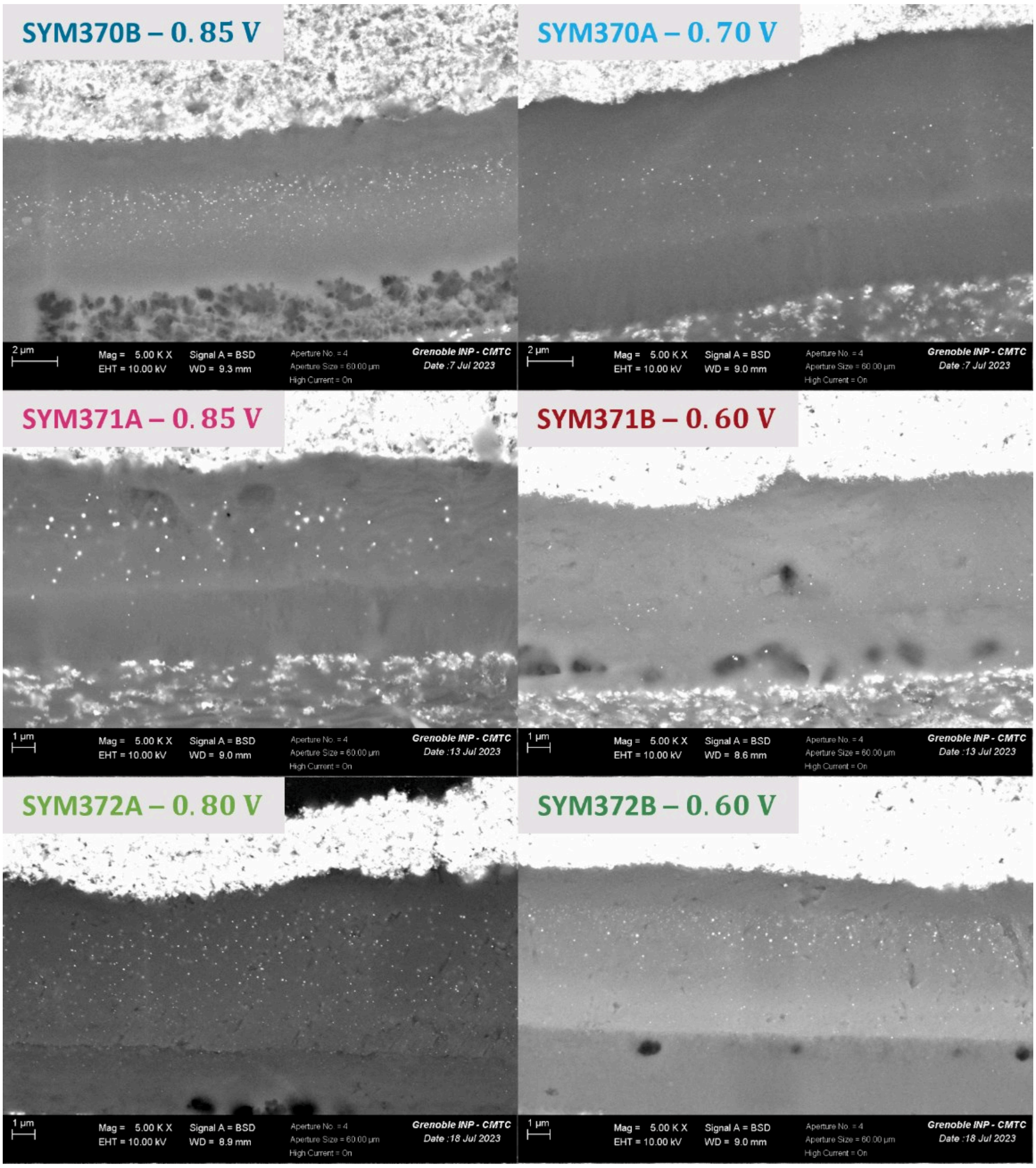

Figure V - 3 - 2: SEM pictures using a BSE detector of all the aged electrodes. High and low voltage degradation groups respectively on the left and on the right

ii. Transmission electron microscopy

As it was previously stated in the beginning of this chapter, the morphology of the Pt/VC nanoparticles did not suffer obvious changes after the preparation of the catalyst coated membrane (CCM) compared to the initial powder state (Figure V - 1 - 3). After electrochemical aging, the electrodes active layers are scratched, the resulting powders imaged and particle size distribution histograms are built to observe the evolution of the isolated nanoparticles size. These aged PSD histograms are shown on Figure V - 3 - 3, and, as awaited, all the mean particle sizes have grown bigger compared to the measured mean particle sizes at powder or sprayed state. Multiple observations can be made from these PSDs. The first one is that for a given batch of electrodes, the high aging voltages cells present lower mean particle sizes than their low aging voltages counterparts. This being not true, once again, for the 371 batch which has suffered experimental issues. It would mean that the low cell voltage working region (and as such, the high current density region) favours the nanoparticles growth with Ostwald ripening mechanisms being major. Also, and quite surprisingly, the particle size distribution, expressed by the standard deviation, is awkwardly similar for a given batch of electrodes. This dispersion can be related to the non-connected particles (glued in Nafion® without any electronic contact with their neighbours) for the low particle size boundary as they are not prone to be degraded owing to their electrical disconnection; they keep their size and are not subjected to the regular potential-induced degradation mechanisms. For the high particle size boundary, however, it is more related to the aging-induced growth of the particle, that was expected to be rather different for the high and low aging cell voltage groups.

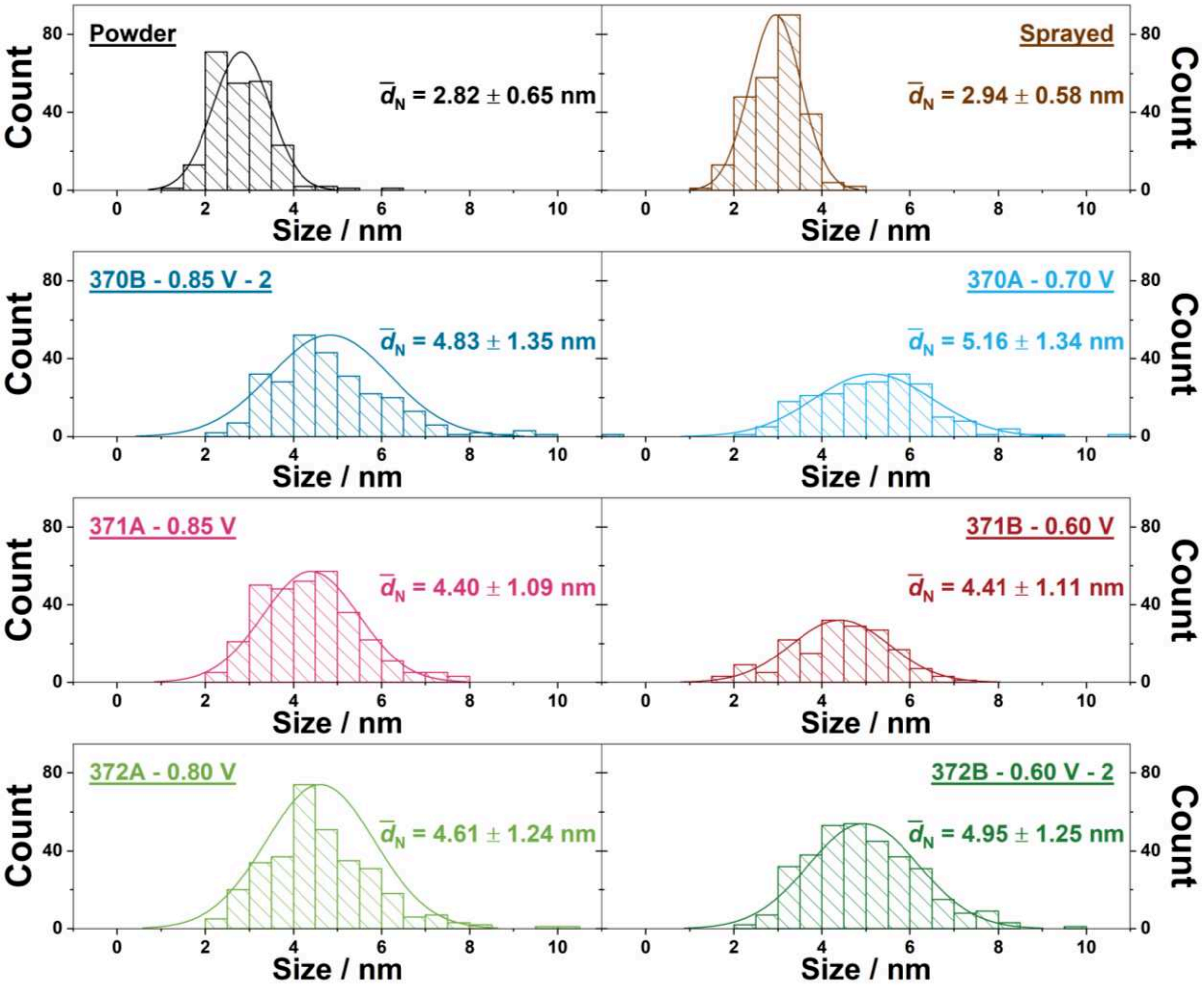

Figure V - 3 - 3: Particles size distribution histograms for the powder, sprayed CCM and the six different aged Pt/VC electrodes tested in this study. The aging voltages are noted on the respective PSD.

Additionally, if one considers only the mean value obtained (and excluding the SYM371 batch that suffered experimental issues), its evolution as a function of the aging cell voltage is absolutely not monotonic, as it is: 4.95, 5.16, 4.61 and $4.83\ \mathrm{nm}$, from low to high aging cell voltages. This means that the cell voltage alone is not a good enough descriptor to explain the evolution of these mean particles sizes. From these values, one can posit that potentiostatic aging at 0.6 V, Pt redeposition is very likely but Pt-ions formation not so, hence the moderate particles growth. On the contrary, aging at 0.8 or 0.85 V promotes Pt-oxides formation, that somehow protects the nanoparticles from severe growth (but not from nanoparticles migration at the carbon surface). So, only the “average” potentiostatic condition, 0.7 V, leads to more consequent growth by Ostwald ripening, Pt deposition (on large crystallites) and dissolution (of small crystallites) being rather equally favourable.

In addition, the defective measurements of the SYM371 batch still give interesting validation/information on the aging mechanism. Indeed, if one considers that the SYM371A-0.85V has been working at lower cell temperature for a non-negligible period of time, the difference in size with the SYM370B-0.85V-2 is only thermal activation-related, which was expected. Also, for the SYM371B-0.60V, the aging is accompanied by the formation of a crack in the membrane, decreasing the current produced by the cell, and thus the amount of water produced at the active sites. This would mean that the additional parameter to take into consideration for the evolution of the particle size may be the amount of water (effective relative humidity) or presence of liquid water in the cell. Having this idea in mind, the presence of water would help the dissolution of platinum (resulting in the high increase of the nanoparticles size at $0.60\ \mathrm{V}$) at a rather similar rate as if it were favoured by the voltage. This hypothesis confirms why rather similar particle sizes are observed for SYM372-0.60V-2 and SYM370A-0.85V-2.

If one wants to take a look at the nanoscale morphology of the aged catalysts, different representative TEM images are presented on Figure V - 3 - 4. It is rather difficult to find or represent general trends from TEM pictures, but here is shown what was more often observed.

The main observation, confirming the previous PSD histograms, is the disappearance of the smaller size nanoparticles ($< 2\ \mathrm{nm}$). Those let behind are believed to be disconnected of the carbon support and thus not prone to degrade electrochemically. Another observation is that particles in areas of huge agglomeration, areas which were already observed in the pristine state of the catalyst (Figure V - 1 - 3), are still present with even blurred shapes. The phenomena happening in these areas cannot be determined and so focus on the external surface of outer carbon particles is made. At these locations, as observed on the high magnification pictures, particles are more distinguishable and counting has been made here as well for the PSDs realization. To the author point of view, it seems that particles of higher diameter that are more isolated can be observed for the low voltage group on the six pictures on the right-hand side of Figure V - 3 - 4.

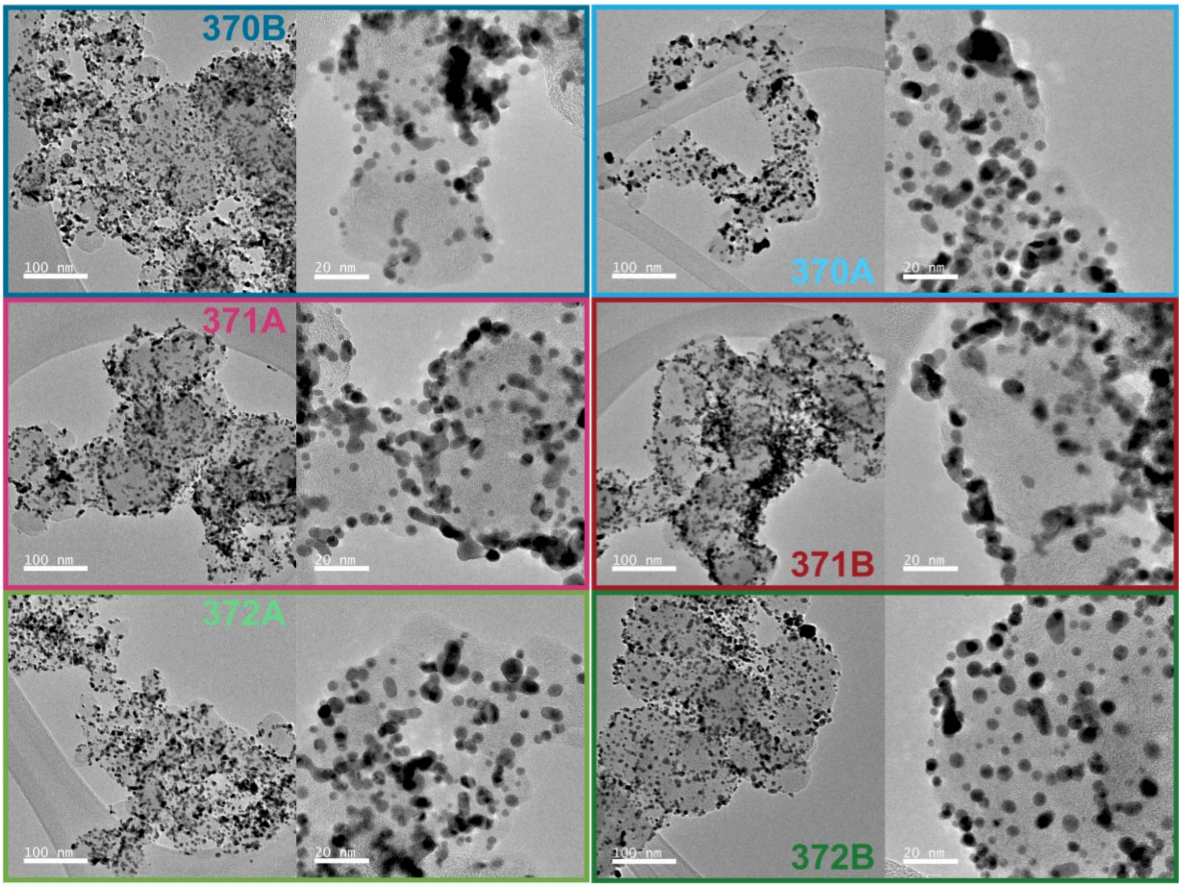

Figure V - 3 - 4: TEM pictures taken after aging on scratched MEA's powders at 50k and 200k magnification. The high voltage group on the left-hand side, from top to bottom: SYM370B-0.85V-2, SYM371A-0.85V and SYM372B-0.80V. The low voltage group on the right-hand side, from top to bottom: SYM370A-0.70V, SYM371B-0.60V and SYM372B-0.60V-2.

One exception though concerns the SYM371B-0.60V electrode for which severe degradation of the catalyst nanoparticles is seen. As the TEM observation happens after final characterisations, which corresponds for this electrode as a true end-of-life (detailed later on), TEM pictures were proposed to observe the impact on the catalyst shape, which is real for sure. For SYM370A-0.70V and SYM372B-0.60V-2, it seems that the main mechanism at stake at low constant potential consisted of the dissolution of the smaller particles at the profit of large ones (Ostwald ripening). For the high voltage group on the other hand, it seems track-like structure of fused/melted nanoparticles, not as distinct as for the pristine state of the catalyst, are more present than for the latter group: agglomeration (and possibly further coalescence) is definitely the major mechanism of degradation at high potentiostatic potential. So, though the differences of particle sizes at EoT are not very different (and neither was the ECSA), the mechanisms leading to these rather similar growths (and ECSA loss) seem to be distinct at low and high constant potential values.

b) X-Ray Diffraction: comparison with reference MEAs, modification of the metallic particles?

The XRD spectra of the aged electrodes are presented in Figure V - 3 - 5 with the different reference MEAs that were presented in the first section of this chapter. For each aged electrode, the single peak (220) that was used to the determination of the initial number and volume averaged particle diameters has changed: it moved from a wide band to a thinner and more defined peak after degradation, which goes when an increase of the crystallites size occurs. This is in line with the particles size growth and ECSA losses witnessed in earlier sections. This increase of the crystallite size $\overline{d}_{\mathrm{XRD}}$, determined using the PsdVgt function, corresponds to similar measured sizes for all aged electrodes: $10-11\ \mathrm{nm}$. As for the evolution of the cathode ECSAs, these observations seem totally independent on the aging voltage applied and all the aged electrodes seem to behave similarly. This large increase can in principle either be related to the direct increase in size of the platinum nanoparticles of the active layer, which would indicate major Ostwald ripening, or linked to the formation of platinum particles that were previously observed inside the membrane. Because the XRD observed growth does not really match with the TEM observed growth, still presenting a huge discrepancy with the measured $\overline{d}_{\mathrm{V}}$, it is postulated here that the second explanation is the good one: XRD probes the Pt nanoparticles that have nucleated in the membrane [95].

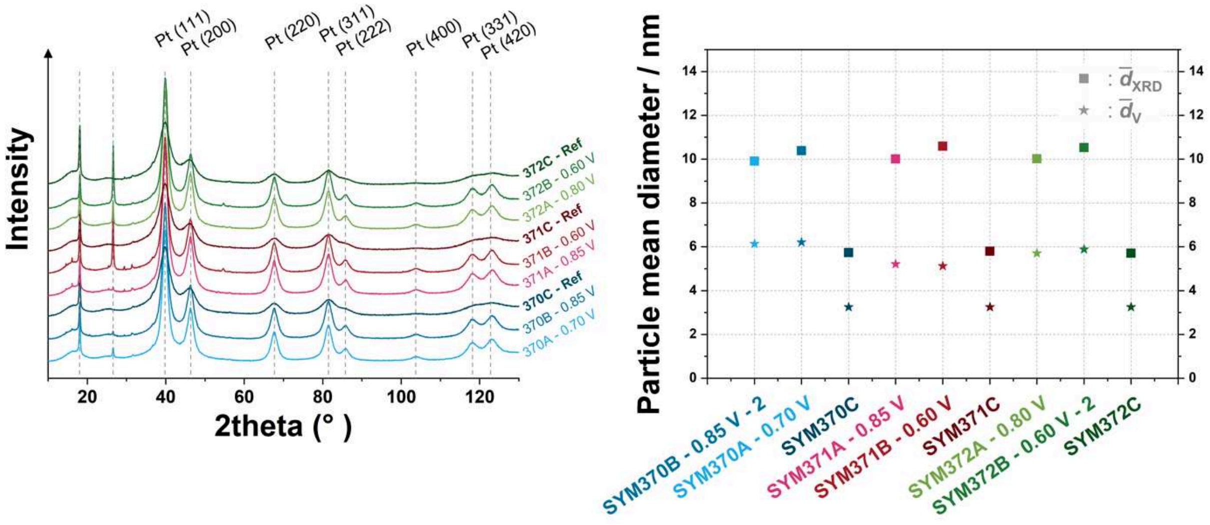

Figure V - 3 - 5: XRD spectra of the aged and reference MEAs (left) and mean particle diameters ($\overline{d}_{XRD}$ and $\overline{d}_{V}$) of the platinum particles (right)

Note that a thin peak appears on some of the electrode XRD spectra (such as SYM371B-0.60V and SYM 372A-0.80V or SYM372B-0.60V-2). This peak is related to the graphitic lattice of carbon but not the carbon of the active layer. This peak appears on the electrode for which the removal of the GDL was more complicated: the GDL's microporous layer (MPL) has transferred on the active layer with some fibres of GDL and when irradiated with X-rays, this resulted in coherent diffraction at this very angle, characteristic of graphite.

c) Raman spectroscopy: comparison with the reference cathode catalyst layers

Raman spectroscopy is finally carried out on these electrodes. After normalization of the peak at *ca.* $1600\ \mathrm{cm}^{-1}$, it does not seem the spectra - given on Figure V - 3 - 6 - changed a lot, in agreement with SEM observations and cathode thicknesses measurements. After separating them in two groups, it was expected to have different behaviours (if carbon corrosion had been major) but the only difference that can be observed is the slight decrease of the region at $1500\ \mathrm{cm}^{-1}$, between the two peaks for the high aging voltage group and the SYM371B-0.60V electrode in the low aging voltage group. It is also possible that the degradations occurring on the carbon of the active layer mainly take place at the vicinity of the membrane and not on the outer surface, which is probed by the Raman spectroscopy, as light is absorbed by dark material such as the whole active layers deposited on the membrane. Thus, it is not possible to have clearer information here either. Nevertheless, the absence of consequent carbon corrosion observed here (for the GDL|active layer interface) matches the absence of major thinning of the cathodes witnessed in SEM.

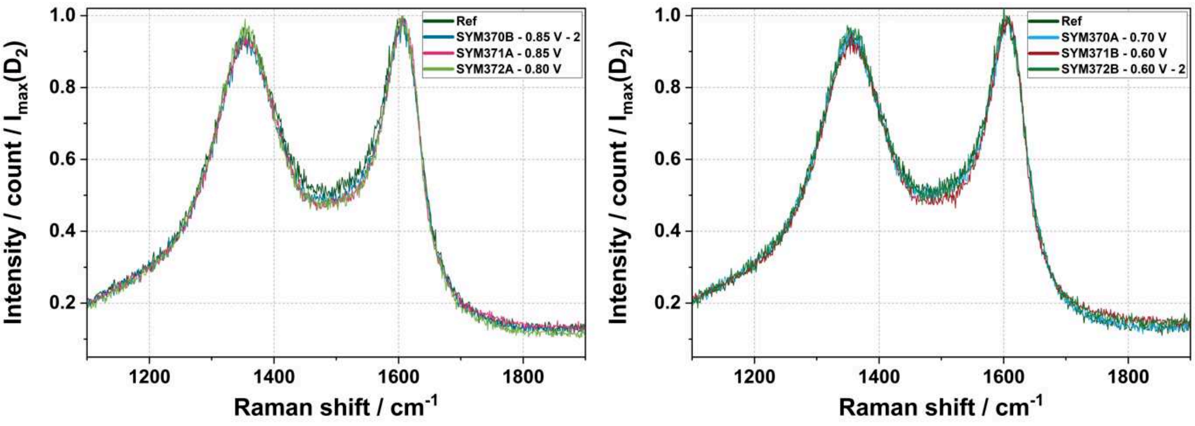

Figure V - 3 - 6: Raman spectra of the aged electrodes separated in the high and low voltage groups, respectively on the left and right sides

4. Discussion

For this discussion, the tested electrodes are separated by their holding voltage in two groups, the high aging voltage (for voltages of 0.80 and $0.85\ \mathrm{V}$) and the low aging voltage (0.60 and $0.70\ \mathrm{V}$) groups.

A first observation is the similar loss of electrochemically active surface area as a function of the aging time (as shown on Figure V - 2 - 8). This loss resulted in a 30 to 40% decrease of the ECSA (from 50 to $30 - 35\ \mathrm{m^2_{Pt}g^{-1}_{Pt}}$). The SEM micrographs analysis of Figure V - 3 - 1 did not reveal any major change of cathode thickness, so one can consider that the dissolution/redeposition of platinum to form bigger particles is the main mechanism explaining the ECSA loss; assuming so (and no loss of Pt from the active layer), the end of test active areas would result in particle of $ca.\,8.5\ \mathrm{nm}$ in size. This of course contradicts the presence of platinum bands inside the membrane for each MEAs, implying platinum mass losses in the cathode active layers of the electrodes. It was however found from TEM micrographs PSDs that there is a non-linear evolution of the nanoparticles number and volume averaged diameters with the aging voltage, which is not found for the crystallite sizes of the aged MEAs, believed to probe the platinum band in the membrane. These considerations lead to mixed aging mechanisms depending on the aging voltage: Ostwald ripening mechanism for voltage below 0.70 V and migration/agglomeration (corroborated by TEM pictures) for 0.80 and 0.85 V aging voltages. Additional platinum dissolution/redeposition in the membrane is observed on all the voltage range studied as well as thermodynamical dissolution of the smaller particles at the profit of the bigger particles.

Despite no effect of the holding cell voltage was observed for the ECSA and cathode thickness losses, more noteworthy variations are observed on the $\mathrm{H_2/O_2}$ polarization curves (see Figure V - 4 - 1), that enable to check the performance evolution during the tests with almost no mass-transport losses. The beginning of test performance assessment leads to rather homogeneous ($ca.\,1\ \mathrm{A\ cm_{geo}^{-2}}$ at $0.80\ \mathrm{V}$ and $ca.\,3.5\ \mathrm{A\ cm_{geo}^{-2}}$ at $0.70\ \mathrm{V}$) behaviours for all electrodes in their initial state, right after the conditioning step. The absence of curve for the SYM371A-0.85V is explained by the addition of this test in the protocol by the author afterwards; it is however assumed to be rather similar to the other electrodes (or at least to the SYM371B-0.60V as it belongs to the same electrodes batch).

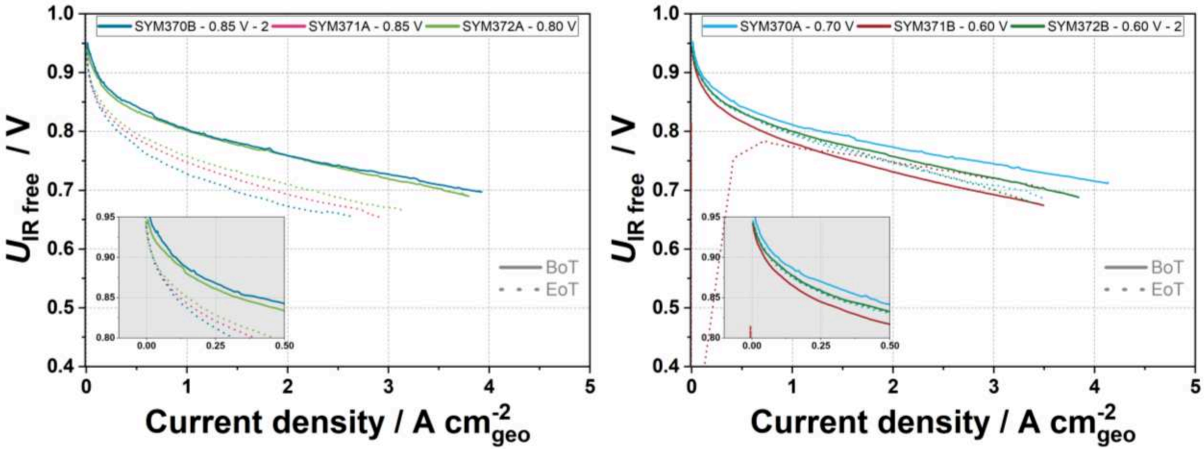

Figure V - 4 - 1: Polarization curves of the high voltage (left) and low voltage (right) aging groups at the beginning of test (straight lines) and end of test (dot lines). The polarization curves are performed at 10 mV s^{-1} and 80°C under a 1.5 stoichiometric gas flows of H_2/O_2 at 0.5 barr.

Significant losses are witnessed for the high aging voltage group in the whole voltage range scanned. On the contrary, the impact on the low voltage group is minimal if not mainly overlapping with BoT performance of the SYM372B-0.60V-2 electrode, SYM370A-0.70V presenting more variations with its initial performance. For the SYM371B-0.60V electrode at end of test, one observes after the backward scan (from high to low voltages) that the cell performance and voltage collapsed during the upward scan, leaving only unmeasurable OCV and the impossibility to control the voltage: the crack formation in $\mathrm{H_2/O_2}$ and high current densities has grown to an irreversible state. Focusing more on the remaining electrodes, it appeared that the aging voltage influenced a lot the ORR kinetics performance of the tested electrodes: while the MEAs tested at voltage under $0.70\ \mathrm{V}$ suffered minor changes on their mass-transport free curves, the MEAs aged at voltage higher than $0.80\ \mathrm{V}$ have lost $ca.\ 40\%$ and more than 50% of their geometric current density at respectively 0.70 (from $ca.\ 3.5$ to $ca.\ 2\ \mathrm{A\ cm_{geo}^{-2}}$) and $0.80\ \mathrm{V}$ (from 1 to less than $0.5\ \mathrm{A\ cm_{geo}^{-2}}$), the more dramatic losses being observed for cells having aged at higher voltage. This is, as mentioned in the 148, related to the progressive formation of a platinum oxide layer on the catalyst particles, decreasing severely their performance and for which only a part can be reversibly reduced by performing cyclic voltammograms. So not only the particles size matters for the performance, the fraction of Pt/Pt-oxides as well.

Gathering all these information, potentiostatic electrochemical impedance spectra were fit using the ideal and non-ideal capacitance distribution models presented in the Potentiostatic Electrochemical Impedance Spectroscopy (PEIS). The non-ideal parameter α was kept equal to 0.95 for most of the electrodes as it enabled a good fit but were tried equal to 0.98 for discrepancies in the low frequency region for SYM370B-0.85V-2 electrode. The different parameters values obtained from these fits are summarized in Figure V - 4 - 2. Values of high frequency resistance were determined using the impedance spectra performed during the conditioning step and found to be averaged to $R_{\mathrm{HF}} = 35 \pm 2\ \mathrm{m\Omega\ cm_{geo}^{2}}$, which is also the case here. However, a rather marked increase of this resistance is observed for the SYM370B-0.85V-2 electrode (SYM371A-0.85V also present variations, possibly ascribed to hydration cycling due to cooling down period, and SYM371B-0.60V having instabilities due to the presence of $\mathrm{H_2}$ at the cathode side owing to the cracked membrane). This increase might be related to a carbon oxidation reaction happening after the long holding time spent at $0.85\ \mathrm{V}$. this was not verified by the Raman spectra, which are however believed to detect only the outer surface of the cathode catalyst layer – while this increased R_{HF} could be related to an increased interfacial contact resistance between the cathode and the membrane (*i.e.* opposite to where Raman was made). For the two other parameters, the double layer capacitance and the protonic resistance, a similar behaviour is observed for all electrodes: these parameters values tend to slightly decrease with time. No sharp increase of the protonic transport resistance due to the formation of the platinum band is observed for any of the electrodes, leaving only a loss of active materials but not impacting side effects on the diffusivity of protons in the membrane or in the ionomer.

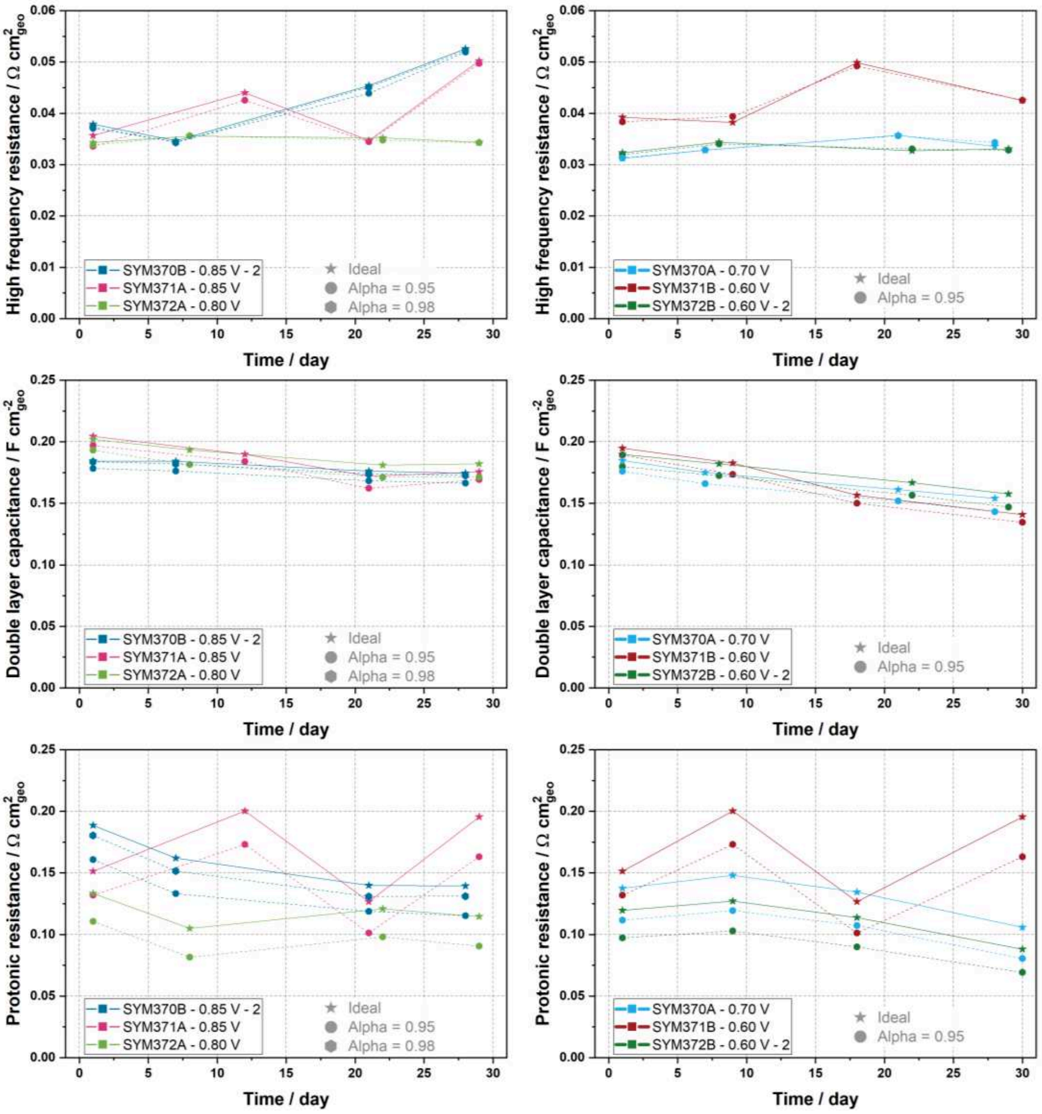

Figure V - 4 - 2: High frequency resistance, double layer capacitance and proton transport resistance determined by PEIS at 0.2 V under H_2/N_2 flows. Parameters were extracted from fits using ideal and non-ideal transmission line models for all the tested electrodes. Right-hand side graphs stand for the high voltage aging group while left-hand side graphs stand for the low voltage aging group.

The aging in potentiostatic conditions at various cell voltages led to dominant degradation of the ORR catalyst, via increased in the platinum nanoparticles size following two different mechanisms (Ostwald ripening and migration/coalescence) but no oxidation of the carbon support. These mechanisms implied similar major decrease of the ECSA, with no sign of voltage dependence. However, the potentiostatic working conditions at high cell voltage (0.80 and 0.85 V) impacted more drastically the cell performances than the low cell voltage (0.70 and 0.60 V); this was very well observed on non-mass-transport limited polarization curves performed under O_2 (more likely to give access to the ORR kinetics performance).

5. Conclusion

This study was established as a first attempt to understand the influence of the cell voltage on the degradation rate of PEMFC single cells of $25\ \mathrm{cm}^2$ by applying constant cell voltages under reactant gases $\mathrm{Air}/\mathrm{H}_2$ for long periods of time and limit as much as possible the impact of intermediate characterizations and corresponding voltage cycling. Six electrodes were subjected to cell voltages ranging from 0.85 to $0.6\ \mathrm{V}$, the working range of PEMFC real system. Several electrochemical markers have been studied along the test, such as the electrochemically active surface area, the permeation current of hydrogen across the membrane and short-circuit current (all measured in H_2/N_2 configuration), as well as the performance of the cell in H_2/O_2 or H_2/air conditions. Physicochemical markers of the cathode catalyst layer and whole MEA were investigated: non-tested electrodes (denominated as reference MEAs) were compared with the aged electrodes. Using cross-section scanning electron microscopy, the thickness of the cathode catalyst layer and the formation of a platinum band in the proton exchange membrane were investigated, while transmission electron microscopy of scrapped active layers enabled to determine the nanoparticle size and distribution, and their organization (round-shaped isolated versus agglomerated in flat rafts). The platinum crystallites size was also investigated, as well as the degree of organization of the Vulcan XC72 carbon using Raman spectroscopy.

The gathered results demonstrate that, in potentiostatic conditions, major corrosion of the carbon support of the Pt nanoparticles can be excluded, resulting in near-absence of thinning of the cathodes in the $ca.\ 700\ \mathrm{hours}$ of the tests. This goes in line with the fact that, in the studied cathode potential interval ($0.6 - 0.85\ \mathrm{V}$), carbon corrosion is essentially a dynamic process [59,211] (and here, potential variations were kept minimal). Also, ECSA losses are rather similar whatever the test conditions, which could appear surprising at first sight. However, combining the electrochemical and physicochemical data, one realizes that the fate of the cathodes is rather different for tests performed at low cell voltages (cathode potential), 0.60 and $0.70\ \mathrm{V}$, and at high cell voltages, 0.80 and $0.85\ \mathrm{V}$. In the former case, the low cell voltage prevents Pt-oxides formation (hence Pt passivation) and minors Pt potential-induced dissolution (which is even slower at 0.60 than 0.70 V) but favours Pt-redeposition; overall, this results in Oswald ripening as the main process of ECSA loss. In the latter case, Pt is likely passivated by its oxides, mitigating both Pt dissolution and redeposition/reduction, hence lowering Oswald ripening; instead, carbon surface groups can form (but are not majorly fully oxidized into CO_2 by Pt-assisted catalysis – Pt being essentially in oxides state), leading to Pt crystallites migration into agglomerates (well witnessed in TEM) and related ECSA losses. Assuming these mechanisms, it is no surprise that the ORR performances (typically measured in H_2/O_2 configuration) remain very high after low potential aging and degrade fast after high potential aging. In the first case, the loss of ECSA is counterbalanced by the Pt nanoparticles growth (large Pt nanoparticles being more intrinsically active than small ones [25,26]), overall resulting in very minor apparent kinetics losses in the high voltage region of the H_2/O_2 polarization plots. In the second one, the loss of ECSA is accompanied by rather irreversible Pt-oxides formation after high-potential holds, resulting is very depreciated apparent ORR kinetics, which is observed in the voltage region over 0.70 V, where a peak for these oxides formation is awaited, but appears strongly modified for the high voltage group.

In addition, one cannot exclude that at the very different cell voltages (cathode potentials) investigated, resulting in very different current densities produced, the water content of the active layers might be significantly different. Although this effect is probably second order compared to that of the potential, it could play a non-negligible role in the degradation of the active layers, liquid water being needed for Pt dissolution/redeposition and carbon corrosion; one cannot exclude that these effects are also at stake in the present tests, but these would be more likely visible at the PEM|active layer interface, which was not the primary focus of the study (thin-slices of cross-sectioned MEAs would have needed to be observed in TEM and Raman, to be capable to localize the degradations).

General conclusion

General conclusion

The proton exchange membrane fuel cells (PEMFC) are investigated as electrochemical generators that would be promising to switch the transportation sector from combustion engines towards less to zero CO_2-emissive propulsion. PEMFCs convert the chemical energy of dihydrogen (H_2) into electrical energy, by reaction with dioxygen (O_2) to produce water. The catalytic assisted oxidation of the H_2 produces protons which will migrate through a protonic conducting membrane to reduce O_2 and form the final product, water, as well as heat and power. Combined with a green approach for the production and purification of hydrogen, it is foreseen as a way to help reduce the greenhouse gases emissions in one of the most emissive economic sector.

To make such a system interesting enough to develop an economy and move an entire field to adopt it, it needs to be cost effective and durable: operation for as long as the current combustion engine lifespan is targeted, as well as "comparable" performance (power density and specific power). This is extremely challenging, and most of the past research strived to provide the best cost to performance ratio and the longest durability possible. Improvements have been made, but remain insufficient, and further improvements require:

(i) High activity catalysts, to maximise the power generated and reduce as much as possible the quantity of rare and costly materials (platinum group metals) used;
(ii) Materials able to sustain several thousands of hours of operation (8 to 40 depending on light or heavy duty).

To this goal, catalysts are developed to increase the performance of the state-of-the-art materials that have been studied so far, but the performance and durability requirement (periodically updated) fixed by organizations such as the US DoE are often never (or only partially) matched, especially at the technical cell level, although laboratory experiments in model cells predicted a better outcome. This thesis questioned this inconsistency and notably aimed at studying a new way to assess the performance of catalyst that could be applied to the new synthesized objects of the literature. Furthermore, durability test measurements have been performed on two state-of-the-art commercial catalysts to understand the aging mechanisms encountered by these materials in accelerated stress test conditions and stationary conditions (two very different modes of operation, that are both relevant to assess PEMFC durability).

In that frame, three catalysts having different properties, from classical platinum on Vulcan carbon (Pt/VC with poorly graphitized carbon support), bi-alloyed platinum cobalt on Vulcan carbon (Pt_3Co/VC) and platinum on graphitized carbon (Pt/GC), were tested in three different environments to assess their catalytic activities for the oxygen reduction reaction:

- Liquid: the rotating disk electrode (RDE), dipping the catalyst layer in a fully liquid environment in which the oxygen is dissolved (at low concentration: 1 mM) and consequently very limited by mass-transport;

- Liquid|gas: a novel setup, called the gas diffusion electrode (GDE), enabling the presence of a liquid electrolyte on top of the catalytic layer while the reactant can be fed from the gas phase, on the other side of the electrode;
- Polymer|gas: a differential PEMFC (DC) used with high gas stoichiometries to get homogeneous performance on the whole surface studied.

This study originated from the fact that novel catalysts fail to maintain the improvement they displayed in RDE at high electrode potentials to the full range of potentials in which the cell works. To understand the problems at stake, low loaded electrodes were prepared to limit as much as possible the mass-transport limitations that could occur (from the proton and oxygen transports). Improvement factors measured in RDE for most performing catalyst (Pt_3Co/VC) were kept and even increased when measured in GDE and DC, attesting that advanced catalysts do maintain their enhancement factors over classical ones at high current density, and therefore that it should be possible to integrate them in PEMFC configuration without losing their activity (which is then "just" an engineering issue). It was nevertheless proven that due to high water amount, it is more complicated with the RDE and GDE to handle catalyst supported on graphitized (thus hydrophobic) carbons. In the end, the GDE was proven to be a really handful setup to test new catalysts with low amount of material needed, and more representative of the final system than the RDE, thanks to which it is possible to study the catalyst on a wider potential range without impending limitations (and without the need to run real PEMFC test for the preliminary screening of the intrinsic catalytic activity).

The introduction in the lab of a new gas diffusion electrode experimental setup helped to unveil catalyst performance and behaviour a step closer to the real system with an easy and ready-to-use device. The best improvement factors obtained, for a famous platinum-cobalt bi-alloyed commercial catalyst, nevertheless were too low to be considered as a next-generation catalyst. New catalysts are awaited at the lab scale to be tested with this new GDE setup and, in comparison with the differential cell, one would be able to correct/adapt the preparation method of the active layer to enable the use of such groundbreaking catalyst in single cell and further integrate them in real PEMFC stacks.

Nevertheless, producing membrane-electrodes assemblies (MEAs) with the best catalyst of the three tested (Pt_3Co/VC) to integrate them in single cell was the next step, so to run a catalyst evaluation for real setup performance and durability assessment. MEAs of $25\ \mathrm{cm}^2$ were produced and studied in a segmented cell to understand the evolution of the performance using various simple accelerated stress test procedures to mimic different phenomena. *Load-cycling* and *hydrogen front*, both AST with upper voltage boundary of $1\ \mathrm{V}$ were found to result in pretty similar and homogeneous performance decay of 60%. In addition, the lower voltage boundary (0.6 and $0.1\ \mathrm{V}$ respectively) had no real impact on the catalyst morphology evolution. The catalyst layer loading (varying from 0.57 to $0.34\ \mathrm{mg_{Pt}\ cm_{geo}^{-2}}$) was found to have neither impact on the initial current density nor on the performance decay for base-load AST, suggesting that in these conditions a reduction of 40% of the platinum loading is feasible while keeping the same performance. S*tarts & stops* and *interplay* ASTs, on the other hand, for which the upper voltage boundary exceeds $1\ \mathrm{V}$ and reaches $1.5\ \mathrm{V}$, revealed detrimental performance losses of more than 80%. Structural changes, and in particular, carbon corrosion which resulted in important mass transport limitations and strong decrease of the open circuit voltage, were reported. Finally, all tests led to similar ECSA losses, this parameter therefore not being a good marker of degradation (despite being the most used in the literature for that purpose).

Potentiostatic aging characterizations were then realized on Pt/VC by separating the 6 aged MEAs in two groups: one of aging voltages above $0.8\ \mathrm{V}$ and the other composed of aging voltages under $0.7\ \mathrm{V}$. It appeared that, from an electrochemical point of view and maybe depending on the experimental conditions used here, there is a clear voltage threshold between $0.8\ \mathrm{V}$ and $0.7\ \mathrm{V}$ that strongly modifies the active layers environment and the degradation mechanisms the electrodes are facing during the test. This results in detrimental performance losses (both under $\mathrm{H_2/Air}$ and $\mathrm{H_2/O_2}$) attributed to the formation of a $\mathrm{Pt-Oxide}$ layer at the surface of the platinum particles, lowering the ORR kinetics for the catalytic layers of the high aging voltages group. Voltage decays (with respect to the aging time) measured under air indicate that the performance loss at $0.5\ \mathrm{A\ cm_{geo}^{-2}}$ is three times higher for the high voltage groups than for the low voltage ones. Morphology of the catalyst might not have changed a lot, regarding the mean particle sizes and the active layer thicknesses, but the catalytic properties have suffered a lot more in high voltage conditions. A low voltage operation appears to be a way to increase one catalyst lifetime (at least in the range of cell voltages studies here). This of course gives ideas for better initial operation of cells at beginning of life; at that stage, their good state of health shall be compatible with larger cell voltage/smaller current operation at a given rated power than at end of life, which could artificially accelerate the degradation of their cathode. Mitigating this effect could be done by a proper system/fluidics management, for sure.

In the light of the degradation investigations, the performance decays in $25\ \mathrm{cm^2}$ single cell for $\mathrm{Pt_3Co}$/VC were shown to be too high in conditions close to the ones fixed by US DoE and, similarly, the stability of a monometallic platinum catalyst in steady-states conditions revealed too fast performance losses, even in the most stable conditions at low voltage. This suggests that a lot more work in the cause of performance loss still has to be done. Despite that regeneration steps exist to refresh, or more accurately reveal the platinum on the inner layers of the platinum particles to regenerate the performance in PEMFC environment, such protocols would surely induce catalyst irreversible dissolution. This loss will impact both the electrochemically active surface area and the performance of the MEAs, accelerating the aging of the core materials. In the light of the results obtained in this thesis, the best solution one can think about to moderate the dissolution of platinum and prevent a $\mathrm{Pt-O}$ layer formation is to work at low cell voltages (between 0.65 and $0.60\ \mathrm{V}$). This however is intrinsically linked to a maximum conversion efficiency of 50% for the system, which would be similar to combustion engine while PEMFC could enable higher overall yield. Another option would be to investigate in the region of $0.75-0.7\ \mathrm{V}$ as the particle size growth was not monotonic in this voltage range and to adapt the balance of plant of the system to the core material, as it was done on the Toyota Mirai to increase the durability of the overall system, instead of trying to adapt the core material to the balance of plant.

Annexes

Annexes

Annexe 1: ECSA homogeneity on the surface of the MEAs at BoT and EoT

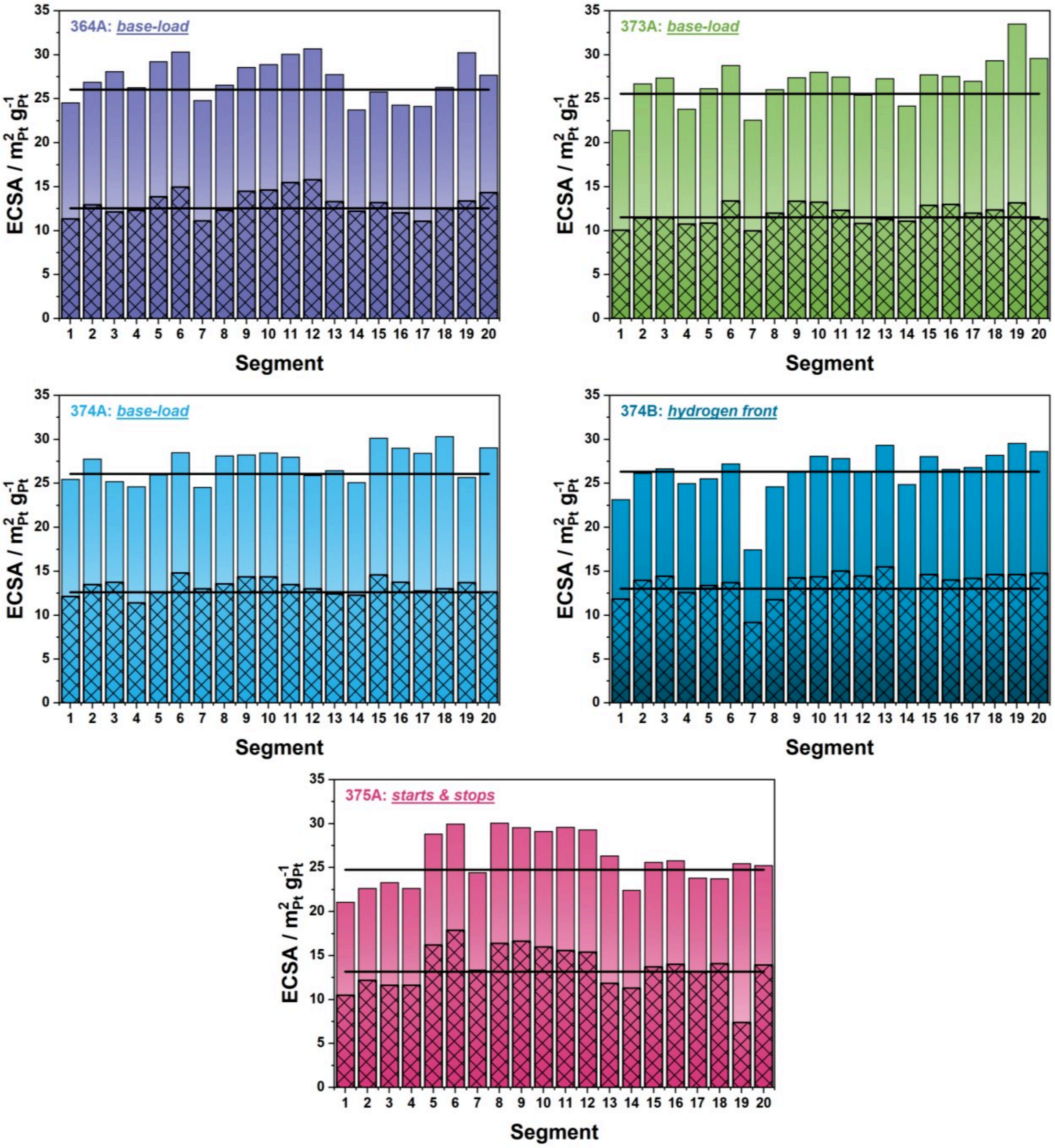

Figure A - 1: Electrochemically active surface area on the surface of the MEAs before and after the aging procedures. ECSA calculated with the mean of the charges of adsorption and desorption of protons measured by correcting the capacitive current using a linear regression in the 0.5-0.6 V region

Annexe 2: Evolution of the cyclic voltammograms under H_2/N_2 flows during the constant voltage aging protocol

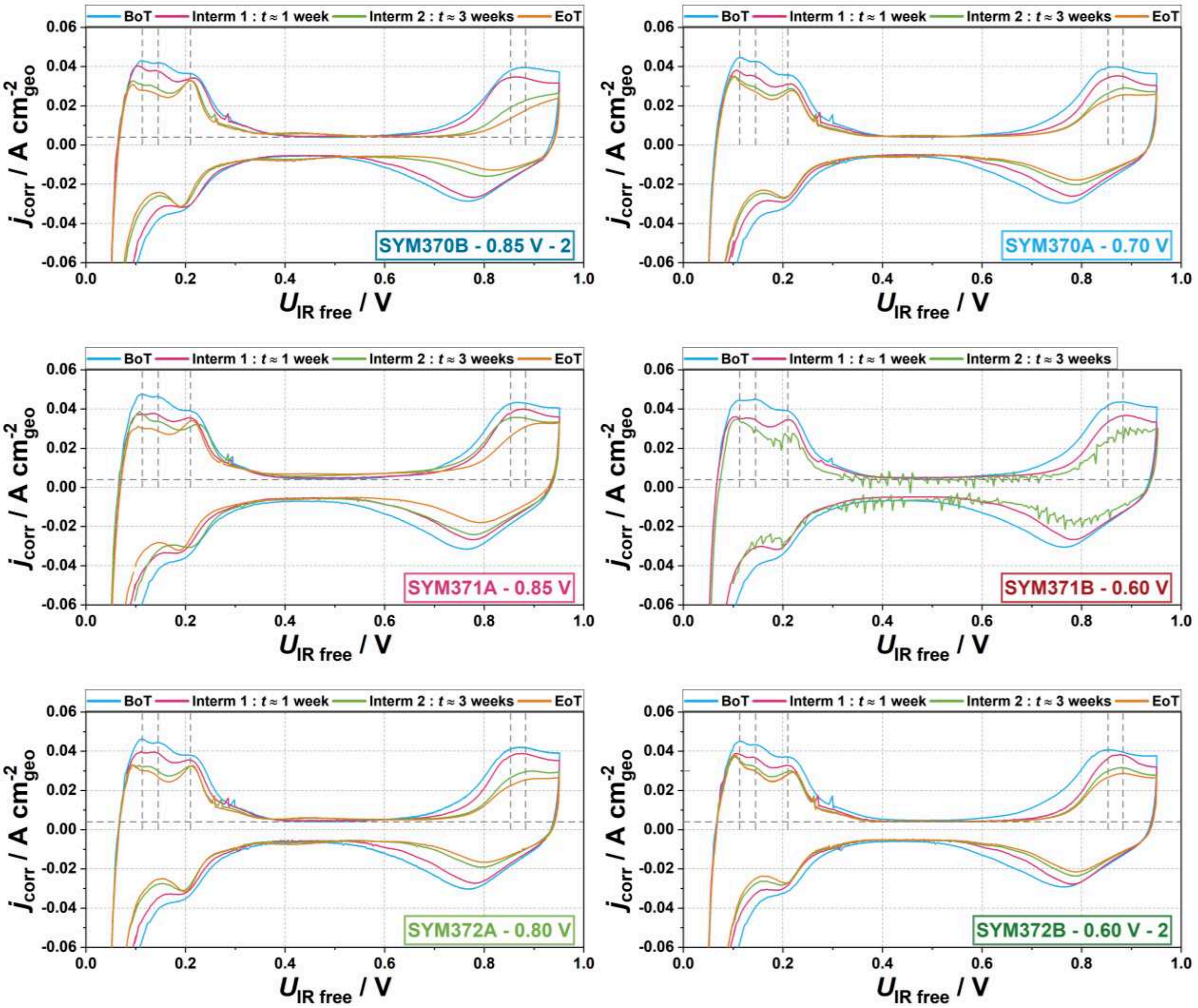

Figure A - 2: Cyclic voltammograms features of the MEAs studied under potentiostatic aging protocol under H_2/N_2 flows at 80°C, 50% RH with scan rate of 150 mV s^{-1}

Annexe 3: Evolution of the polarization curves under Air/H2 flows during the constant potential aging protocol

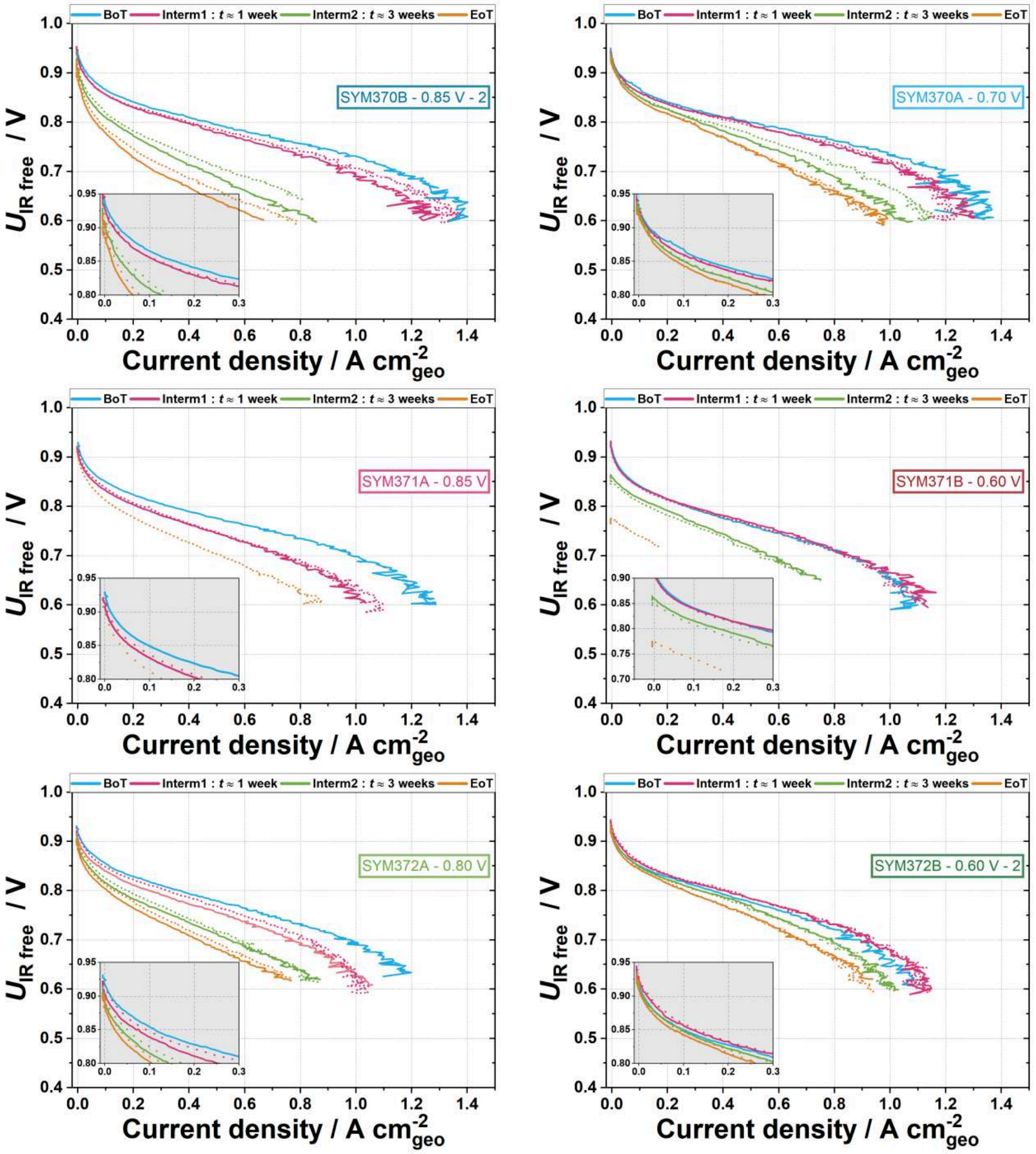

Figure A - 3: Polarization curves under Air/H2 flows for the different intermediate characterization during the constant aging protocol for all the aged MEAs. Curves obtained at 80°C, 50% RH, 10 mV s-1 and stoichiometric coefficient of 1.5 for both gases. Straight line are polarization curves performed prior to H_2/N_2 characterizations and dot lines are performed after these characterizations.

Bibliography

Bibliography

[1] W.R. Grove, On the Gas Voltaic Battery.--Experiments Made with a View of Ascertaining the Rationale of Its Action and Its Application to Eudiometry, Philosophical Transactions of the Royal Society of London, 1843. http://archive.org/details/jstor-108377 (accessed October 22, 2023).

[2] D.K. Lynn, H.S. Murray, J.B. McCormick, J.R. Huff, Simulated performance of solid polymer electrolyte fuel-cell-powered vehicles, SAE Technical Papers (1983). https://doi.org/10.4271/830351.

[3] L.J. Nuttall, J.F. McElroy, Technical and economic feasibility of a solid polymer electrolyte fuel cell powerplant for automotive applications, SAE Technical Papers (1983). https://doi.org/10.4271/830348.

[4] M. Warshay, P.R. Prokopius, The fuel cell in space: yesterday, today and tomorrow, Journal of Power Sources 29 (1990) 193–200. https://doi.org/10.1016/0378-7753(90)80019-A.

[5] W. Vielstich, A. Lamm, H.A. Gasteiger, eds., Handbook of fuel cells, Wiley, Chichester, England ; New York, 2003.

[6] H.A. Gasteiger, W. Vielstich, H. Yokokawa, eds., Handbook of fuel cells, John Wiley & Sons, Ltd, Chichester, 2009.

[7] K.A. Burke, Fuel Cells for Space Science Applications, (2003).

[8] W. Grot, DISCOVERY AND DEVELOPMENT OF NAFION PERFLUORINATED MEMBRANES., Chemistry and Industry (London) (1985) 647–649.

[9] M.S. Wilson, J.A. Valerio, S. Gottesfeld, Low platinum loading electrodes for polymer electrolyte fuel cells fabricated using thermoplastic ionomers, Electrochimica Acta 40 (1995) 355–363. https://doi.org/10.1016/0013-4686(94)00272-3.

[10] P. Costamagna, S. Srinivasan, Quantum jumps in the PEMFC science and technology from the 1960s to the year 2000: Part I. Fundamental scientific aspects, Journal of Power Sources 102 (2001) 242–252. https://doi.org/10.1016/S0378-7753(01)00807-2.

[11] P. Costamagna, S. Srinivasan, Quantum jumps in the PEMFC science and technology from the 1960s to the year 2000: Part II. Engineering, technology development and application aspects, Journal of Power Sources 102 (2001) 253–269. https://doi.org/10.1016/S0378-7753(01)00808-4.

[12] Briques technologiques et démonstrateurs hydrogène, Agir pour la transition écologique | ADEME (n.d.). https://agirpourlatransition.ademe.fr/entreprises/aides-financieres/20230310/briques-technologiques-demonstrateurs-hydrogene (accessed October 23, 2023).

[13] Présentation de la stratégie nationale pour le développement de l’hydrogène décarboné en France, (n.d.). https://www.economie.gouv.fr/presentation-strategie-nationale-developpement-hydrogene-decarbone-france (accessed October 23, 2023).

[14] European Clean Hydrogen Alliance, (n.d.). https://single-market-economy.ec.europa.eu/industry/strategy/industrial-alliances/european-clean-hydrogen-alliance_en (accessed October 23, 2023).

[15] COMMUNICATION FROM THE COMMISSION TO THE EUROPEAN PARLIAMENT, THE COUNCIL, THE EUROPEAN ECONOMIC AND SOCIAL COMMITTEE AND THE COMMITTEE OF THE REGIONS A hydrogen strategy for a climate-neutral Europe, 2020. https://eur-lex.europa.eu/legal-content/EN/TXT/?uri=CELEX:52020DC0301 (accessed October 22, 2023).

[16] J. Sampson, Hydrogen Insights 2023, Hydrogen Council (2023). https://hydrogencouncil.com/en/hydrogen-insights-2023/ (accessed October 23, 2023).

[17] S. Gottesfeld, T.A. Zawodzinski, Polymer Electrolyte Fuel Cells, in: Advances in Electrochemical Science and Engineering, John Wiley & Sons, Ltd, 1997: pp. 195–301. https://doi.org/10.1002/9783527616794.ch4.

[18] C. Coutanceau, M. Chatenet, D. Jones, G. Maranzana, 12 Materials for proton-exchange fuel cell for mobility and stationary applications, in: 12 Materials for Proton-Exchange Fuel Cell for Mobility and Stationary Applications, De Gruyter, 2021: pp. 399–432. https://doi.org/10.1515/9783110596274-020.

[19] J.K. Nørskov, J. Rossmeisl, A. Logadottir, L. Lindqvist, J.R. Kitchin, T. Bligaard, H. Jónsson, Origin of the Overpotential for Oxygen Reduction at a Fuel-Cell Cathode, J. Phys. Chem. B 108 (2004) 17886–17892. https://doi.org/10.1021/jp047349j.

[20] V. Tripković, E. Skúlason, S. Siahrostami, J.K. Nørskov, J. Rossmeisl, The oxygen reduction reaction mechanism on Pt(111) from density functional theory calculations, Electrochimica Acta 55 (2010) 7975–7981. https://doi.org/10.1016/j.electacta.2010.02.056.

[21] A. Damjanovic, V. Brusic, Electrode kinetics of oxygen reduction on oxide-free platinum electrodes, Electrochimica Acta 12 (1967) 615–628. https://doi.org/10.1016/0013-4686(67)85030-8.

[22] V. Stamenkovic, T.J. Schmidt, N.M. Markovic, P.N. Ross, Surface composition effects in electrocatalysis: Kinetics of oxygen reduction on well-defined Pt{sub 3}Ni and Pt{sub 3}Co alloy surfaces, Journal of Physical Chemistry B: Materials, Surfaces, Interfaces, Amp Biophysical 106 (2002). https://doi.org/10.1021/jp021182h.

[23] E.A. Ticianelli, C.R. Derouin, A. Redondo, S. Srinivasan, Methods to Advance Technology of Proton Exchange Membrane Fuel Cells, J. Electrochem. Soc. 135 (1988) 2209–2214. https://doi.org/10.1149/1.2096240.

[24] M. Chatenet, L. Dubau, N. Job, F. Maillard, The (electro)catalyst|membrane interface in the Proton Exchange Membrane Fuel Cell: Similarities and differences with non-

electrochemical Catalytic Membrane Reactors, Catalysis Today 156 (2010) 76–86. https://doi.org/10.1016/j.cattod.2010.02.028.

[25] Y. Takasu, N. Ohashi, X.-G. Zhang, Y. Murakami, H. Minagawa, S. Sato, K. Yahikozawa, Size effects of platinum particles on the electroreduction of oxygen, Electrochimica Acta 41 (1996) 2595–2600. https://doi.org/10.1016/0013-4686(96)00081-3.

[26] O. Antoine, Y. Bultel, R. Durand, P. Ozil, Electrocatalysis, diffusion and ohmic drop in PEMFC: Particle size and spatial discrete distribution effects, Electrochimica Acta 43 (1998) 3681–3691. https://doi.org/10.1016/S0013-4686(98)00126-1.

[27] O. Antoine, Y. Bultel, R. Durand, Oxygen reduction reaction kinetics and mechanism on platinum nanoparticles inside Nafion®, Journal of Electroanalytical Chemistry 499 (2001) 85–94. https://doi.org/10.1016/S0022-0728(00)00492-7.

[28] B.E. Conway, G. Jerkiewicz, Relation of energies and coverages of underpotential and overpotential deposited H at Pt and other metals to the ‘volcano curve’ for cathodic H2 evolution kinetics, Electrochimica Acta 45 (2000) 4075–4083. https://doi.org/10.1016/S0013-4686(00)00523-5.

[29] J. Greeley, I.E.L. Stephens, A.S. Bondarenko, T.P. Johansson, H.A. Hansen, T.F. Jaramillo, J. Rossmeisl, I. Chorkendorff, J.K. Nørskov, Alloys of platinum and early transition metals as oxygen reduction electrocatalysts, Nature Chem 1 (2009) 552–556. https://doi.org/10.1038/nchem.367.

[30] N. Markovic, H. Gasteiger, Kinetics of Oxygen Reduction on Pt(hkl) Electrodes: Implications for the Crystallite Size Effect with Supported Pt Electrocatalysts, J. Electrochem. Soc. 144 (1997).

[31] C. Chen, Y. Kang, Z. Huo, Z. Zhu, W. Huang, H.L. Xin, J.D. Snyder, D. Li, J.A. Herron, M. Mavrikakis, M. Chi, K.L. More, Y. Li, N.M. Markovic, G.A. Somorjai, P. Yang, V.R. Stamenkovic, Highly Crystalline Multimetallic Nanoframes with Three-Dimensional Electrocatalytic Surfaces, Science 343 (2014) 1339–1343. https://doi.org/10.1126/science.1249061.

[32] X. Huang, Z. Zhao, L. Cao, Y. Chen, E. Zhu, Z. Lin, M. Li, A. Yan, A. Zettl, Y.M. Wang, X. Duan, T. Mueller, Y. Huang, High-performance transition metal–doped Pt_3Ni octahedra for oxygen reduction reaction, Science 348 (2015) 1230–1234. https://doi.org/10.1126/science.aaa8765.

[33] C. Cui, L. Gan, M. Heggen, S. Rudi, P. Strasser, Compositional segregation in shaped Pt alloy nanoparticles and their structural behaviour during electrocatalysis, Nature Mater 12 (2013) 765–771. https://doi.org/10.1038/nmat3668.

[34] M. Wakisaka, Y. Hyuga, K. Abe, H. Uchida, M. Watanabe, Facile preparation and electrochemical behavior of Pt100−xCox(111) single-crystal electrodes in 0.1 M HClO4, Electrochemistry Communications 13 (2011) 317–320. https://doi.org/10.1016/j.elecom.2011.01.013.

[35] M. Wakisaka, S. Morishima, Y. Hyuga, H. Uchida, M. Watanabe, Electrochemical behavior of Pt–Co(111), (100) and (110) alloy single-crystal electrodes in 0.1 M HClO4 and 0.05 M H2SO4 solution as a function of Co content, Electrochemistry Communications 18 (2012) 55–57. https://doi.org/10.1016/j.elecom.2012.02.008.

[36] T. Toda, H. Igarashi, H. Uchida, M. Watanabe, Enhancement of the Electroreduction of Oxygen on Pt Alloys with Fe, Ni, and Co, J. Electrochem. Soc. 146 (1999) 3750–3756. https://doi.org/10.1149/1.1392544.

[37] N. Wakabayashi, M. Takeichi, H. Uchida, M. Watanabe, Temperature Dependence of Oxygen Reduction Activity at Pt−Fe, Pt−Co, and Pt−Ni Alloy Electrodes, J. Phys. Chem. B 109 (2005) 5836–5841. https://doi.org/10.1021/jp046204+.

[38] H. Yano, M. Kataoka, H. Yamashita, H. Uchida, M. Watanabe, Oxygen Reduction Activity of Carbon-Supported Pt−M (M = V, Ni, Cr, Co, and Fe) Alloys Prepared by Nanocapsule Method, Langmuir 23 (2007) 6438–6445. https://doi.org/10.1021/la070078u.

[39] M. Wakisaka, S. Mitsui, Y. Hirose, K. Kawashima, H. Uchida, M. Watanabe, Electronic Structures of Pt−Co and Pt−Ru Alloys for CO-Tolerant Anode Catalysts in Polymer Electrolyte Fuel Cells Studied by EC−XPS, J. Phys. Chem. B 110 (2006) 23489–23496. https://doi.org/10.1021/jp0653510.

[40] L. Dubau, F. Maillard, M. Chatenet, J. André, E. Rossinot, Nanoscale compositional changes and modification of the surface reactivity of Pt3Co/C nanoparticles during proton-exchange membrane fuel cell operation, Electrochimica Acta 56 (2010) 776–783. https://doi.org/10.1016/j.electacta.2010.09.038.

[41] L. Dubau, T. Asset, R. Chattot, C. Bonnaud, V. Vanpeene, J. Nelayah, F. Maillard, Tuning the Performance and the Stability of Porous Hollow PtNi/C Nanostructures for the Oxygen Reduction Reaction, ACS Catal. 5 (2015) 5333–5341. https://doi.org/10.1021/acscatal.5b01248.

[42] M. Wakisaka, S. Kobayashi, S. Morishima, Y. Hyuga, D.A. Tryk, M. Watanabe, A. Iiyama, H. Uchida, Unprecedented dependence of the oxygen reduction activity on Co content at Pt Skin/Pt–Co(111) single crystal electrodes, Electrochemistry Communications 67 (2016) 47–50. https://doi.org/10.1016/j.elecom.2016.03.015.

[43] S. Kobayashi, M. Aoki, M. Wakisaka, T. Kawamoto, R. Shirasaka, K. Suda, D.A. Tryk, J. Inukai, T. Kondo, H. Uchida, Atomically Flat Pt Skin and Striking Enrichment of Co in Underlying Alloy at Pt$_3$Co(111) Single Crystal with Unprecedented Activity for the Oxygen Reduction Reaction, ACS Omega 3 (2018) 154–158. https://doi.org/10.1021/acsomega.7b01793.

[44] H. Yano, N. Takao, M. Arao, M. Matsumoto, T. Itoh, H. Imai, A. Iiyama, J. Inukai, H. Uchida, Potential Cycle-Induced Change in the Crystal Structure of a Pt-Skin/PtCo Alloy Nanostructured Electrocatalyst for Fuel Cells, ACS Appl. Nano Mater. 2 (2019) 7473–7477. https://doi.org/10.1021/acsanm.9b02251.

[45] T. Yoshida, K. Kojima, Toyota MIRAI Fuel Cell Vehicle and Progress Toward a Future Hydrogen Society, Electrochem. Soc. Interface 24 (2015) 45. https://doi.org/10.1149/2.F03152if.

[46] T. Yoshizumi, H. Kubo, M. Okumura, Development of High-Performance FC Stack for the New MIRAI, in: 2021: pp. 2021-01–0740. https://doi.org/10.4271/2021-01-0740.

[47] L. Dubau, J. Durst, F. Maillard, L. Guétaz, M. Chatenet, J. André, E. Rossinot, Further insights into the durability of Pt3Co/C electrocatalysts: Formation of “hollow” Pt nanoparticles induced by the Kirkendall effect, Electrochimica Acta 56 (2011) 10658–10667. https://doi.org/10.1016/j.electacta.2011.03.073.

[48] L. Dubau, M. Lopez-Haro, J. Durst, L. Guétaz, P. Bayle-Guillemaud, M. Chatenet, F. Maillard, Beyond conventional electrocatalysts: hollow nanoparticles for improved and sustainable oxygen reduction reaction activity, J. Mater. Chem. A 2 (2014) 18497–18507. https://doi.org/10.1039/C4TA03975K.

[49] T. Asset, R. Chattot, J. Nelayah, N. Job, L. Dubau, F. Maillard, Structure-Activity Relationships for the Oxygen Reduction Reaction in Porous Hollow PtNi/C Nanoparticles, ChemElectroChem 3 (2016) 1591–1600. https://doi.org/10.1002/celc.201600300.

[50] R. Chattot, O. Le Bacq, V. Beermann, S. Kühl, J. Herranz, S. Henning, L. Kühn, T. Asset, L. Guétaz, G. Renou, J. Drnec, P. Bordet, A. Pasturel, A. Eychmüller, T.J. Schmidt, P. Strasser, L. Dubau, F. Maillard, Surface distortion as a unifying concept and descriptor in oxygen reduction reaction electrocatalysis, Nature Mater 17 (2018) 827–833. https://doi.org/10.1038/s41563-018-0133-2.

[51] A. Ly, T. Asset, P. Atanassov, Integrating nanostructured Pt-based electrocatalysts in proton exchange membrane fuel cells, Journal of Power Sources 478 (2020) 228516. https://doi.org/10.1016/j.jpowsour.2020.228516.

[52] Hydrogen and Fuel Cell Technologies Office Multi-Year Research, Development, and Demonstration Plan, Energy.Gov (n.d.). https://www.energy.gov/eere/fuelcells/articles/hydrogen-and-fuel-cell-technologies-office-multi-year-research-development (accessed April 13, 2023).

[53] New Energy and Industrial Technology Development Organization, (n.d.). https://www.nedo.go.jp/english/ (accessed October 24, 2023).

[54] T. Suzuki, A. Iiyama, N. Kubo, N. Saito, K. Shinohara, S. Shimotori, Y. Sugawara, K. Yamada, (Invited) Toward the Future Fuel Cell -Challenge for 2040-, ECS Trans. 92 (2019) 3. https://doi.org/10.1149/09208.0003ecst.

[55] F. GLOAGUEN, R. DURAND, Simulations of PEFC cathodes: an effectiveness factor approach, Journal of Applied Electrochemistry 27 (1997) 1029–1035. https://doi.org/10.1023/A:1018478324564.

[56] Y. Bultel, P. Ozil, R. Durand, Modelling the mode of operation of PEMFC electrodes at the particle level: influence of ohmic drop within the active layer on electrode performance,

Journal of Applied Electrochemistry 28 (1998) 269–276. https://doi.org/10.1023/A:1003207514936.

[57] K. Kinoshita, Carbon: electrochemical and physicochemical properties, (1988). https://www.osti.gov/biblio/6047751 (accessed October 24, 2023).

[58] F. Maillard, P.A. Simonov, E.R. Savinova, Carbon Materials as Supports for Fuel Cell Electrocatalysts, in: P. Serp, J.L. Figueiredo (Eds.), Carbon Materials for Catalysis, John Wiley & Sons, Inc., Hoboken, NJ, USA, 2008: pp. 429–480. https://doi.org/10.1002/9780470403709.ch12.

[59] L. Castanheira, W.O. Silva, F.H.B. Lima, A. Crisci, L. Dubau, Carbon Corrosion in Proton-Exchange Membrane Fuel Cells: Effect of the Carbon Structure, the Degradation Protocol, and the Gas Atmosphere, ACS Catal. (2015).

[60] T. Mittermeier, A. Weiß, F. Hasché, G. Hübner, H.A. Gasteiger, PEM Fuel Cell Start-up/Shut-down Losses vs Temperature for Non-Graphitized and Graphitized Cathode Carbon Supports, J. Electrochem. Soc. 164 (2017) F127–F137. https://doi.org/10.1149/2.1061702jes.

[61] K. Kodama, A. Shinohara, N. Hasegawa, K. Shinozaki, R. Jinnouchi, T. Suzuki, T. Hatanaka, Y. Morimoto, Catalyst Poisoning Property of Sulfonimide Acid Ionomer on Pt (111) Surface, J. Electrochem. Soc. 161 (2014) F649. https://doi.org/10.1149/2.051405jes.

[62] H. Jinnai, R.J. Spontak, T. Nishi, Transmission Electron Microtomography and Polymer Nanostructures, Macromolecules 43 (2010) 1675–1688. https://doi.org/10.1021/ma902035p.

[63] T. Takeshita, Y. Kamitaka, K. Shinozaki, K. Kodama, Y. Morimoto, Evaluation of ionomer coverage on Pt catalysts in polymer electrolyte membrane fuel cells by CO stripping voltammetry and its effect on oxygen reduction reaction activity, Journal of Electroanalytical Chemistry 871 (2020) 114250. https://doi.org/10.1016/j.jelechem.2020.114250.

[64] M. Ko, E. Padgett, V. Yarlagadda, A. Kongkanand, D.A. Muller, Revealing the Nanostructure of Mesoporous Fuel Cell Catalyst Supports for Durable, High-Power Performance, J. Electrochem. Soc. 168 (2021) 024512. https://doi.org/10.1149/1945-7111/abe28e.

[65] V. Yarlagadda, M.K. Carpenter, T.E. Moylan, R.S. Kukreja, R. Koestner, W. Gu, L. Thompson, A. Kongkanand, Boosting Fuel Cell Performance with Accessible Carbon Mesopores, ACS Energy Lett. 3 (2018) 618–621. https://doi.org/10.1021/acsenergylett.8b00186.

[66] M. Tempelaere, M. Zimmermann, M. Chatenet, 3D-structured electrocatalysts for improved mass-transfer in proton-exchange membrane fuel cell cathodes, Current Opinion in Electrochemistry 41 (2023) 101353. https://doi.org/10.1016/j.coelec.2023.101353.

[67] S. Murata, M. Imanishi, S. Hasegawa, R. Namba, Vertically aligned carbon nanotube electrodes for high current density operating proton exchange membrane fuel cells, Journal of Power Sources 253 (2014) 104–113. https://doi.org/10.1016/j.jpowsour.2013.11.073.

[68] C. Lee, W.J.M. Kort-Kamp, H. Yu, D.A. Cullen, B.M. Patterson, T.A. Arman, S. Komini Babu, R. Mukundan, R.L. Borup, J.S. Spendelow, Grooved electrodes for high-power-density fuel cells, Nat Energy 8 (2023) 685–694. https://doi.org/10.1038/s41560-023-01263-2.

[69] A. Ghielmi, P. Vaccarono, C. Troglia, V. Arcella, Proton exchange membranes based on the short-side-chain perfluorinated ionomer, Journal of Power Sources 145 (2005) 108–115. https://doi.org/10.1016/j.jpowsour.2004.12.068.

[70] M. Emery, M. Frey, M. Guerra, G. Haugen, K. Hintzer, K.H. Lochhaas, P. Pham, D. Pierpont, M. Schaberg, A. Thaler, M. Yandrasits, S. Hamrock, The Development of New Membranes for Proton Exchange Membrane Fuel Cells, ECS Trans. 11 (2007) 3. https://doi.org/10.1149/1.2780909.

[71] R. Jinnouchi, K. Kudo, K. Kodama, N. Kitano, T. Suzuki, S. Minami, K. Shinozaki, N. Hasegawa, A. Shinohara, The role of oxygen-permeable ionomer for polymer electrolyte fuel cells, Nat Commun 12 (2021) 4956. https://doi.org/10.1038/s41467-021-25301-3.

[72] A. Kusoglu, A.Z. Weber, New Insights into Perfluorinated Sulfonic-Acid Ionomers, Chem. Rev. 117 (2017) 987–1104. https://doi.org/10.1021/acs.chemrev.6b00159.

[73] M. Uchida, PEFC catalyst layers: Effect of support microstructure on both distributions of Pt and ionomer and cell performance and durability, Current Opinion in Electrochemistry 21 (2020) 209–218. https://doi.org/10.1016/j.coelec.2020.02.019.

[74] A. Kongkanand, M.F. Mathias, The Priority and Challenge of High-Power Performance of Low-Platinum Proton-Exchange Membrane Fuel Cells, J. Phys. Chem. Lett. 7 (2016) 1127–1137. https://doi.org/10.1021/acs.jpclett.6b00216.

[75] K. Malek, M. Eikerling, Q. Wang, T. Navessin, Z. Liu, Self-Organization in Catalyst Layers of Polymer Electrolyte Fuel Cells, J. Phys. Chem. C 111 (2007) 13627–13634. https://doi.org/10.1021/jp072692k.

[76] K. Malek, T. Mashio, M. Eikerling, Microstructure of Catalyst Layers in PEM Fuel Cells Redefined: A Computational Approach, Electrocatal 2 (2011) 141–157. https://doi.org/10.1007/s12678-011-0047-0.

[77] W. Olbrich, T. Kadyk, U. Sauter, M. Eikerling, Review—Wetting Phenomena in Catalyst Layers of PEM Fuel Cells: Novel Approaches for Modeling and Materials Research, J. Electrochem. Soc. 169 (2022) 054521. https://doi.org/10.1149/1945-7111/ac6e8b.

[78] A. Katzenberg, A. Chowdhury, M. Fang, A.Z. Weber, Y. Okamoto, A. Kusoglu, M.A. Modestino, Highly Permeable Perfluorinated Sulfonic Acid Ionomers for Improved Electrochemical Devices: Insights into Structure–Property Relationships, J. Am. Chem. Soc. 142 (2020) 3742–3752. https://doi.org/10.1021/jacs.9b09170.

[79] N. Macauley, R.D. Lousenberg, M. Spinetta, S. Zhong, F. Yang, W. Judge, V. Nikitin, A. Perego, Y. Qi, S. Pedram, J. Jankovic, I.V. Zenyuk, H. Xu, Highly Durable Fluorinated High Oxygen Permeability Ionomers for Proton Exchange Membrane Fuel Cells, Advanced Energy Materials 12 (2022) 2201063. https://doi.org/10.1002/aenm.202201063.

[80] J.P. Braaten, N.N. Kariuki, D.J. Myers, S. Blackburn, G. Brown, A. Park, S. Litster, Integration of a high oxygen permeability ionomer into polymer electrolyte membrane fuel cell cathodes for high efficiency and power density, Journal of Power Sources 522 (2022) 230821. https://doi.org/10.1016/j.jpowsour.2021.230821.

[81] F.D. Coms, H. Liu, J.E. Owejan, Mitigation of Perfluorosulfonic Acid Membrane Chemical Degradation Using Cerium and Manganese Ions, ECS Trans. 16 (2008) 1735. https://doi.org/10.1149/1.2982015.

[82] F. Coms, C. Gittleman, A. Brenner, R. Jiang, US Patent for Chemical durability using synergystic mitigation strategies Patent (Patent # 9,083,050 issued July 14, 2015) - Justia Patents Search, (n.d.). https://patents.justia.com/patent/9083050 (accessed October 24, 2023).

[83] M. Watanabe, H. Uchida, Y. Seki, M. Emori, P. Stonehart, Self-Humidifying Polymer Electrolyte Membranes for Fuel Cells, J. Electrochem. Soc. 143 (1996) 3847–3852. https://doi.org/10.1149/1.1837307.

[84] L. Daniel, A. Bonakdarpour, D.P. Wilkinson, Benefits of platinum deposited in the polymer membrane subsurface on the operational flexibility of hydrogen fuel cells, Journal of Power Sources 471 (2020) 228418. https://doi.org/10.1016/j.jpowsour.2020.228418.

[85] A. Ohma, K. Shinohara, A. Iiyama, T. Yoshida, A. Daimaru, Membrane and Catalyst Performance Targets for Automotive Fuel Cells by FCCJ Membrane, Catalyst, MEA WG, ECS Trans. 41 (2011) 775. https://doi.org/10.1149/1.3635611.

[86] S. Stariha, N. Macauley, B.T. Sneed, D. Langlois, K.L. More, R. Mukundan, R.L. Borup, Recent Advances in Catalyst Accelerated Stress Tests for Polymer Electrolyte Membrane Fuel Cells, J. Electrochem. Soc. 165 (2018) F492–F501. https://doi.org/10.1149/2.0881807jes.

[87] B.T. Sneed, D.A. Cullen, R. Mukundan, R.L. Borup, K.L. More, PtCo Cathode Catalyst Morphological and Compositional Changes after PEM Fuel Cell Accelerated Stress Testing, J. Electrochem. Soc. 165 (2018) F3078–F3084. https://doi.org/10.1149/2.0091806jes.

[88] R.L. Borup, J.R. Davey, F.H. Garzon, D.L. Wood, M.A. Inbody, PEM fuel cell electrocatalyst durability measurements, Journal of Power Sources 163 (2006) 76–81. https://doi.org/10.1016/j.jpowsour.2006.03.009.

[89] F.A. de Bruijn, V.A.T. Dam, G.J.M. Janssen, Review: Durability and Degradation Issues of PEM Fuel Cell Components, Fuel Cells 8 (2008) 3–22. https://doi.org/10.1002/fuce.200700053.

[90] B. Vion-Dury, M. Chatenet, L. Guétaz, F. Maillard, Determination of Aging Markers and their Use as a Tool to Characterize Pt/C Nanoparticles Degradation Mechanism in Model PEMFC Cathode Environment, ECS Trans. 41 (2011) 697. https://doi.org/10.1149/1.3635604.

[91] E.F. Holby, W. Sheng, Y. Shao-Horn, D. Morgan, Pt nanoparticle stability in PEM fuel cells: influence of particle size distribution and crossover hydrogen, Energy Environ. Sci. 2 (2009) 865–871. https://doi.org/10.1039/B821622N.

[92] P.J. Ferreira, G.J. la O', Y. Shao-Horn, D. Morgan, R. Makharia, S. Kocha, H.A. Gasteiger, Instability of Pt ⁄ C Electrocatalysts in Proton Exchange Membrane Fuel Cells: A Mechanistic Investigation, J. Electrochem. Soc. 152 (2005) A2256. https://doi.org/10.1149/1.2050347.

[93] E. Padgett, V. Yarlagadda, M.E. Holtz, M. Ko, B.D.A. Levin, R.S. Kukreja, J.M. Ziegelbauer, R.N. Andrews, J. Ilavsky, A. Kongkanand, D.A. Muller, Mitigation of PEM Fuel Cell Catalyst Degradation with Porous Carbon Supports, J. Electrochem. Soc. 166 (2019) F198–F207. https://doi.org/10.1149/2.0371904jes.

[94] X. Tuaev, S. Rudi, P. Strasser, The impact of the morphology of the carbon support on the activity and stability of nanoparticle fuel cell catalysts, Catal. Sci. Technol. 6 (2016) 8276–8288. https://doi.org/10.1039/C6CY01679K.

[95] E. Guilminot, A. Corcella, F. Charlot, F. Maillard, M. Chatenet, Detection of Pt z + Ions and Pt Nanoparticles Inside the Membrane of a Used PEMFC, J. Electrochem. Soc. 154 (2006) B96. https://doi.org/10.1149/1.2388863.

[96] T. Akita, A. Taniguchi, J. Maekawa, Z. Siroma, K. Tanaka, M. Kohyama, K. Yasuda, Analytical TEM study of Pt particle deposition in the proton-exchange membrane of a membrane-electrode-assembly, Journal of Power Sources (2006).

[97] E. Guilminot, A. Corcella, M. Chatenet, F. Maillard, F. Charlot, G. Berthomé, C. Iojoiu, J.-Y. Sanchez, E. Rossinot, E. Claude, Membrane and Active Layer Degradation upon PEMFC Steady-State Operation: I. Platinum Dissolution and Redistribution within the MEA, J. Electrochem. Soc. 154 (2007) B1106. https://doi.org/10.1149/1.2775218.

[98] R.L. Borup, A. Kusoglu, K.C. Neyerlin, R. Mukundan, R.K. Ahluwalia, D.A. Cullen, K.L. More, A.Z. Weber, D.J. Myers, Recent developments in catalyst-related PEM fuel cell durability, Current Opinion in Electrochemistry 21 (2020) 192–200. https://doi.org/10.1016/j.coelec.2020.02.007.

[99] M. Pourbaix, H. Zhang, A. Pourbaix, Presentation of an Atlas of Chemical and Electrochemical Equilibria in the Precence of a Gaseous Phase, Materials Science Forum 251–254 (1997) 143–148. https://doi.org/10.4028/www.scientific.net/MSF.251-254.143.

[100] L. Dubau, F. Maillard, M. Chatenet, L. Guetaz, J. André, E. Rossinot, Durability of Pt3Co / C Cathodes in a 16 Cell PEMFC Stack: Macro/Microstructural Changes and Degradation Mechanisms, J. Electrochem. Soc. 157 (2010) B1887. https://doi.org/10.1149/1.3485104.

[101] J. Durst, M. Chatenet, F. Maillard, Impact of metal cations on the electrocatalytic properties of Pt/C nanoparticles at multiple phase interfaces, Phys. Chem. Chem. Phys. 14 (2012) 13000. https://doi.org/10.1039/c2cp42191g.

[102] C. Bas, N.D. Albérola, L. Flandin, Effects of contaminant on thermal properties in perfluorinated sulfonic acid membranes, Journal of Membrane Science 363 (2010) 67–71. https://doi.org/10.1016/j.memsci.2010.07.001.

[103] J. Braaten, A. Kongkanand, S. Litster, Oxygen Transport Effects of Cobalt Cation Contamination of Ionomer Thin Films in Proton Exchange Membrane Fuel Cells, ECS Trans. 80 (2017) 283–290. https://doi.org/10.1149/08008.0283ecst.

[104] C. Lee, X. Wang, J.-K. Peng, A. Katzenberg, R.K. Ahluwalia, A. Kusoglu, S. Komini Babu, J.S. Spendelow, R. Mukundan, R.L. Borup, Toward a Comprehensive Understanding of Cation Effects in Proton Exchange Membrane Fuel Cells, ACS Appl. Mater. Interfaces 14 (2022) 35555–35568. https://doi.org/10.1021/acsami.2c07085.

[105] C. Bas, L. Flandin, A.-S. Danerol, E. Claude, E. Rossinot, N.D. Alberola, Changes in the chemical structure and properties of a perfluorosulfonated acid membrane induced by fuel-cell operation, Journal of Applied Polymer Science 117 (2010) 2121–2132. https://doi.org/10.1002/app.31386.

[106] E. Moukheiber, C. Bas, L. Flandin, Understanding the formation of pinholes in PFSA membranes with the essential work of fracture (EWF), International Journal of Hydrogen Energy 39 (2014) 2717–2723. https://doi.org/10.1016/j.ijhydene.2013.03.031.

[107] L. Dubau, L. Castanheira, F. Maillard, M. Chatenet, O. Lottin, G. Maranzana, J. Dillet, A. Lamibrac, J. Perrin, E. Moukheiber, A. ElKaddouri, G. De Moor, C. Bas, L. Flandin, N. Caqué, A review of PEM fuel cell durability: materials degradation, local heterogeneities of aging and possible mitigation strategies, WIREs Energy Environ. 3 (2014) 540–560. https://doi.org/10.1002/wene.113.

[108] G. De Moor, C. Bas, N. Charvin, E. Moukheiber, F. Niepceron, N. Breilly, J. André, E. Rossinot, E. Claude, N.D. Albérola, L. Flandin, Understanding Membrane Failure in PEMFC: Comparison of Diagnostic Tools at Different Observation Scales, Fuel Cells 12 (2012) 356–364. https://doi.org/10.1002/fuce.201100161.

[109] L. Dubau, L. Castanheira, M. Chatenet, F. Maillard, J. Dillet, G. Maranzana, S. Abbou, O. Lottin, G. De Moor, A. El Kaddouri, C. Bas, L. Flandin, E. Rossinot, N. Caqué, Carbon corrosion induced by membrane failure: The weak link of PEMFC long-term performance, International Journal of Hydrogen Energy 39 (2014) 21902–21914. https://doi.org/10.1016/j.ijhydene.2014.07.099.

[110] L. Dubau, L. Castanheira, G. Berthomé, F. Maillard, An identical-location transmission electron microscopy study on the degradation of Pt/C nanoparticles under oxidizing, reducing and neutral atmosphere, Electrochimica Acta 110 (2013) 273–281. https://doi.org/10.1016/j.electacta.2013.03.184.

[111] Y. Shao-Horn, W.C. Sheng, S. Chen, P.J. Ferreira, E.F. Holby, D. Morgan, Instability of Supported Platinum Nanoparticles in Low-Temperature Fuel Cells, Top Catal 46 (2007) 285–305. https://doi.org/10.1007/s11244-007-9000-0.

[112] M.F. Mathias, R. Makharia, H.A. Gasteiger, J.J. Conley, T. Fuller, C. Gittleman, S.S. Kocha, Two Fuel Cell Cars In Every Garage?, Electrochem. Soc. Interface 14 (2005) 24. https://doi.org/10.1149/2.F05053IF.

[113] J. Dillet, D. Spernjak, A. Lamibrac, G. Maranzana, R. Mukundan, J. Fairweather, S. Didierjean, R.L. Borup, O. Lottin, Impact of flow rates and electrode specifications on degradations during repeated startups and shutdowns in polymer-electrolyte membrane fuel cells, Journal of Power Sources 250 (2014) 68–79. https://doi.org/10.1016/j.jpowsour.2013.10.141.

[114] L.M. Roen, C.H. Paik, T.D. Jarvi, Electrocatalytic Corrosion of Carbon Support in PEMFC Cathodes, Electrochem. Solid-State Lett. 7 (2003) A19. https://doi.org/10.1149/1.1630412.

[115] J. Durst, A. Lamibrac, F. Charlot, J. Dillet, L.F. Castanheira, G. Maranzana, L. Dubau, F. Maillard, M. Chatenet, O. Lottin, Degradation heterogeneities induced by repetitive start/stop events in proton exchange membrane fuel cell: Inlet vs. outlet and channel vs. land, Applied Catalysis B: Environmental 138–139 (2013) 416–426. https://doi.org/10.1016/j.apcatb.2013.03.021.

[116] K. More, R. Borup, K. Reeves, Identifying Contributing Degradation Phenomena in PEM Fuel Cell Membrane Electride Assemblies Via Electron Microscopy, ECS Trans. 3 (2006) 717. https://doi.org/10.1149/1.2356192.

[117] K.L. More, Microstructural Characterization Of PEM Fuel Cell MEAs, (2006).

[118] L. Dubau, J. Durst, F. Maillard, M. Chatenet, J. André, E. Rossinot, Heterogeneities of Aging within a PEMFC MEA, Fuel Cells 12 (2012) 188–198. https://doi.org/10.1002/fuce.201100073.

[119] M.B. Sassin, Y. Garsany, B.D. Gould, K. Swider-Lyons, Impact of Compressive Stress on MEA Pore Structure and Its Consequence on PEMFC Performance, J. Electrochem. Soc. 163 (2016) F808–F815. https://doi.org/10.1149/2.0291608jes.

[120] M.B. Sassin, Y. Garsany, R.W. Atkinson, R.M.E. Hjelm, K.E. Swider-Lyons, Understanding the interplay between cathode catalyst layer porosity and thickness on transport limitations en route to high-performance PEMFCs, International Journal of Hydrogen Energy 44 (2019) 16944–16955. https://doi.org/10.1016/j.ijhydene.2019.04.194.

[121] Y. Garsany, R.W. Atkinson, B.D. Gould, K.E. Swider-Lyons, High power, Low-Pt membrane electrode assemblies for proton exchange membrane fuel cells, Journal of Power Sources 408 (2018) 38–45. https://doi.org/10.1016/j.jpowsour.2018.10.073.

[122] R.K.F. Della Bella, B.M. Stühmeier, H.A. Gasteiger, Universal Correlation between Cathode Roughness Factor and H2 /Air Performance Losses in Voltage Cycling-Based Accelerated Stress Tests, J. Electrochem. Soc. 169 (2022) 044528. https://doi.org/10.1149/1945-7111/ac67b8.

[123] L. Castanheira, L. Dubau, F. Maillard, Accelerated Stress Tests of Pt/HSAC Electrocatalysts: an Identical-Location Transmission Electron Microscopy Study on the Influence of Intermediate Characterizations, Electrocatalysis 5 (2014) 125–135. https://doi.org/10.1007/s12678-013-0173-y.

[124] R. Makharia, M.F. Mathias, D.R. Baker, Measurement of Catalyst Layer Electrolyte Resistance in PEFCs Using Electrochemical Impedance Spectroscopy, J. Electrochem. Soc. 152 (2005) A970. https://doi.org/10.1149/1.1888367.

[125] Y. Liu, M.W. Murphy, D.R. Baker, W. Gu, C. Ji, J. Jorne, H.A. Gasteiger, Proton Conduction and Oxygen Reduction Kinetics in PEM Fuel Cell Cathodes: Effects of Ionomer-to-Carbon Ratio and Relative Humidity, Journal of The Electrochemical Society (n.d.).

[126] T. Gaumont, Résistance protonique d’électrodes de piles à combustible à membrane (PEMFC) : effets de l’humidité et des dégradations, These de doctorat, Université de Lorraine, 2017. https://www.theses.fr/2017LORR0002 (accessed October 2, 2023).

[127] T. Gaumont, Measurement of protonic resistance of catalyst layers as a tool for degradation monitoring, Internationaljournalofhydrogenenergy (2017).

[128] F. Chabot, Analyse de la structure et des propriétés du conducteur protonique des électrodes de PEMFC par diffusion de neutrons aux petits angles et par électrochimie : impact des cycles accélérés de dégradations, These de doctorat, Université Grenoble Alpes, 2022. https://www.theses.fr/2022GRALI085 (accessed October 2, 2023).

[129] O. Antoine, R. Durand, RRDE study of oxygen reduction on Pt nanoparticles inside Nafion: H2O2 production in PEMFC cathode conditions, Journal of Applied Electrochemistry 30 (2000) 839–844. https://doi.org/10.1023/A:1003999818560.

[130] C.C. Herrmann, G.G. Perrault, A.A. Pilla, Dual reference electrode for electrochemical pulse studies, Anal. Chem. 40 (1968) 1173–1174. https://doi.org/10.1021/ac60263a011.

[131] M. Tregaro, Electrocatalyseurs de l’oxydation de l’hydrogène en présence de polluants - Application à la purification/compression de l’hydrogène, These de doctorat, Université Grenoble Alpes, 2021. https://www.theses.fr/2021GRALI067 (accessed October 2, 2023).

[132] L. Pan, S. Ott, F. Dionigi, P. Strasser, Current challenges related to the deployment of shape-controlled Pt alloy oxygen reduction reaction nanocatalysts into low Pt-loaded cathode layers of proton exchange membrane fuel cells, Current Opinion in Electrochemistry 18 (2019) 61–71. https://doi.org/10.1016/j.coelec.2019.10.011.

[133] R. Riasse, C. Lafforgue, F. Vandenberghe, F. Micoud, A. Morin, M. Arenz, J. Durst, M. Chatenet, Benchmarking proton exchange membrane fuel cell cathode catalyst at high current density: A comparison between the rotating disk electrode, the gas diffusion electrode and differential cell, Journal of Power Sources 556 (2023) 232491. https://doi.org/10.1016/j.jpowsour.2022.232491.

[134] Warsaw University, Department of Chemistry, Pasteura 1, 02-093 Warsaw, Poland, M. Łukaszewski, Electrochemical Methods of Real Surface Area Determination of Noble Metal Electrodes – an Overview, Int. J. Electrochem. Sci. (2016) 4442–4469. https://doi.org/10.20964/2016.06.71.

[135] M. Chatenet, L. Guétaz, F. Maillard, Electron Microscopy to Study MEA Materials and Structure Degradation, in: Handbook of Fuel Cells – Vol. 6, H. A. Gasteiger, W. Vielstich and H. Yokokawa Eds., John Wiley & Sons, Chichester, 2009: pp. 844–860.

[136] L. Reimer, Particle Optics of Electrons, in: L. Reimer (Ed.), Transmission Electron Microscopy: Physics of Image Formation and Microanalysis, Springer, Berlin, Heidelberg, 1993: pp. 19–49. https://doi.org/10.1007/978-3-662-21556-2_2.

[137] Electron Beam Sample interactions, (n.d.). Wikimedia Commons. at <https://commons.wikimedia.org/wiki/File:Electron_Interaction_with_Matter.svg>.

[138] S. Trasatti, O.A. Petrii, Real surface area measurements in electrochemistry, Journal of Electroanalytical Chemistry 327 (1992) 353–376. https://doi.org/10.1016/0022-0728(92)80162-W.

[139] A. Renouprez, SMALL ANGLE SCATTERING OF X-RAYS, in: D.H. Everett, R.H. Ottewill (Eds.), Surface Area Determination, Butterworth-Heinemann, 1970: pp. 361–367. https://doi.org/10.1016/B978-0-408-70077-1.50036-1.

[140] P. Scherrer, Bestimmung der Größe und der inneren Struktur von Kolloidteilchen mittels Röntgenstrahlen, Nachr. Ges. Wiss (1918) 98–100.

[141] M.A. Pimenta, G. Dresselhaus, M.S. Dresselhaus, A. Jorio, R. Saito, Studying disorder in graphite-based systems by Raman spectroscopyw, (2007).

[142] T. Yoda, H. Uchida, M. Watanabe, Effects of operating potential and temperature on degradation of electrocatalyst layer for PEFCs, Electrochimica Acta 52 (2007) 5997–6005. https://doi.org/10.1016/j.electacta.2007.03.049.

[143] M. Hara, M. Lee, C.-H. Liu, B.-H. Chen, Y. Yamashita, M. Uchida, H. Uchida, M. Watanabe, Electrochemical and Raman spectroscopic evaluation of Pt/graphitized carbon black catalyst durability for the start/stop operating condition of polymer electrolyte fuel cells, Electrochimica Acta 70 (2012) 171–181. https://doi.org/10.1016/j.electacta.2012.03.043.

[144] S. Ünsal, R. Girod, C. Appel, D. Karpov, M. Mermoux, F. Maillard, V.A. Saveleva, V. Tileli, T.J. Schmidt, J. Herranz, Decoupling the Contributions of Different Instability Mechanisms to the PEMFC Performance Decay of Non-noble Metal O2-Reduction Catalysts, J. Am. Chem. Soc. (2023).

[145] W. Vielstich, A. Lamm, H.A. Gasteiger, eds., Handbook of fuel cells: fundamentals, technology, and applications, Wiley, Chichester, England ; New York, 2003.

[146] F. Jaouen, J. Herranz, M. Lefevre, J.-P. Dodelet, U.I. Kramm, I. Herrmann, P. Bogdanoff, J. Maruyama, T. Nagaoka, A. Garsuch, J.R. Dahn, T. Olson, S. Pylypenko, P. Atanassov, E.A. Ustinov, Cross-Laboratory Experimental Study of Non-Noble-Metal Electrocatalysts for the Oxygen Reduction Reaction, 1 (2009).

[147] K. Artyushkova, M.J. Workman, I. Matanovic, M.J. Dzara, C. Ngo, S. Pylypenko, A. Serov, P. Atanassov, Role of Surface Chemistry on Catalyst/Ionomer Interactions for Transition

Metal–Nitrogen–Carbon Electrocatalysts, ACS Appl. Energy Mater. 1 (2018) 68–77. https://doi.org/10.1021/acsaem.7b00002.

[148] C. Roiron, Catalyseurs sans platine à base de cryogels de carbone pour la réaction de réduction de l'oxygène dans les PEMFC, phdthesis, Université Grenoble Alpes [2020-....], 2021. https://theses.hal.science/tel-03513064 (accessed October 6, 2023).

[149] V. Gridin, J. Du, S. Haller, P. Theis, K. Hofmann, G.K.H. Wiberg, U.I. Kramm, M. Arenz, GDE vs RDE: Impact of operation conditions on intrinsic catalytic parameters of FeNC catalyst for the oxygen reduction reaction, Electrochimica Acta (2023) 142012. https://doi.org/10.1016/j.electacta.2023.142012.

[150] S. Ünsal, Catalyst Aggregate Size Effect on the Mass Transport Properties of Non-Noble Metal Catalyst Layers for PEMFC Cathodes, Journal of The Electrochemical Society (2023).

[151] B.G. Pollet, Let's Not Ignore the Ultrasonic Effects on the Preparation of Fuel Cell Materials, Electrocatalysis 5 (2014) 330–343. https://doi.org/10.1007/s12678-014-0211-4.

[152] M.B. Sassin, Y. Garsany, B.D. Gould, K.E. Swider-Lyons, Fabrication Method for Laboratory-Scale High-Performance Membrane Electrode Assemblies for Fuel Cells, Anal. Chem. 89 (2017) 511–518. https://doi.org/10.1021/acs.analchem.6b03005.

[153] B.G. Pollet, S.S. Kocha, Using Ultrasound to Effectively Homogenise Catalyst Inks: Is this Approach Still Acceptable? : Recommendations on the use of ultrasound for mixing catalyst inks, Johnson Matthey Technology Review 66 (2022) 61–76. https://doi.org/10.1595/205651321X16196162869695.

[154] I. Takahashi, S.S. Kocha, Examination of the activity and durability of PEMFC catalysts in liquid electrolytes, Journal of Power Sources 195 (2010) 6312–6322. https://doi.org/10.1016/j.jpowsour.2010.04.052.

[155] Y. Garsany, I.L. Singer, K.E. Swider-Lyons, Impact of film drying procedures on RDE characterization of Pt/VC electrocatalysts, Journal of Electroanalytical Chemistry 662 (2011) 396–406. https://doi.org/10.1016/j.jelechem.2011.09.016.

[156] Y. Garsany, J. Ge, J. St-Pierre, R. Rocheleau, K.E. Swider-Lyons, Analytical Procedure for Accurate Comparison of Rotating Disk Electrode Results for the Oxygen Reduction Activity of Pt/C, J. Electrochem. Soc. 161 (2014) F628–F640. https://doi.org/10.1149/2.036405jes.

[157] T. Lazaridis, B.M. Stühmeier, H.A. Gasteiger, H.A. El-Sayed, Capabilities and limitations of rotating disk electrodes versus membrane electrode assemblies in the investigation of electrocatalysts, Nat Catal 5 (2022) 363–373. https://doi.org/10.1038/s41929-022-00776-5.

[158] O. Antoine, Y. Bultel, R. Durand, Oxygen reduction reaction kinetics and mechanism on platinum nanoparticles inside Nafion®, Journal of Electroanalytical Chemistry 499 (2001) 85–94. https://doi.org/10.1016/S0022-0728(00)00492-7.

[159] Y. Bultel, L. Genies, O. Antoine, P. Ozil, R. Durand, Modeling impedance diagrams of active layers in gas diffusion electrodes: diffusion, ohmic drop effects and multistep reactions,

Journal of Electroanalytical Chemistry 527 (2002) 143–155. https://doi.org/10.1016/S0022-0728(02)00835-5.

[160] J. Bett, K. Kinoshita, K. Routsis, P. Stonehart, A comparison of gas-phase and electrochemical measurements for chemisorbed carbon monoxide and hydrogen on platinum crystallites, Journal of Catalysis 29 (1973) 160–168. https://doi.org/10.1016/0021-9517(73)90214-5.

[161] P. Stonehart, P.N. Ross, The use of porous electrodes to obtain kinetic rate constants for rapid reactions and adsorption isotherms of poisons, Electrochimica Acta 21 (1976) 441–445. https://doi.org/10.1016/0013-4686(76)85123-7.

[162] C.M. Zalitis, D. Kramer, A.R. Kucernak, Electrocatalytic performance of fuel cell reactions at low catalyst loading and high mass transport, Phys. Chem. Chem. Phys. 15 (2013) 4329. https://doi.org/10.1039/c3cp44431g.

[163] C.M. Zalitis, J. Sharman, E. Wright, A.R. Kucernak, Properties of the hydrogen oxidation reaction on Pt/C catalysts at optimised high mass transport conditions and its relevance to the anode reaction in PEFCs and cathode reactions in electrolysers, Electrochimica Acta 176 (2015) 763–776. https://doi.org/10.1016/j.electacta.2015.06.146.

[164] C. Jackson, L.F.J.M. Raymakers, M.J.J. Mulder, A.R.J. Kucernak, Assessing electrocatalyst hydrogen activity and CO tolerance: Comparison of performance obtained using the high mass transport ‘floating electrode’ technique and in electrochemical hydrogen pumps, Applied Catalysis B: Environmental 268 (2020) 118734. https://doi.org/10.1016/j.apcatb.2020.118734.

[165] C. Jackson, X. Lin, P.B.J. Levecque, A.R.J. Kucernak, Toward Understanding the Utilization of Oxygen Reduction Electrocatalysts under High Mass Transport Conditions and High Overpotentials, ACS Catal. 12 (2022) 200–211. https://doi.org/10.1021/acscatal.1c03908.

[166] C. Lafforgue, F. Vandenberghe, R. Riasse, M. Tregaro, M. Heitzmann, P. Schott, J.-F. Blachot, F. Micoud, M. Chatenet, (Invited) Benchmarking Carbon-Supported Pt-Based Oxygen Reduction Reaction Electrocatalysts for PEMFC Cathodes, Meet. Abstr. MA2020-02 (2020) 2319. https://doi.org/10.1149/MA2020-02362319mtgabs.

[167] G.K.H. Wiberg, M. Fleige, M. Arenz, Gas diffusion electrode setup for catalyst testing in concentrated phosphoric acid at elevated temperatures, Review of Scientific Instruments 86 (2015) 024102. https://doi.org/10.1063/1.4908169.

[168] B.A. Pinaud, A. Bonakdarpour, L. Daniel, J. Sharman, D.P. Wilkinson, Key Considerations for High Current Fuel Cell Catalyst Testing in an Electrochemical Half-Cell, J. Electrochem. Soc. 164 (2017) F321–F327. https://doi.org/10.1149/2.0891704jes.

[169] M. Inaba, A.W. Jensen, G.W. Sievers, M. Escudero-Escribano, A. Zana, M. Arenz, Benchmarking high surface area electrocatalysts in a gas diffusion electrode: measurement of oxygen reduction activities under realistic conditions, Energy Environ. Sci. 11 (2018) 988–994. https://doi.org/10.1039/C8EE00019K.

[170] S. Alinejad, J. Quinson, J. Schröder, J.J.K. Kirkensgaard, M. Arenz, Carbon-Supported Platinum Electrocatalysts Probed in a Gas Diffusion Setup with Alkaline Environment: How Particle Size and Mesoscopic Environment Influence the Degradation Mechanism, ACS Catal. 10 (2020) 13040–13049. https://doi.org/10.1021/acscatal.0c03184.

[171] J. Schröder, J. Quinson, J.K. Mathiesen, J.J.K. Kirkensgaard, S. Alinejad, V.A. Mints, K.M.Ø. Jensen, M. Arenz, A New Approach to Probe the Degradation of Fuel Cell Catalysts under Realistic Conditions: Combining Tests in a Gas Diffusion Electrode Setup with Small Angle X-ray Scattering, J. Electrochem. Soc. 167 (2020) 134515. https://doi.org/10.1149/1945-7111/abbdd2.

[172] K. Ehelebe, D. Seeberger, M.T.Y. Paul, S. Thiele, K.J.J. Mayrhofer, S. Cherevko, Evaluating Electrocatalysts at Relevant Currents in a Half-Cell: The Impact of Pt Loading on Oxygen Reduction Reaction, J. Electrochem. Soc. 166 (2019) F1259–F1268. https://doi.org/10.1149/2.0911915jes.

[173] K. Ehelebe, J. Knöppel, M. Bierling, B. Mayerhöfer, T. Böhm, N. Kulyk, S. Thiele, K.J.J. Mayrhofer, S. Cherevko, Platinum Dissolution in Realistic Fuel Cell Catalyst Layers, Angew. Chem. Int. Ed. 60 (2021) 8882–8888. https://doi.org/10.1002/anie.202014711.

[174] D. Zhang, J. Du, J. Quinson, M. Arenz, On the electro-oxidation of small organic molecules: Towards a fuel cell catalyst testing platform based on gas diffusion electrode setups, Journal of Power Sources 522 (2022) 230979. https://doi.org/10.1016/j.jpowsour.2022.230979.

[175] K. Ehelebe, N. Schmitt, G. Sievers, A.W. Jensen, A. Hrnjić, P. Collantes Jiménez, P. Kaiser, M. Geuß, Y.-P. Ku, P. Jovanovič, K.J.J. Mayrhofer, B. Etzold, N. Hodnik, M. Escudero-Escribano, M. Arenz, S. Cherevko, Benchmarking Fuel Cell Electrocatalysts Using Gas Diffusion Electrodes: Inter-lab Comparison and Best Practices, ACS Energy Lett. 7 (2022) 816–826. https://doi.org/10.1021/acsenergylett.1c02659.

[176] M. Fontana, Direct growth of carbon nanotubes forests on carbon fibers to replace microporous layers in proton exchange membrane fuel cells, (2021).

[177] P. Lauf, V. Lloret, M. Geuß, C.C. Collados, M. Thommes, K.J.J. Mayrhofer, K. Ehelebe, S. Cherevko, Characterization of Oxygen and Ion Mass Transport Resistance in Fuel Cell Catalyst Layers in Gas Diffusion Electrode Setups, Journal of The Electrochemical Society (2023).

[178] N.C. Röttcher, Y.-P. Ku, M. Minichova, K. Ehelebe, S. Cherevko, Comparison of methods to determine electrocatalysts' surface area in gas diffusion electrode setups: a case study on Pt/C and PtRu/C, J. Phys. Energy 5 (2023) 024007. https://doi.org/10.1088/2515-7655/acbe1b.

[179] J. Durst, C. Simon, F. Hasché, H.A. Gasteiger, Hydrogen Oxidation and Evolution Reaction Kinetics on Carbon Supported Pt, Ir, Rh, and Pd Electrocatalysts in Acidic Media, J. Electrochem. Soc. 162 (2015) F190–F203. https://doi.org/10.1149/2.0981501jes.

[180] S. Gilman, Measurement of hydrogen adsorption by the multipulse potentiodynamic (mpp) method, Journal of Electroanalytical Chemistry (1959) 7 (1964) 382–391. https://doi.org/10.1016/0022-0728(64)80026-7.

[181] F. Maillard, S. Schreier, M. Hanzlik, E.R. Savinova, S. Weinkauf, U. Stimming, Influence of particle agglomeration on the catalytic activity of carbon-supported Pt nanoparticles in CO monolayer oxidation, Phys. Chem. Chem. Phys. 7 (2005) 385–393. https://doi.org/10.1039/B411377B.

[182] F. Maillard, E.R. Savinova, U. Stimming, CO monolayer oxidation on Pt nanoparticles: Further insights into the particle size effects, Journal of Electroanalytical Chemistry 599 (2007) 221–232. https://doi.org/10.1016/j.jelechem.2006.02.024.

[183] H.A. Gasteiger, S.S. Kocha, B. Sompalli, F.T. Wagner, Activity benchmarks and requirements for Pt, Pt-alloy, and non-Pt oxygen reduction catalysts for PEMFCs, Applied Catalysis B: Environmental 56 (2005) 9–35. https://doi.org/10.1016/j.apcatb.2004.06.021.

[184] S.K. Roy, M.E. Orazem, B. Tribollet, Interpretation of Low-Frequency Inductive Loops in PEM Fuel Cells, J. Electrochem. Soc. 154 (2007) B1378. https://doi.org/10.1149/1.2789377.

[185] S.K. Roy, M.E. Orazem, Error Analysis of the Impedance Response of PEM Fuel Cells, J. Electrochem. Soc. 154 (2007) B883. https://doi.org/10.1149/1.2747533.

[186] S. Kabir, D.J. Myers, N. Kariuki, J. Park, G. Wang, A. Baker, N. Macauley, R. Mukundan, K.L. More, K.C. Neyerlin, Elucidating the Dynamic Nature of Fuel Cell Electrodes as a Function of Conditioning: An ex Situ Material Characterization and in Situ Electrochemical Diagnostic Study, ACS Appl. Mater. Interfaces 11 (2019) 45016–45030. https://doi.org/10.1021/acsami.9b11365.

[187] S. Touhami, M. Crouillere, J. Mainka, J. Dillet, C. Nayoze-Coynel, C. Bas, L. Dubau, A. El Kaddouri, F. Dubelley, F. Micoud, M. Chatenet, Y. Bultel, O. Lottin, Anode defects' propagation in polymer electrolyte membrane fuel cells, Journal of Power Sources 520 (2022) 230880. https://doi.org/10.1016/j.jpowsour.2021.230880.

[188] S. Nösberger, Using a pressurized GDE setup to analyze effects of temperature and relative humidity on CO-stripping measurements on a commercial Pt/C ORR catalyst, Electrochemistry Communications (2023).

[189] C.A. Reiser, L. Bregoli, T.W. Patterson, J.S. Yi, J.D. Yang, M.L. Perry, T.D. Jarvi, A Reverse-Current Decay Mechanism for Fuel Cells, Electrochem. Solid-State Lett. 8 (2005) A273. https://doi.org/10.1149/1.1896466.

[190] R. Makharia, S. Kocha, P. Yu, M.A. Sweikart, W. Gu, F. Wagner, H.A. Gasteiger, Durable PEM Fuel Cell Electrode Materials: Requirements and Benchmarking Methodologies, ECS Trans. 1 (2006) 3–18. https://doi.org/10.1149/1.2214540.

[191] S. Komini Babu, D. Spernjak, J. Dillet, A. Lamibrac, G. Maranzana, S. Didierjean, O. Lottin, R.L. Borup, R. Mukundan, Spatially resolved degradation during startup and shutdown

in polymer electrolyte membrane fuel cell operation, Applied Energy 254 (2019) 113659. https://doi.org/10.1016/j.apenergy.2019.113659.

[192] J. Zhang, B.A. Litteer, W. Gu, H. Liu, H.A. Gasteiger, Effect of Hydrogen and Oxygen Partial Pressure on Pt Precipitation within the Membrane of PEMFCs, J. Electrochem. Soc. 154 (2007) B1006. https://doi.org/10.1149/1.2764240.

[193] M. Ronovsky, L. Pan, M. Klingenhof, I. Martens, L. Fusek, P. Kus, R. Chattot, M. Mirolo, F. Dionigi, H. Burdett, J. Sharman, P. Strasser, A.M. Bonastre, J. Drnec, Assessing Utilization Boundaries for Pt-Based Catalysts in an Operating Proton-Exchange Membrane Fuel Cell, ACS Appl. Energy Mater. 6 (2023) 8660–8665. https://doi.org/10.1021/acsaem.3c01243.

[194] Z. Zhao, L. Castanheira, L. Dubau, G. Berthomé, A. Crisci, F. Maillard, Carbon corrosion and platinum nanoparticles ripening under open circuit potential conditions, Journal of Power Sources 230 (2013) 236–243. https://doi.org/10.1016/j.jpowsour.2012.12.053.

[195] F. Maillard, L. Dubau, J. Durst, M. Chatenet, J. André, E. Rossinot, Durability of Pt3Co/C nanoparticles in a proton-exchange membrane fuel cell: Direct evidence of bulk Co segregation to the surface, Electrochemistry Communications 12 (2010) 1161–1164. https://doi.org/10.1016/j.elecom.2010.06.007.

[196] M.K. Debe, A.K. Schmoeckel, G.D. Vernstrom, R. Atanasoski, High voltage stability of nanostructured thin film catalysts for PEM fuel cells, Journal of Power Sources 161 (2006) 1002–1011. https://doi.org/10.1016/j.jpowsour.2006.05.033.

[197] D.J.S. Sandbeck, M. Inaba, J. Quinson, J. Bucher, A. Zana, M. Arenz, S. Cherevko, Particle Size Effect on Platinum Dissolution: Practical Considerations for Fuel Cells, ACS Appl. Mater. Interfaces 12 (2020) 25718–25727. https://doi.org/10.1021/acsami.0c02801.

[198] D.J.S. Sandbeck, N.M. Secher, F.D. Speck, J.E. Sørensen, J. Kibsgaard, I. Chorkendorff, S. Cherevko, Particle Size Effect on Platinum Dissolution: Considerations for Accelerated Stability Testing of Fuel Cell Catalysts, ACS Catal. 10 (2020) 6281–6290. https://doi.org/10.1021/acscatal.0c00779.

[199] R. Borup, J. Meyers, B. Pivovar, Y.S. Kim, R. Mukundan, N. Garland, D. Myers, M. Wilson, F. Garzon, D. Wood, P. Zelenay, K. More, K. Stroh, T. Zawodzinski, J. Boncella, J.E. McGrath, M. Inaba, K. Miyatake, M. Hori, K. Ota, Z. Ogumi, S. Miyata, A. Nishikata, Z. Siroma, Y. Uchimoto, K. Yasuda, K. Kimijima, N. Iwashita, Scientific Aspects of Polymer Electrolyte Fuel Cell Durability and Degradation, Chem. Rev. 107 (2007) 3904–3951. https://doi.org/10.1021/cr050182l.

[200] A.B. LaConti, H. Liu, C. Mittelsteadt, R.C. McDonald, POLYMER ELECTROLYTE MEMBRANE DEGRADATION MECHANISMS IN FUEL CELLS – FINDINGS OVER THE PAST 30 YEARS AND COMPARISON WITH ELECTROLYZERS, ECS Transactions (2006).

[201] M. Inaba, T. Kinumoto, M. Kiriake, R. Umebayashi, A. Tasaka, Z. Ogumi, Gas crossover and membrane degradation in polymer electrolyte fuel cells, Electrochimica Acta (2006).

[202] V.O. Mittal, H.R. Kunz, J.M. Fenton, Membrane Degradation Mechanisms in PEMFCs, J. Electrochem. Soc. 154 (2007) B652. https://doi.org/10.1149/1.2734869.

[203] C. Iojoiu, E. Guilminot, F. Maillard, M. Chatenet, J.-Y. Sanchez, E. Claude, E. Rossinot, Membrane and Active Layer Degradation Following PEMFC Steady-State Operation: II. Influence of on Membrane Properties, J. Electrochem. Soc. 154 (2007) B1115. https://doi.org/10.1149/1.2775282.

[204] J.Y. Howe, C.J. Rawn, L.E. Jones, H. Ow, Improved crystallographic data for graphite, Powder Diffraction 18 (2003) 150–154. https://doi.org/10.1154/1.1536926.

[205] T. Soboleva, X. Zhao, K. Malek, Z. Xie, T. Navessin, S. Holdcroft, On the Micro-, Meso-, and Macroporous Structures of Polymer Electrolyte Membrane Fuel Cell Catalyst Layers, ACS Appl. Mater. Interfaces 2 (2010) 375–384. https://doi.org/10.1021/am900600y.

[206] T. Soboleva, K. Malek, Z. Xie, T. Navessin, S. Holdcroft, PEMFC Catalyst Layers: The Role of Micropores and Mesopores on Water Sorption and Fuel Cell Activity, ACS Appl. Mater. Interfaces 3 (2011) 1827–1837. https://doi.org/10.1021/am200590w.

[207] S. Proch, K. Kodama, M. Inaba, K. Oishi, N. Takahashi, Y. Morimoto, The “Particle Proximity Effect” in Three Dimensions: a Case Study on Vulcan XC 72R, Electrocatalysis 7 (2016) 249–261. https://doi.org/10.1007/s12678-016-0302-5.

[208] F.B. Spingler, A. Phillips, T. Schuler, M.C. Tucker, A.Z. Weber, Investigating fuel-cell transport limitations using hydrogen limiting current, International Journal of Hydrogen Energy 42 (2017) 13960–13969. https://doi.org/10.1016/j.ijhydene.2017.01.036.

[209] T. Schuler, A. Chowdhury, A.T. Freiberg, B. Sneed, F.B. Spingler, M.C. Tucker, K.L. More, C.J. Radke, A.Z. Weber, Fuel-Cell Catalyst-Layer Resistance via Hydrogen Limiting-Current Measurements, J. Electrochem. Soc. 166 (2019) F3020–F3031. https://doi.org/10.1149/2.0031907jes.

[210] J.W.M. Frenken, P. Stoltze, Are Vicinal Metal Surfaces Stable?, PHYSICAL REVIEW LETTERS 82 (1999).

[211] L. Castanheira, L. Dubau, M. Mermoux, G. Berthome, N. Caque, E. Rossinot, M. Chatenet, Carbon Corrosion in Proton-Exchange Membrane Fuel Cells: From Model Experiments to Real-Life Operation in Membrane Electrode Assemblies, ACS Catal. (2014).

[212] T.V. Reshetenko, J. St-Pierre, Separation Method for Oxygen Mass Transport Coefficient in Gas and Ionomer Phases in PEMFC GDE, Journal of The Electrochemical Society (2014).

Résumé and Abstract

La prise de conscience progressive à l'échelle mondiale de la nécessaire limitation des rejets de gaz à effet de serre induit un engouement important pour le développement des piles à combustible comme générateur électrochimique appliqué au domaine des transports légers et lourds. Cependant, l'essor de ce type de système ne peut se faire qu'en élaborant de meilleurs catalyseurs pour le cœur de pile, l'assemblage membrane-électrodes (AME). Cette amélioration passe par la recherche de performances plus élevées ainsi que d'une durée de vie plus importante des matériaux et assemblages.

Ce travail s'intéresse en premier lieu à l'établissement, à l'échelle du laboratoire, d'un protocole portant sur une électrode à gaz (GDE) permettant la détermination, dans des conditions modèles mais toutefois les plus représentatives possibles du système réel, des performances de matériaux état de l'art et/ou synthétisés en interne. Une partie importante des travaux de cette thèse s'articule également sur des tests de durabilité de catalyseurs commerciaux. Ces études sont réalisées selon deux visions de test différentes. La dégradation accélérée d'un Pt_3Co/VC suivant des protocoles établis à l'échelle mondiale (US DoE et FCCJ) montre l'importance du domaine de tension dans lequel évolue l'AME, autant au niveau de la borne supérieure qu'inférieure. La seconde étude est réalisée à tension de cellule contrôlée (constante) pour évaluer et comprendre les mécanismes de dégradation d'un catalyseur Pt/VC. Ces études sont réalisées en alliant mesures électrochimiques en banc de test et analyse des matériaux ; elles révèlent l'importance du contrôle de la tension d'une cellule, ce qui implique de mettre l'AME au cœur des considérations de gestion d'un système réel.

The worldwide and progressive awareness of the necessity to limit greenhouse gases emissions lead to a general enthusiasm on the development of fuel cells as electrochemical generators, to address the field of light and heavy transportation. However, the rise of this kind of system cannot avoid the production of better catalyst and better engineered membrane-electrodes assemblies (MEA), the core of the system. This improvement comes by accessing both higher performances and durability.

This work is firstly focused on the development at the lab scale of a test protocol on a gas diffusion electrode (GDE) enabling the determination, in model but nevertheless as representative as possible of a real system, of the performance of state-of-the-art or lab-synthesized materials. A major part of this thesis work addresses durability tests on commercial catalysts. These studies are realised with two scopes in mind. The accelerated stress test of Pt_3Co/VC following established globally used protocols (US DoE and FCCJ) shows the importance of the voltage range in which the MEA is working, both for the lower and upper voltage boundaries. The second study is done at controlled cell voltage to evaluate and understand the degradation mechanisms of a Pt/VC catalyst. These studies are realised using both electrochemical measurements on a test bench and *post-mortem* analyses of the materials and reveal the significance of the cell voltage control, which implies to put the MEA at the heart of a system balance of plant.